NORTHWESTERN UNIVERSITY

The Influence of Covalency on Spin-Orbit Coupling Transfer Through Metal-Metal Bonds

A DISSERTATION

SUBMITTED TO THE GRADUATE SCHOOL
IN PARTIAL FULFULLIMENT OF THE REQUIREMENTS

for the degree

DOCTOR OF PHILOSOPHY

Field of Chemistry

By

Scott Christopher Coste

EVANSTON, ILLINOIS

September 2019

ABSTRACT

The Influence of Covalency on Spin-Orbit Coupling Transfer Through Metal-Metal Bonds

Scott Christopher Coste

Spin-orbit coupling (SOC) is a powerful phenomenon that dictates the functional properties of transition metal complexes essential for information processing, catalysis, and magnetism. Though it is relegated to lower energy scales within the orbital description of first-row transition metal complexes, SOC impacts crucial aspects of electronic structure such as promoting spin-forbidden processes. Therefore, developing approaches to modulate SOC in first-row metal complexes would propel our fundamental understanding of electronic structure and allow tailoring of metal complexes to the aforementioned applications. An attractive platform to probe the nature of SOC relies on using heterobimetallic complexes where we can systematically alter specific parameters through synthetic design. In this approach, heavy main group metals, such as tin, act as ligands to first-row transition metals as an external source of SOC. This splits the key components of SOC onto two different metals which each can be independently varied and interrogated. We hypothesize this metal-metal bond covalency directly affects the transferal of SOC between the two atoms. In this dissertation, I design and explore systems to test how metal-ligand covalency influences SOC through magnetic anisotropy. Chapter 1 will discuss the interplay of ligand field and SOC contributions towards magnetic anisotropy through a review of the literature, and how I approached assessing the influence of covalency on magnetic anisotropy using heavy group 14 metal donors. Chapter 2 explores how subtle control over the local coordination environment influences magnetic anisotropy allowing us to tailor first-row transition metal complexes towards

two different applications, molecular magnetism and quantum information processing. Chapter 3 reports a study highlighting the importance of spin-orbital overlap with ligand donor orbitals in ionic versus covalently bound heavy donor atoms. Chapter 4 outlines an approach to studying the influence of metal-metal bond covalency using ligand field theory in complexes with high-spin ground states. In Chapter 5, I spectroscopically probe covalency and periodic trends in a series of high-spin tin-transition metal complexes. Using the aggregate experimental data, I investigate how these periodic trends influence SOC transfer from tin using a molecular orbital approach.

ACKNOWLEDGEMENTS

I would like to start by acknowledging my Ph.D. advisor, Prof. Danna Freedman. I am greatly indebted for the opportunity to have worked as one of her earlier students and watch the lab flourish into an amazing research group. Your immeasurable care for your students has allowed me to grow into the scientist I am now through your countless advice, unconditional support, and character-defining challenges. I want to thank you for everything you have provided. I would also like to thank my committee members, Prof. Thomas O'Halloran, Prof. Mercouri Kanatzidis, and Prof. Omar Farha for their advice, support, and constructive criticism over the course of my graduate experience. I also thank Prof. Tom Meade for serving as chair on my qualifying exam.

Over the past 6 years, I am grateful to have had the privilege to work alongside many bright, insightful, and experienced scientific collaborators who helped me flourish as a scientist. I would like to thank Prof. Bess Vlaisavljevich for her instrumental work as a theory collaborator. I want to thank Dr. Michael Hu, Dr. E. Ercan Alp, and Dr. Dale Brewe for their help with X-ray spectroscopy and scattering measurements at the Advanced Photon Source. Additionally, I would like to thank Dr. Johan van Tol, Dr. Andrew Ozarowski, Prof. Stephen Hill, and Dr. Matthew Krzyaniak for their assistance and insight with electron paramagnetic resonance spectroscopy. I would also like to thank Charlotte Stern and Dr. Christos Malliakas for their help and expertise with X-ray diffraction.

I am deeply grateful for mentors who have put up with me over the years and provided me with indispensable advice. I am lucky to have had Prof. Joe Zadrozny, Prof. John Anderson, and Nicolaas Vermeulen bestow their scientific, professional, and personal advice upon me which

allowed me to develop and grow at home and in lab. You have all guided me through critical points in my scientific career and are amazing role models as a scientist I hope to become one day.

Words cannot express the gratitude I owe to the friends I met during my time in graduate school. Particularly, I need to acknowledge Dr. Majed Fataftah (the other pillar) and Dr. Sam Clarke who were there for me through the best of times and the worst of times. I also need to thank other colleagues in the Freedman and Harris labs throughout my time at Northwestern. I would not have persevered if it weren't for your continued support and friendship throughout the whole process. This includes Dr. Michael Graham, Ryan Klein, Dr. James Walsh, Dr. Jordan DeGayner, Arash Banisafar, Dr. Audrey Gallagher, Dr. Kang Du, Dr. Alexandra Gaudette, Tyler Pearson, Raymund Yu, Kelsey Collins, Alison Altman, Daniel Laorenza, Jeremy Moses Amdur, and everyone else who I have had the pleasure to work with. Outside of our immediate lab, I would also like to thank Ian Gibbs-Hall, Mr. Steve, Alex Lou, David Barsoum, Joe Accardo, Dr. Andrea Carlini, Edon Vitaku, Dr. Chris Forman, and Dr. Matthew Moschitto. Outside of the department, I would like to thank my bouldering team (50 Sends!) Sammy Sarett, Tomas Andreani, Eileen Bui, Cody and Krissy Vinci, and Mahreen Mahgul. I would also like to thank Jennifer Zhu for your support, love, and companionship. You were all my family away from home.

Most importantly, I need to thank my family who without, I would not be where I am today. The lifelong support, guidance, and unconditional love of my parents, Cathy and Randy, and step-parents, Cathy and Kevin, allowed me to achieve my goals of becoming a scientist. I also want to acknowledge those who shaped my scientific curiosities over the years including Grandma Gin, Mark Provost, Grandpa Pierre, Grandma Marilyn, Dave Havlik, and David and Marilyn Paulus. I am also grateful to my best buds at home Adam, Chris, Jon, and Michael for all the fun times

throughout the years and hopefully more to come. Lastly, I wanted to make a special acknowledgement for my brother Kevin Coste who has shaped my life in so many ways. You were always there for me, even to teach me my first lessons in chemistry.

LIST OF ABBREVIATIONS

AOM	Angular overlap model
Bu	Butyl
CASPT2	Complete active space from second order perturbation theory
CASSCF	Complete active space self-consistent field
18c6	18-crown-6
DFT	Density functional theory
EBO	Effective bond order
EPR	Electron paramagnetic resonance
Et_2O	Diethyl ether
LMCT	Ligand to metal charge transfer
MeOH	Methanol
Ph	Phenyl
^{Ph,Me}Tp	Hydrotris(3-phenyl-5-methylpyrazolyl) borate
PPN	Bis(triphenylphosphine)iminum
QIP	Quantum information processing
QTM	Quantum tunneling of the magnetization
SMM	Single-molecule magnet
SOC	Spin-orbit coupling
SOMO	Singly-occupied molecular orbital
SQUID	Superconducting quantum interference device
Tp*	Hydrotris(3,5-dimethylpyrazole)borate

Triphos	1, 1, 1-Tris(diphenylphosphinomethyl)ethane
UV-Vis-NIR	Ultraviolet-visible-near-infrared
XAS	X-ray absorption spectroscopy
XMCD	X-ray magnetic circular dichroism
ZFS	Zero-field splitting

To my friends and family

Table of Contents

List of Figures

List of Tables

Chapter One: Introduction

This section was written in collaboration with the co-authors listed above.

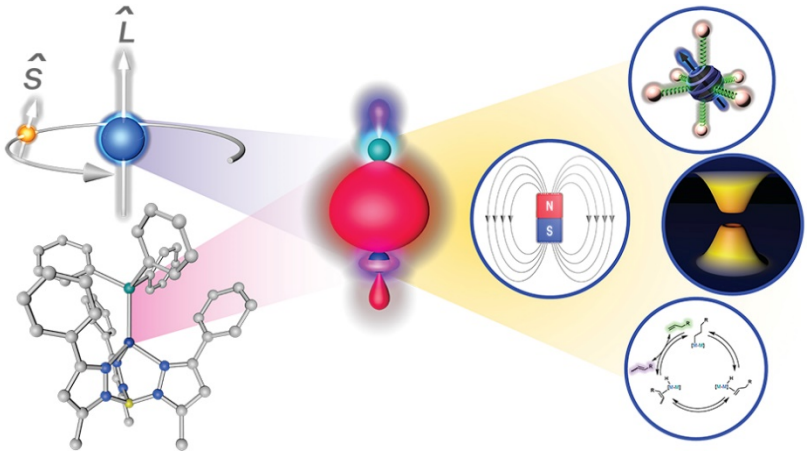

1.1 Background

Spin-orbit coupling (SOC) is a powerful phenomenon which impacts the character and relative energy of atomic orbitals, with more significant effects manifesting in the heavier elements. Fundamentally, SOC can be defined as the interaction between the two key components of a magnetic moment: an electron's spin (*S*) and orbital angular momentum (*L*). SOC is responsible for many effects across a myriad of fields. In core electron-based spectroscopy experiments, for example, spin-orbit coupling is a vital element to describe the electronic structure of orbitals (e.g. $4d_{3/2}$ and $4d_{5/2}$ in gold as found in X-ray photoelectron spectroscopy)[1] and the splitting of yellow sodium D-lines lying at the intersection of astronomy and magnetism.[2,3] Similarly, in condensed matter physics, SOC is crucial in enabling the electronic structure which creates topological insulators by providing an internal magnetic field.[4,5,6]

Closer to inorganic chemistry, SOC is an essential component of the d-orbital manifold description but is frequently relegated to lower energy scale interactions. Despite its relatively small energetic contribution, SOC impacts crucial properties such as magnetism,[7,8] excited state dynamics,[9,10,11] quantum coherence,[12] and catalytic pathway determination.[13,14,15] Within catalysis, SOC enhances intersystem crossing rates, thereby promoting spin-forbidden pathways along a reaction coordinate, accelerating the sluggish cleavage of strong bonds.[16,17] SOC also generates magnetic anisotropy essential for single molecule magnets

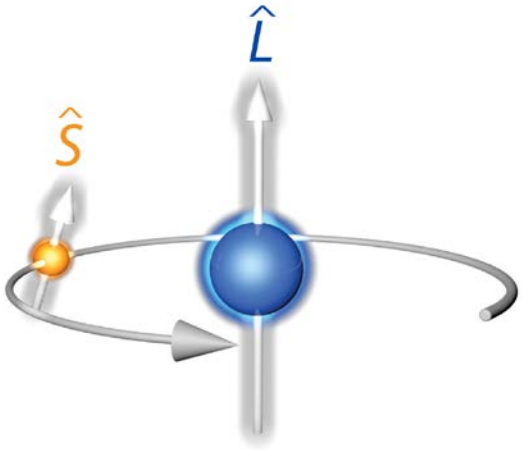

Figure 1.1 An abstract representation of spin-orbit coupling to illustrate the two critical components, an electron's intrinsic spin (*S*) and orbital angular momentum (*L*).

by mediating coupling to excited states, providing molecules with preferred orientation of the magnetization.[18,19,20] Developing new approaches to tune SOC would propel our fundamental understanding of electronic structure in coordination complexes and guide the tailoring of complexes towards such applications.

Transition metal complexes provide an excellent platform to probe the fundamental nature of SOC, especially through the lens of bimetallic complexes. Here, we can isolate a first-row transition metal with weak spin-orbit coupling and bind it to a heavy main-group element, thereby separating the two key components of SOC into two atoms, each of which can be varied and interrogated. The aggregate picture of electronic structure provides insight into the SOC contribution through systematic modulation of the metal-metal interaction. To understand these dynamics, we first must consider each contribution to the energies of the valence orbitals: the ligand field strength, electron-electron repulsion, and SOC. First-row transition metals are sensitive towards each of these parameters. Crucially, in first-row metal complexes, comparable ligand field and electronic repulsion energies also allow for access to high spin states. Additionally, first-row metals feature relatively low SOC due to the nominal Z_{eff}^2 dependence of SOC.[21,22] The combination of these attributes makes them perfectly suited for an investigation of the impact of SOC from heavy elements.

Using heavy diamagnetic elements to modulate SOC has deep precedent, dating back to the well-studied heavy-atom effect, wherein heavy atoms enhance SOC-mediated processes.[23,24] This effect dramatically impacts the photophysical properties of molecules where SOC enhances singlet to triplet transition rates underpinning its importance to luminescent materials. Using diamagnetic elements to impact SOC also has significant precedent within the solid state literature where

unusually large magnetocrystalline anisotropies exist in magnetic materials such as FePt and MnBi.[25–28] Our approach to tune SOC transfer between two metals could provide insight into the properties of such solid state materials through isolation of the fundamental two-atom interaction in a molecule. This model will inform the design of new magnetic materials.

1.1.2 Measuring spin-orbit coupling

As a fundamentally atomic phenomenon directly measuring the SOC component in the d-orbital manifold is challenging in molecular compounds. To ascertain SOC in transition metal complexes, quantifiable properties impacted by SOC such as intersystem crossing rates and magnetic anisotropy can serve as proxies. A powerful approach to measure SOC is through electron paramagnetic resonance (EPR) spectroscopy and superconducting quantum interference device (SQUID) magnetometry, which are capable of probing magnetic anisotropy through the axial zero-field splitting parameter (D), the second-order orbital contribution. In most first-row transition metal complexes, orbital angular momentum is quenched by the ligand field, however, this second-order term incorporates orbital angular momentum into the electronic structure. Zero-field splitting arises through coupling of the ground electronic states to excited states through SOC, which underpins it's use as a proxy. Each excited state's contribution to D is inversely proportional to its energy separation from the ground state and proportional to the effective SOC constant squared, ξ_{eff}^2.[29] Therefore, SOC and the ligand field are delicately intertwined in their contributions to D, underpinning the importance of SOC in electronic structure. Thus, early examples of the heavy-atom effect aimed at probing what chemical factors influenced the spectroscopic signatures of biologically relevant ions. To understand contributions from SOC to D, a comprehensive understanding of the ligand field, electronic structure, and the excited state manifold of the

complex is required. The following examples demonstrate some ways that *D* has seen use as a proxy for SOC and outline some of the challenges of using this parameter to measure SOC.

1.2 The interplay of SOC and ligand field influence on magnetic anisotropy

The influence of SOC on *D* via the heavy-atom effect is best illustrated in high-spin Mn^{2+} complexes. Here, the electronically isotropic $^6A_1$ ground state (depicted in Figure 1.2) is relatively resistant to ligand field changes because all transitions are formally spin-forbidden requiring significant energy to overcome the cost of spin-pairing. Duboc and coworkers observed that the zero-field splitting of Mn^{2+}-halide complexes generally trend as $|D_I| > |D_{Br}| > |D_{Cl}|$, correlating with the halide SOC.[30] Using a combination of EPR spectroscopy and density functional theory (DFT), Neese and coworkers determined that *D* in Mn^{2+}-halide complexes is indeed proportional to the metal and halide SOC contributions, $\zeta_{Mn}\zeta_X$ (where X = Cl, Br, and I).[31,32] The dominance of heavy-ligand SOC on magnetic anisotropy in many Mn^{2+} complexes can be attributed to multiple opposite, but similar in magnitude, contributions to *D* neutralizing each other in the symmetric electronic environment. However, stronger ligand fields can overcome ligand SOC in the isotropic $^6A_1$ ground state by lowering the excited quartet state energies such as in isoelectronic Fe^{3+} porphyrin complexes.[33,34] This implies that the weak ligand field, in conjunction with the electronic symmetry, about Mn^{2+} allows ligand SOC to dominate *D* in these complexes.

In many other first-row transition metal complexes, where the electronic structure is not isotropic, the ligand field can dominate contributions to *D*. This is particularly true for Co^{2+} complexes whose odd electron count can promote large *D* values by introducing energetically low-lying excited states as illustrated in Figure 1.2.[35] Long and coworkers synthesized the series $[Co(EPh)_4]^{2-}$ (E = O, S, and Se), and determined via magnetometry that changing the donor atom

from O to Se yielded an increase in *D* from −11.1(3) to −83(1) cm^{-1}.[36] Thorough investigation of the electronic absorption spectra and concomitant ligand field analysis demonstrated that the trend in *D* correlated with a change in the Racah *B* parameter, reflecting the softness of the ligand donors. Neese and coworkers confirmed through *ab initio* methods that the weaker ligand field of the heavier donors indeed had a greater influence over *D* than the ligand SOC in this system.[37]

In complexes with more metal-ligand covalency, both SOC and ligand field can contribute similarly to *D*.[38,39,40] Experimentally quantifying the effect of ligand SOC on *D* then requires sufficient knowledge of its ligand field influence to deconvolute the two competing factors.

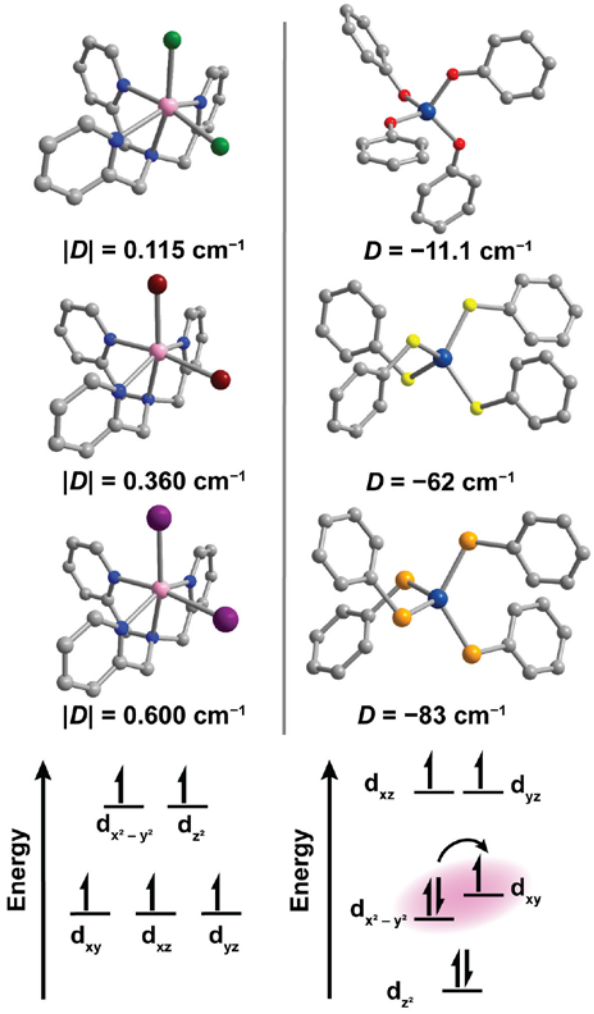

Figure 1.2 Examples of the two extremes of ligand SOC contributions to *D*. The isotropic, weak ligand field of Mn^{2+} allows ligand SOC to govern D whereas the ligand field dominates in the Co^{2+} complexes shown here.[32,36] Pink, cobalt blue, green, burgundy, purple, red, yellow, orange, blue, and gray spheres represent manganese, cobalt, chlorine, bromine, iodine, oxygen, sulfur, selenium, nitrogen, and carbon atoms, respectively, and hydrogen atoms have been omitted for clarity.

Using the rich absorption spectra of $S = 1$ Ni^{2+}, Desrochers and coworkers quantified the differing ligand field strength of axial halide donors in the series [Tp*NiX] (where Tp^{*-} = hydrotris(3,5-dimethylpyrazole)borate and X = Cl^-, Br^-, and I^-).[41] Using EPR spectroscopy, they observed |*D*|

increase from 3.93(2) to 23.01(4) cm^{-1} between the Cl and I congeners, which correlates to the change in halide SOC constants. Through an angular overlap modal (AOM) analysis of the d-d transitions, they determined the ligand field changes throughout the halide series cannot account for the magnetic anisotropy enhancement. Consequently, they showed that the halide SOC facilitates the increase of $|D|$ in the series where the effective SOC constant, ξ_{eff}, of Ni^{2+} exceeds its free-ion value (630 cm^{-1}) by up to 370 cm^{-1} in [Tp*NiI]. Despite a clear change in ligand field affecting *D* throughout a series, this study illustrates how ligand SOC can still play a demonstrable role in magnetic anisotropy.

In addition to the ligand field effects, prior theoretical research supports the chemically intuitive concept that metal-ligand covalency impacts SOC transfer.[39,42] Many experiments on the heavy-atom effect thus far have relied on using electronegative donors to change *D*.[43–47] An intuitive way to engender a more covalent metal-ligand interaction is to use relatively electropositive donors. It is worth noting that several groups have begun exploring this approach using pnictogen and transition metal-based donors.[48,49] Though to maximize the SOC of first-row transition metals, heavier ligands with more covalent interactions are necessary. Specifically, systematic analyses of bonding between heavy main group elements and high-spin paramagnetic transition metals remain scarce in the literature.

1.3 From ligand-based effects to heterobimetallic complexes

Earlier and heavier p-block metals and metalloids are ideal donors to generate covalent bonds to first-row transition metals due to their electropositivity relative to common ligand donors. However, in their most common oxidation states, the p- block elements become more Lewis acidic moving down the groups due to the relativistic contraction of the s-orbitals and radial expansion

of the p orbitals.[50] It is therefore difficult to incorporate such heavy donors into the primary coordination sphere of paramagnetic first-row metals.

A successful approach to facilitate such metal-metal interactions relies on utilizing the supporting framework of scaffold ligands. In an initial attempt to overcome the challenge of stabilizing an interaction between two polycationic ions, we targeted a ligand scaffold that contains two binding pockets capable of accommodating two positively charged metal ions. [51] For this study we used high-spin Mn^{2+} because it has an isotopic electronic structure that is immune to ligand field distortions. This allowed us to comfortably attribute any notable deviations in the magnetic behavior expected for Mn^{2+} to the influence of Bi^{3+}. Towards this end, we used the tripodal nonadentate ligand, 1,1,1-tris[(3-methoxysalicylideneamino)methyl]ethane (H_3L_1), to stabilize an interaction between Mn^{2+} and Bi^{3+}, the heaviest ion stable to radioactive decay (Figure 1.3). The three anionic phenoxy donors provide a bridging support such that the bismuth is in the secondary coordination sphere of Mn^{2+}. Importantly, this ligand enforces the closest Mn^{2+}-Bi^{3+} distance in a paramagnetic heterobimetallic complex, 3.2163(5) Å. Given the high spin-orbit coupling of Bi^{3+}, we anticipated that the Bi^{3+} proximity would have a profound effect on the magnetic properties of this complex.

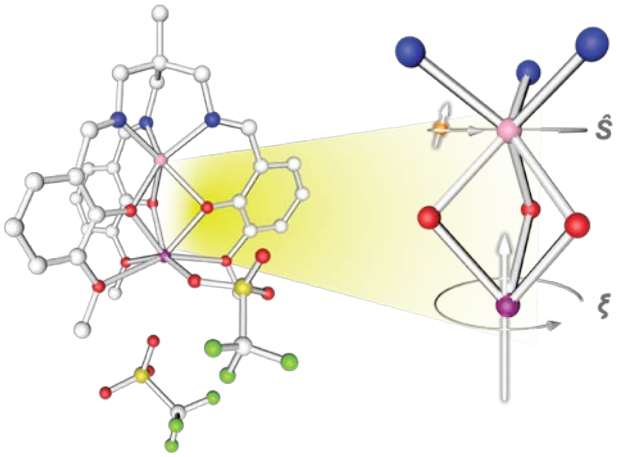

Figure 1.3 Molecular structure of $[L_1MnBi(OTf)_2]$ where purple, pink, red, blue, gray, yellow, and green represent bismuth, manganese, oxygen, nitrogen, carbon, sulfur, and fluorine atoms respectively.

Upon characterization *via* SQUID-based magnetometry and EPR spectroscopy, we determined that the high-spin Mn^{2+} center exhibits a substantially larger *D* value than complexes with similar (six-coordinate N_xO_y) primary coordination spheres. The $|D|$ value of 0.70(2) cm^{-1} was approximately twice that of the next highest (0.32 cm^{-1})[52] for a six-coordinate complex with an N_xO_y coordination sphere and approximately four-fold greater than that of the mono-metallated Mn^{2+} complex of the same ligand ($|D|$ = 0.168 cm^{-1}).[53] Indeed, the magnetic properties of this complex most closely resemble those of Mn^{2+} compounds featuring direct bonds to heavy halide ions such as Br^- and I^-. Because the primary coordination sphere could not be reasonably implicated in the manifestation of these magnetic properties, we proposed that the heavy Bi^{3+} ion in the secondary coordination sphere was strongly influencing the magnetic properties. This hypothesis is further supported by the work of Duboc and coworkers in their observation of the highest $|D|$ measured for a manganous ion, 1.46(1) cm^{-1}.[54] Their system featured five-coordinate Mn^{2+}coordinated by polyoxotungstate ions which featured heavy tungsten atoms in the secondary coordination sphere. Together, these results suggest that even SOC originating from the secondary coordination sphere metal can influence magnetic anisotropy in high-spin Mn^{2+}.

1.4 SOC transfer via direct, covalent bonding

Theoretical investigations into heavy-atom effects suggest that inner sphere covalency would more greatly affect SOC transfer.[55,56] Intuitively, a covalent bond in the primary coordination sphere would allow more electron density, i.e. SOC, to be shared between the two metal centers than an ionic bond. We need to address the challenge of creating a bonding interaction between two highly Lewis acidic metals which also harbors unpaired spins.

Many complexes bearing covalent bonds between first-row metals and main group metals feature electron rich transition metals, such as zero-valent or reduced carbonyl compounds shown in Figure 1.4a,[57,58] whose strong ligand field environment promote spin pairing.[59–62] If one were to analyze the bonding in such complexes within the context of a metal-ligand interaction, the transition metal acts Lewis basic providing the electrons constituting the bond with the Lewis acidic main group metal.[63,64] An example to illustrate this approach to generating a covalent bond is shown in Figure 1.4a, $[Bi(Fe(CO)_4)_4]^{3-}$, where the anionic $[Fe(CO)4]^{2-}$ moiety reacts with an oxidizing bismuth precursor, $NaBiO_3$ or $BiCl_3$, to form a highly covalent bond. We note that higher nuclearity transition metal-main group metal carbonyl clusters have allowed isolation of paramagnetic ground states such as the $[Bi_2Co_4(CO)_{11}]^-$ $S = ½$ compound shown in Figure 1.4b.[65,66] However, inspection of the molecular orbital diagram indicates that the singly-occupied molecular orbitals (SOMOs) have little main group element character. Furthermore, the complex reactivity and bonding of clusters do not allow for facile synthetic modification to investigate factors influencing covalency and magnetism relative to dinuclear coordination complexes. To use magnetic anisotropy as a proxy for SOC transfer, less electron-rich transition metals will be necessary to stabilize paramagnetic ground states. Therefore,

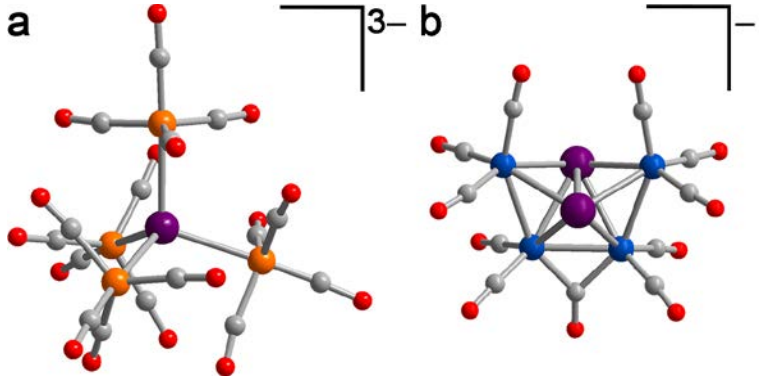

Figure 1.4 Molecular structures of (a) diamagnetic $[Bi(Fe(CO)_4)_4]^{3-}$, an example of a heavy main group metal-transition metal bonded complex, and (b) $S = ½$ $[Bi_2Co_4(CO)_{11}]^-$, one of the few paramagnetic heavy main group-transition metal clusters. Purple, orange, cobalt blue, red, and gray spheres represent bismuth, iron, cobalt, oxygen, and carbon atoms respectively; hydrogen atoms have been omitted for clarity.

the polarity of the classic transition metal-main group metal bond will need to be reversed to allow Lewis basic main group metal fragments to act as heavy ligands towards transition metal ions.

Chapter Two: Transformation of the Coordination Complex $[Co(C_3S_5)_2]^{2-}$ from a Molecular Magnet to a Potential Qubit

Reprinted with permission from

Fataftah, M. S.; Coste, S. C.; Vlaisavljevich, B.; Zadrozny, J. M.; Freedman, D. E. *Chemical Science* **2016**, 7, 6160–6166.

This work was performed in collaboration with the co-authors listed above.

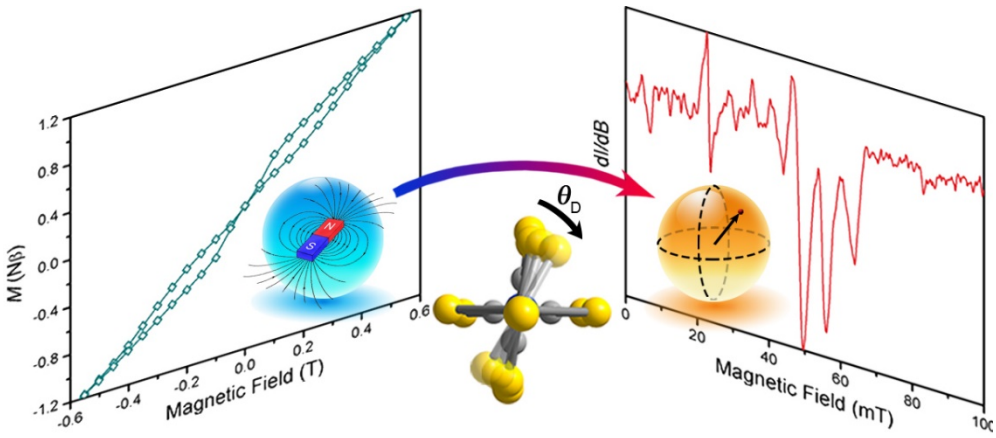

2.1 Introduction

A bottom-up approach to synthesizing functional components of information storage devices is vital for molecular spintronics. Within this area, paramagnetic high-spin coordination complexes are attractive candidates for spin-based data storage and information processing devices owing to their readily tunable M_S states. The field of molecular magnetic information processing can be bisected into two distinct areas: classical high-density information storage and quantum information processing (QIP).[1,2] Each of the two applications requires fundamentally distinct design principles. Classical data storage necessitates molecules that display magnetic hysteresis, in an analogous fashion to bulk magnets, while QIP requires spectroscopically addressable transitions for manipulation. The key quantity differentiating the suitability of high-spin molecules to the aforementioned applications is the presence of transverse zero-field splitting (E), which mixes the M_S states of a spin, S. In classical data storage applications, the mixing induces quantum tunnelling of magnetization (QTM) and destabilizes information stored in the orientation of the magnetic moment. Thus, the minimization of E is an overarching design principle.[3] In contrast, high-spin coordination complexes with non-negligible E are attractive candidates as molecular hosts for QIP. Here, the M_S mixing promoted by E induces relaxation of spectroscopic selection rules thus enabling otherwise forbidden transitions to function as candidate qubits. This latter property is highly advantageous for the design of multi-qubit molecular processors.[4,5] Thus, E is a crucial parameter that gates the respective application of coordination complexes in either classical or quantum information processing.

Commanding the delicate interplay of parameters required to tune E requires careful consideration of coordination geometry and electronic structure for a metal ion. Yet, explicit

studies illustrating the influence of specific structural changes on magnitude and sign of *E* are relatively rare, in contrast to the axial zero-field splitting (*D*), which is reasonably well understood. Tuning and measuring changes in *D* is well established from the field of single-molecule magnets (SMMs).[6,7] These species are a class of paramagnetic molecules that feature an energy barrier for spin reversal,[8] that promotes their utility for classical* data storage. While there is ample literature concerning maximizing *D*, and thus the spin reversal barrier ($U = DS^2$), considerably fewer reports are devoted to understanding the rational tuning of *E* through ligand field variations.[9,10] A large body of literature exists on magneto-structural correlations in systems with large, negative *D* values. Yet, in such systems it is very difficult to probe *E* spectroscopically or magnetically. This extremely challenging, and occasionally prohibitive, nature of direct measurement of *E* generates an absence of direct correlations of changes in *E* to the observation of magnetic hysteresis or qubit viability. To ameliorate the spectroscopic elusiveness of *E* we employed ac magnetic susceptibility as a probe of the emergence of QTM, which is a bulk proxy for *E*, as it enables QTM through admixture of M_S levels.

Electron paramagnetic resonance (EPR) spectroscopy is an invaluable technique to measure the zero-field splitting (ZFS) parameters of magnetic molecules. Yet, owing to the limited operational microwave frequencies currently available, it is often difficult to use the technique to study complexes with highly axial anisotropy ($D >> E$). Fortunately, ac susceptibility is a powerful probe of slow magnetic relaxation in which QTM, facilitated by a number of factors including *E*, is often a prominent relaxation pathway at low temperatures. Ac susceptibility is an indispensable technique for the investigation of magnetic properties such as magnetic ordering and spin glass behaviour in solid state materials,[11] yet, it is rarely the key technique employed to inspect *E* in

coordination complexes. Herein, we report tuning the coordination geometry in a series of $S = {}^3/_2$ pseudo-tetrahedral Co^{2+} complexes, $A_2[Co(C_3S_5)_2]$ (A = Bu_4N^+ (**1**), Ph_4P^+ (**2**), PPN^+ (**3**), $[K(18c6)]^+$ (**4**)). Across **1** – **4**, we observe a diminishing value of E by monitoring the low temperature quantum tunneling of magnetization. Importantly, concomitant with a decrease in E, a transition of the utility of the molecule from quantum to classical information application occurs, as evidenced by the observation of an L-band (1.36 GHz) EPR signal for **1** and magnetic hysteresis for **4**.

2.2 Results and Discussion

Investigation of whether small structural changes can induce a transition in viability from the quantum to classical regime of information processing poses an appreciable challenge due to the synthetic requirement of varying one zero-field splitting parameter while maintaining the same electronic structure. To approach this, we focused on the 4,5-dimercapto-1,3-dithiole-2-thionate ($C_3S_5^{2-}$) ligand motivated by its denticity and planarity, which guides late transition metal ions toward four-coordinate geometries with subtle deviations away from D_{2d} idealized symmetry. Here, the majority of such deviations amount to variation in the interligand dihedral angle (θ_d) between the planes defined by the $C_3S_5^{2-}$ planar ligands (Fig. 2.1). Each member of the series of $[Co(C_3S_5)_2]^{2-}$

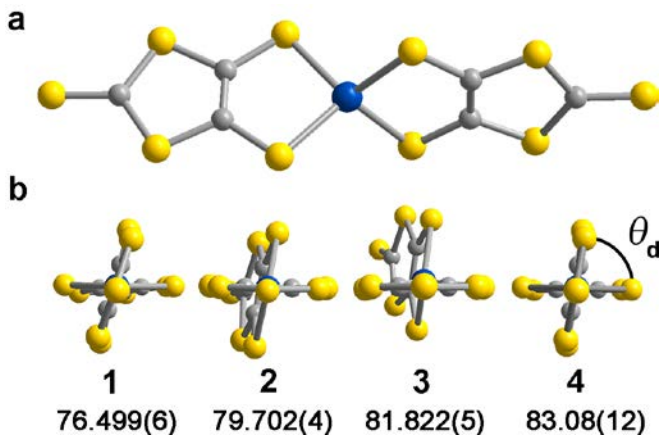

Figure 2.1 (a) Molecular structure of $[Co(C_3S_5)_2]^{2-}$ as determined by X-ray crystallography for **2**. The blue, yellow, and grey spheres represent Co, S, and C atoms respectively. (b) Depiction of the variation in dihedral angle across compounds **1** – **4**.

complexes was synthesized via ligation of the bidentate, nuclear-spin free ligand, 4,5-dimercapto-1,3-dithiole-2-thionate ($C_3S_5^{2-}$), to $CoCl_2$ in MeOH followed by the addition of the appropriate cation (Bu_4N^+ (**1**), Ph_4P^+ (**2**), PPN^+ (**3**) and $[K(18\text{-c-}6)]^+$ (**4**)) to affect precipitation of the desired salt. Single-crystal X-ray diffraction studies of all complexes reveal an elongated pseudo-tetrahedral coordination environment surrounding the Co^{2+} center, as illustrated in Fig. 2.1a. Several metrical parameters are remarkably consistent across the series. First, the average Co–S bond distances in all complexes are comparable (2.305(8) Å) and are consistent with the average Co–S distances reported for tetrahedral coordinated high-spin $Co^{2+}S_4$ complexes in the literature.[12] Further, individual S–Co–S bite angles in **1** – **4** do not deviate significantly from the average value of the series (93.9(3)°). Yet, despite this consistency, a distortion away from D_{2d} symmetry is observed as a function of counterion in **1** – **4** (Fig. 2.1). Indeed, a twist of the planar $C_3S_5^{2-}$ ligands relative to one another distorts the dihedral angles away from the ideal angle of 90°, as illustrated in Fig. 2.1b. Across the series of compounds, the dihedral angle ranges from 76.499(6)° to 83.08(12)° in **1** and **4**, respectively. The low-coordinate nature of the Co^{2+} complexes imparts flexibility, allowing the dihedral angle to remain flexible while maintaining the ~94° bite angle. Importantly, the invariant

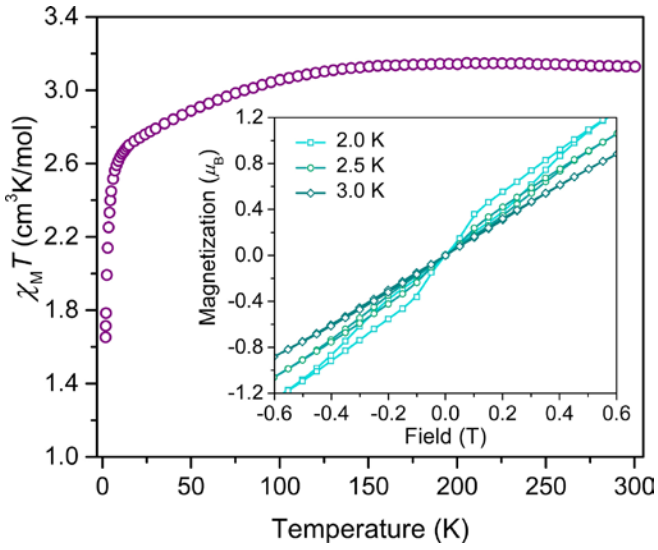

Figure 2.2 Temperature dependent magnetic susceptibility ($\chi_M T$) of a polycrystalline powder of **4** collected under an applied field of 0.1 T. Inset: Overlay of hysteresis curves collected on 4 at 2 K, 2.5 K, and 3 K at a scan rate of 8 mT/s.

bite angle across the series imposes a near degeneracy of the $d_{x^2-y^2}$ and d_{xy} orbitals resulting in the large axial anisotropy previously observed in $[Co(C_3S_5)_2]^{2-}$.[10,**13**] This specific structural variation observed across the series presents a unique opportunity to study the influence of a specific subtle distortion in the ligand field on the slow magnetic relaxation by inducing non-negligible rhombicity ($E/D \neq 0$) with minimal influence on D (i.e. the height of the spin reversal barrier). Importantly, the nearest intermolecular Co•••Co distances are nearly constant in the series, ranging from 8.66(8) to 10.14(7) Å. This consistency is an effective control for dipolar interactions between the paramagnetic centers, thereby highlighting the dominance of changes in the ligand field as the most important influence on relaxation processes.

To probe the magnetic structure of compounds **1** – **4**, variable-temperature dc magnetic susceptibility measurements were performed under an applied dc field of 0.1 T between 1.8 and 300 K. The relatively uniform 300 K $\chi_M T$ values of 3.0 – 3.3 cm^3K/mol supports assignment of a $S = {}^3/_2$ ground state with large g_{iso} values in the range of 2.53 – 2.65, consistent with other highly axial cobalt thiolate complexes.[7*d,g*] As an illustrative example, the 300 K $\chi_M T$ value of **4** persists with decreasing temperature until ~175 K, whereupon the value gradually decreases to 2.6 cm^3K/mol at 10 K (Fig. 2.2) At temperatures lower than 10 K, the $\chi_M T$ rapidly declines with decreasing temperature. In all complexes, the gradual decline in $\chi_M T$ below 150 K is indicative of a large axial ZFS, as expected owing to the structural similarity with other previously reported pseudo-tetrahedral Co^{2+} complexes.[6*d,g*] Determination of the magnitude and sign of the zero-field splitting parameters proceeded through collection and fitting the variable-temperature, variable-field magnetization data (see Figure S2.1). The program DAVE 2.0[**14**] was employed to fit the data with the spin Hamiltonian $\hat{H} = D\hat{S}_z^2 + E(\hat{S}_x^2 - \hat{S}_y^2) + g_{iso}\mu_B \boldsymbol{SH}$. The parameter D is the axial zero-

field splitting parameter, E is the transverse zero-field splitting parameter, $\hat{S}_i$ (i = x,y,z) are the spin operators, g_{iso} is the isotropic g value, μ_B is the Bohr magneton, $\boldsymbol{S}$ is the spin, and $\boldsymbol{H}$ is the magnetic field. Our fits consistently estimate D to range from −161 to −187 cm^{-1} for **1** – **4**. We note the difficulty in accurately determining the magnitude of D, and more significantly E, from magnetization data of microcrystalline sample of highly magnetically anisotropic complexes, especially considering the difficulty in ensuring a randomly oriented microcrystalline sample. However, simulations of the magnetization curves with E values up to 3 cm^{-1} do not change the appearance of the magnetization curves due to the low rhombicity of the complex, thus precluding accurate determination of this parameter by dc magnetometry. Indeed, it is particularly challenging to assess low energy differences via magnetometry data alone, particularly when the value of D is significantly larger than E, thus masking the impact of altering this parameter. Nevertheless, the validity of these fits is supported by theoretical calculations as illustrated below.

Investigation of the influence of θ_d on the dynamic magnetic properties first proceeded via acquisition of variable field magnetization data below 5 K to search for magnetic hysteresis, a property suggestive of classical data storage. Of this series, the least distorted compound, **4**, is the only species to display magnetic hysteresis. Variable-temperature hysteresis curves reveal that the behaviour persists until 3 K, when the open loop collapses completely. Compound **4** is only one of very few mononuclear transition metal complexes exhibiting hysteresis at temperatures accessible above 1.5 K measured at relatively low scan rates.[15] Since hysteresis was only observed

in a single species of this series, this illustrates the significant influence of subtle distortions of the immediate ligand sphere on the magnetic properties of $[Co(C_3S_5)_2]^{2-}$.

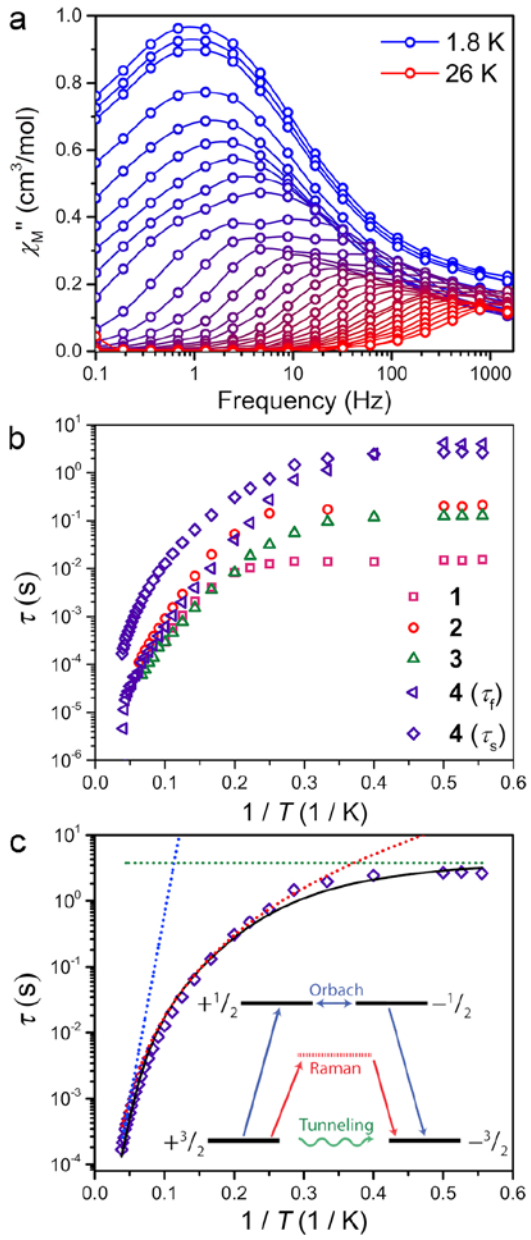

Figure 2.3 (a) Variable temperature out-of-phase ac susceptibility of **4** between 0.1 and 1500 Hz collected from 1.8 to 26 K collected under zero dc field. (b) Overlay of the temperature dependent relaxation times of compounds **1** – **4**. (c) Fit to the slow relaxation process (τ_s) of **4** in the temperature range of 1.8 to 26 K. The fit, and the inset, highlight contributions from Orbach (blue), Raman (red) and QTM (green) relaxation processes and their origins.

The presence of magnetic hysteresis in a single species of the series is surprising given the nearly identical zero-field splitting parameters determined from the dc susceptibility and magnetization data. Thus, ac magnetic susceptibility experiments, which yield information on the exact relaxation processes responsible for spin reversal, were pursued to search for the impact of subtle differences in the ZFS values. Specifically, we searched to correlate *E* with data obtained from dynamic magnetic measurements. One feature, which enables us to probe the ZFS parameters, is the presence of slow magnetic relaxation, which manifests by the observation of a peak in the out-of-phase component of ac susceptibility (χ_M''). When this slow relaxation is induced by negative

axial anisotropy, it is the hallmark of single-molecule magnet behaviour. Investigation of compounds **1** – **4** by variable temperature ac-susceptibility under zero applied dc field revealed a signal in the χ_M'' component of the ac susceptibility indicating a slowly relaxing magnetic moment. At 1.8 K, **1** – **4** all exhibit a peak in χ_M'' with maxima occurring at 0.7 to 10 Hz, respectively. The data sets for each complex exhibit two distinguishable or slightly overlapping peaks, a consequence of changing ac field frequencies enabling access to different pathways for reversal. Several examples of this behaviour are documented in the literature.[16] For **1** – **3**, the fast relaxation peak, which occurs at higher frequencies, exhibits little discernible temperature dependence, whereas **4** possesses two readily distinguishable peaks in χ_M'', both of which can be tracked throughout the temperature range of study (see Fig. 2.3a). Close inspection of the temperature dependence of the χ_M'' peak in **1** – **4** reveals a temperature independent regime below 3 K, where QTM is the operative relaxation pathway. Above 3 K, the peak in χ_M'' shifts to higher frequencies with increasing temperature until it disappears from the accessible frequency window at 15 K. However, **4** is notable in that its χ_M'' peaks can be monitored at temperatures up to 26 K, thus permitting a more thorough analysis of the temperature dependence of its relaxation times (τ). Akin to the dc susceptibility data, **1** – **3** display similar behaviour to each other, while **4** is, again an outlier, corroborating the observation of magnetic hysteresis in **4**, and further suggesting a minimum value for *E* in **4**.

The temperature dependence of the magnetic relaxation time yields mechanistic information regarding spin reversal, information that is highly sensitive to structural changes in magnetic systems. Thus, the variable frequency and temperature ac susceptibility data were fit to a general Debye model[17] to extract the spin relaxation times (τ) for each compound. Compound **4** is a slight

exception here, requiring a modified two-site Debye model.[18] The extracted relaxation times for **1** – **4**, presented in Fig. 2.3b, highlight the temperature independent regime below 3 K at zero dc field, owing to QTM[3] or possibly avalanche processes.[19] Above 3 K however, all compounds exhibit thermally activated relaxation, often attributed to two-phonon mediated Raman and Orbach spin relaxation processes, which impart a T^n and exponential dependence on T for τ, respectively.[20] In order to understand the relative contributions of each pathway in **1** – **4**, we fit the temperature profiles of τ to account for QTM, Raman, and Orbach relaxation according to the equation, $\tau^{-1} = \nu_{\mathrm{QTM}} + BT^n + \tau_0^{-1} e^{U_{\mathrm{eff}}/kT}$. ν_{QTM} is the tunnelling frequency, T is the temperature, k is Boltzmann's constant, U_{eff} is the effective spin-reversal barrier, B is the Raman coefficient, and τ_0^{-1} is the attempt frequency. The fit to the slow relaxation process (τ_s) in **4**, presented as an illustrative example in Fig. 2.3c, highlights the relative contributions of the various relaxation processes across the temperature range of measurement. Below 3 K, QTM is the dominant relaxation pathway as indicated by the temperature independence of the relaxation time. With increasing temperature, Raman relaxation begins to take effect, inducing the observed curvature in the temperature profile of τ, up to 22 K where Orbach relaxation dominates as indicated by the linear temperature dependence on the logarithm of τ.

Fitting the high temperature data to an Orbach relaxation process yields effective relaxation barriers (U_{eff}) in the range of 31 – 35 cm^{-1} for **1** – **3**, while the slow relaxation time in **4** exhibits a barrier of 91 cm^{-1}, one of the largest reported barriers for mononuclear transition metal complexes (see Fig. 2.3c).[21] The glaring disagreement between our theoretically expected barrier ($U_{\mathrm{eff}} = 2D = 320\ \mathrm{cm}^{-1}$) and the observed ones suggests the potential overestimation of D, or more likely the inappropriate assignment of an Orbach process at the higher temperatures of analysis.[22]

Regardless, the low temperature relaxation times draw attention toward the stark differences in the QTM frequency (v_{QTM}) between compounds **1** – **4**, which range two orders of magnitude, ranging from 61 Hz to 0.26 Hz for **1** and **4**, respectively.

The chelating coordination mode of the planar ligand in compounds **1** – **4** provides a unique opportunity to investigate a select magneto-structural correlation in $[Co(C_3S_5)_2]^{2-}$. To exclude the influence of counterion nuclear spins on QTM,[23] and to focus our study on the variable dihedral angle, we synthesized the deuterated analogue of **2** for comparison. We probed this compound by ac susceptibility and determined there was no statistically significant difference between its properties and those of its protiated counterpart (see supplementary information for further discussion). There is a striking and unexpected correlation between the dihedral angle of the dithiolate ligands in **1** – **4** with v_{QTM} extracted from ac susceptibility measurements. Compound **1**, possessing a dihedral angle of 76.5(1)°, exhibits the highest v_{QTM} (61 Hz), whereas **4**, bearing the least distorted angle of 83.1(1)°, exhibits the lowest frequency for QTM (0.26 Hz). We note that **2** and **3** do not rigorously follow the proposed trend, which we attribute to the canted binding mode of the $C_3S_5^{2-}$ ligand that induces a slight deviation from the ligand field trend.

Correlation between v_{QTM} and θ_d is credited to deviation from D_{2d} symmetry (i.e. $\theta_d < 90°$). Inspection of the qualitative *d*-orbital splitting diagram in Fig. 4 highlights the extent to which the near degeneracy of the d_{xy} and $d_{x^2-y^2}$ orbitals is removed, imposed by the invariant bite angle of the $C_3S_5^{2-}$ ligand across the series, thus distorting the pseudo-tetrahedral complex from T_d to D_{2d} symmetry. Our analysis is further supported by computational studies that reveal the lowest lying electronic excited state is relatively constant across the series, indicating relatively minor changes to the energies of the d_{xy} and $d_{x^2-y^2}$ orbitals. The low-coordinate nature of these complexes, as well

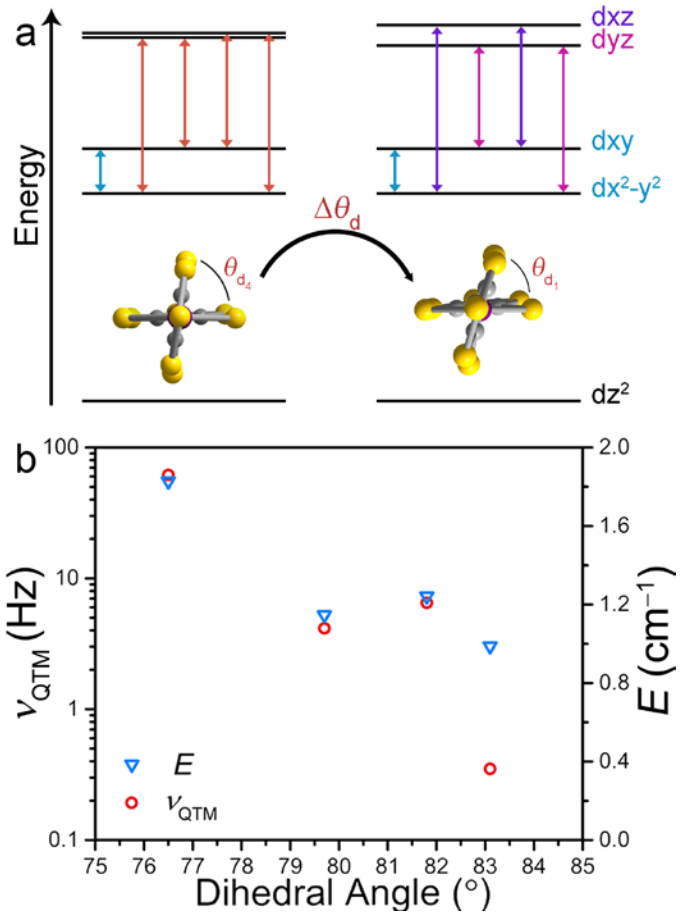

Figure 2.4 (a) Illustration of the d-orbital splitting for $[Co(C_3S_5)_2]^{2-}$ as a function of deviation from ideal D_{2d} symmetry. The arrows highlight the various transitions contributing to D (blue) and E (purple and pink). (b) E (blue triangles) and ν_{QTM} (red circles) as a function of the variable dihedral angle. The error on ν_{QTM} is smaller than the size of the data points.

as the rigidity of the binding mode of the planar ligand, imposes selective distortion of the dihedral angle due to crystal packing forces. Twisting of the dihedral angle away from 90° breaks the degeneracy of the d_{xz} and d_{yz} orbitals in the above d-orbital energy diagram. The incomplete cancellation of the contributions from transitions to d_{xz} and d_{yz} orbitals results in a nonzero E component of zero-field splitting. As depicted in the d-orbital splitting diagram in Fig. 2.4a, the energy separation between the d_{xz} and d_{yz} widens as the dihedral twist increases, thus resulting in a larger E component of ZFS. The values of E for compounds **1** – **4** were determined through a wave function based approach. State-averaged CASSCF/CASPT2 calculations of **1**-**4** were performed as implemented in the Molcas 8.0 software package.[24,25] The lowest 40 doublet and 10 quartet states (the full d-manifold) were included and used in subsequent state-interaction calculations in order to determine the effects of

spin orbit coupling and ultimately the D and E parameters (see supplementary information for details).

With increasing deviation of θ_d from 90°, v_{QTM} increases as a result of an increasing E that facilitates mixing of the M_S levels and magnetization tunneling through the spin-reversal barrier. Compounds **1** – **4** enable us to utilize ac susceptibility as an indirect probe of E, a value inherently difficult to measure in highly axially anisotropic complexes, through measurement of the QTM frequency. The results summarized in Fig. 2.4b clearly support our magneto-structural and *d*-orbital splitting analysis and illustrate the utility of employing ac susceptibility as an indirect probe of E in **1**–**4**.

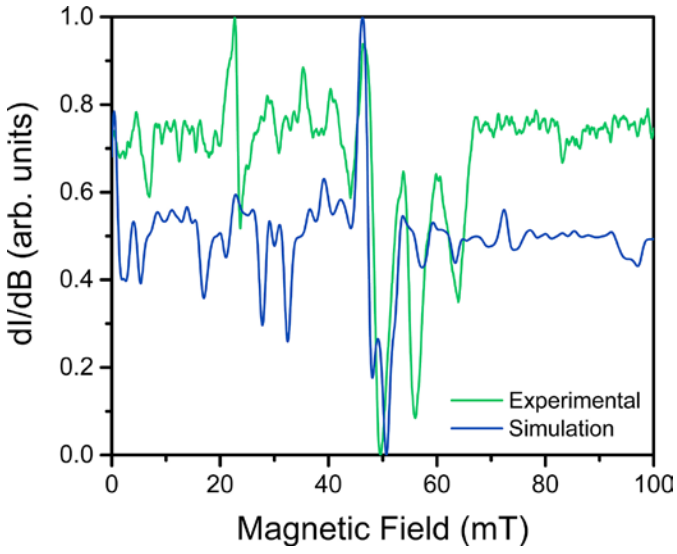

Figure 2.5 Overlay of the experimental cw-EPR spectrum (green) and simulation (blue). The experimental spectrum was collected on 1 at L-band (v = 1.368 GHz) at 110 K. The simulation was performed in EasySpin using an effective spin Hamiltonian ($S' = {}^1/_2$) with rhombic g-values and a rhombic hyperfine interaction (g_i, A_i, i = x, y, z). The blue spectrum was simulated using the following parameters: g'_x = 0.79(5), g'_y = 0.84(3), g'_z = 6.8(2), A'_x = 142(1) MHz, A'_y = 149(1) MHz, A'_z = 2026(1) MHz.

Utility of a coordination complex for quantum computing is predicated on the ability to manipulate its spin. Practically, this necessitates the observation of an EPR transition for pulsed manipulation. Yet, prior investigations of **2** revealed EPR silence and the unfeasibility of addressing any transitions as a consequence of a large, negative D and small E.[4] However, the surprising correlation between the dihedral angle and QTM frequency provided the motivation to investigate the possibility of addressing intra-Kramers transitions within the $M_S = \pm{}^3/_2$ doublet at

very low magnetic fields. Previously, we demonstrated that the extremely small value of E in **2** prevented observation of this transition; by increasing E with increasing distortion from D_{2d} symmetry across this series we created the potential for an EPR accessible transition. Yet, in order to access said transitions, low frequency EPR is necessary to bring the resonance to a field accessible by commercial spectrometers (< 1.4 T). Thus, we investigated the two extremes in the series, **1** and **4**, by the rare application of L-band (1.368 GHz) EPR spectroscopy to high-spin cobalt ions. Remarkably, while **4**, which possesses the smallest E, elicited no signal, the cw-EPR spectrum of **1** reveals a rich signal, displaying a multitude of resonances between 10 and 70 mT (see Fig. 2.5). The energetically well-isolated $M_S = \pm^3/_2$ Kramers doublet permitted treatment of the spectrum as an effective $S' = {}^1/_2$, with highly anisotropic effective g'-values. Simulation of the spectrum in EasySpin[26] allowed assignment of the observed features, which are attributed to very weak transitions within the hyperfine structure of the $\pm^3/_2$ Kramers doublet due to electronuclear interactions with the $I = {}^7/_2$ nuclear spin of the ^{59}Co nucleus (see ESI S2.16). The observation of resonances in the cw-EPR spectrum of the species with the largest value of E (**1**), concomitant with observation of hysteresis in the species with the smallest value of E (**4**), clearly demonstrates the impact of θ_d on the potential utility of the system. For **4**, the θ_d leads to a low E, inducing magnetic hysteresis and potential for classical information storage. In **1**, however, the θ_d leads to a larger E, which negates the hysteresis but enables access to EPR transitions at low frequency, and thus potential application for QIP. The actual potential of the system for QIP will be evaluated via pulsed L-band studies in a future study.

2.3 Outlook

Deriving magneto-structural correlations in high-spin molecular species is vital for creating design principles to develop components for classical information storage, spintronics, and quantum information processing. Specifically, the foregoing results further develop the impact of specific structural and electronic changes on application for classical versus quantum computing schemes. Our analysis of highly uniaxially anisotropic complexes reveals an unequivocal trend between increased QTM frequencies with increased deviation from D_{2d} symmetry owing to the concurrent increase in the magnitude of E. This drastic influence of a single structural distortion of $[Co(C_3S_5)_2]^{2-}$ permitted the application of ac susceptibility as an indirect probe of E throughout the series. Consequently, the subtle distortion of θ_d away from D_{2d} symmetry led to the observation of both magnetic hysteresis and addressable EPR transitions in the two extremes of θ_d, respectively. The discovery that $[Co(C_3S_5)_2]^{2-}$ bridges the fields of SMMs and QIP through subtle structural distortions opens new avenues to investigate the suitability of transition metal complexes for applications in quantum and classical information processing

2.4 Supplementary Information

General Considerations. All compounds were manipulated and handled under a dinitrogen atmosphere in a Vacuum Atmospheres Nexus II glovebox. All glassware was either oven-dried at 150 °C for at least 4 hours or flame-dried prior to use. Acetonitrile (MeCN), tetrahydrofuran (THF), and diethylether (Et_2O) were dried using a commercial solvent purification system from Pure Process Technology and stored over 3 or 4 Å sieves for a minimum of one day prior to use. Methanol (MeOH) was dried using the commercial solvent purification system followed by distillation under dinitrogen prior to use. Deuterated MeCN was purchased from Cambridge Isotope Labs, deoxygenated by three successive freeze-pump-thaw cycles, filtered through a pad of activated alumina, and stored over 4 Å sieves prior to use. $CoCl_2$ was prepared from $CoCl_2 \cdot 6H_2O$ by following the method of Horvath as applied for preparation of $MnCl_2$.[27] 4,5-bis(benzoylthio)1,3-dithiole-2-thione (benzoyl dmit) was prepared according to literature procedures.[28] $(Ph_4P)_2[Co(C_3S_5)_3]$ **(1)** and the deuterated counterion, d_{20}-Ph_4P were synthesized according to previously reported procedures.[29,30,31] d_{20}-Ph_4P•**2** was synthesized in an identical manner to its protiated analogue, using d_{20}-Ph_4P^+ as the counterion. All other chemicals were used as received.

$(Bu_4N)_2[Co(C_3S_5)_3]$ (1). NaOMe (215 mg, 3.98 mmol) was combined with benzoyl dmit (862 mg, 2.12 mmol) in 10 mL of MeOH and was allowed to stir for an hour to yield a dark red solution, to which $CoCl_2$ (128 mg, 0.99 mmol) was added and allowed to stir for two hours. A solution of Bu_4NBr (660 mg, 2.05 mmol) in 2 mL of MeOH was added dropwise leading to the formation of a dark purple precipitate. The mixture was stored in the freezer at -35C overnight leading to the

formation of purple block shaped crystals. The crystals were filtered and washed with 10 mL of Et_2O. The crystals were redissolved in approximately 15 mL hot MeCN, filtered through diatomaceous earth, after which Et_2O was slowly diffused into the solution to produce dark purple block shaped crystals (336 mg, 36.8 %) suitable for X-ray diffraction. IR (cm^{-1}): 3054(w), 3037(w), 3016(w), 2985(w), 1582(s), 1482(s), 1434(vs), 1405(vs), 1338(m), 1311(m), 1185(m), 1160(m), 1104(vs), 1051(s), 1025(vs), 994(vs), 894(m), 848(w), 838(w), 752(s), 717(vs), 682(vs), 643(w) 615(w), and 519(vs). Anal. Calcd. for $C_{40}H_{75}N_3S_{10}Co$: 47.17 %C; 7.40 %H; 2.89 %N. Found: 47.49 %C; 7.03 %H; 3.00 %N.

$(PPN)_2[Co(C_3S_5)_2]$ (3). NaOMe (54.4 mg, 1.00 mmol) was combined with benzoyl dmit (200.8 mg, 0.49 mmol) in 15 mL of MeOH and was allowed to stir for an hour yielding a dark red solution, at which time $CoCl_2$ (31.4 mg, 0.24 mmol) in 5 mL of MeOH was added and allowed to stir over night. Neat PPNCl (281.4 mg, 0.49 mmol) was added to the reaction mixture leading to the formation of a microcrystalline solid. The mixture was stirred for an additional hour, then filtered at which point the resulting magenta solid was washed with 30 mL of MeOH then 10 mL of Et_2O. The collected solid was dried and weighed to be 326.0 mg of crude product. The crude product was then redissolved in MeCN and filtered through diatomaceous earth. Et_2O was then allowed to diffuse into the MeCN solution to produce dark magenta elongated plates shaped crystals. IR (cm^{-1}): 3050(w), 1587(w), 1481(m), 1435(m), 1405(m), 1299(m), 1279(m), 1260(s), 1180(w), 1162(w), 1112(s), 1053(m), 1027(s), 997(m), 928(w), 897(w), 850(w), 800(w), 742(m), 720(vs), 690(vs), 615(w), 531(vs), 506(s), 496(vs), 463(m), and 446(w). Anal. Calcd. for $C_{78}H_{60}CoN_2P_4S_{10}$: 61.28 %C; 3.96 %H; 1.83 %N. Found: 60.98 %C; 3.89 %H; 1.82 %N.

[(18c6)K]$_2$[Co(C$_3$S$_5$)$_2$] (4) KOMe (101.8 mg, 1.45 mmol) and benzoyl dmit (297.1 mg, 0.73 mmol) were stirred in 15 mL of MeOH for an hour yielding a dark red solution. $CoCl_2$ (47.5mg, 0.37 mmol) in 2 mL of MeOH was subsequently added to the reaction mixture and allowed to stir for an hour at which point 18-crown-6 (208.5 mg, 0.79 mmol) in 2 mL of MeOH was added to the solution. The resulting solution was allowed to stir overnight. After removal of the solvent *in vacuo*, 20 mL of THF was added to the solid residue. The mixture was then stirred briefly, then pumped down to dryness in vacuo followed by further drying at 65°C for 2 h. This procedure was repeated twice. The solid was then redissolved in THF and filtered through diatomaceous earth. Et_2O was allowed to diffuse into the resulting THF solution to produce dark magenta elongated plate-like crystals. IR (cm^{-1}): 2885(m), 2864(m), 2821(w), 2743(w), 1468(w), 1451(w), 1415(m), 1349(sh), 1282(w), 1247(w), 1099(vs), 1049(s), 1025(vs), 999(m), 958(m), 891(m), 834(m), 771(w), 522(w), 461(sh). Anal. Calcd. for $C_{38}H_{64}CoO_{14}S_{10}K_2$: 37.95 %C; 5.36 %H. Found: 38.12 %C; 5.30 %H.

Magnetic Measurements. Magnetic data were collected using a Quantum Design MPMS-XL SQUID magnetometer. Measurements for all compounds were obtained on finely ground microcrystalline powders. The compounds were restrained in a frozen eicosane matrix and flame sealed in a quartz tube under vacuum or wrapped tightly within a polyethylene bag. In this latter case, the sample was prepared under a dinitrogen atmosphere and transferred to the SQUID in a Schlenk tube under a flow of Ar gas. Dc susceptibility measurements were collected in the temperature range 1.8–300 K under dc fields of 0.1, 0.5 and 1 T. Dc magnetization measurements were performed under applied magnetic fields of 1, 2, 3, 4, 5, 6 and 7 T in the temperature range of 1.8–10 K. Dc magnetic susceptibility data were corrected for diamagnetic contributions from

the sample holder and eicosane as well as for the core diamagnetism of each sample, estimated using Pascal's constants.[32] Ac susceptibility were performed on all compounds in the temperature range of 1.8 K to 15 K, between frequencies of 1 to 1500 Hz with an oscillating magnetic field of 4 Oe at zero-applied dc field. Prior to full characterization, variable dc field magnetization data was collected from 0 to 4 T at 100 K to ensure the absence of curvature associated with ferromagnetic impurities. Errors reported in Figures S4 and S5 on the magnetic parameters for simulation of the dc magnetic data were attained via successive simulation of the data in search for the upper and lower limits on the values before the simulation deviated from the experimental data significantly, by maintain the residual sum of errors below the value of 0.1.

X-ray Diffraction. Single crystal diffraction data collections were performed on single crystals coated with Paratone-N oil and mounted on a MicroMounts™ rod. The crystals were frozen while coated in Paratone-N oil under a stream of N_2 during the measurement. Structures for **1**, **2**, **4**, **5** were collected with a Bruker KAPPA APEX-II diffractometer equipped with a Mo Kα (λ = 0.71073 Å) sealed tube diffraction source with a graphite monochromater, and a Bruker APEX-II detector. Data for **3** were collected on a MICROSTAR X-ray source of Cu Kα (λ = 1.54056 Å) radiation with a Bruker SMART APEX CCD area detector. Raw data were integrated and corrected for Lorentz and polarization effects using Bruker Apex2 v. 2013.[33] Absorption corrections were applied using SADABS.[34] Space group assignments were determined by examination of systematic absences, *E*-statistics, and successive refinement of the structures. The crystal structure was solved by direct methods with the aid of successive difference Fourier maps in SHELXS[35] operated with the OLEX2 interface.[36] The crystals showed no significant decay during data collection. Thermal parameters were refined anisotropically for all non-hydrogen

atoms in the main body, solvents of crystallization, and counterions. Hydrogen atoms were placed in ideal positions and refined using a riding model for all structures.

L-Band EPR spectroscopy Measurements. L-band (1.367-1.388 GHz) EPR spectroscopy was performed in the National Biomedical EPR Facility at the Medical College of Wisconsin (MCW) on a home built instrument, the details of which are described elsewhere.[37] Samples were finely ground powders restrained in eicosane and sealed under vacuum in Wilmad 4 mm outer diameter quartz tubes. The magnetic field was calibrated with the g = 2.0036 resonance of 2,2-diphenyl-1-picrylhydrazyl (DPPH). Spectra were recorded with 10 dB microwave power attenuation (0.1 mW incident power at 1.36 GHz) and 0.4 mT (4 G) with field modulation at 100 kHz. Spectra of 30 s scan time with a time constant of 0.064 ms were averaged over a period of 3 minutes at 110 K and background spectra were recorded on samples of frozen 18 MΩ water (Millipore) to ensure confidence in sample signal assignment.

All Other Physical Measurements. Combustion analysis of all complexes was performed by Midwest Microlab (Indianapolis, IN). Infrared spectra were recorded on a Bruker Alpha FTIR spectrometer equipped with an attenuated total reflectance accessory. Solution-phase NMR spectra were collected with an Agilent Au 400 MHz spectrometer. Proton NMR spectra are referenced to $CDCl_3$ at 7.26 ppm. UV-vis spectra were collected on a Varian Cary 5000 spectrometer in MeCN.

Computational Details. Complete active space self-consistent field calculations with corrections from second order perturbation theory (CASSCF/CASPT2) were performed on the experimental geometry for complexes **1**-**4**.[38-40] The active space included the 3d and 4d orbitals on the cobalt center and the eight valence electrons resulting in an (8*e*,10*o*) active space. Scalar relativistic effects were treated through the use of the Douglas-Kroll-Hess (DKH) Hamiltonian[41,42]

and ANO-RCC basis sets of triple-ζ quality were employed with the following contractions: 6s5p3d2f1g for cobalt and 5s4p2d1f for sulfur, and 4s3p2d1f for carbon[43,44] Higher CI roots were computed in order to include the lowest lying excited states which is essential if one wishes to obtain reliable magnetic properties. To this end, electronic states consisting of excitations in the full *d*-manifold were included for a total of 40 doublet and 10 quartet states. CASPT2 calculations were performed for each spin-free state as implemented in the Molcas 8.0 software package.[45] Cholesky decomposition was used in combination with local exchange (LK) screening to reduce the cost of the two electron integrals.[46] Spin orbit coupling effects were computed a posteriori using the state interaction approach (RAS-SI).[47] The diagonal elements of this effective Hamiltonian were replaced with the CASPT2 energies in the so-called SOCASPT2 approach. The RASSI spin-orbit states that were obtained were then introduced into the SINGLE-ANISO module in order to calculate the magnetic properties (*g*, *D*, and *E*) of the complexes.[48]

Discussion of fitting temperature dependence of τ. The temperature dependence of τ was fit for **1** – **4** under zero applied magnetic field accounting for only two contributors to relaxation. Quantum tunneling of magnetization serves as a temperature independent relaxation process that dominates the relaxation at the lowest temperature of measurement, as indicated by the plateau in the relaxation profiles. The curvature observed in the temperature dependence of $\boldsymbol{\tau}$ at higher temperatures can be adequately fit by the inclusion of a Raman process, imparting a T^n dependence on the relaxation behavior. However, careful consideration of the exponent is required. For all variable-temperature relaxation data collected under zero-applied magnetic field, the Raman exponent was held constant at $n = 5$, as expected for complexes in which a ground spin multiplets state is present owing to coupling between nuclear and electronic spins of the Co^{2+} center.

Improvements to the fits can be attained by allowing the exponent to vary, whereby it fluctuates between 4.5 and 5.5 for the **1** – **4**. The only relaxation profile which necessitated the inclusion of an Orbach process is the fast relaxation process (τ_f) in **4**. However, it is worth noting the significant errors associated with τ_f at higher temperatures owing to the difficulty in resolving the fast relaxation process above 20 K.

Fitting the slow component of the temperature relaxation profile of **4** (τ_s) can proceed by either inclusion of an Orbach relaxation mechanism, as presented in Figure 3c of the manuscript, by excluding, as presented in Figure S12. Both fits yield a similar goodness-of-fit parameter, with minor discrepancies, where the sum of the squared residuals (SSR) was 1.4 vs 1.36 for the fits with and without the Orbach process, respectively. Inclusion of the Orbach process was performed by fitting the maximum number of high temperature data points, while holding the Raman exponent constant at $n = 5$. Inclusion of data points below 22 K led to deviation of the Raman exponent from $n = 5$. The U_{eff} value reported in the manuscript therefore represents the lower limit by including the maximum number of data points.

Discussion of exclusion of dipolar coupling from QTM. Three factors facilitate and permit quantum tunneling of magnetization through the double well potential in single-molecule magnets: transverse anisotropy (E), exchange interactions, and dipolar coupling to nearby nuclear and electronic spins. In compounds **1** – **4**, in order to correlate E with the QTM frequency, the deuterated analogue of **2**, $(d^{20}\text{-}Ph_4P)_2[Co(C_3S_5)_2]$, was synthesized and investigated by ac susceptibility under zero-applied dc magnetic field. The variable-temperature relaxation profile was identical to its protiated analogue, **2**. Due to the lack of exchange interactions in these mononuclear complexes, dipolar interactions were the only consideration. Due to the absence of

nuclear spins in the immediate ligand field, there are two nuclear spin contributors remaining, the nuclear spin of the cobalt itself, which cannot be controlled for, and those originating from counterions. Compound **2** possesses the closest Co···H through-space distance of 2.998(2) Å relative to **1**, **3** and **4** possessing 3.208(3) Å and 3.035(3) Å and 3.098(1) Å distances, respectively. Furthermore, the shortest Co···Co intermolecular distance of 8.66(1) Å in **2** was that present in **2** as well. This permitted us to exclude the convoluting influence of counterion nuclear spins as well as intermolecular electronic dipolar interactions between adjacent cobalt spin centers from our analysis.

Modelling L-band cw spectrum. Owing to the well-isolated lowest lying Kramers doublet ($M_S = \pm^3/_2$), no contributions from $M_S = \pm$½ Kramers doublet are apparent in the cw spectrum, and the large energy separation between the two Kramers doublet ($\Delta = 2D \sim 320\ cm^{-1}$) no inter-Kramers are possible at the frequency measurement. Due to these considerations, the cw EPR spectrum presented in Figure 5 in the main manuscript can be phenomenologically described using an effective spin model, $S' = {}^1/_2$, with rhombic g-values hyperfine coupled to the $I = {}^7/_2$ cobalt nucleus (^{59}Co, 100 % $I = {}^7/_2$ abundant). The cw-EPR spectrum was modeled in EasySpin[49] using the effective spin Hamiltonian, $\hat{H}' = \mu_B g_i' \boldsymbol{SH} + \boldsymbol{I}\boldsymbol{A}_i'\boldsymbol{S}$ (i = x, y, z), with the following parameters: g'_x = 0.79(5), g'_y = 0.84(3), g'_z = 6.8(2), A'_x = 142(1) MHz, A'_y = 149(1) MHz, A'_z = 2026(1) MHz. The effective g-values and hyperfine (A') parameters can be transformed back to the $S = {}^3/_2$ g-values and A constants using the rhombicity factor ($\eta = E/D$) determined by computation, $\eta = 0.015$, using previous reported methods.[50] The new $S = {}^3/_2$ Hamiltonian parameters are: g_x =2.37, g_y = 2.52, g_z = 2.26, A_x = 426 MHz ($1.42 \times 10^{-2}\ cm^{-1}$), A_y = 447 MHz ($1.49 \times 10^{-2}\ cm^{-1}$). A_z = 675 MHz ($2.25 \times 10^{-2}\ cm^{-1}$). Determination of rhombicity from the effective spin Hamiltonian parameters

determined above is complicated by the *g*-value, which is heavily intertwined with the value of |*E*/*D*|. Therefore accurate determination of the rhombicity factor without accurate *g*-values for the $S = {}^3/_2$ model is difficult and unreliable.

Noteworthy, the spectrum cannot be accurately simulated in EasySpin as an $S = {}^3/_2$ complex with large, negative *D* and a small *E* because the simulations include transitions from the $M_S = \pm{}^1/_2$ Kramers doublet. Owing to the extremely weak intensities of the transitions observed at L-band frequency, low Boltzmann population of the $M_S = \pm$½ Kramers doublet leads to signals that originate between the $M_S = \pm{}^1/_2$ states, and overwhelm the signals originating from the lowest energy Kramers doublet. These signals are most likely not observed experimentally due to the fast spin-lattice relaxation of the excited M_S Kramers doublet.[51] Because T_1 relaxation times is not a parameter EasySpin accounts for in simulation of cw-EPR spectra, the spectrum is best modelled using an effective spin model, as described above.

Table S2.1. Crystallographic information for the structural refinement of 1.

Empirical Formula	$C_{38}H_{72}CoN_2S_{10}$
Formula weight	1171.48 g/mol
Temperature	100(2) K
Wavelength	0.71073 Å
Crystal System	Monoclinic
Space Group	*C*2/c
Unit Cell Dimensions	a = 18.3767(16) Å, α = 90.0˚ b = 8.6094(7) Å, β = 100.972(5)˚ c = 31.158(3) Å, γ = 90.0˚
Volume	4839.5(8) Å^3
Z	4
Density (calculated)	1.285 Mg/m^3
Absorption coefficient	0.81 mm^{-1}
F_{000}	1211.9
Crystal color	Red
Crystal size	0.21 × 0.19 × 0.15 mm^3
θ range	2.76 to 52.48˚
Index ranges	$-11 \le h \le 11$ $-20 \le k \le 21$ $-23 \le l \le 21$
Reflections collected	26262
Independent reflections	25142 [R_{int} = 0.0726]
Completeness to θ = 52.48˚	94.9 %
Absorption correction	Multi-scan
Maximum and minimum transmission	0.655 and 0.745
Refinement method	Full-matrix least-squares on F^2
Data / restraints / parameters	10963 / 10 / 235
Goodness-of-fit on F^{2a}	1.128
Final R indices [I > 2σ(I) = 10408 data]^b	R_1 = 5.91 %, wR_2 = 10.93 %
R indices (all data, 0.80 Å)	R_1 = 7.91 %, wR_2 = 15.55 %
Largest diff. peak and hole	0.45 and –0.39 e.Å^{-3}

^{a} GooF = $[\Sigma[w(F_o^2-F_c^2)^2] / (n-p)]^{1/2}$ where n is the number of reflections and p is the total number of parameters refined. $^b R_1 = \Sigma||F_o|-|F_c|| / \Sigma|F_o|$; $wR_2 = [\Sigma[w(F_o^2-F_c^2)^2] / \Sigma[w(F_o^2)^2]]^{1/2}$

Table S2.2. Crystallographic information for the structural refinement of 3.

Empirical Formula	$C_{78}H_{60}CoN_2P_4S_{10}$
Formula weight	1171.48 g/mol
Temperature	100(2) K
Wavelength	0.71073 Å
Crystal System	Triclinic
Space Group	*P*–1
Unit Cell Dimensions	a = 9.6547(4) Å, α = 90.0˚
	b = 20.7112(11) Å, β = 90.966(3)˚
	c = 35.6907(15) Å, γ = 90.0˚
Volume	7135.7(6) Å^3
Z	8
Density (calculated)	1.423 Mg/m^3
Absorption coefficient	0.798 mm^{-1}
F_{000}	3156
Crystal color	Red
Crystal size	0.21 × 0.19 × 0.15 mm^3
θ range	2.76 to 52.48˚
Index ranges	$-9 \le h \le 10$
	$-20 \le k \le 7$
	$-36 \le l \le 36$
Reflections collected	26553
Independent reflections	10408 [R_{int} = 0.0492]
Completeness to θ = 52.48˚	94.9 %
Absorption correction	Multi-scan
Maximum and minimum transmission	0.655 and 0.745
Refinement method	Full-matrix least-squares on F^2
Data / restraints / parameters	10963 / 0 / 856
Goodness-of-fit on F^{2a}	1.062
Final R indices [I > 2σ(I) = 10408 data]^b	R_1 = 4.56 %, wR_2 = 10.68 %
R indices (all data, 0.80 Å)	R_1 = 6.64 %, wR_2 = 12.28 %
Largest diff. peak and hole	0.643 and –0.632 e.Å^{-3}

^{a} GooF = $[\Sigma[w(F_o^2-F_c^2)^2] / (n-p)]^{1/2}$ where n is the number of reflections and p is the total number of parameters refined. $^b R_1 = \Sigma||F_o|-|F_c|| / \Sigma|F_o|$; $wR_2 = [\Sigma[w(F_o^2-F_c^2)^2] / \Sigma[w(F_o^2)^2]]^{1/2}$

Table S2.3. Crystallographic information for the structural refinement of 4.

Empirical Formula	$C_{56}H_{43}CoNP_2S_{10}$
Formula weight	1171.48 g/mol
Temperature	100(2) K
Wavelength	0.71073 Å
Crystal System	Monoclinic
Space Group	$P2_1/c$
Unit Cell Dimensions	a = 9.8761(16) Å, α = 90.0˚
	b = 17.519(3) Å, β = 92.211(5)˚
	c = 37.115(6) Å, γ = 90.0˚
Volume	6423.7(18) Å^3
Z	8
Density (calculated)	1.392 Mg/m^3
Absorption coefficient	0.78 mm^{-1}
F_{000}	2832.0
Crystal color	Red
Crystal size	0.21 × 0.19 × 0.15 mm^3
θ range	2.76 to 52.48˚
Index ranges	$-12 \le h \le 11$
	$-19 \le k \le 21$
	$-45 \le l \le 45$
Reflections collected	40791
Independent reflections	8264 [R_{int} = 0.0492]
Completeness to θ = 52.48˚	99.8 %
Absorption correction	Multi-scan
Maximum and minimum transmission	0.192 and 0.259
Refinement method	Full-matrix least-squares on F^2
Data / restraints / parameters	12230 / 0 / 677
Goodness-of-fit on F^{2a}	1.098
Final R indices [I > 2σ(I) = 10408 data]^b	R_1 = 8.88 %, wR_2 = 30.64 %
R indices (all data, 0.80 Å)	R_1 = 13.24 %, wR_2 = 26.47 %
Largest diff. peak and hole	0.72 and –0.73 e.Å^{-3}

[a] GooF = $[\Sigma[w(F_o^2-F_c^2)^2] / (n-p)]^{1/2}$ where n is the number of reflections and p is the total number of parameters refined. [b] $R_1 = \Sigma||F_o|-|F_c|| / \Sigma|F_o|$; $wR_2 = [\Sigma[w(F_o^2-F_c^2)^2] / \Sigma[w(F_o^2)^2]\ ]^{1/2}$

Table S2.4. Fit parameters to the variable-temperature magnetic susceptibility of 1 – 4.

Compound	$\|D\|$ (cm^{-1})	E (cm^{-1})	$g_{\parallel}$	$g_{\perp}$
1	123(4)	0	3.04(5)	2.18(2)
2	127(3)	0	3.1(3)	2.34(5)
3	119(6)	0	3.02(6)	2.07(3)
4	130(4)	0	3.07(4)	2.11(6)

Table S2.5. Fit parameters to the variable-temperature, variable-field magnetization curves for 1 – 4.

Compound	D (cm^{-1})	E (cm^{-1})	g_{iso}
1	−187(6)	0	3.06(4)
2	−161(8)	0	3.24(5)
3	−177(5)	0	2.95(5)
4	−166(10)	0	3.06(5)

Table S2.6. Zero-field splitting parameters (D & E) and isotropic g-value for 1 – 4 computed at the SO-CASPT2 level of theory. The full manifold of 40 doublet states and 10 quartet states were included in the calculation. Values for D and E are reported in wavenumbers.

Compound	D (cm^{-1})	E (cm^{-1})	g_{iso}
1	−113.7	1.828	3.160
2	−116.4	1.147	3.219
3	−105.7	1.242	3.159
4	−118.0	0.988	3.275

Table S2.7. The first eight states of the zero-field splitting computed at the SO-CASPT2 level of theory including excitations in the full *d*-manifold. Energies are referenced to the lowest states in the series and are reported in cm^{-1}. The ninth state lies between 3900 and 4300 cm^{-1} above the eighth state.

SO-State	**1**	**2**	**3**	**4**
1	490	185	0	1249
2	490	185	0	1249
3	717	418	212	1486
4	717	418	212	1486
5	1231	910	796	1959
6	1231	910	796	1959
7	1536	1220	1085	2275
8	1536	1220	1085	2275

Table S2.8. Cole-Cole plot fitting parameters for 1 under 0 Oe dc applied field. χ_T and χ_S are the isothermal and adiabatic magnetic susceptibilities, respectively. χ_T therefore takes on the value of χ'_M in the low-frequency limit, while χ_S takes on the value of χ'_M in the high-frequency limit.

Temperature (K)	χ_T **(cm^3/mol)**	χ_S **(cm^3/mol)**	τ **(s)**	α
1.8	5.75	1.34	1.55×10^{-2}	0.34
1.9	5.43	1.25	1.42×10^{-2}	0.34
2	5.31	1.17	1.51×10^{-2}	0.34
2.5	4.31	0.92	1.39×10^{-2}	0.36
3.0	3.63	0.75	1.40×10^{-2}	0.37
3.5	3.20	0.65	1.42×10^{-2}	0.36
4.0	2.77	0.59	1.25×10^{-2}	0.34
4.5	2.48	0.54	1.04×10^{-2}	0.29
5.0	2.25	0.48	8.22×10^{-3}	0.27
6.0	1.83	0.40	4.10×10^{-3}	0.18
7.0	1.61	0.29	2.09×10^{-3}	0.18
8.0	1.36	0.24	1.04×10^{-3}	0.14
9.0	1.19	0.21	5.81×10^{-4}	0.10
10.0	1.07	0.18	3.54×10^{-4}	8.7×10^{-2}

Table S2.9. Cole-Cole plot fitting parameters for 2′ (d_{20}-2) under 0 Oe dc applied field.

Temperature (K)	χ_T **(cm^3/mol)**	χ_S **(cm^3/mol)**	τ **(s)**	α
2	5.55	0.96	0.156	0.43
3	3.64	0.70	0.11	0.36
4	2.62	0.61	4.61×10^{-2}	0.19
5	2.08	0.44	1.59×10^{-2}	0.14
6	1.75	0.26	6.25×10^{-3}	0.13
7	1.50	0.14	2.78×10^{-3}	0.14
8	1.30	6.98×10^{-2}	1.42×10^{-3}	0.13
9	1.16	6.76×10^{-2}	8.58×10^{-4}	0.10
10	1.03	0	5.44×10^{-4}	0.10
11	0.98	0	3.71×10^{-4}	0
12	0.99	0	2.61×10^{-4}	8.28×10^{-2}
13	0.91	0	1.89×10^{-4}	6.1×10^{-2}
14	0.85	0	1.41×10^{-4}	5.5×10^{-2}
15	0.79	0	1.07×10^{-4}	3.6×10^{-2}

Table S2.10. Cole-Cole plot fitting parameters for 3 under 0 Oe dc applied field.

Temperature (K)	χ_T **(cm^3/mol)**	χ_S **(cm^3/mol)**	τ **(s)**	α
1.8	5.93	0.99	0.12	0.38
1.9	5.55	1.11	0.13	0.34
2.0	4.81	0.90	0.12	0.35
2.5	4.08	0.79	0.12	0.34
3.0	2.83	0.65	9.45×10^{-2}	0.26
3.5	2.46	0.47	5.52×10^{-2}	0.23
4.0	2.14	0.41	3.16×10^{-2}	0.19
4.5	1.89	0.39	1.81×10^{-2}	0.13
5.0	1.67	0.44	3.54×10^{-3}	4.1×10^{-2}
6.0	1.14	2.85×10^{-2}	3.61×10^{-3}	0.23
7.0	0.93	2.75×10^{-2}	1.51×10^{-3}	0.19
8.0	0.81	0	7.78×10^{-4}	0.16
9.0	0.72	0	4.55×10^{-4}	0.14
10	0.64	0	2.94×10^{-4}	0.12
11	0.62	3.04×10^{-2}	2.00×10^{-4}	0.11
12	0.54	0	1.39×10^{-4}	9.9×10^{-2}
13	0.50	0	1.08×10^{-4}	7.4×10^{-2}
14	0.45	0	7.82×10^{-5}	0
15	0.43	0	6.10×10^{-5}	0

Table S2.11. Cole-Cole plot fitting parameters for 4 under 0 Oe dc applied field. χ_f and χ_s are the isothermal susceptibilities for the fast and slow relaxation components, respectively, while χ_0 is the adiabatic susceptibility.

Temperature (K)	χ_s **(cm^3/mol)**	α_s	τ_s**(s)**	χ_f **(cm^3/mol)**	α_f	τ_f **(s)**	χ_0 **(cm^3/mol)**
1.8	9.0	0.22	2.37	11.4	0.65	2.76	0.15
1.9	9.3	0.28	2.72	12.6	0.65	3.91	0.16
2.0	9.1	0.27	2.70	12.4	0.65	4.17	0.15
2.5	6.9	0.29	2.43	9.8	0.63	2.46	0.12
3.0	5.0	0.35	1.94	7.9	0.60	1.14	0.12
3.5	4.8	0.39	1.42	7.4	0.57	0.72	0.11
4.0	3.2	0.38	0.82	5.0	0.55	0.27	0.10
4.5	2.8	0.88	0.40	2.4	0.50	6.0×10^{-2}	0.0
5.0	2.3	0.0	0.31	2.2	0.47	2.8×10^{-2}	0.10
6.0	1.88	0.0	0.13	1.6	0.43	1.0×10^{-2}	0.07
7.0	1.59	0.08	5.64×10^{-2}	1.1	0.36	3.2×10^{-3}	0.07
8.0	1.39	0.0	3.48×10^{-2}	1.0	0.40	2.0×10^{-3}	0.016
9.0	1.23	0.0	2.02×10^{-2}	0.80	0.37	1.1×10^{-3}	0.016
10	1.11	0.0	1.26×10^{-2}	0.73	0.36	6.1×10^{-4}	0.0
11	1.01	0.0	8.58×10^{-3}	0.64	0.34	3.9×10^{-4}	0.0
12	0.92	0.0	5.67×10^{-3}	0.56	0.30	2.5×10^{-4}	0.0
13	0.86	0.0	4.09×10^{-3}	0.51	0.28	1.9×10^{-4}	0.0
14	0.80	0.0	2.96×10^{-3}	0.48	0.29	1.4×10^{-4}	0.0
15	0.75	0.0	2.16×10^{-3}	0.45	0.32	1.1×10^{-4}	0.0
16	0.70	0.0	1.62×10^{-3}	0.40	0.26	7.1×10^{-5}	0.0
17	0.66	0.0	1.27×10^{-3}	0.39	0.26	5.9×10^{-5}	0.0
18	0.62	0.0	9.79×10^{-4}	0.37	0.27	5.5×10^{-5}	0.0
19	0.59	0.0	7.86×10^{-4}	0.33	0.29	3.9×10^{-5}	0.0
20	0.56	0.0	6.08×10^{-4}	0.31	0.30	3.5×10^{-5}	0.0
21	0.53	0.0	4.89×10^{-4}	0.28	0.18	2.7×10^{-5}	0.0
22	0.51	0.0	4.07×10^{-4}	0.27	0.19	2.3×10^{-5}	0.0
23	0.49	0.0	3.42×10^{-4}	0.26	0.19	1.8×10^{-5}	0.0
24	0.46	0.0	2.53×10^{-4}	0.23	0.19	1.1×10^{-5}	0.0
25	0.45	0.0	2.16×10^{-4}	0.21	0.19	5.0×10^{-6}	0.0
26	0.43	0.0	1.68×10^{-4}	0.18	0.19	1.0×10^{-6}	0.0

Table S2.12. Fitting parameters for the temperature dependent relaxation profile for 1 – 4.

Compound	*A* (QTM)	*B* (Raman)	*n*	*C* (Orbach)	U_{eff} (cm^{-1})
1	61.75	2.63×10^{-2}	5	0	0
2	4.15	8.67×10^{-3}	5	0	0
2′	4.62	1.68×10^{-2}	5	0	0
3	6.5	2.94×10^{-2}	5	0	0
4_s	0.38	6.29×10^{-4}	5	0	0
4_s (alternate)	0.26	4.5×10^{-3}	4.1	700000	130
4_f	0.12	3.17×10^{-3}	5.4	5×10^{11}	270

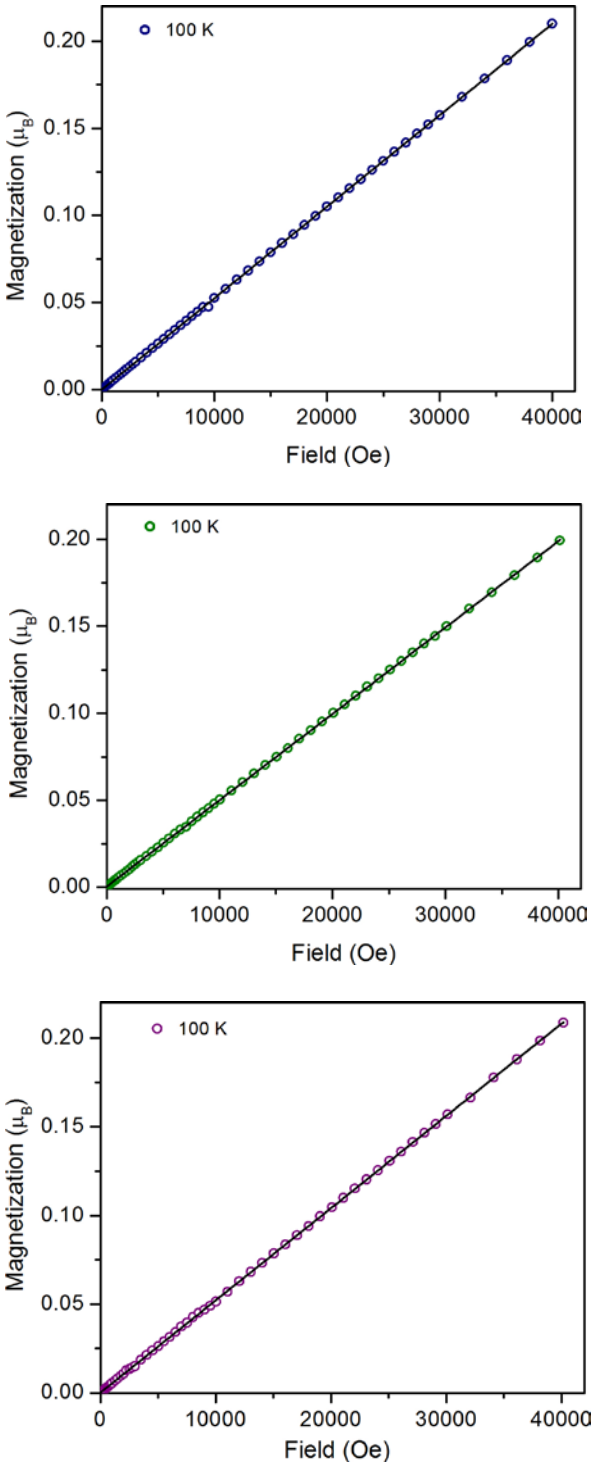

Figure S2.1. Variable-field magnetization of polycrystalline samples of 1, 3 and 4 (top to bottom, respectively) restrained under eicosane acquired at 100 K. The black line is a linear fit to the data illustrating the absence of ferromagnetic impurities.

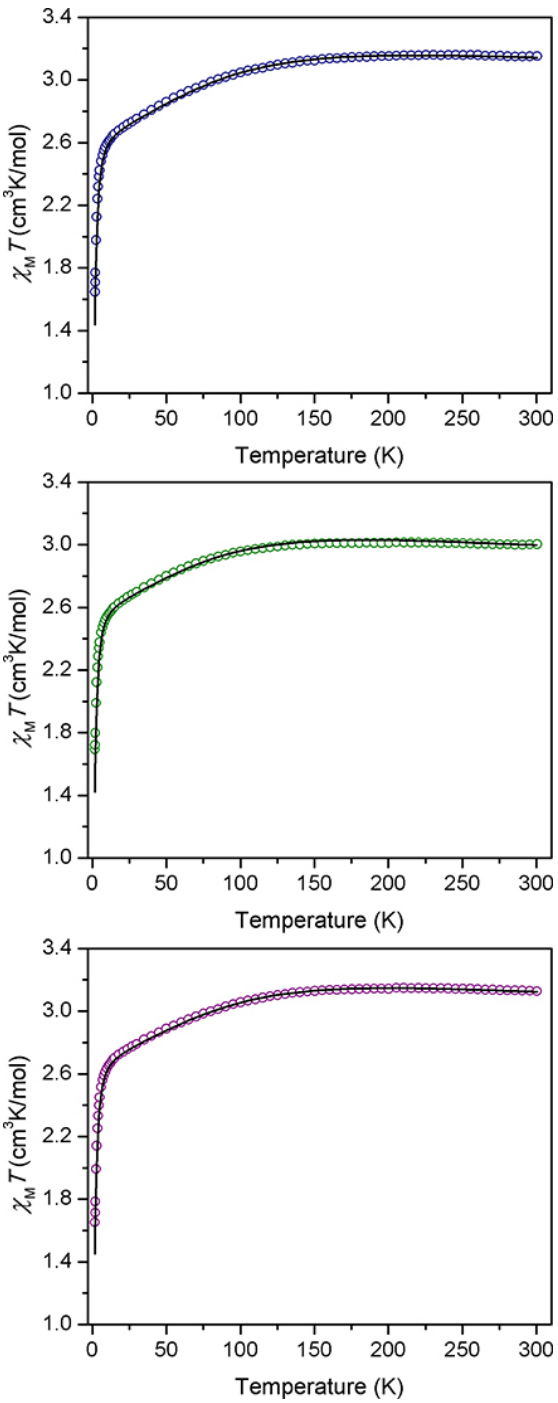

Figure S2.2. Variable-temperature dc magnetic susceptibility data for 1, 3 and 4 (top to bottom respectively) collected from 1.8 K to 300 K under a dc field of 1 T. The black lines indicate simulated data obtained from the best fits to the 1 T data. The fits were performed using the spin Hamiltonian, $\hat{H} = D\hat{S}_z^2 + E(\hat{S}_x^2 - \hat{S}_y^2) + (g_{\parallel} + g_{\perp})\mu_B SH$ in DAVE 2.0, with E constrained to a value of zero.

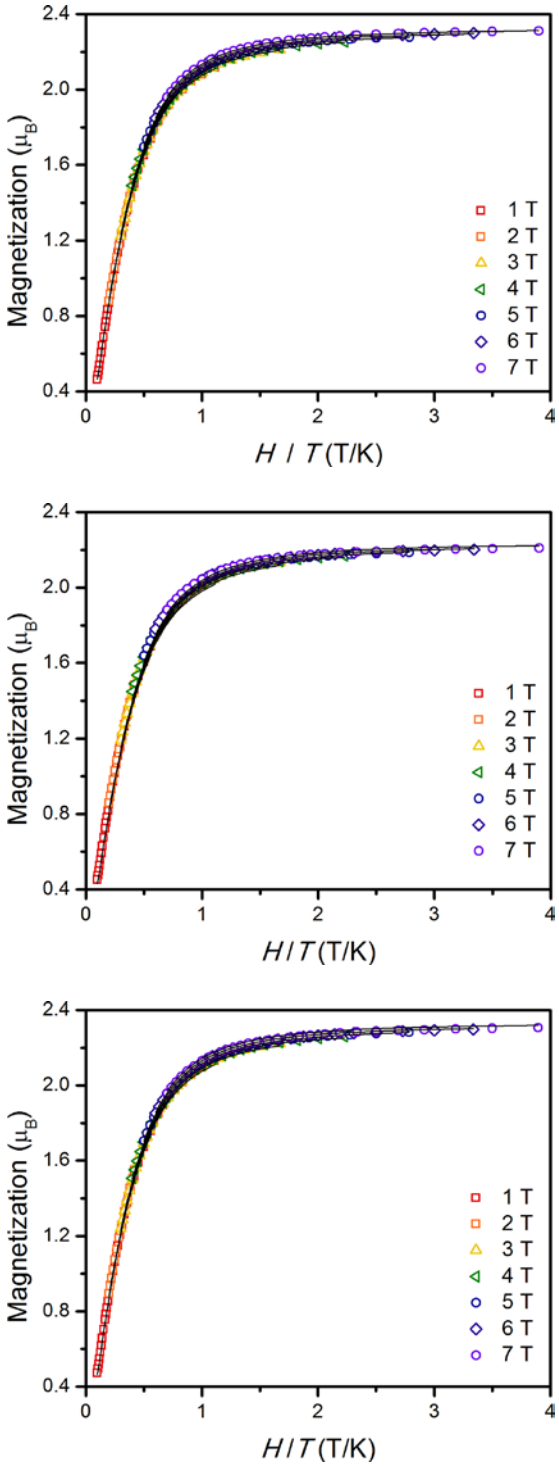

Figure S2.3. Variable-temperature, variable-field magnetization data for 1, 3 and 4 (top to bottom, respectively) collected between 1.8 and 10 K from 1 to 7 T in 1 T increments. Black lines are simulations of the data obtained from fits using DAVE 2.0 and the spin Hamiltonian, $\hat{H} = D\hat{S}_z^2 + E(\hat{S}_x^2 - \hat{S}_y^2) + g_{iso}\mu_B SH$. E was held constant at zero throughout the fits owing the low rhombicity (E/D << 0.1).

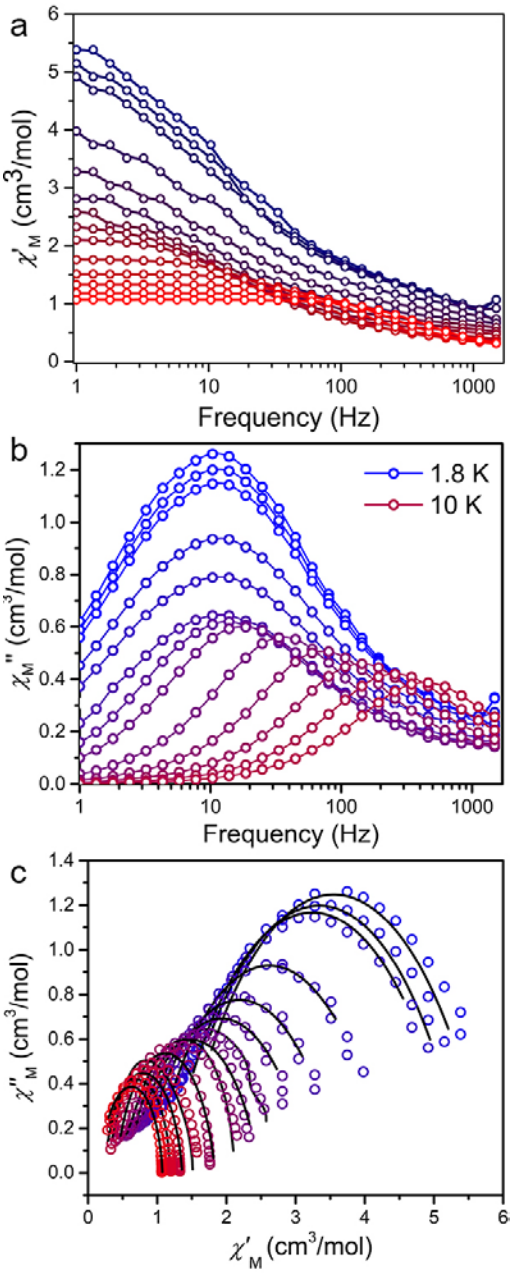

Figure S2.4. a. Variable-temperature, variable frequency in-phase ac susceptibility data collected under zero applied dc field in the temperature range of 1.8 to 10 K for 1. The solid lines are guides for the eye. b. Variable-temperature, variable frequency out of phase ac susceptibility data collected under zero applied dc field in the temperature range of 1.8 to 10 K for 1. The solid lines are guides for the eye. c. Cole-Cole plots for 1 under zero applied dc field. The plots were generated from the in-phase (χ'_M) and out of-phase (χ''_M) ac susceptibility data and fit using the generalized Debye model (black lines).

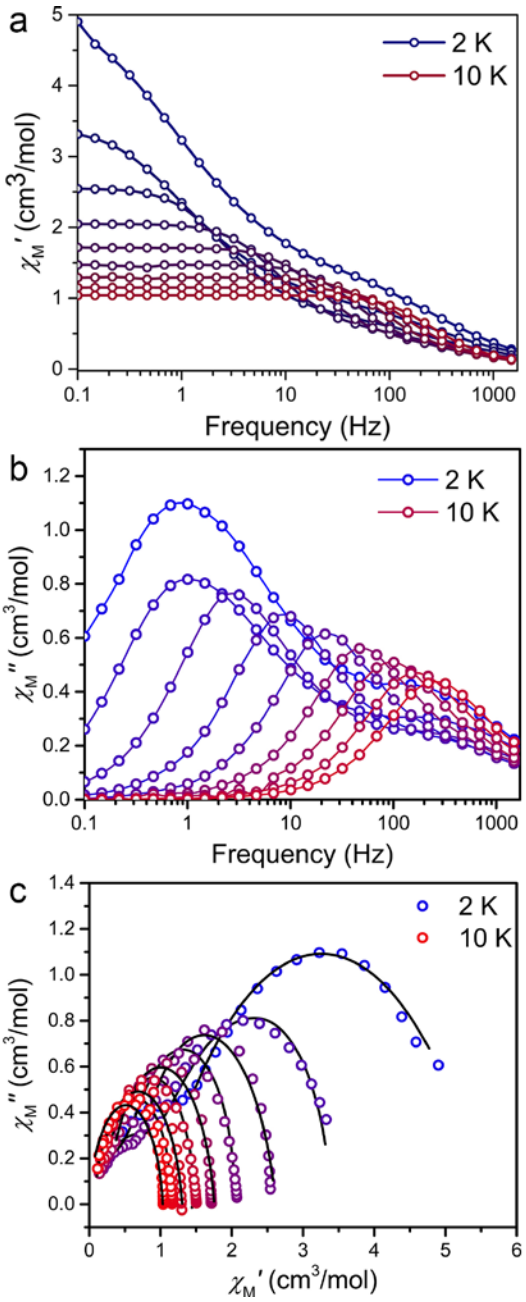

Figure S2.5. a. Variable-temperature, variable frequency in-phase ac susceptibility data collected under zero applied dc field in the temperature range of 1.8 to 26 K for 2′ (d_{20}-2). The solid lines are guides for the eye. b. Variable-temperature, variable frequency out of phase ac susceptibility data collected under zero applied dc field in the temperature range of 1.8 to 26 K for d_{20}-2. The solid lines are guides for the eye. c. Cole-Cole plots for d_{20}-2 under zero applied dc field. The plots were generated from the in-phase (χ'_M) and out of-phase (χ''_M) ac susceptibility data and fit using the generalized Debye model (black lines).

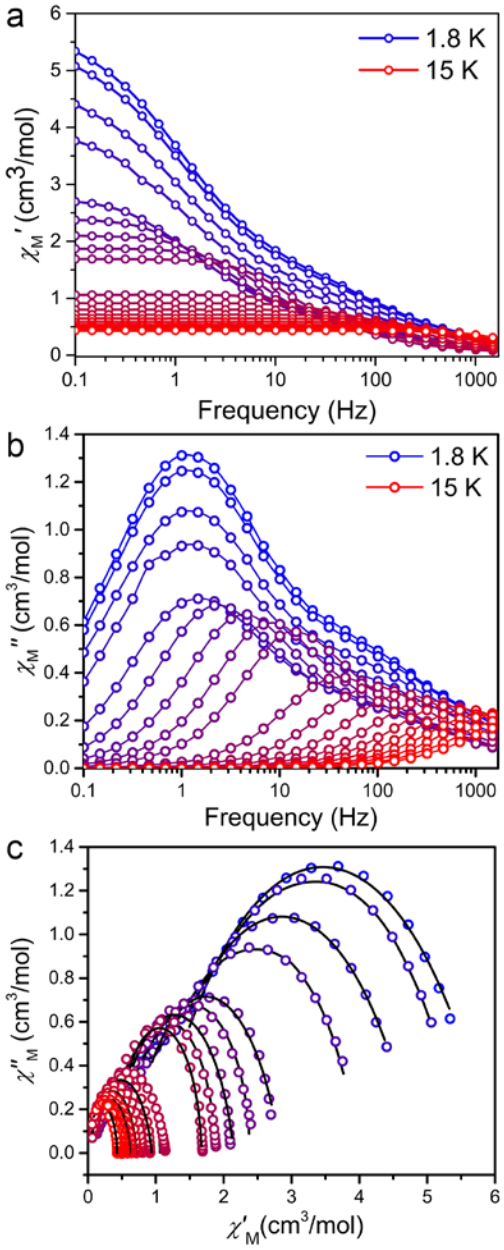

Figure S2.6. a. Variable-temperature, variable frequency in-phase ac susceptibility data collected under zero applied dc field in the temperature range of 1.8 to 15 K for 3. The solid lines are guides for the eye. b. Variable-temperature, variable frequency out of phase ac susceptibility data collected under zero applied dc field in the temperature range of 1.8 to 15 K for 3. The solid lines are guides for the eye. c. Cole-Cole plots for 3 under zero applied dc field. The plots were generated from the in-phase (χ'_M) and out of-phase (χ''_M) ac susceptibility data and fit using the generalized Debye model (black lines).

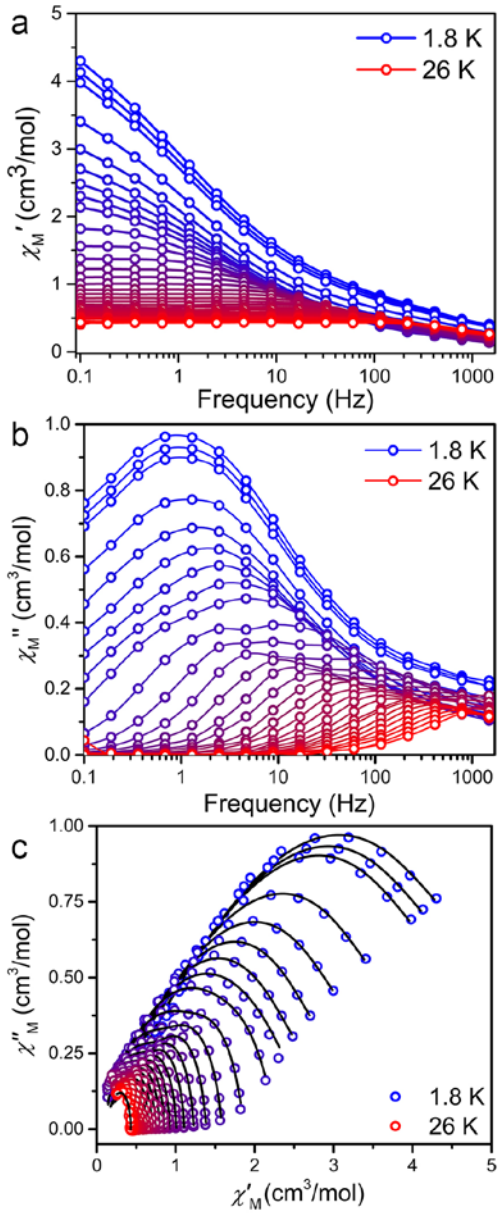

Figure S2.7. a. Variable-temperature, variable frequency in-phase ac susceptibility data collected under zero applied dc field in the temperature range of 1.8 to 26 K for 4. The solid lines are guides for the eye. b. Variable-temperature, variable frequency out of phase ac susceptibility data collected under zero applied dc field in the temperature range of 1.8 to 26 K for 4. The solid lines are guides for the eye. c. Cole-Cole plots for 4 under zero applied dc field. The plots were generated from the in-phase (χ'_M) and out of-phase (χ''_M) ac susceptibility data and fit using a two site generalized Debye model (black lines).

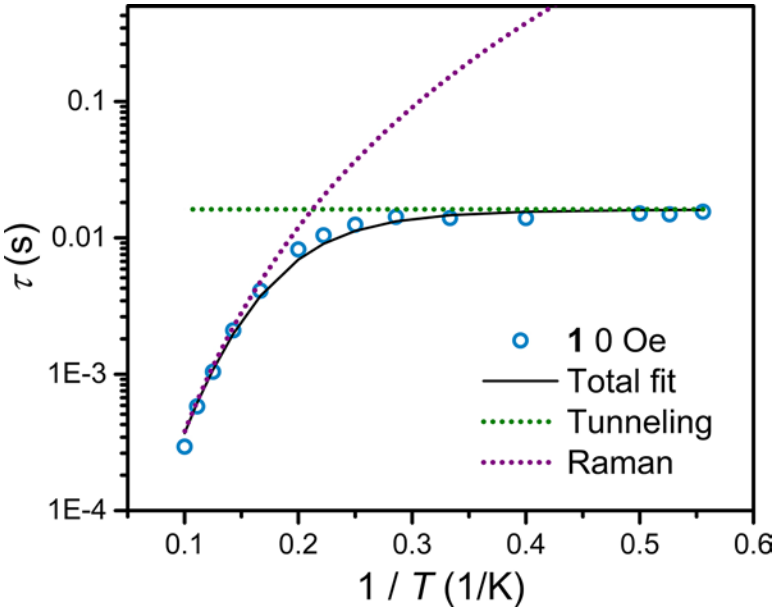

Figure S2.8. Fit to the variable temperature relaxation profile of 1 under zero applied dc field. The data were extracted from the Cole-Cole fits presented in Figure S4. The black line represents the total fit to the relaxation profile accounting for Raman (dotted purple line) and QTM (dotted green line) relaxation mechanisms.

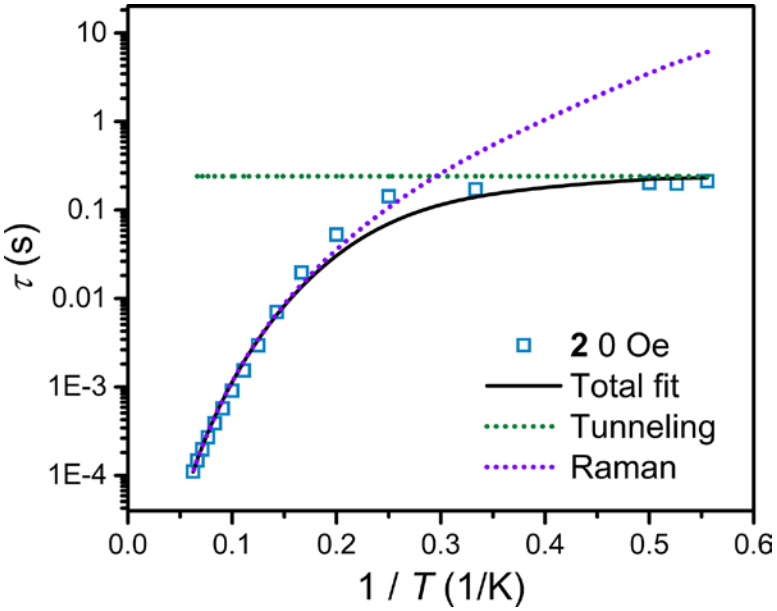

Figure S2.9. Fit to the variable temperature relaxation profile of 2 under zero applied dc field. The data were extracted from the Cole-Cole fits reported previously.[3] The black line represents the total fit to the relaxation profile accounting for Raman (dotted purple line) and QTM (dotted green line) relaxation mechanisms.

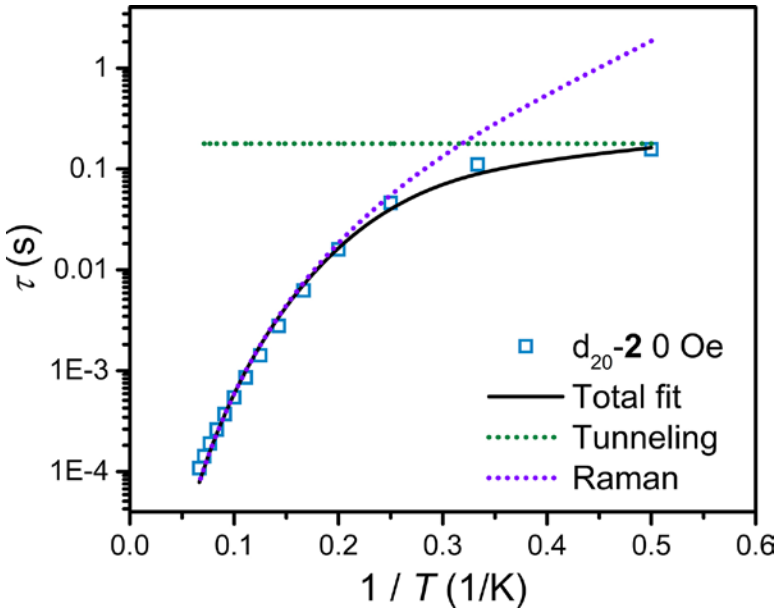

Figure S2.10. Fit to the variable temperature relaxation profile of d_{20}-2 under zero applied dc field. The data were extracted from the Cole-Cole fits presented in Figure S7. The black line represents the total fit to the relaxation profile accounting for Raman (dotted purple line) and QTM (dotted green line) relaxation mechanisms.

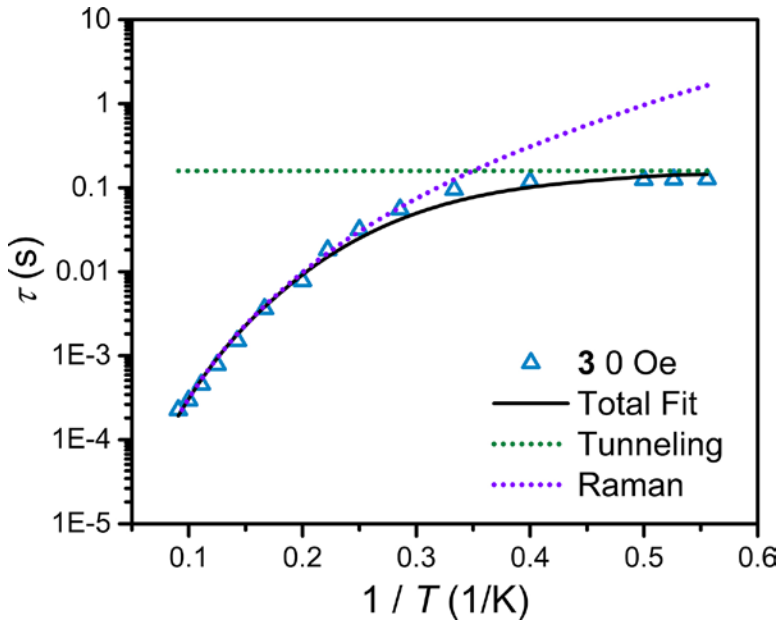

Figure S2.11. Fit to the variable temperature relaxation profile of 3 under zero applied dc field. The data were extracted from the Cole-Cole fits presented in Figure S5. The black line represents the total fit to the relaxation profile accounting for Raman (dotted purple line) and QTM (dotted green line) relaxation mechanisms.

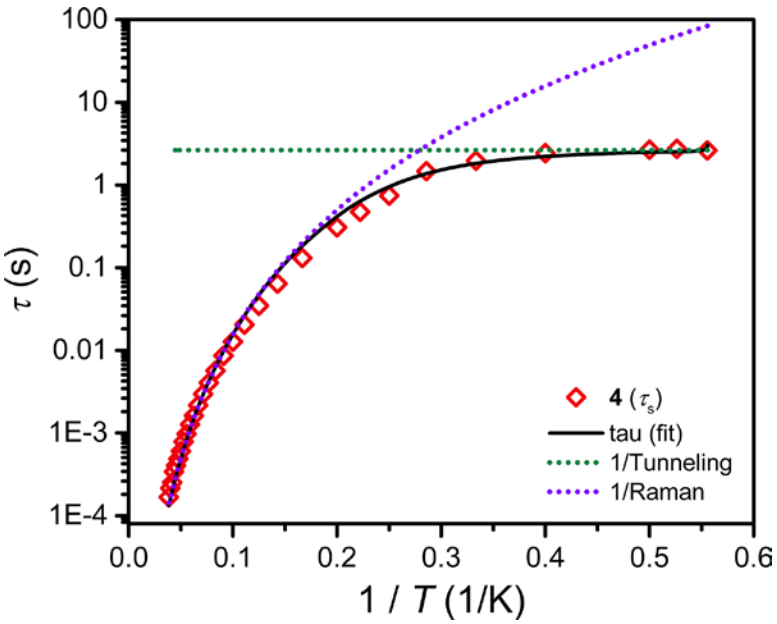

Figure S2.12. Fit to the variable temperature slow relaxation profile (τ_s) of 4 under zero applied dc field. This is an alternate fit to the data presented in the main manuscript in Figure 3c, excluding an Orbach process. The data were extracted from the Cole-Cole fits presented in Figure S6. The black line represents the total fit to the relaxation profile accounting for Raman (dotted purple line) and QTM (dotted green line) relaxation mechanisms.

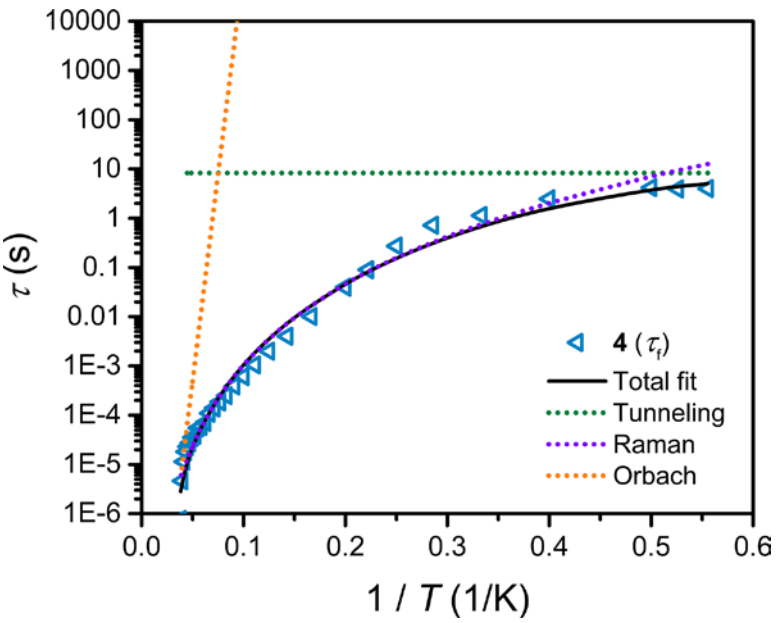

Figure S2.13. Fit to the variable temperature relaxation profile of the fast relaxation pathway for 4 under zero applied dc field. The data were extracted from the Cole-Cole fits presented in Figure S6. The black line represents the total fit to the relaxation profile accounting for Orbach (orange dotted line), Raman (dotted purple line) and QTM (dotted green line) relaxation mechanisms.

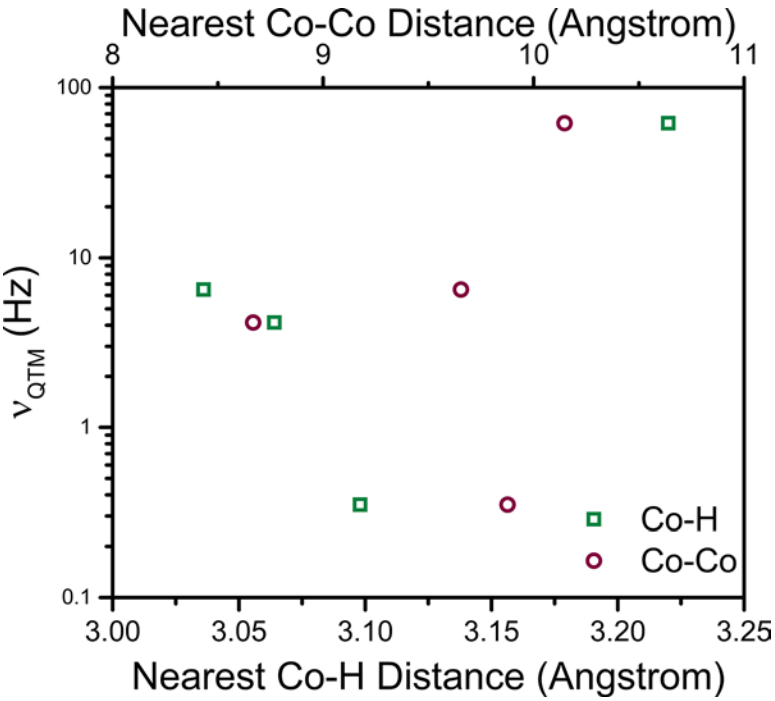

Figure S2.14. Overlay of nearest Co···Co and Co···H distances for 1 – 4 versus the quantum tunneling of magnetization frequency. The plot illustrates the absence of any trend across the series, whereby the complex with the fastest frequency possesses the longest Co···Co and Co···H distances.

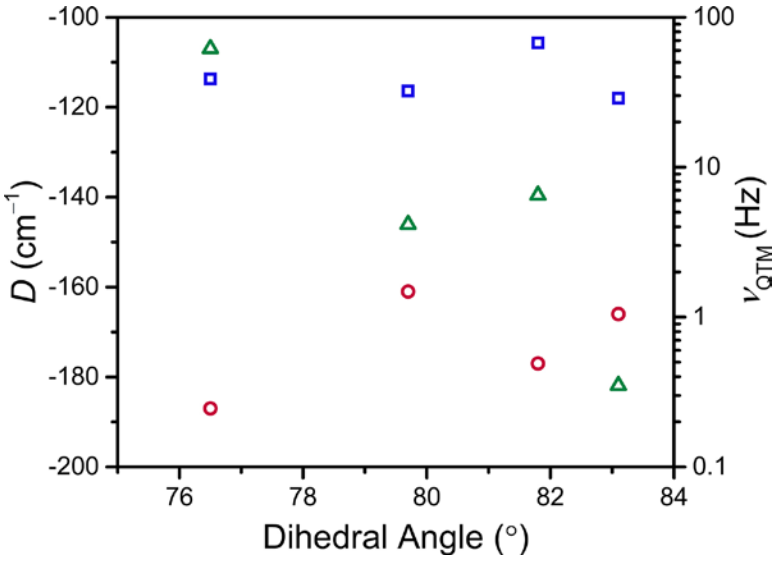

Figure S2.15. Overlay of the experimental (red circles) and calculated (blue squares) axial zero-field splitting (D, left axis) and ν_{QTM} (green triangles, right axis) plotted as a function of the dihedral angle between the two planar $C_3S_5^{2-}$ in $[Co(C_3S_5)_2]^{2-}$ illustrating the absence of any trends.

-

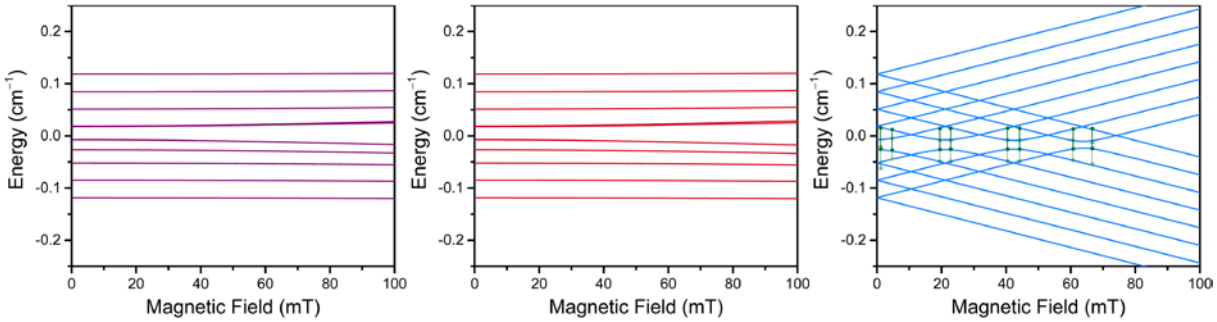

Figure S2.16. Left: Zeeman diagram simulated along the x-direction. Middle: Zeeman diagram simulated along the y-direction. Right: Zeeman diagram simulated along the z-direction. The green bars highlight the predicted transitions between the electro-nuclear hyperfine coupled states within the $M_S = {}^3/_2$ Kramers doublet. The Zeeman diagrams were simulated in EasySpin at L-band frequency ($\nu = 1.368$ GHz) at 110 K. The diagrams were simulated using an effective spin Hamiltonian ($S' = ½$) with the following effective g′-values and A′ constants: $g'_x = 0.79(5)$, $g'_y = 0.84(3)$, $g'_z = 6.8(2)$, $A'_x = 142(1)$ MHz, $A'_y = 149(1)$ MHz, $A'_z = 2026(1)$ MHz.

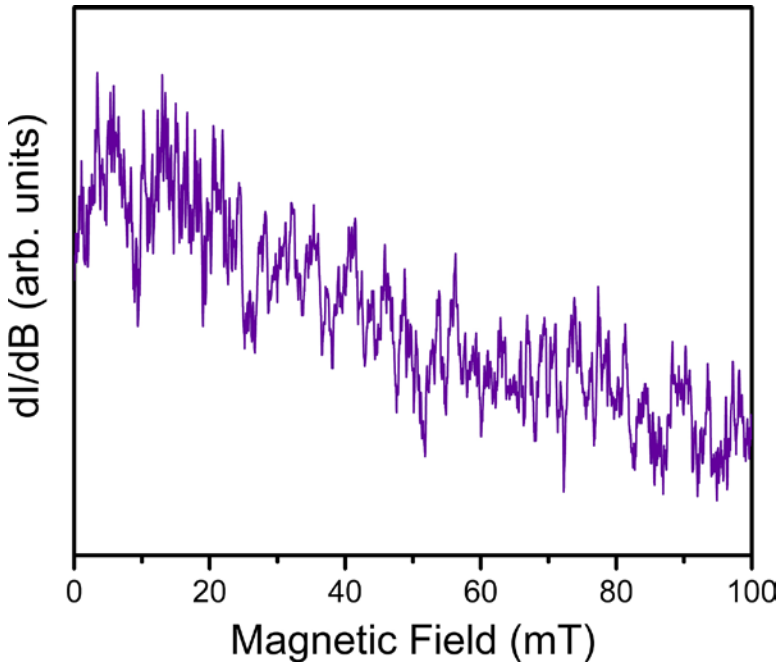

Figure S2.17. Cw-EPR spectrum of 18 MΩ water (Millipore) collected at L-band frequency (v = 1.368 GHz) at 110 K. The spectrum was collected over the same number of scans and scan times as the experimental spectrum in Figure 5 to ensure confidence in signal assignment.

Chapter 3: Magnetic Anisotropy from Main Group Elements: Halides versus Group 14 Elements

Reprinted with permission from:

Coste, S. C.; Vlaisavljevich, B.; Freedman D. E. *Inorganic Chemistry* **2017**, 56, 8195–8202.

This section was written in collaboration with the co-authors listed above.

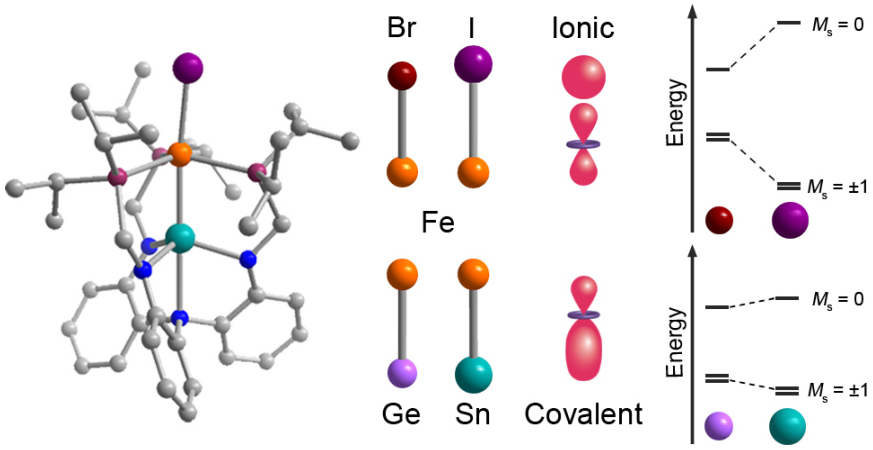

3.1 Introduction

The ability to synthetically tune spin-orbit coupling in first row transition metal complexes impacts fields ranging from molecular magnetism,[1,2] to catalysis,[3–8] and phosphors.[9–11] Fundamentally, spin-orbit coupling is a relativistic effect responsible for generating an interaction between the two components of a magnetic moment, spin (S) and orbital angular momentum (L). Spin-orbit coupling scales with effective nuclear charge as Z_{eff}^4, thereby engendering small values of spin-orbit coupling constants for first row transition metals, relative to their third row counterparts.[12] As spin-orbit coupling dictates key aspects in a plethora of systems, including intersystem crossing rates in luminescent materials and magnetic anisotropy in single-molecule magnets, control over spin-orbit coupling in first row transition metals is a vital goal for coordination chemistry. To augment magnetic anisotropy in first row transition metal complexes, unusual synthetic strategies are required to enhance and modulate spin-orbit coupling. Toward that end, over the past decade, synthetic chemists demonstrated the power of tuning ligand field geometries to precisely control the incorporation of orbital-angular momentum in mononuclear transition metal complexes.[13–16] Careful consideration of ligand field effects led to hundreds of strongly anisotropic single-molecule magnets.[17–25] Yet, outside of the realm of molecular magnetism, this work is inherently limited in application by its reliance on low coordination numbers and rigidly symmetric ligand fields.

An attractive strategy to enhance the spin-orbit coupling in first row transition metal complexes is to introduce heavy diamagnetic elements into their primary coordination sphere. This alternate approach, which has precedent in the electron paramagnetic resonance (EPR) spectroscopy literature,[26–29] can be envisioned as a ligand based heavy atom effect whereby spin-orbit coupling

is incorporated through a heavy diamagnetic element. Here, the magnetic moment is effectively separated into two atoms, a spin bearing atom and an orbital angular momentum bearing atom, and spin-orbit coupling is reconstituted through a bonding interaction. This effect manifests in the enhancement in singlet to triplet transition rates in organic molecules, which underlies its use to designing luminescent materials.[30,31] Further, there are a handful of examples of the external heavy atom effect enhancing magnetic anisotropy in transition metal complexes from the use of heavy chalcogenides or halides as ligands. [32– 38]

A combination of chemical intuition and prior theoretical research suggests that the amount of covalency in the metal-ligand interaction is directly related to the transfer of magnetic anisotropy from the ligand to the transition metal.[27,38] Understanding the relative impact of covalency arising from different groups within the periodic table could propel the use of heavy main group elements as sources of magnetic anisotropy. As our two end points, we sought to create a series of complexes wherein we could compare the impact of increased mass between halides and group 14 elements as ligands. In transition metal-main group element interactions, halides offer weakly covalent interactions, while group 13 – 15 elements offer increased covalency owing to their relative electropositivity. If covalency scales with magnetic anisotropy, the group 14 elements would impact magnetic anisotropy in a more significant manner than the halides.

Herein, we report a series of isostructural Fe^{2+} complexes designed to test the relative impact of halides versus group 14 elements. Synthesis of this series was facilitated by a rigid framework binding iron to a group 14 element with an open coordination site for halide ligation. Employing this synthetic strategy, we synthesized, and isolated the four new paramagnetic complexes [N(o-($NCH_2P(iPr_2)$)$C_6H_4)_3$GeFeBr] (**1**), [N(o-($NCH_2P(iPr_2)$)$C_6H_4)_3$GeFeI] (**2**), [N(o-

$(NCH_2P(iPr_2))C_6H_4)_3SnFeBr]$ (**3**), and $[N(o\text{-}(NCH_2P(iPr_2))C_6H_4)_3SnFeI]$ (**4**), which feature covalent bonds to a group 14 element (Ge^{2+} or Sn^{2+}).

3.2 Results and Discussion

To enable the study of magnetic anisotropy induced by heavy metals we targeted a series of four compounds with different main group elements bound to an iron center. Realizing a covalent bond between a paramagnetic transition metal and a main group metal is inherently difficult due to the Lewis acidic nature of the two species.[39] Heterobimetallic complexes containing such metal-metal bonds almost exclusively feature electron-rich transition metals such as carbonyl complexes.[40–43] In such cases, the strong ligand field surrounding the transition metal engenders diamagnetic complexes. Therefore, the synthesis of heterobimetallic complexes featuring paramagnetic transition metal-heavy main group metal bonds poses a unique synthetic challenge. A successful approach to facilitate metal-metal bonding relies on utilizing the supporting framework of ligand scaffolds. Recently, Lu and coworkers demonstrated the capacity for a phosphinoamide ligand to mediate Ni^0-group 13 element bonds. However, in these complexes, the zero valent, diamagnetic Ni behaves as a base towards the acidic group 13 element.[44,45] In order to target heterobimetallic complexes with paramagnetic first row transition metals, the polarity of the bond must be reversed. Towards this goal, we exploited the lone pair of heavier divalent group 14 elements, which can act as Lewis bases towards acidic transition metals.[46,47] We accessed the

Scheme 3.1 Synthesis of compounds **1** – **4** (E = Ge, Sn; X = Br, I).

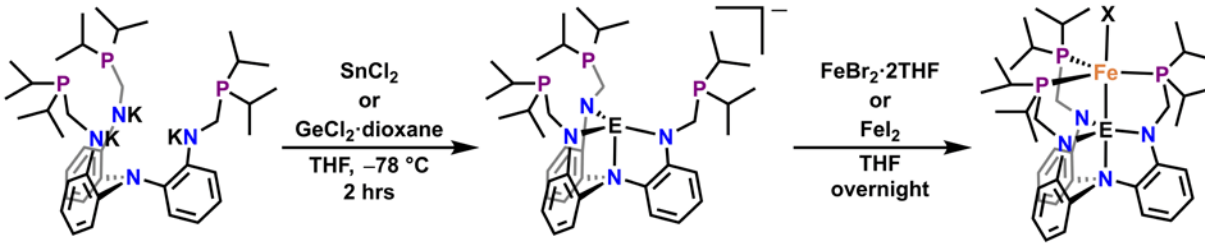

series of heterobimetallic complexes via a two-step salt metathesis in THF. The first metalation of the ligand's tripotassium salt with $SnCl_2$ or $GeCl_2$·dioxane is performed at −78 ˚C, with subsequent metalation at room temperature with $FeBr_2$·2THF or FeI_2 affords the neutral, heterobimetallic compounds. We purified compounds **1** – **4** by recrystallization from a concentrated solution of diethyl ether to obtain bright red crystals suitable for X-ray diffraction experiments. Further synthetic details are available in the supplementary information.

Single crystal X-ray diffraction studies revealed compounds **1** – **4** to be isostructural, as illustrated in Figure 3.1. We note that while **2** crystallizes with a different unit cell, its molecular geometry remains similar to **1**, **3**, and **4** implying only a change in molecular packing. All four compounds distort from idealized C_{3v} symmetry where both metal centers adopt a distorted trigonal bipyramidal geometry. The bottom pocket of the structure features the first azagermatrane and azastannatrane moieties isolated with divalent group 14 elements where tetravalent species are the common state within the atrane ligand platform. The equatorial nitrogen-germanium (1.9306(6) Å and 1.918(4) Å for **1** and **2**) and nitrogen-tin bonds (2.091(4) Å and 2.096(2) Å for **3** and **4**) agree well with other germylene and stannylene compounds.[48,49] Compounds **1** and **2** feature Fe–Ge bond distances of

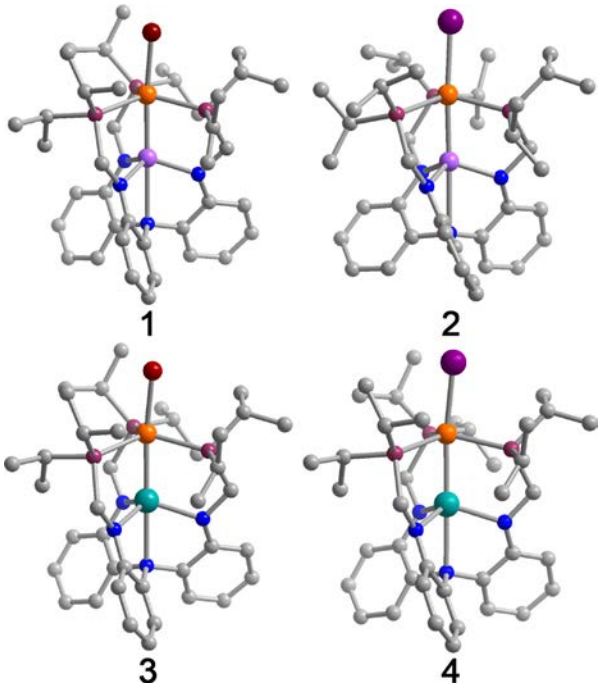

Figure 3.1 Molecular structures of **1** – **4** determined from single crystal X-ray diffraction. Orange, turquoise, pink, red, violet, plum, blue and grey spheres represent Fe, Sn, Ge, Br, I, P, N and C atoms respectively.

2.3764(3) and 2.35584(5) Å, respectively, and the Fe–Sn distances in **3** and **4** are 2.4828(5) and 2.47930(7) Å. All metal-metal bonds are shorter than the sum of their covalent radii (2.52 Å for Fe–Ge and 2.71 Å for Fe–Sn)[50] and well within the range reported in ferrous heterobimetallic complexes.[51,52] Each iron center puckers out of the plane defined by the three equatorial phosphine ligands by 0.41(4) Å. The average Fe–P distances of 2.33(2) Å in **1** and **2** are in accordance with previously reported triplet Fe(II) complexes.

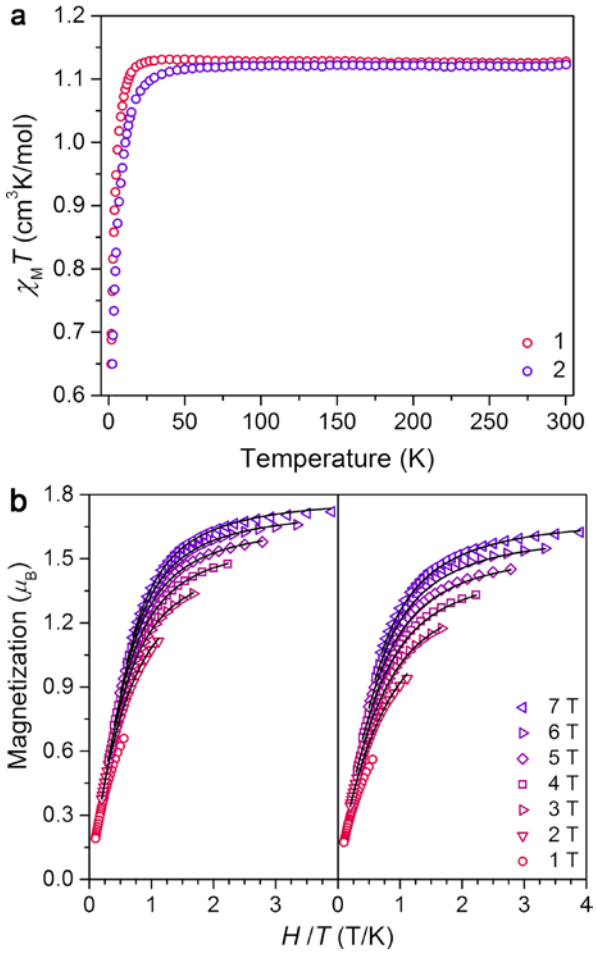

Figure 3.2 (a) Variable-temperature dc susceptibility data for **1** and **2** with H_{dc} = 0.1 T. (b) Variable-temperature, variable-field magnetization for **1** and **2**; black lines represent the best fit. The parameters for the fit are given in Table S3.6.

Compounds **3** and **4** feature longer distances of 2.38(2) Å, but are still shorter than those observed in high-spin Fe(II) compounds.[53–55] The complexes here represent, to the best of our knowledge, the first crystallographically characterized iron-tin and iron-germanium bonds in a paramagnetic species.

Comparison between the impact of group 14 elements versus halides on magnetic properties was facilitated by SQUID-based magnetometry. Variable temperature dc magnetic susceptibility

Table 3.1 Summary of magnetic and Mössbauer parameters and e–e orbital set transition for **1** – **4**.

	1	**2**	**3**	**4**
g_{iso} [a]	2.12	2.12	2.11	2.15
D (cm^{-1}) [b]	−11.8(3)	−15.5(4)	−12.1(4)	−17.9(3)
δ (mm/s)	0.541(4)	0.510(4)	0.669(4)	0.657(2)
ΔE_Q (mm/s)	0.554(6)	0.358(5)	0.559(7)	0.421(5)
λ_{e-e} (nm)	1456	1501	1390	1457

a Obtained from value of $\chi_M T$ at 300 K. *b* Determined by fits of variable-temperature, variable-field magnetization data.

data allows us to probe the spin state of the compounds and provides initial insight into magnetic anisotropy. Susceptibility data were acquired on polycrystalline samples of **1** – **4**. All compounds exhibit room temperature $\chi_M T$ values within the range of 1.11 – 1.15 cm^3K/mol, consistent with an S = 1 Fe(II) center (Figure 3.2a and Figures S3.3–S3.4). The triplet spin state of the Fe(II) centers prompted us to further probe the electronic structure of these species with theoretical calculations. In selecting the appropriate methodology, we employed complete active space SCF calculations with energy corrections from second-order perturbation theory (CASSCF/CASPT2), as this approach properly treats triplet spin states. We confirm the ground states of **1** – **4** as S = 1 states at the CASPT2 level of theory with the lowest lying S = 0 and S = 2 states falling between 34 – 36 kcal/mol higher in energy. We attribute the stabilization of the triplet ground state to the relatively strong ligand field provided by the phosphine and group 14 donors.

In all compounds, the room temperature $\chi_M T$ value persists until low temperatures where the iodide compounds diverge from their bromide congeners. At 60 K, **2** and **4** feature a drop to 0.65 cm^3K/mol at 1.8 K whereas **1** and **3** maintain their room temperature value until 30 K, whereby the $\chi_M T$ values decreases to 0.64 cm^3K/mol at 1.8 K. We attribute the decrease in $\chi_M T$ to axial zero-field splitting, *D.* The decline in susceptibility for compounds with axial zero field splitting is due to the depopulation of M_S levels with decreasing temperature. Therefore, the difference in

the low temperature curvature suggests that the iodide-containing species exhibit larger magnetic anisotropy as indicated by the increase in $|D|$ values.

To ascertain the relative impact on magnetic anisotropy of the covalent versus ionic moieties, we required a precise determination of axial zero field splitting. To establish the sign and magnitude of D, we acquired variable-temperature, variable-field magnetization data (Figure 3.2b and Figures S3.5–S3.6). The program DAVE 2.0 was employed to simulate the data with the spin Hamiltonian $\hat{H} = D[\hat{S}_z^2 - {}^1/_3 S(S+1)] + (g_\perp + g_\parallel)\mu_B \boldsymbol{SH}$, where D is the axial zero-field splitting parameter, S and $\hat{S}_z$ are the spin operators, $g_\perp$ and $g_\parallel$ are the perpendicular and parallel g-values, respectively, μ_B is the Bohr magneton, and $\boldsymbol{H}$ is the applied magnetic field.[56] The D values we extracted from the simulations (shown in Table 3.1) range from −11.8 to −17.9 cm^{-1} in compounds **1** – **4**, respectively. In order to confirm our assignment of the sign for D, we performed a survey of the residual as a function of the three fitted parameters in the program PHI.[57] We surveyed from +20 cm^{-1} to −20 cm^{-1} for D and from 1.8 to 2.5 for both $g_\perp$ and $g_\parallel$. The results, shown in Figures S3.7–S3.10, indicate that the simulated parameters in Table 1 are the global minimum, thus corroborating the negative sign of D.

The compounds containing heavier elements consistently have larger $|D|$ values in accordance with the heavy atom effect, and our observation of $|D|$ increasing with heavier halides is consistent with previous studies in 3d transition metal complexes.[26–29,32–38] However, the change in $|D|$ is relatively small with respect to other examples of the heavy atom effect. Furthermore, it is interesting to note that throughout the series, changing the halide mass influences $|D|$ more so than changing the group 14 element mass. This is most evident when comparing **1** and **3**, where the change in $|D|$ is within error. As the Fe–X (X = Br^-, I^-) bond is relatively ionic, our initial

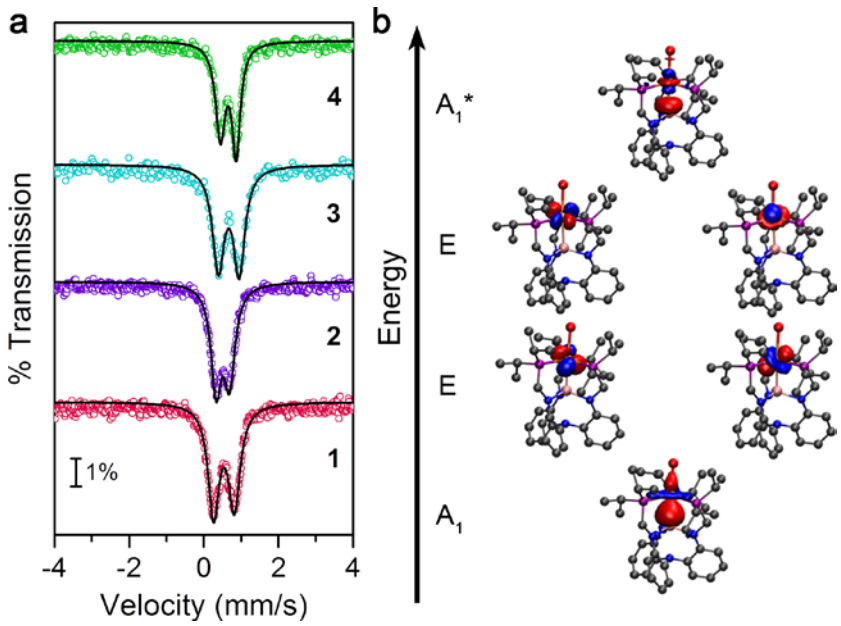

Figure 3.3 (a) Mössbauer spectra for powder samples of **1** – **4** collected at 80 K. Open circles represent the experimental data and the black lines represent fits to the spectra. The parameters are given in Table 3.1. (b) Natural orbitals of the 3d manifold for **1**. Figures S3.18–S3.20 show the natural orbitals for **2** – **4**.

hypothesis was that less spin-orbit coupling would be imparted onto the iron center because the electrons are polarized towards the electronegative halide. Nonetheless, larger $|D|$ values in **3** and **4** suggests increased spin-orbit coupling at the Fe(II) center from the heavy group 14 elements, but further details concerning the electronic structure are required to elucidate the impact of each element on the magnetic properties.

We employed ^{57}Fe Mössbauer spectroscopy to investigate the influence of each axial ligands' covalency on the Fe(II) electronic ground state. As the isomer shift (δ) is a direct measure of the electron density of the s-orbital at the nucleus of Fe center, it provides a valuable probe of both the oxidation state and metal-ligand covalency. The spectra of all four compounds, displayed in Figure 3.3a, feature single quadrupolar doublets, whose isomer shifts are summarized in Table 3.1. The isomer shifts are comparable to other reported triplet spin ferrous complexes existing in an electron rich environment.[55] We note that δ remains unchanged between the compounds containing differing halides which matches previous observations,[58,59] however, δ increases by ~ 0.1 mm/s

Table 3.2 Percentage of atomic contributions to select active orbitals from CASSCF (8*e*, 11*o*) calculations. Decomposition was performed using the Hirshfeld charge decomposition scheme. (E = Ge, Sn; X = Br, I).

Orbital	Compound	E	Fe	X
σ (A_1)	**1**	24.1	47.9	3.4
	2	22.1	47.7	4.8
	3	22.6	50.5	2.9
	4	21.8	51.1	3.7
d^2 (E) (xz, yz)	**1**	2.8	84.9	1.3
	2	2.9	85.0	1.5
	3	3.1	84.7	1.4
	4	3.2	84.8	1.5
d^1 (E) (x^2-y^2, xy)	**1**	0.6	89.7	2.2
	2	0.6	89.2	2.3
	3	0.7	90.4	2.2
	4	0.7	90.3	2.3
σ* (A_1*)	**1**	16.9	60.5	4.2
	2	15.5	60.4	5.1
	3	17.5	57.8	4.1
	4	17.4	57.1	4.8

upon increasing the mass of the group 14 element owing to its strong sigma-donating ability. The difference observed between the δ of the Ge and Sn complexes reflects the varying Ge–Fe and Sn–Fe bond strengths.

The previous success of CASSCF/CASPT2 calculations in modeling metal-metal bonding recommended them as a mechanism to further shed light on varying the axial ligand covalency. The computations show that compounds **1** – **4** have formal bond orders of 1.0 between the group 14 element and iron; the natural orbitals are shown in Figure 3b. However, both the effective bond order (EBO) calculated from CASSCF occupation numbers (Figure S3.17–S3.20) and Mayer bond orders suggest a bond order slightly weaker than a single bond (see Table S3.15). Nonetheless, both analyses indicate that the Ge–Fe bond is slightly stronger than the Sn–Fe bond. A Hirshfeld charge decomposition analysis of the sigma bond further corroborates this observation (Table 3.2). By partitioning the molecular orbitals into their respective atomic contributions, we can see that the electron density between the germanium and iron is shared slightly more than that of tin and iron. This observation is also in agreement with the δ differences from Mössbauer spectroscopy, which indicated the iron nucleus in complexes **1** and **2** was slightly electron deficient compared to **3** and **4**. It is evident that changing the group 14 element more directly influences the electron

density at the Fe(II) nucleus as opposed to the halides, however, there is no discernable trend between magnetic anisotropy and δ. The Mössbauer data and calculations demonstrate that the increased value of $|D|$ found in the iodine congeners cannot be attributed to increased covalency indicating a new hypothesis for this behavior is required.

To more precisely probe the orbital interactions between iron and the axial ligands, we turned to the quadrupole splitting parameter (ΔE_Q) from Mössbauer spectroscopy, which reflects asymmetry in the electronic configuration about the ^{57}Fe nucleus. Compounds **1** – **4** feature relatively small quadrupole splitting for ferrous compounds (Table 3.1), however, we can rationalize the small splitting with the qualitative d-orbital splitting diagram of the d^6 Fe(II) shown in Figure 3.4b. Owing to the relatively strong ligand field, a $^3A_1$ electronic ground state is expected, and is supported by dc susceptibility measurements and electronic absorption spectroscopy. The small quadrupole splitting thus arises from the symmetric occupation of unpaired electrons in the approximately degenerate d_{xy} and $d_{x^2-y^2}$ orbitals in the distorted C_{3v} symmetric compounds. Since the d_{z^2} orbital remains unoccupied, any perturbation to the quadrupole splitting will arise from a change in the valence E orbital sets. Close inspection of the quadrupole doublets reveals that ΔE_Q for the iodide congeners are consistently lower than that of their bromide congeners, while changing the group 14 element has a comparatively smaller influence on ΔE_Q. This observation suggests the halides are interacting more strongly with the valence orbitals than the group 14 elements.

The correlations between ΔE_Q and varying axial ligands prompted us to investigate atomic contributions to the valence orbital sets. Interestingly, Hirshfeld charge decomposition analysis of the SOMOs demonstrate there is a larger contribution from the halide than from the group 14 elements (see Table 3.2). The contribution from the halides are ~2.3 % compared to the weaker ~0.7 % from the group 14 elements. While both axial ligands have minimal SOMO character, the halide will more greatly affect the valence d_{xy} and $d_{x^2-y^2}$ orbitals as it has three times the contribution than the group 14 elements. Since this orbital has a larger contribution from the halide, excitations from the ground state into this orbital, the lowest lying triplet state, will be more affected by changing the halide mass.

As *D* arises from coupling of the electronic ground state to excited states through SOC, accurate determination of the frontier orbital energies will elucidate the role of changing axial ligands on the magnetic anisotropy. We quantitatively probed the electronic states *via* UV-Vis-NIR (Figure 3.4a and S3.11) absorption spectra. All complexes exhibit an intense absorption in the UV region which was previously attributed to the $\pi-\pi^*$ transition of the ligand backbone.[44]

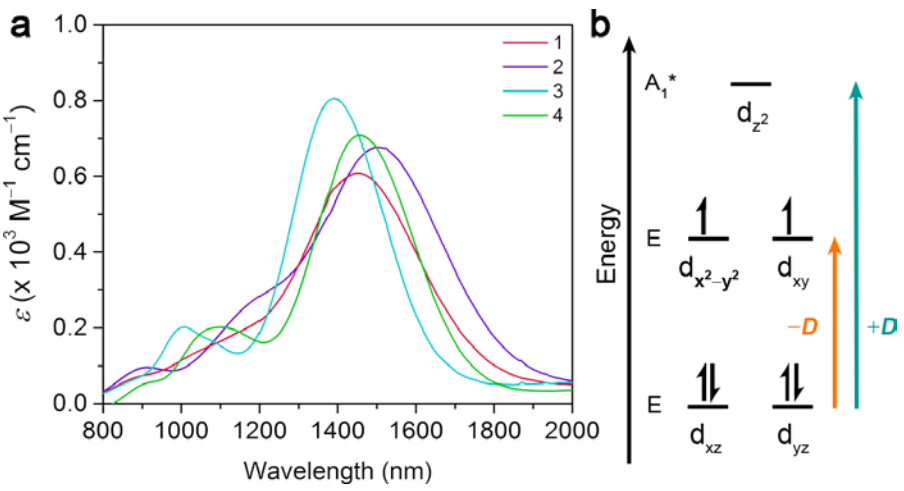

Figure 3.4 (a) NIR absorption spectra of **1** – **4** measured in $CDCl_3$ at room temperature. (b) Qualitative d-orbital splitting diagram with major contributions to *D* highlighted.

The visible region of the spectra feature absorptions with ε on the order of 10^4 $M^{-1}cm^{-1}$ which we assign as LMCT bands from both the phosphines (~415 nm

and ~530 nm) and the halides (~470 nm). The NIR region features absorptions between 800 and 1500 nm for complexes **1** – **4** with ε values less than 10^3 $M^{-1}cm^{-1}$. We attribute the most intense bands in all NIR spectra (1400 – 1500 nm) to d – d transitions between the E ($d_{x^2-y^2}$, d_{xy}) and the E (d_{xz}, d_{yz}) orbital sets. It is worth noting that this energy in the iodide compounds is smaller than their bromide congeners. The transitions between 800 and 1400 nm are d – d transitions to other low-lying triplet states, and their presence confirms a slight distortion from C_{3v} symmetry breaking the degeneracy within the two E orbital sets. Unfortunately, the charge transfer bands in the UV-Vis region mask the transitions to the d_{z^2} orbital. Our assignments are corroborated by the electronic absorption spectra in the isoelectronic Co(III) complexes reported by Levason and coworkers.[60]

To elucidate the degree of magnetic anisotropy transfer from the various main group elements, we need to consider the ligand field, which requires careful inspection of our frontier orbitals and the origin of *D*. The sign and magnitude of *D* is dependent on the energies of the d – d excited states because the ground state couples to these excited states through spin-orbit coupling.[61] The symmetry relationship between the orbitals involved in the excitation dictate the sign of the contribution. Specifically, it depends on the change in value of the magnetic quantum number (Δm_l). With respect to our qualitative d-orbital splitting diagram, the excitation from (d_{xz}, d_{yz}) to the ($d_{x^2-y^2}$, d_{xy}) orbitals, $\Delta m_l = 1$, is expected to produce a positive contribution to *D*. Similarly, the excitation from the (d_{xz}, d_{yz}) orbital set to A_1 produces a positive contribution, whereas the ($d_{x^2-y^2}$, d_{xy}) to A_1 separation does not contribute. From the qualitative d-orbital splitting diagram in Figure 3.3b, which both the ^{57}Fe Mössbauer and electronic absorption spectra support, we expect a positive *D*. However, fits to the magnetic data and a survey of magnetic parameters strongly

indicate that *D* is negative. The complexes reported here represent a unique case of magnetically characterized complexes where the sign of *D* is unexpectedly negative. Mallah and coworkers reported similar observations, and rationalized that the two E orbital sets mix in the ground state as they belong to the same irreducible representation in the C_{3v} point group.[62−65] Additionally, previous computational studies by Neese and coworkers agreed and determined the energy separation between the E orbital sets dictate the negative contribution towards *D*.[66] In their report, they confirm that the energy separation between the (d_{xz}, d_{yz}) and d_{z^2} orbitals contributes positively towards *D*. Therefore, we expect similar qualitative contributions to *D* as depicted in Figure 3.4b.

We can experimentally verify the qualitative description of *D*, and how the iodide complexes more greatly influence it, using the foregoing analyses of the electronic structure. While the contributions involving the d_{z^2} orbital are non-negligible, we expect their contribution to be relatively small in magnitude owing to the lack of an observed transition in the UV-Vis spectra at energies lower than 550 nm (~18,000 cm^{-1}). Further, the CASPT2 calculations estimate they are as high as 23,000 cm^{-1} and this transition is higher for the germanium complexes than the tin complexes. Thus, the energy separation between the two e orbital sets in compounds **1** – **4** dominate the contributions to *D*, and these will contribute to a negative sign for *D*. Indeed, these separations in the NIR absorption spectra are consistently lower for the iodide complexes than the bromide complexes agreeing with the general trend in *D*. Magnetic parameters computed using the spin-orbit CASPT2 (SO-CASPT2) support the qualitative contributions to *D*, where values of −15.4, −16.2, −13.1, and −16.0 cm^{-1} were calculated for **1** – **4**, respectively. Both the sign and order of magnitude are in good agreement with experiment, however, the trend could not be fully reproduced with accuracy. While the calculated *D* value does reproduce the effect of changing the

halide, the more subtle effect of changing from Ge to Sn would likely require a higher level of theory than CASPT2 to be resolved. Importantly, the calculations performed used the 12 lowest lying triplet states (Figure S3.12) to determine the magnetic parameters, which is a strong support for our qualitative approach to determining *D*.

In the comparison between the halide and group 14 element impact on magnetic anisotropy, we argue that the subtlety of increases in $|D|$ throughout the series arise from the differing contributions of axial ligands to the ground and first excited states. As the axial ligands are primarily sigma bonding, the only interaction with these orbitals are via π interactions. Therefore, the π-donating ability of the halides and the π-accepting ability of the main group metals dictate the observed trend in magnetic anisotropy. This symmetry-driven argument is supported by the Hirshfeld charge decomposition analysis where the halides are consistently more prevalent in the SOMOs than the group 14 elements. Consequently, the halides possess a larger spin density than the group 14 elements, and contribute more significantly towards the ground and first excited states dictating the magnetic anisotropy.

3.3 Conclusions

Synthetic control over spin-orbit coupling in first row transition metals is essential for the development of new magnetic, phosphorescent, and catalytic compounds. The heavy atom effect, in this respect, offers an attractive method to enhance the spin-orbit coupling of first row transition metals to match that of their heavier counterparts. Towards the development of design principles in transferring spin orbit coupling, we studied magnetic anisotropy as a function of covalency by comparing halides to electropositive group 14 elements. By utilizing the basic lone pair of divalent group 14 elements, we isolated covalently bonded main group elements with a paramagnetic iron

center. Through increasing the mass of axial ligands, we found the triplet Fe(II) complexes exhibit an increase in zero-field splitting from –11.8 cm^{-1} to –17.9 cm^{-1}. Comparison across the series illustrated a more pronounced influence on magnetic anisotropy from the halides relative to group 14 elements owing to a larger contribution to the electronic ground and first excited triplet states. The foregoing results highlight the importance of spin-bearing molecular orbitals' interaction with the heavy element providing spin-orbit coupling. Future work will focus on employing this design approach to create transition metal-metal group element complexes with magnetic anisotropy comparable to lanthanides.

3.4 Supplementary Information

Experimental Details.

General Considerations. All compounds were manipulated and handled under a dinitrogen atmosphere in an MBraun Unilab Pro glovebox. All glassware was either oven-dried at 150 °C for at least four hours or flame-dried prior to use. Acetonitrile (MeCN), tetrahydrofuran (THF), diethylether (Et_2O), and benzene were dried using a commercial solvent purification system from Pure Process Technology and stored over 3 or 4 Å sieves for a minimum of one day prior to use. Deuterated MeCN, chloroform, and toluene were purchased from Cambridge Isotope Labs, deoxygenated by three successive freeze-pump-thaw cycles, filtered through a pad of activated alumina, and stored over 3 or 4 Å sieves prior to use. 2,2',2''-tri(diisopropylphosphinomethylamino)triphenylamine[67] and the tripotassium salt[68] (K_3L) were prepared according to literature procedures. $FeBr_2$·2THF was prepared by soxhlet extraction of $FeBr_2$ into THF. All other chemicals were used as received.

[LGeFeBr](1). A cold solution of K_3L (500 mg, 0.63 mmol) in 120 mL THF was added dropwise to a stirring solution of $GeCl_2$·dioxane (146 mg, 0.63 mmol) in 20 mL THF at −78 ˚C. The slightly cloudy, yellow solution was stirred for 0.5 hours at this temperature, and then it was stirred at room temperature for 2 hours. The mixture was subsequently pumped down to dryness. The tan solid was taken up in 20 mL MeCN, filtered through a Celite pad on a fritted filter, and then pumped down again. The remaining solid was triturated with Et_2O until there was no coloration in the washings yielding a white solid (130 mg), which was assumed to be [KLGe]. This was dissolved in 10 mL THF then added dropwise to a 10 mL THF solution of $FeBr_2$·2THF (59.2 mg, 0.16 mmol) while stirring; the solution turned red immediately. The resultant solution was allowed to stir at

room temperature overnight. Subsequently, the mixture was filtered over Celite, then pumped down and dried for 1 hr. The red residue was taken up into benzene, filtered through Celite then pumped down again. Crystalline product suitable for single crystal X-ray diffraction was obtained by concentrating a solution of the product in Et_2O and storing it at –35 ˚C (99.9 mg, 16.5%). IR (ATR, cm^{-1}): 3056 (w), 2965 (w), 2926 (w), 2867 (w), 2805 (w), 1594 (m), 1484 (s), 1450 (m), 1381 (w), 1320 (m), 1301 (s), 1257 (m), 1231 (m), 1187 (w), 1158 (w), 1113 (s), 1075 (m), 1043 (m), 1031 (m), 958 (w), 925 (w), 910 (w), 869 (s), 826 (w), 782(w), 771(w), 741 (vs), 712 (m), 628 (s), 598 (s), 558 (w), 540 (m), 479 (w), 466 (w), 451 (w), and 432 (w). UV-Vis-NIR ($CDCl_3$) λ_{max}, nm (ε): 412 (3140), 457 (sh, 1995), 519 (1730), 901 (sh, 73), 1456 (607). ^{1}H NMR (500 MHz, d_8-toluene, 298 K): δ 33.35, 12.22, 10.24, 9.56, 7.87, 6.49, 3.63, 2.68, –9.87 ppm. Anal. Calcd. for $C_{39}H_{60}N_4P_3GeFeBr{\cdot}0.75(Et_2O)$: 53.56 %C; 7.22 %H; 5.94 %N. Found: 53.38 %C; 7.49 %H; 5.76 %N.

[LGeFeI](2). The iodide congener of **1** was made in an analogous method except that FeI_2 (50.9 mg, 0.16 mmol) was used instead of $FeBr_2{\cdot}2THF$. Yield: 69.3 mg (10.9%). IR (ATR, cm^{-1}): 3056 (w), 2953 (w), 2914 (w), 2849 (w), 2812 (w), 1594 (m), 1485 (s), 1450 (s), 1381 (w), 1365 (w), 1319 (s), 1300 (s), 1259 (m), 1238 (m), 1185 (w), 1155 (m), 1123 (m), 1083 (w), 1040 (m), 1031 (m), 963 (w), 922 (w), 910 (w), 872 (s), 826 (m), 771 (m), 739 (vs), 627 (s), 598 (m), 561 (w), 537 (m), 479 (w), and 447 (w). UV-Vis-NIR ($CDCl_3$) λ_{max}, nm (ε): 417 (3954), 467 (sh, 2372), 527 (2049), 911 (95), 1193 (sh, 281), 1501 (676). ^{1}H NMR (500 MHz, d_8-toluene, 298 K): δ 37.27, 18.99, 12.27, 10.31, 5.68, 1.96, –1.06, –8.91 ppm. Anal. Calcd. for $C_{39}H_{60}N_4P_3GeFeI{\cdot}(Et_2O)$: 51.27 %C; 7.00 %H; 5.56 %N. Found: 51.53 %C; 7.19 %H; 5.72 %N.

[LSnFeBr](3). A cold solution of K_3L (500 mg, 0.63 mmol) in 120 mL THF was added dropwise to a stirring solution of $SnCl_2$ (119 mg, 0.63 mmol) in 20 mL THF at −78 ˚C. The slightly cloudy, yellow solution was stirred for 0.5 hours at this temperature, it was then stirred at room temperature for 2 hours. The mixture was then pumped down to dryness. The tan solid was taken up in 20 mL MeCN, filtered through a Celite pad on a fritted filter, and then pumped down again. The remaining solid was triturated with Et_2O until there was no coloration in the washings yielding a white solid (282 mg) which was assumed to be [KLSn]. This was dissolved in 10 mL THF then added dropwise to a 10 mL THF solution of $FeBr_2$·2THF (121.4 mg, 0.34 mmol) while stirring; the solution turned red immediately. The resultant solution was allowed to stir at room temperature overnight. Subsequently, the mixture was filtered over Celite, then pumped down. The red residue was taken up into benzene, filtered through Celite then pumped down again. Crystalline product suitable for single crystal X-ray diffraction was obtained by concentrating a solution of the product in Et_2O and storing it at **–**35 ˚C (166.4 mg, 26.2%). IR (ATR, cm^{-1}): 3055 (w), 2954 (w), 2925 (w), 2868 (w), 2796 (w), 1594 (m), 1567 (w), 1476 (s), 1449 (s), 1381 (w), 1323 (s), 1301 (s), 1248 (m), 1235 (m), 1188 (m), 1150 (w), 1118 (s), 1076 (w), 1042 (m), 1030 (m), 958 (w), 927 (w), 902 (w), 864 (s), 824 (m), 740 (vs), 669 (w), 624 (s), 595 (s), 551 (w), 536 (m), 477 (w), 465 (w), 447 (w), and 434 (w). UV-Vis-NIR ($CDCl_3$) λ_{max}, nm (ε): 409 (4021), 467 (sh, 2164), 528 (2934), 1002 (186), 1390 (818). ^{1}H NMR (500 MHz, d_8-toluene, 298 K): δ 36.25, 29.47, 11.34, 10.72, 8.08, 2.32, −3.59, −22.74 ppm. Anal. Calcd. for $C_{39}H_{60}N_4P_3SnFeBr$·1.25(Et_2O): 51.56 %C; 7.13 %H; 5.46 %N. Found: 51.56 %C; 7.13 %H; 5.50 %N.

[LSnFeI](4). The iodide congener of **3** was synthesized in an analogous method with the replacement of $FeBr_2$·2THF by FeI_2 (104.5 mg, 0.34 mmol). Yield: 131.5 mg (19.8%). IR (ATR,

cm^{-1}): 3055 (w), 2963 (w), 2921 (w), 2866 (w), 2797 (w), 1592 (m), 1564 (w), 1475 (s), 1449 (s), 1380 (w), 1322 (s), 1299 (s), 1249 (m), 1235 (m), 1189 (m), 1150 (w), 1113 (s), 1072 (w), 1042 (m), 1031 (m), 957 (w), 927 (w), 902 (w), 863 (s), 824 (m), 741 (vs), 667 (w), 623 (s), 593 (s), 556 (w), 532 (m), 477 (w), 452 (w), and 430 (w). UV-Vis-NIR ($CDCl_3$) λ_{max}, nm (ε): 416 (4792), 476 (sh, 1947), 537 (2603), 921(56), 1101 (201), 1457 (709). ^{1}H NMR (500 MHz, d_8-toluene, 298 K): δ 29.19, 11.49, 10.80, 8.33, 6.59, 2.39 –1.62, –25.49 ppm. Anal. Calcd. for $C_{39}H_{60}N_4P_3SnFeI$**:** 47.83 %C; 6.17 %H; 5.72 %N. Found: 47.64 %C; 6.16 %H; 5.54 %N.

Magnetic Measurements. Magnetic data were collected using a Quantum Design MPMS-XL SQUID magnetometer. Measurements for all compounds were obtained on finely ground microcrystalline powders. The compounds were restrained in a frozen eicosane matrix and flame sealed in a quartz tube under vacuum. Dc susceptibility measurements were collected in the temperature range 1.8–300 K under dc fields of 0.1, 0.5 and 1 T. Dc magnetization measurements were performed under applied magnetic fields of 1, 2, 3, 4, 5, 6 and 7 T in the temperature range of 1.8–10 K. Dc magnetic susceptibility data were corrected for diamagnetic contributions from the sample holder and eicosane as well as for the core diamagnetism of each sample, estimated using Pascal's constants.[69] Prior to full characterization, variable dc field magnetization data was collected from 0 to 4 T at 100 K to ensure the absence of curvature associated with ferromagnetic impurities.

X-ray Diffraction. Single crystal diffraction data collections were performed on single crystals coated with Paratone-N oil and mounted on a MicroMounts^{TM} rod. The crystals were frozen while coated in Paratone-N oil under a stream of N_2 during the measurement. Structures for **1**, **2**, and **3** were collected on a MICROSTAR X-ray source of Cu Kα (λ = 1.54056 Å) radiation with a Bruker

SMART APEX CCD area detector. Data for **4** was collected with a Bruker KAPPA APEX-II diffractometer equipped with a Mo Kα (λ = 0.71073 Å) sealed tube diffraction source with a graphite monochromater, and a Bruker APEX-II detector. Raw data were integrated and corrected for Lorentz and polarization effects using Bruker Apex2 v. 2013.[70] Absorption corrections were applied using SADABS.[71] Space group assignments were determined by examination of systematic absences, *E*-statistics, and successive refinement of the structures. The crystal structure was solved by direct methods with the aid of successive difference Fourier maps in SHELXS[6] operated with the OLEX2 interface.[72] The crystals showed no significant decay during data collection. Thermal parameters were refined anisotropically for all non-hydrogen atoms in the main body, solvents of crystallization, and counterions. Hydrogen atoms were placed in ideal positions and refined using a riding model for all structures.

Zero-field ^{57}Fe Mössbauer Spectroscopic Measurements. All measurements were performed under zero applied magnetic field and at 80 K on ca. 60 mg of ground, microcrystalline samples. Samples were loaded into a circular plastic cap of 1 cm^2 area under an inert atmosphere covered in Paratone-N oil and transferred quickly to the cryostat to avoid sample decomposition. Spectra were collected with a constant acceleration spectrometer and a ^{57}Co/Rh source. Prior to measurements, the spectrometer was calibrated at 295 K with α-Fe foil. Spectra were analyzed using the WMOSS Mössbauer Spectral Analysis Software (www.wmoss.org).

All Other Physical Measurements. Combustion analysis of all complexes was performed by Midwest Microlab (Indianapolis, IN). Infrared spectra were recorded on a Bruker Alpha FTIR spectrometer equipped with an attenuated total reflectance accessory. Solution-phase NMR spectra were collected with an Agilent DD2 500 MHz spectrometer. Proton NMR spectra are referenced

to d_8-toluene or d_3-MeCN at 6.97 and 1.94 ppm, respectively. UV-vis-NIR spectra were collected on a Varian Cary 5000 spectrometer in $CDCl_3$.

Computational Details. Geometry optimizations were performed with density functional theory (DFT) for all four complexes **1**–**4** using the PBE functional and the def2-TZVP basis set for all atoms as implemented in the Turbomole software package.[73–75] The resolution of the identify (RI) approximation was employed.[76–78] Although a full geometry optimization was performed and these structures were in good agreement with experiment (see Table S3.12), zero field splitting parameters are very sensitive to the geometry of the first coordination sphere. Therefore, the structures that were used for all calculations in the main text were optimized with PBE/def2-TZVP; however, the position of the metals, halogen, and the coordinating nitrogen and phosphorous atoms were fixed at the experimental geometry; only the remaining atoms were optimized. These structures were 1.5, 2.8, 1.6, and 1.5 kcal/mol higher in energy for structures **1**–**4**, respectively, than the fully optimized geometries (see Tables S3.11-S3.12).

To study the bonding in this series of compounds, complete active space self-consistent field calculations with corrections from second order perturbation theory (CASSCF/CASPT2) were performed on the constrained DFT optimized geometries described above.[79–81] First, CASPT2 calculations were performed for the lowest singlet, triplet, and quintet states as implemented in the Molcas 8.0 software package.[82] The active space includes eight electrons in eleven orbitals (8*e*,11*o*). The orbitals included are the Fe 3d and correlating 4d orbitals along with the 4s orbital on Ge (or 5s for complexes with Sn). Scalar relativistic effects were included through the use of the Douglas-Kroll-Hess (DKH) Hamiltonian and ANO-RCC basis sets were employed with the following contractions: Fe 6s5p3d2f1g, Ge 6s5p3d2f1g, Sn 7s6p4d2f1g, Br 6s5p3d1f, I

7s6p4d2f1g, N 3s2p1d, P 4s3p1d, C 3s2p, and H 1s.[83–86] Cholesky decomposition was used in combination with local exchange (LK) screening to reduce the cost of the two electron integrals.[87–90] In the CASPT2 calculations, an imaginary shift of 0.2 and an IPEA shift of 0.25 were applied. LoProp and Mulliken atomic charges were computed as implemented in Molcas 8.0 while the Hirshfeld charge decompositions (CDA) scheme,[91–93] used to compute the percent contributions of each atom to select molecular orbitals, (see Tables S3.13-S3.14 and Table 3.2 in the manuscript for LoProp, Mulliken, and Hirsheld results) and Mayer bond orders (Table S3.15) were calculated using the MultiWFN software package.[94,95]

In additional to the CASPT2 calculations described above for the lowest energy singlet, triplet, and quintet states, state averaged CASSCF calculations were performed to examine the low-lying excited states and compute the zero field splitting parameters. We performed two sets of calculations. The first set included only triplet states truncating after single excitations into the unoccupied $3d_{z2}$ orbital (double excitations into this orbital were excluded as were excitations in higher energy unoccupied orbitals). Spin orbit coupling effects were computed *a posteriori* using the state interaction approach (RASSI).[96] The diagonal elements of this effective Hamiltonian were replaced with the CASPT2 energies, the so-called spin-orbit CASPT2 (SO-CASPT2) method. The RASSI spin-orbit states that were obtained were then introduced into the SINGLE-ANISO module in order to calculate the magnetic properties (*D* and *E*) of the complexes (see Table S3.7). Since it is well-known that truncating the number of excitations when computing magnetic properties can lead to truncation errors, we also computed the full *d*-manifold for an Fe(II) center using SA-CASSCF (50 singlet states, 45 triplet states, and 5 quintet states). In this case, CASPT2 calculations were not performed but the same approach was applied to compute *D* and *E*

parameters but in this case using CASSCF energies (see Table S3.8). The lowest 12 spin orbit states consisted of mixing between triplet spin-free states. Additionally, the sign and magnitude of the two sets of *D* values were in good agreement. We performed other tests including a varying number of $S = 0$, $S = 1$, and $S = 2$ states include in the state averaging procedure and, provided that truncations were made at consistent energies for all three spins, the *D* and *E* parameters remained between ~ −10 to −17 for all of the cases we explored. For this reason, we expect that the deviations we observe between our calculated values and experimental values is likely too small (order of wavenumbers) to be resolved at the CASPT2 level and would require other levels of theory (such as MRCI) that are very computationally intensive and give the size of our molecules outside our reach.

Table S3.1 | Crystallographic information for the structural refinement of **1**.

Empirical Formula	$C_{43}H_{70}BrFeGeN_4OP_3$
Formula weight	959.84 g/mol
Temperature	100 K
Wavelength	1.54178 Å
Crystal System	Monoclinic
Space Group	$P2_1/c$
Unit Cell Dimensions	a = 11.6789(3) Å, α = 90.0˚
	b = 16.2409(4) Å, β = 101.0830(10)˚
	c = 23.9498(6) Å, γ = 90.0˚
Volume	4457.98(19) Å^3
Z	4
Density (calculated)	1.430 g/cm^3
Absorption coefficient	5.791 mm^{-1}
F_{000}	2006.0
Crystal color	Red
Crystal size	0.132 × 0.077 × 0.064 mm^3
2θ range	7.714 to 136.174˚
Index ranges	$-13 \leq h \leq 13$
	$-14 \leq k \leq 19$
	$-28 \leq l \leq 28$
Reflections collected	34370
Independent reflections	7916 [R_{int} = 0.0371]
Completeness to 2θ = 136.174˚	97.4 %
Absorption correction	Multi-scan
Maximum and minimum transmission	0.5209 and 0.4094
Refinement method	Full-matrix least-squares on F^2
Data / restraints / parameters	7916 / 0 / 512
Goodness-of-fit on F^{2a}	1.028
Final R indices [I > 2σ(I)]^b	R_1 = 3.02 %, wR_2 = 7.38 %
R indices (all data)	R_1 = 3.57 %, wR_2 = 7.70 %
Largest diff. peak and hole	1.09 and –0.55 e.Å^{-3}

[a] GooF = $[\Sigma[w(F_o^2-F_c^2)^2] / (n-p)]^{1/2}$ where n is the number of reflections and p is the total number of parameters refined. [b] $R_1 = \Sigma||F_o|-|F_c|| / \Sigma|F_o|$; $wR_2 = [\Sigma[w(F_o^2-F_c^2)^2] / \Sigma[w(F_o^2)^2]]^{1/2}$

Table S3.2 | Crystallographic information for the structural refinement of **2**.

Empirical Formula	$C_{43}H_{70}IFeGeN_4OP_3$
Formula weight	1007.28g/mol
Temperature	100 K
Wavelength	1.54178 Å
Crystal System	Monoclinic
Space Group	$P2_1/n$
Unit Cell Dimensions	a = 12.7401(3) Å, α = 90.0˚
	b = 22.7758(6) Å, β = 92.5570(10)˚
	c = 15.8241(4) Å, γ = 90.0˚
Volume	4587.0(2) Å^3
Z	4
Density (calculated)	1.459 g/cm^3
Absorption coefficient	9.892 mm^{-1}
F_{000}	2080.0
Crystal color	Red
Crystal size	0.172 × 0.159 × 0.055 mm^3
2θ range	7.764 to 136.418˚
Index ranges	$-15 \leq h \leq 15$
	$-27 \leq k \leq 25$
	$-17 \leq l \leq 19$
Reflections collected	39389
Independent reflections	8266 [R_{int} = 0.0271]
Completeness to 2θ = 136.174˚	98.6 %
Absorption correction	Multi-scan
Maximum and minimum transmission	0.2213 and 0.1014
Refinement method	Full-matrix least-squares on F^2
Data / restraints / parameters	8266 / 0 / 501
Goodness-of-fit on F^{2a}	1.077
Final R indices [I > 2σ(I)]^b	R_1 = 2.92 %, wR_2 = 9.03 %
R indices (all data)	R_1 = 3.03 %, wR_2 = 9.35 %
Largest diff. peak and hole	0.71 and –1.11 e.Å^{-3}

^{a} GooF = $[\Sigma[w(F_o^2-F_c^2)^2] / (n-p)]^{1/2}$ where n is the number of reflections and p is the total number of parameters refined. $^b R_1 = \Sigma||F_o|-|F_c|| / \Sigma|F_o|$; $wR_2 = [\Sigma[w(F_o^2-F_c^2)^2] / \Sigma[w(F_o^2)^2]]^{1/2}$

Table S3.3 | Crystallographic information for the structural refinement of **3**.

Empirical Formula	$C_{43}H_{70}BrFeSnN_4OP_3$
Formula weight	1006.39 g/mol
Temperature	100 K
Wavelength	1.54178 Å
Crystal System	Monoclinic
Space Group	$P2_1/c$
Unit Cell Dimensions	a = 11.7144(2) Å, α = 90.0˚ b = 16.2856(3) Å, β = 101.0700(10)˚ c = 23.9816(5) Å, γ = 90.0˚
Volume	4489.99(15) Å^3
Z	4
Density (calculated)	1.489 g/cm^3
Absorption coefficient	9.349 mm^{-1}
F_{000}	2080.0
Crystal color	Red
Crystal size	0.061 × 0.043 × 0.031 mm^3
2θ range	7.512 to 136.35˚
Index ranges	$-13 \le h \le 13$ $-18 \le k \le 18$ $-28 \le l \le 27$
Reflections collected	50255
Independent reflections	7968 [R_{int} = 0.0492]
Completeness to 2θ = 136.35˚	97.0 %
Absorption correction	Multi-scan
Maximum and minimum transmission	0.2366 and 0.1256
Refinement method	Full-matrix least-squares on F^2
Data / restraints / parameters	7968 / 0 / 501
Goodness-of-fit on F^{2a}	1.064
Final R indices [I > 2σ(I)]^b	R_1 = 3.69 %, wR_2 = 7.92 %
R indices (all data)	R_1 = 4.88 %, wR_2 = 8.56 %
Largest diff. peak and hole	1.73 and –0.71 e.Å^{-3}

^{a} GooF = $[\Sigma[w(F_o^2-F_c^2)^2] / (n-p)]^{1/2}$ where n is the number of reflections and p is the total number of parameters refined. $^b R_1 = \Sigma||F_o|-|F_c|| / \Sigma|F_o|$; $wR_2 = [\Sigma[w(F_o^2-F_c^2)^2] / \Sigma[w(F_o^2)^2]]^{1/2}$

Table S3.4 | Crystallographic information for the structural refinement of **4**.

Empirical Formula	$C_{43}H_{70}IFeSnN_4OP_3$
Formula weight	1053.38 g/mol
Temperature	100 K
Wavelength	0.71073 Å
Crystal System	Monoclinic
Space Group	$P2_1/c$
Unit Cell Dimensions	a = 11.7530(3) Å, α = 90.0˚ b = 16.2402(4) Å, β = 101.6120(10)˚ c = 24.5393(7) Å, γ = 90.0˚
Volume	4588.0(2) Å^3
Z	4
Density (calculated)	1.525 g/cm^3
Absorption coefficient	1.675 mm^{-1}
F_{000}	2152.0
Crystal color	Red
Crystal size	0.129 × 0.121 × 0.051 mm^3
2θ range	3.026 to 60.278˚
Index ranges	$-16 \le h \le 16$ $-22 \le k \le 22$ $-34 \le l \le 34$
Reflections collected	197891
Independent reflections	13538 [R_{int} = 0.0166]
Completeness to θ = 52.48˚	99.8 %
Absorption correction	Multi-scan
Maximum and minimum transmission	0.2599 and 0.2236
Refinement method	Full-matrix least-squares on F^2
Data / restraints / parameters	13538 / 0 / 512
Goodness-of-fit on F^{2a}	1.177
Final R indices [I > 2σ(I) = 10408 data]^b	R_1 = 2.21 %, wR_2 = 6.33 %
R indices (all data, 0.80 Å)	R_1 = 2.9 %, wR_2 = 7.50 %
Largest diff. peak and hole	1.01 and –1.08 e.Å^{-3}

^{a} GooF = $[\Sigma[w(F_o^2-F_c^2)^2] / (n-p)]^{1/2}$ where n is the number of reflections and p is the total number of parameters refined. $^b R_1 = \Sigma||F_o|-|F_c|| / \Sigma|F_o|$; $wR_2 = [\Sigma[w(F_o^2-F_c^2)^2] / \Sigma[w(F_o^2)^2]]^{1/2}$

Table S3.5 | Fit parameters to the variable-temperature magnetic susceptibility of 1 – 4.

Compound	D (cm^{-1})	$g_{\parallel}$	$g_{\perp}$
1	–12.1(6)	2.38(2)	1.98(1)
2	–14.3(9)	2.15(2)	2.10(1)
3	–12.1(6)	2.44(2)	1.92(2)
4	–15.2(8)	2.33(1)	2.04(1)

Table S3.6 | Fit parameters to the variable-temperature, variable-field magnetization curves for 1 – 4.

Compound	D (cm^{-1})	$g_{\parallel}$	$g_{\perp}$
1	−11.8(3)	2.45(3)	1.89(2)
2	−15.5(4)	2.15(3)	2.11(2)
3	−12.1(4)	2.44(4)	1.92(3)
4	−17.9(3)	2.34(3)	2.08(3)

Table S3.7 | Zero field splitting parameters calculated with CASPT2 using the twelve triplet states shown in Figure S12.

Compound	D (cm^{-1})	E (cm^{-1})
1	–15.4	0.7
2	–16.2	1.0
3	–13.1	0.6
4	–16.0	0.7

Table S3.8 | Zero field splitting parameters calculated with CASSCF using the full Fe(II) d-manifold (50 singlets, 45 triplets, and 5 quintets).

Compound	D (cm^{-1})	E (cm^{-1})
1	–13.6	0.4
2	–11.6	0.6
3	–12.7	0.4
4	–14.2	0.4

Table S3.9│ Relative energies of spin states in kcal/mol using an (8e, 11o) active space at the CASPT2 level of theory.

Spin State	1	2	3	4
Triplet	0	0	0	0
Quintet	35.7	36.3	36.0	36.6
Singlet	34.0	34.7	35.8	35.0

Table S3.10│ Relative energies of spin states in kcal/mol using an (8e, 11o) active space at the CASPT2 level of theory for the twelve lowest energy triplet states of 1–4.

State	1	2	3	4
T_0	0	0	0	0
T_1	14.0	13.9	15.1	14.1
T_2	20.5	20.6	21.1	20.1
T_3	21.9	22.3	22.7	21.5
T_4	31.0	28.5	34.5	31.8
T_5	33.9	36.9	33.4	33.3
T_6	70.6	69.7	67.5	66.8
T_7	71.0	71.3	67.9	67.4
T_8	78.2	76.6	70.9	69.8
T_9	79.5	78.2	71.0	70.0
T_{10}	88.6	87.4	78.9	77.9
T_{11}	89.3	88.3	78.1	79.4

Table S3.11│ Selected experimental geometric parameters for the fully optimized PBE/def2-TZVP geometry with the experimental values to which they were constrained. (E = Ge, Sn; X = Br, I)

Compound	E–Fe (Å)	Fe–X (Å)	E–N_{avg} (Å)	E–N_{axial} (Å)	Fe–P_{avg} (Å)	E–Fe–X (°)
1	2.3764(3)	2.3764(3)	1.9306(6)	2.484(2)	2.33(2)	172.95(2)
2	2.35584(5)	2.55695(5)	1.918(4)	2.53637(5)	2.32(2)	176.1136(9)
3	2.4828(5)	2.3660(7)	2.091(4)	2.410(3)	2.38(2)	172.50(3)
4	2.47930(7)	2.54335(7)	2.096(2)	2.40858(7)	2.38(2)	172.6158(3)

Table S3.12│ Selected geometric parameters from the fully optimized PBE/def2-TZVP structure to be compared with Table S3.11. Difference in energy between the full and constrained optimizations is also given in kcal/mol (constrained structure is higher in energy). (E = Ge, Sn; X = Br, I)

Compound	E–Fe (Å)	Fe–X (Å)	E–N_{avg} (Å)	E–N_{axial} (Å)	Fe–P_{avg} (Å)	E–Fe–X (°)	ΔE (kcal/mol)
1	2.396	2.395	1.965	2.489	2.347	174.6	1.5
2	2.399	2.590	1.964	2.495	2.354	174.7	2.8
3	2.504	2.383	2.134	2.439	2.398	174.4	1.6
4	2.505	2.574	2.134	2.443	2.404	174.4	1.5

Table S3.13 | LoProp charges from the CASSCF (8*e*,11*o*) calculations. (E = Ge, Sn; X = Br, I)

Compound	E	Fe	X	N_{avg}	P_{avg}
1	0.69	0.67	–0.72	–0.38	0.49
2	0.68	0.63	–0.67	–0.38	0.49
3	0.88	0.64	–0.72	–0.41	0.49
4	0.88	0.59	–0.67	–0.41	0.49

Table S3.14 | Mulliken charges from the CASSCF (8*e*,11*o*) calculations. (E = Ge, Sn; X = Br, I)

Compound	E	Fe	X	N_{avg}	P_{avg}
1	1.50	0.04	–0.53	–1.08	0.66
2	1.46	0.10	–0.52	–1.07	0.60
3	1.49	0.12	–0.54	–1.06	0.62
4	1.49	0.03	–0.51	–1.06	0.62

Table S3.15 | Effective bond order (EBO) and Mayer bond orders. (E = Ge, Sn; X = Br, I)

Compound	E–Fe EBO	E–Fe Mayer	Fe–X Mayer
1	0.871	0.837	0.551
2	0.876	0.823	0.670
3	0.855	0.783	0.562
4	0.854	0.784	0.664

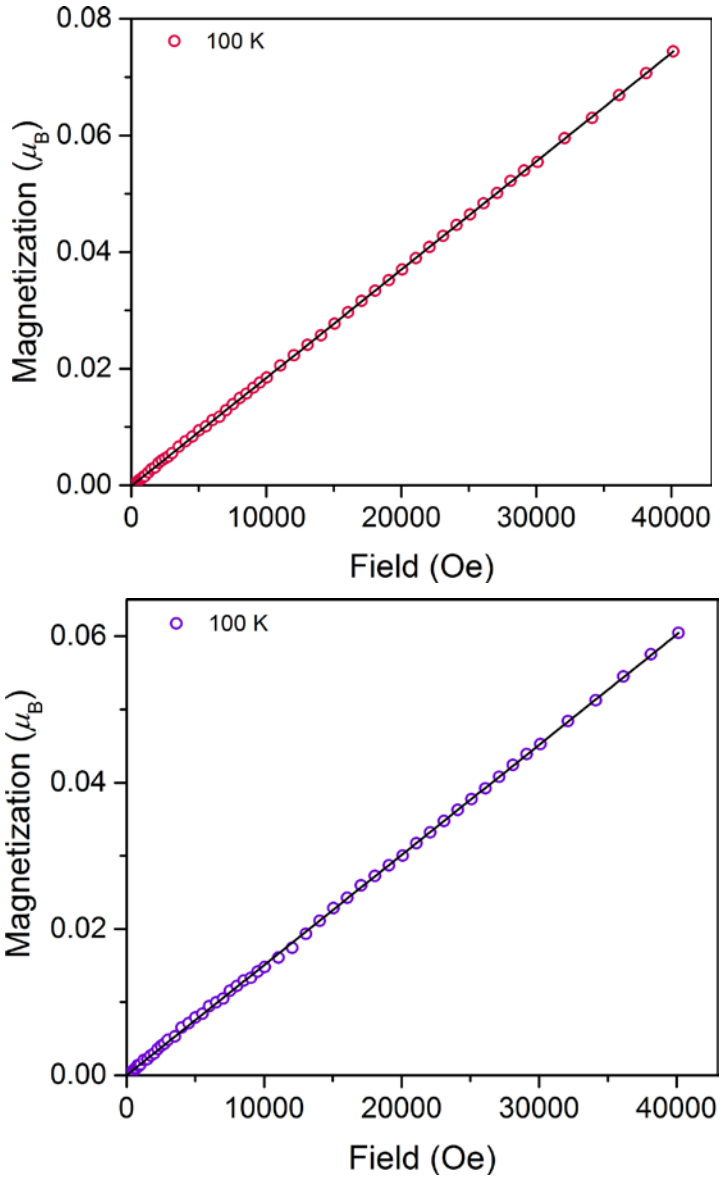

Figure S3.2 | Variable-field magnetization of polycrystalline samples of 1 (top), 2(bottom) restrained under eicosane acquired at 100 K. The black line is a linear fit to the data illustrating the absence of ferromagnetic impurities.

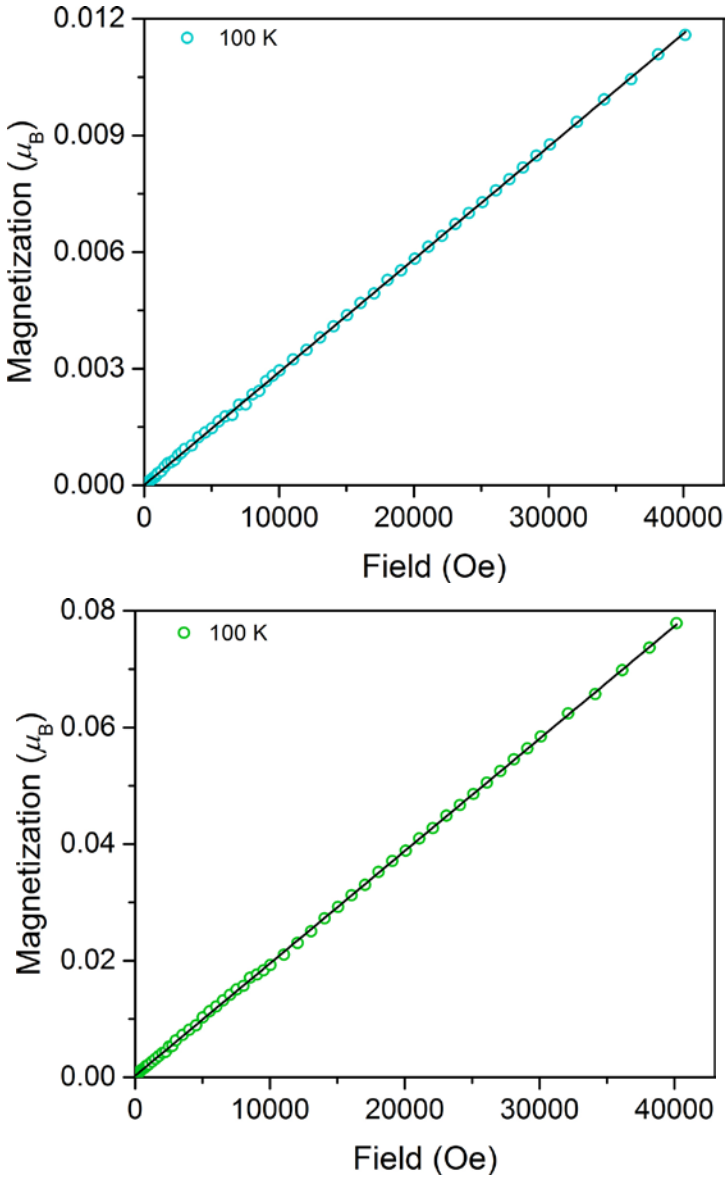

Figure S3.2 | Variable-field magnetization of polycrystalline samples of 3 (top), 4 (bottom) restrained under eicosane acquired at 100 K. The black line is a linear fit to the data illustrating the absence of ferromagnetic impurities.

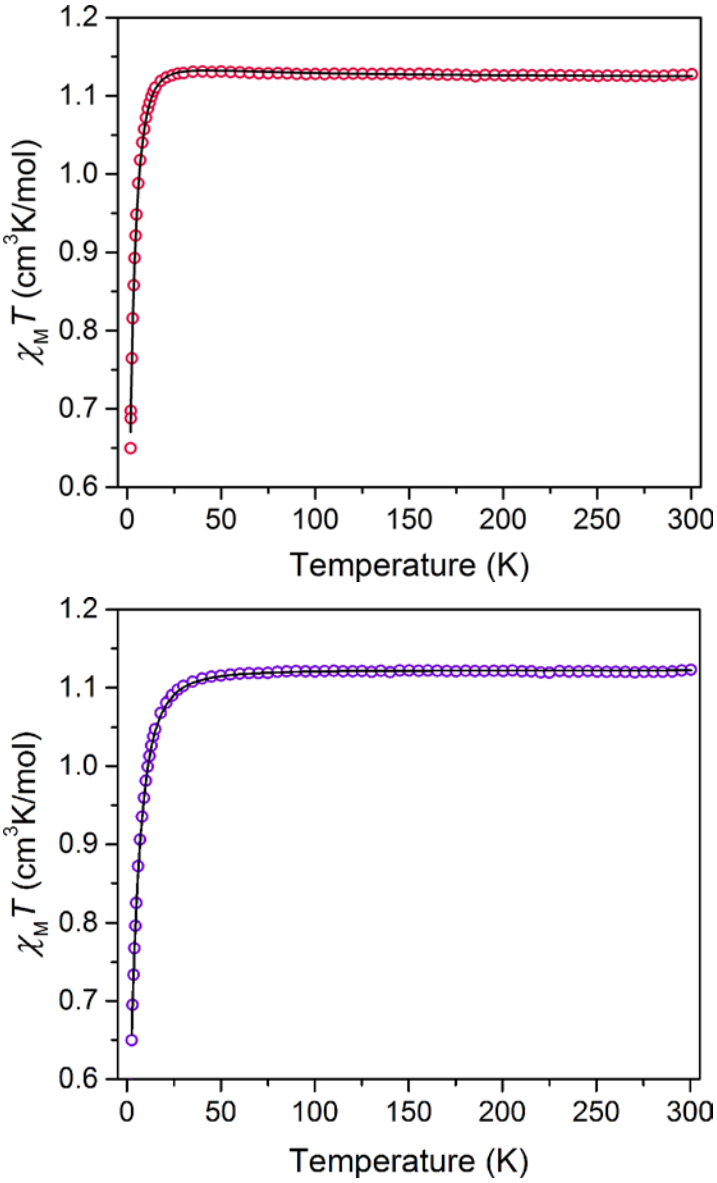

Figure S3.3 | Variable-temperature dc magnetic susceptibility data for **1** (top) and **2** (bottom) collected from 1.8 K to 300 K under a dc field of 0.1 T. The black lines represent simulated data obtained from the best fits. The fits were performed using the spin Hamiltonian, $\hat{H} = D[\hat{S}_z^2 - {}^1/_3S(S + 1)] + (g_\perp + g_\parallel)\mu_B\mathbf{SH}$ in DAVE 2.0.

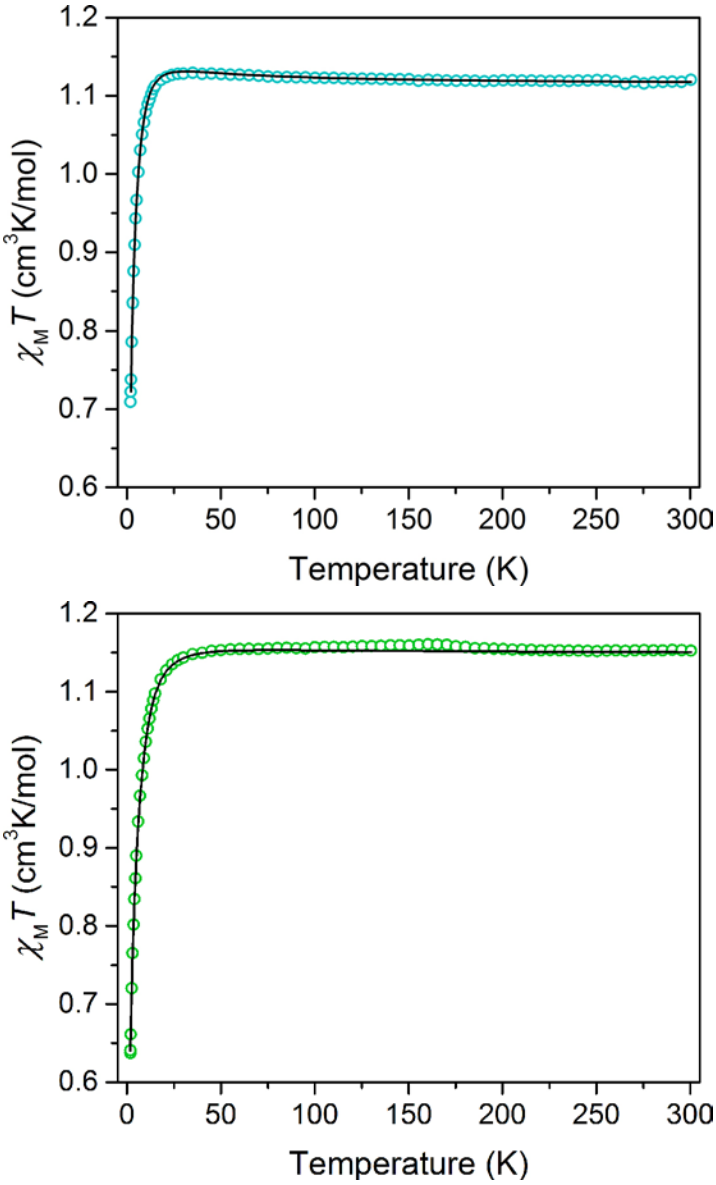

Figure S3.4 | Variable-temperature dc magnetic susceptibility data for **3** (top) and **4** (bottom) collected from 1.8 K to 300 K under a dc field of 0.1 T. The black lines represent simulated data obtained from the best fits. The fits were performed using the spin Hamiltonian, $\hat{H} = D[\hat{S}_z^2 - {}^1/_3S(S + 1)] + (g_\perp + g_\parallel)\mu_B\mathbf{SH}$ in DAVE 2.0.

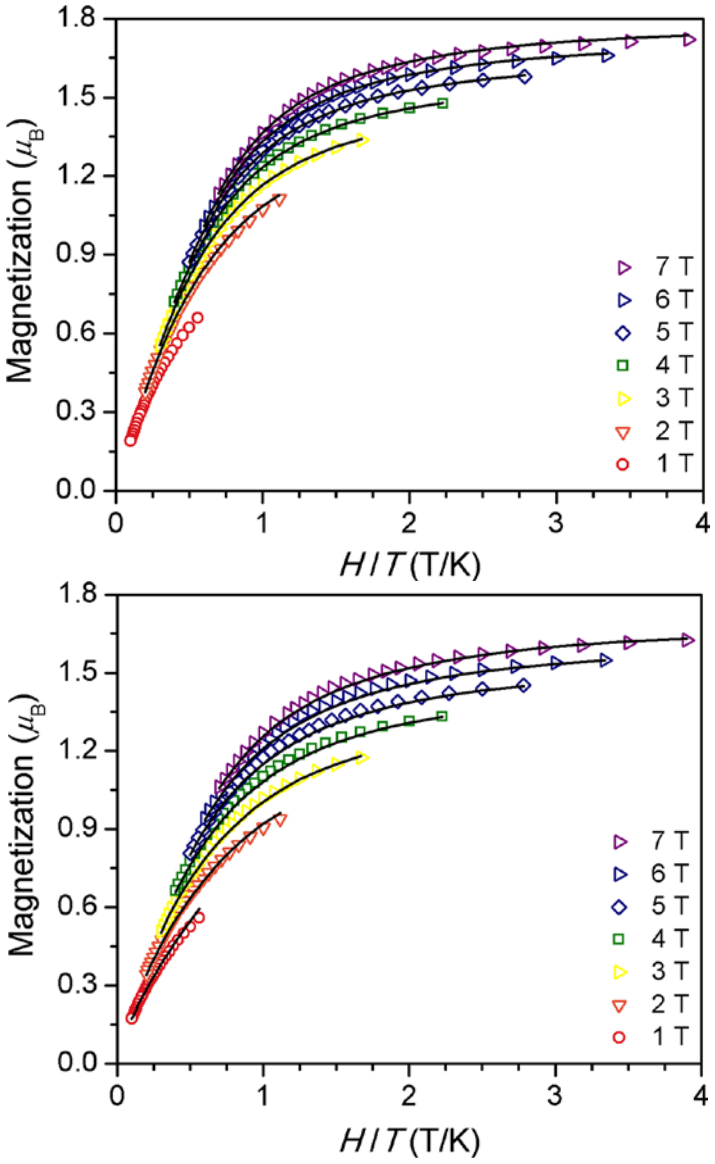

Figure S3.5 | Variable-temperature, variable-field magnetization data for 1 (top) and 2 (bottom) collected between 1.8 and 10 K from 1 to 7 T in 1 T increments. Black lines are simulations of the data obtained from fits using DAVE 2.0 and the spin Hamiltonian, $\hat{H} = D[\hat{S}_z^2 - {}^1/_3S(S + 1)] + (g_\perp + g_\parallel)\mu_B SH$.

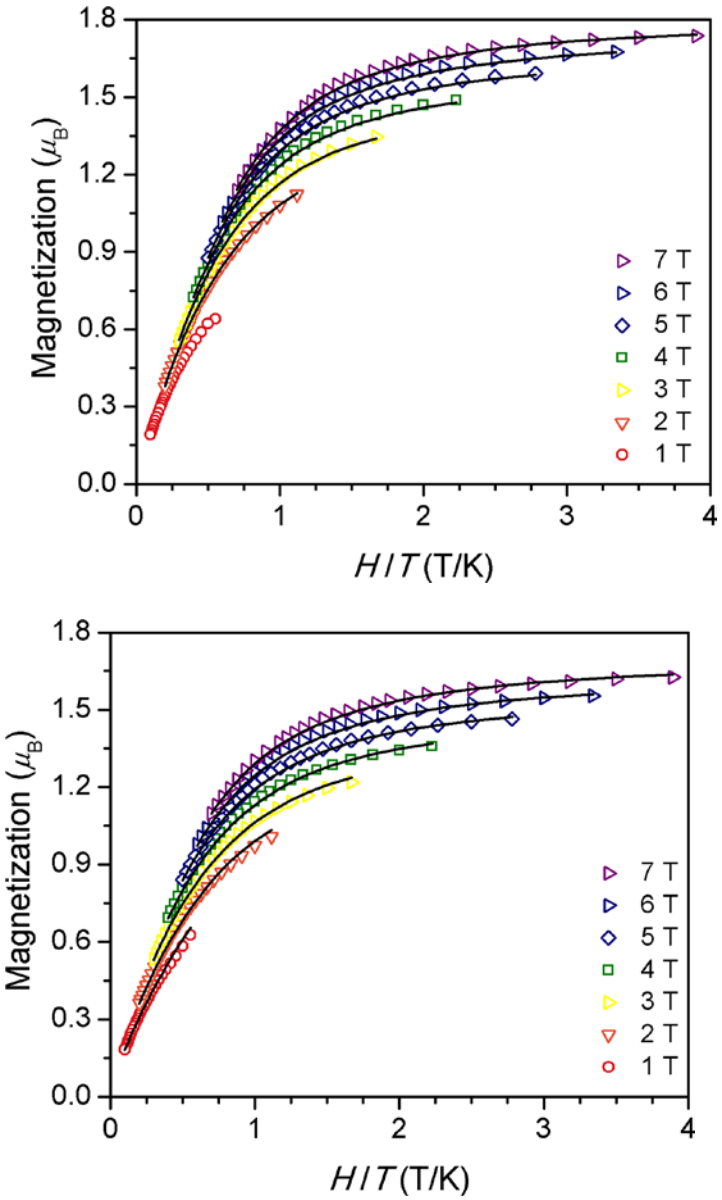

Figure S3.6 | Variable-temperature, variable-field magnetization data for **3** (top) and **4** (bottom) collected between 1.8 and 10 K from 1 to 7 T in 1 T increments. Black lines are simulations of the data obtained from fits using DAVE 2.0 and the spin Hamiltonian, $\hat{H} = D[\hat{S}_z^2 - {}^1/_3S(S + 1)] + (g_\perp + g_\parallel)\mu_B\mathbf{SH}$.

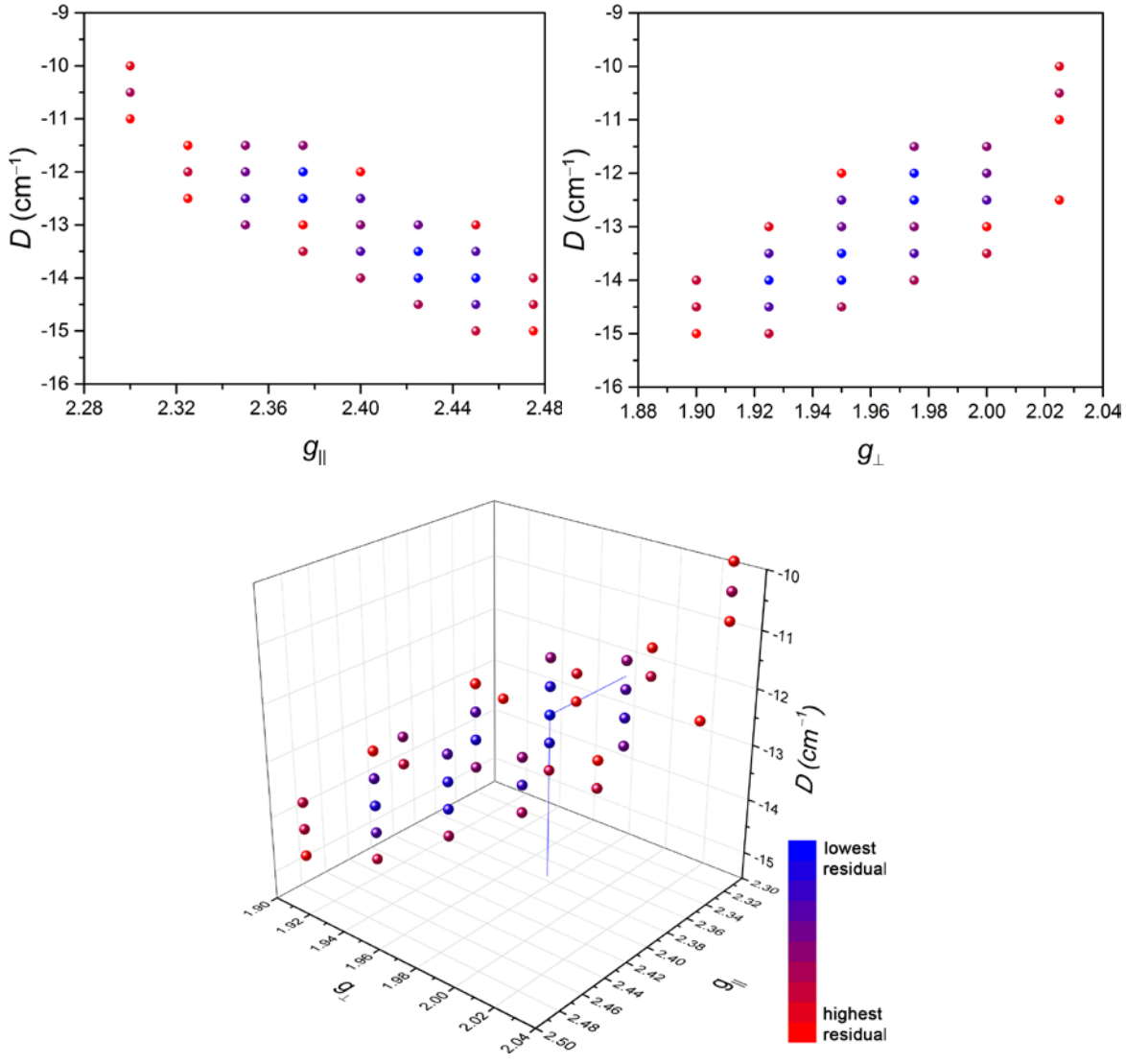

Figure S3.7 | Three dimensional and cross-sectional plots from the simulations with lowest residual error against the dc magnetic susceptibility and variable-field, variable-temperature magnetization data of **1** after a survey over the following parameter space: D = –20 to +20 cm^{-1} in steps of 0.5 cm^{-1}; $g_{\parallel}$ = 2.0 to 2.5 in steps of 0.025; $g_{\perp}$ = 1.7 to 2.2 in steps of 0.025. Total number of simulations: 35,720. Blue drop lines indicate the global minimum. This survey was performed using the program PHI.

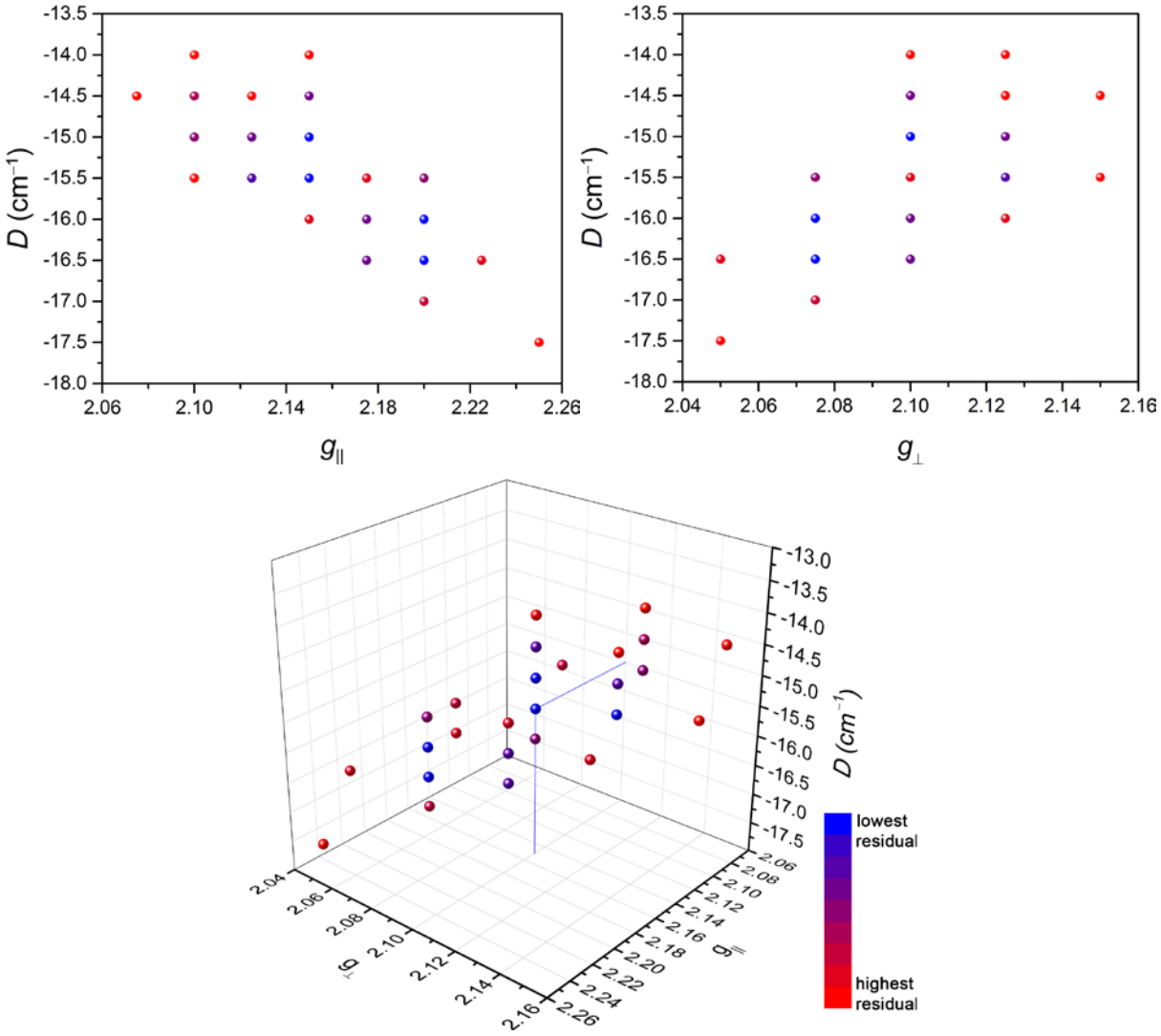

Figure S3.8 | Three dimensional and cross-sectional plots from the simulations with lowest residual error against the dc magnetic susceptibility and variable-field, variable-temperature magnetization data of 2 after a survey over the following parameter space: D = –20 to +20 cm^{-1} in steps of 0.5 cm^{-1}; $g_{\parallel}$ = 2.0 to 2.5 in steps of 0.025; $g_{\perp}$ = 1.7 to 2.2 in steps of 0.025. Total number of simulations: 35,720. Blue drop lines indicate the global minimum. This survey was performed using the program PHI.

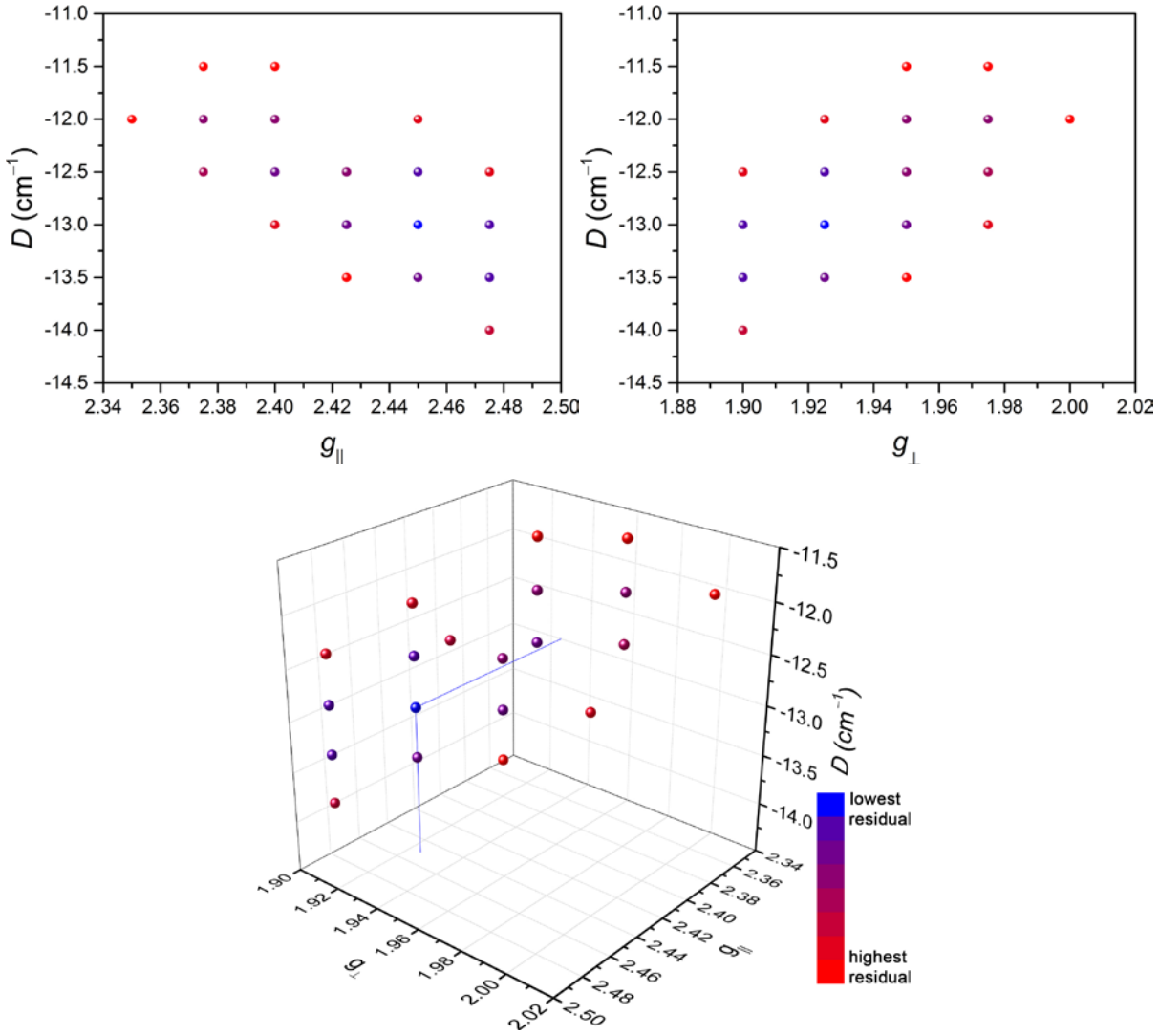

Figure S3.9 | Three dimensional and cross-sectional plots from the simulations with lowest residual error against the dc magnetic susceptibility and variable-field, variable-temperature magnetization data of 3 after a survey over the following parameter space: D = –20 to +20 cm^{-1} in steps of 0.5 cm^{-1}; $g_{\parallel}$ = 2.0 to 2.5 in steps of 0.025; $g_{\perp}$ = 1.7 to 2.2 in steps of 0.025. Total number of simulations: 35,720. Blue drop lines indicate the global minimum. This survey was performed using the program PHI.

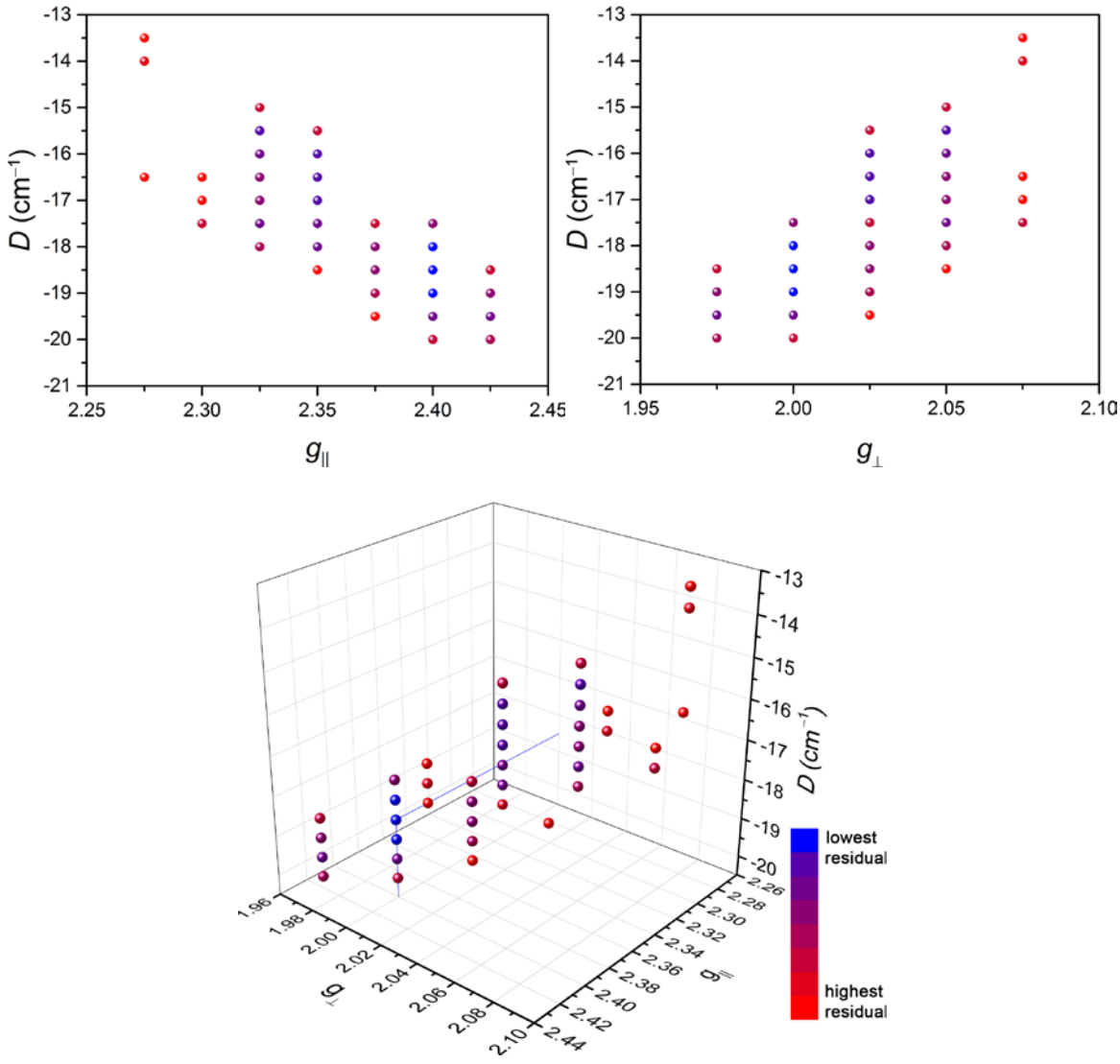

Figure S3.10 | Three dimensional and cross-sectional plots from the simulations with lowest residual error against the dc magnetic susceptibility and variable-field, variable-temperature magnetization data of **4** after a survey over the following parameter space: D = –20 to +20 cm^{-1} in steps of 0.5 cm^{-1}; $g_{\parallel}$ = 2.0 to 2.5 in steps of 0.025; $g_{\perp}$ = 1.7 to 2.2 in steps of 0.025. Total number of simulations: 35,720. Blue drop lines indicate the global minimum. This survey was performed using the program PHI.

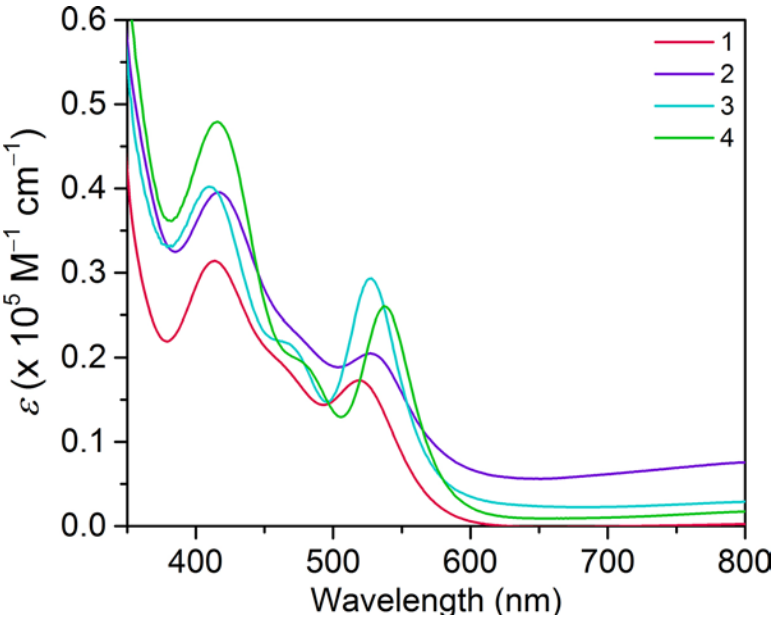

Figure S3.11 | UV-Visible absorption spectra of complexes 1 – 4 in $CDCl_3$ measured at room temperature.

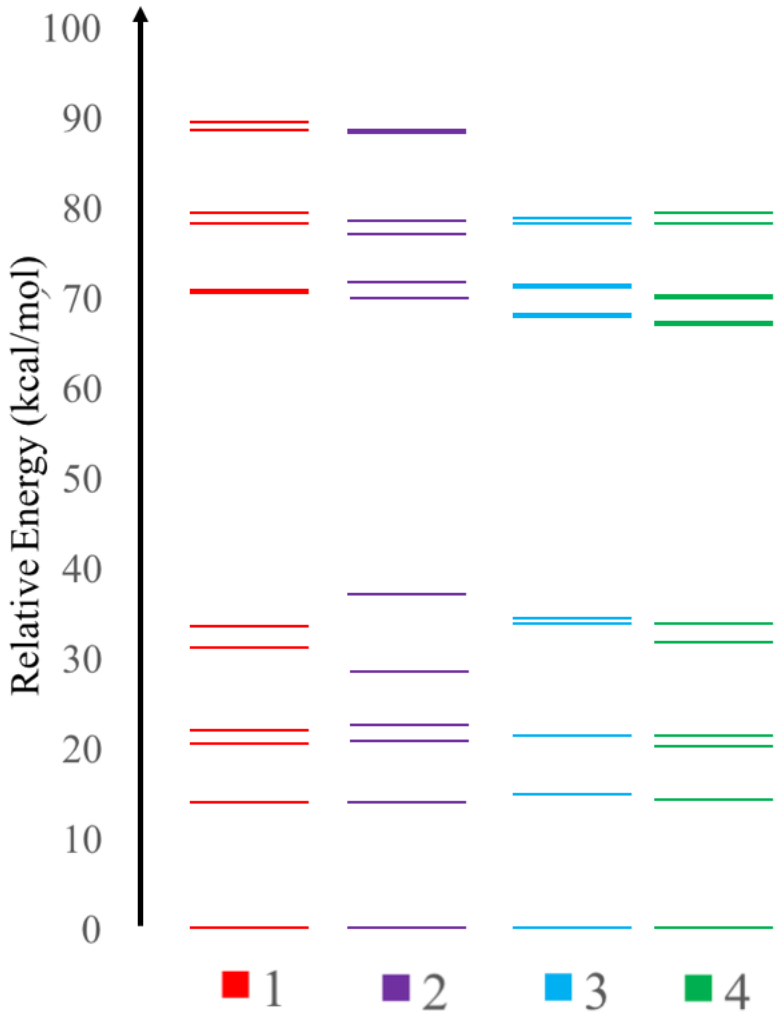

Figure S3.12 | Plot showing relative energies of spin states in kcal/mol using an (8e, 11o) active space at the CASPT2 level of theory for the twelve lowest energy triplet states (values in Table S10). States T_1-T_6 include those with excitations into the SOMOs and states T_7-T_{11} have excitations into the σ* orbital.

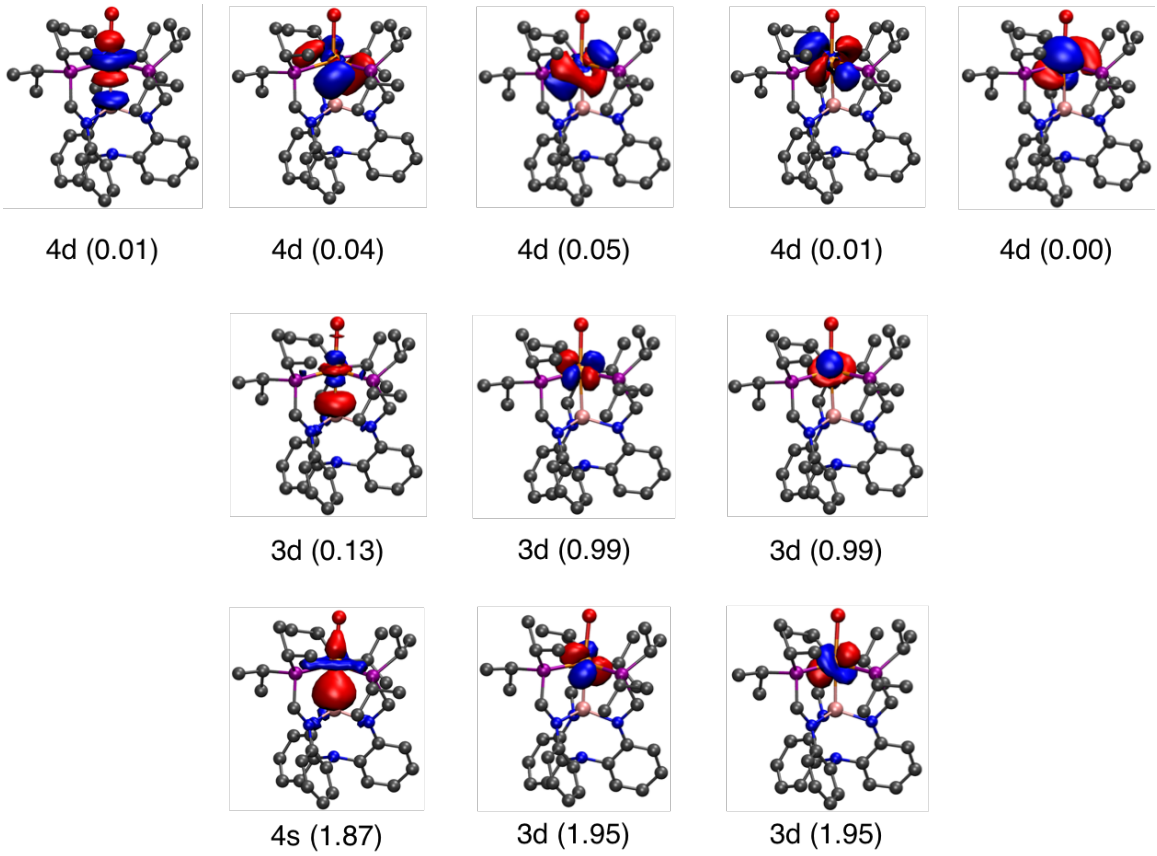

Figure S3.13 | The 11 active natural orbitals (and their corresponding occupation numbers) for the triplet ground state of **1**.

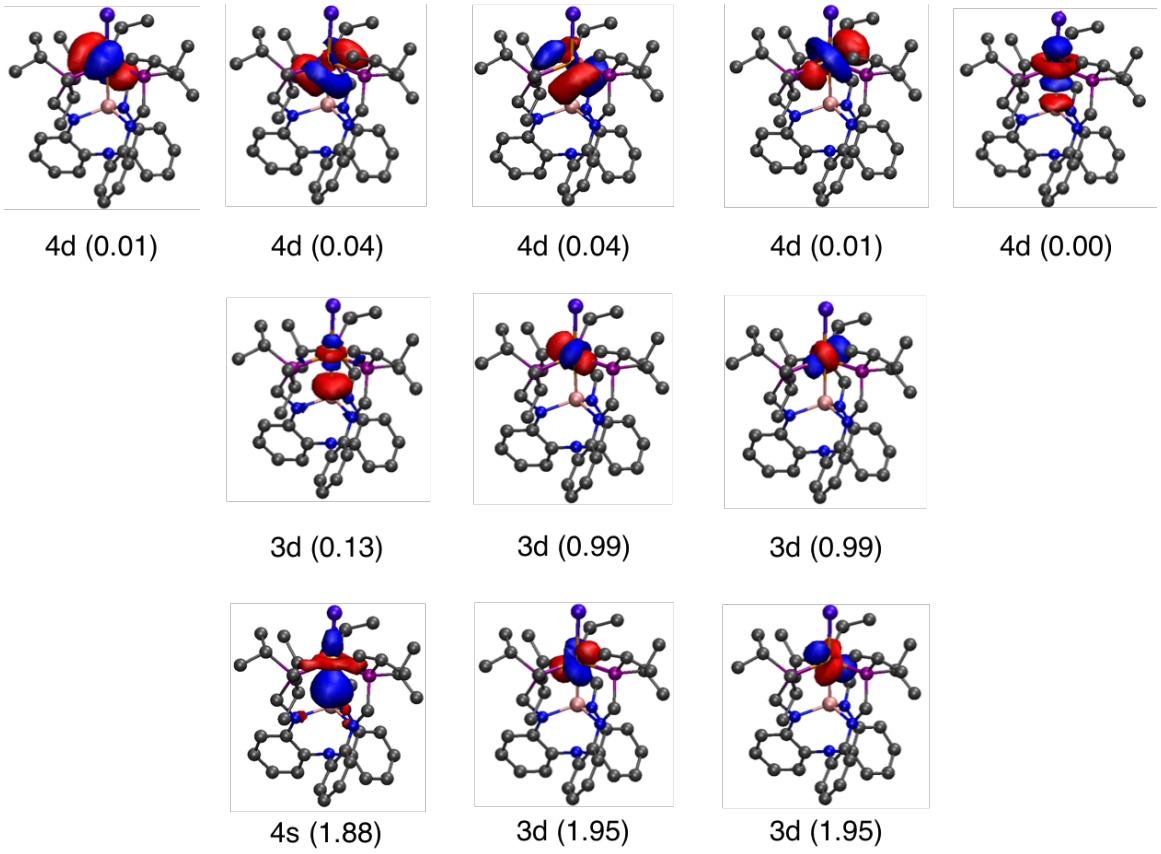

Figure S3.14 | The 11 active natural orbitals (and their corresponding occupation numbers) for the triplet ground state of 2.

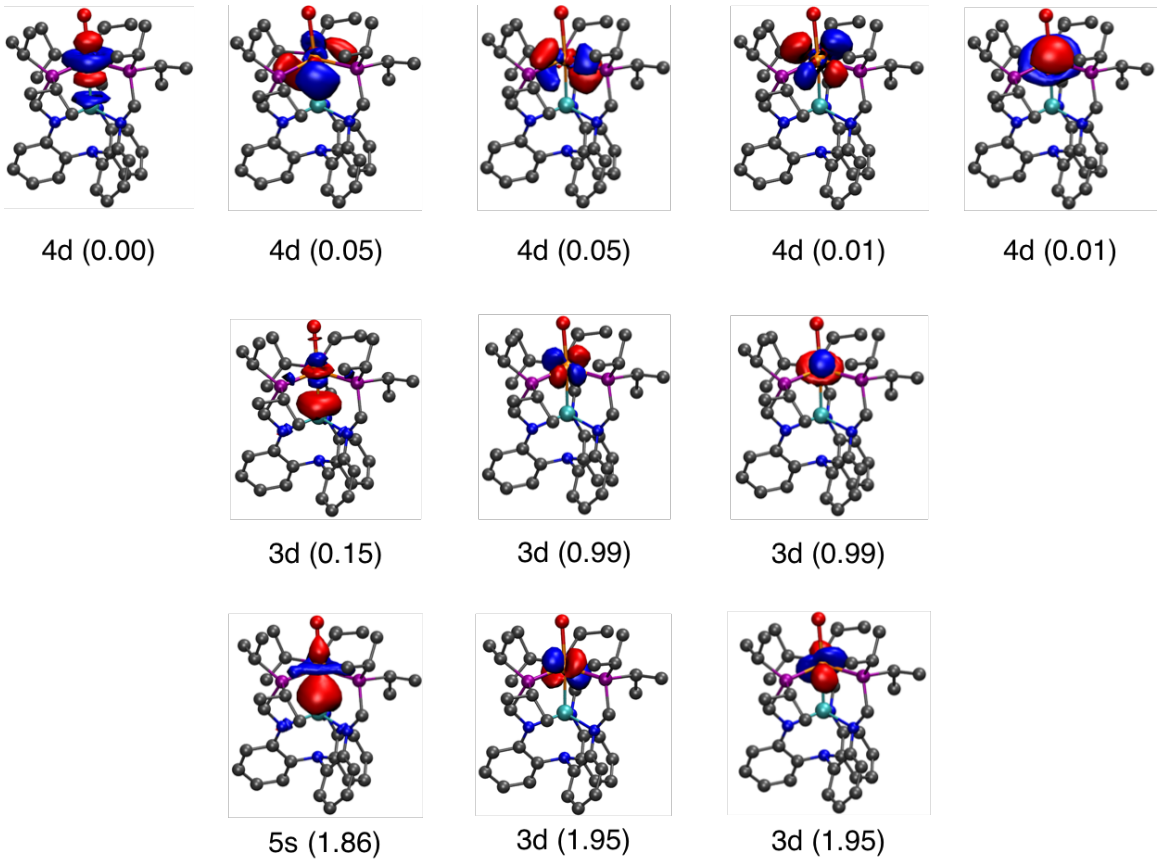

Figure S3.15 | The 11 active natural orbitals (and their corresponding occupation numbers) for the triplet ground state of 3.

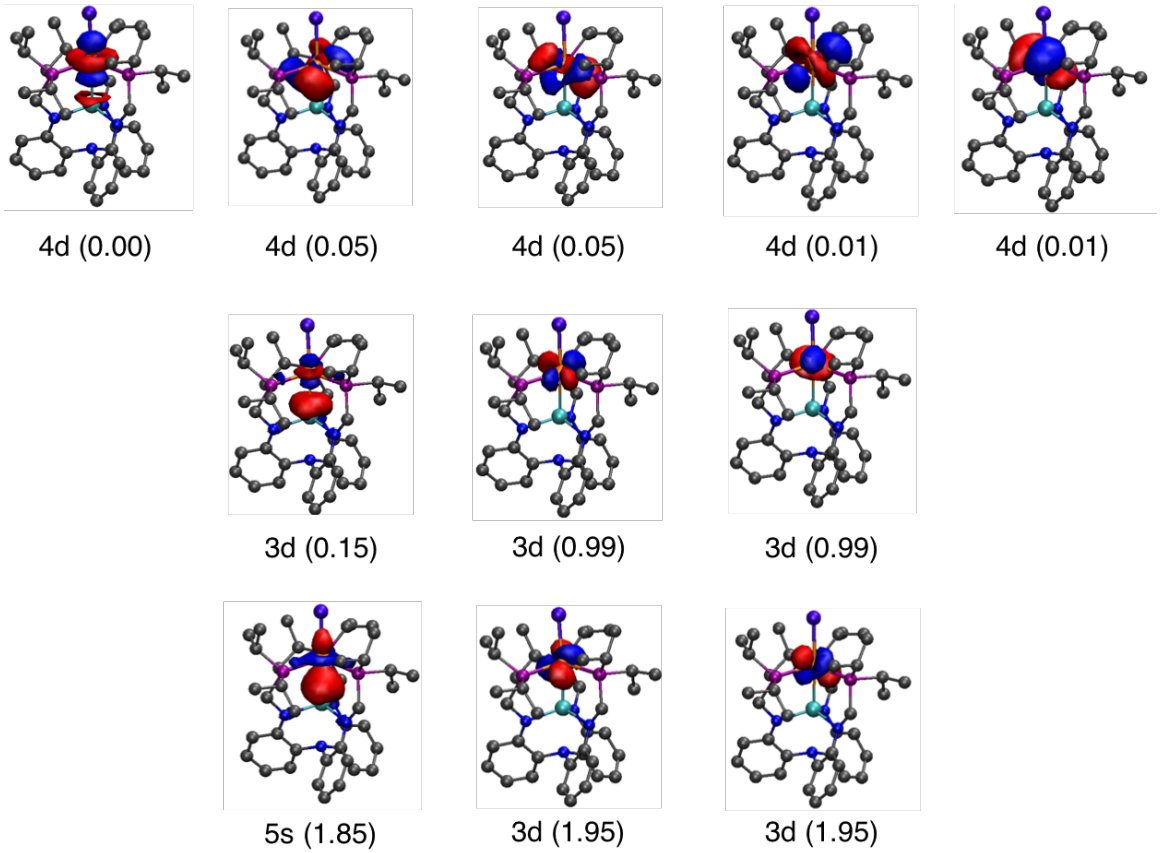

Figure S3.16 | The 11 active natural orbitals (and their corresponding occupation numbers) for the triplet ground state of 4.

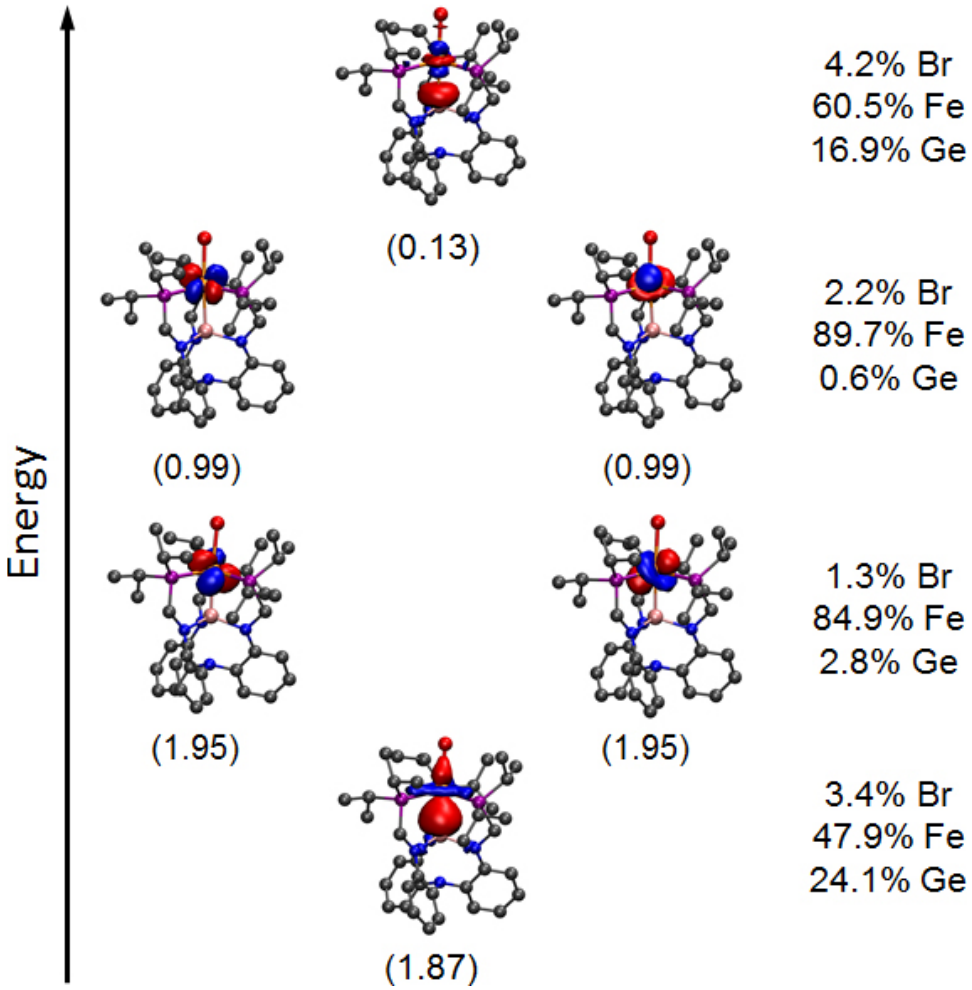

Figure S3.17 | Select active orbitals from the (8e,11o) active space (and occupation numbers) for 1. Atomic contributions to the molecular orbitals were computed via Hirshfeld decomposition and are given for the three heaviest elements. The values given for the two doubly occupied 3d orbitals and two SOMOs are averages.

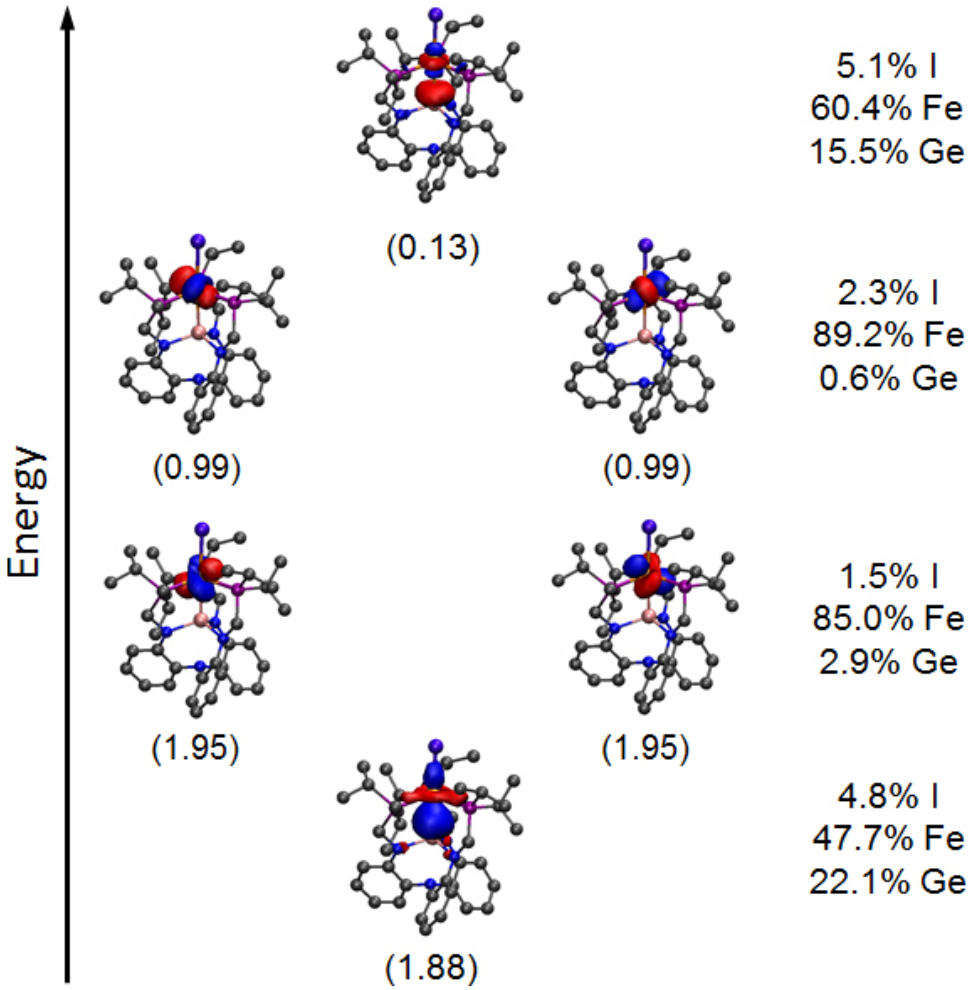

Figure S3.18 | Select active orbitals from the (8e,11o) active space (and occupation numbers) for 2. Atomic contributions to the molecular orbitals were computed via Hirshfeld decomposition and are given for the three heaviest elements. The values given for the two doubly occupied 3d orbitals and two SOMOs are averages.

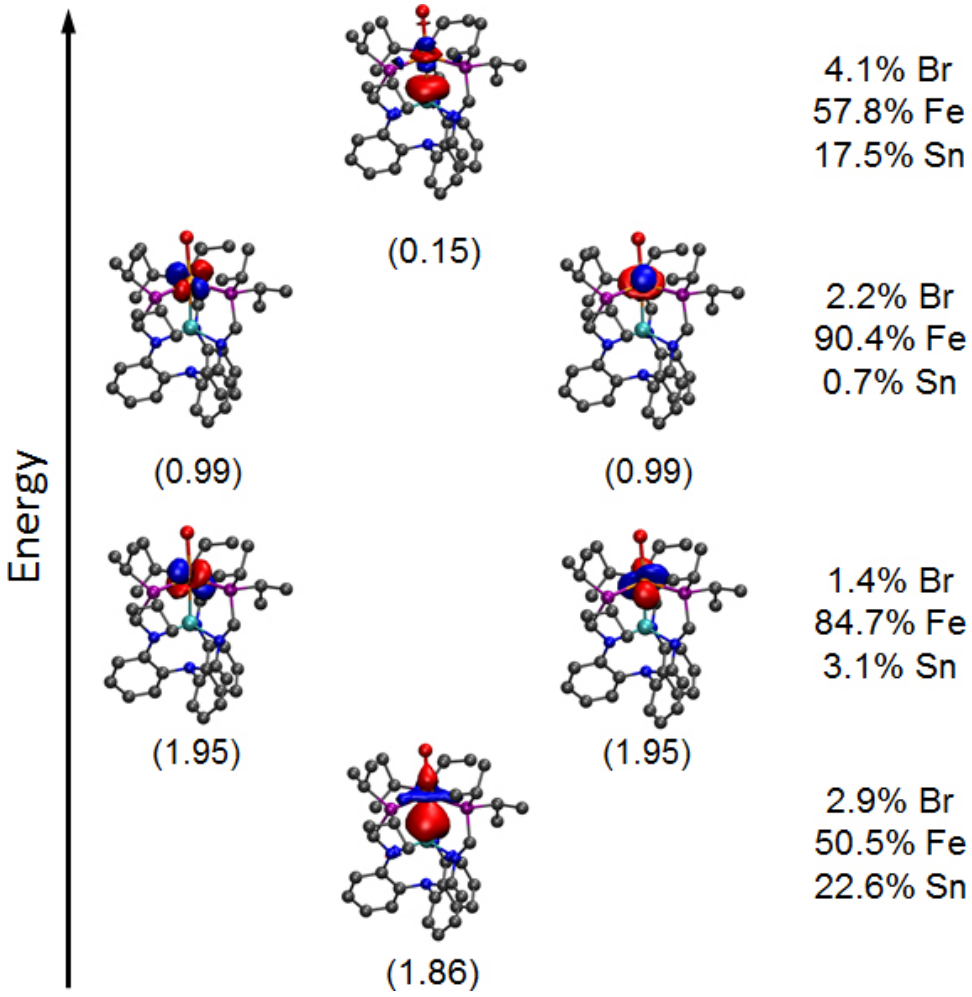

Figure S3.19 | Select active orbitals from the (8e,11o) active space (and occupation numbers) for 3. Atomic contributions to the molecular orbitals were computed via Hirshfeld decomposition and are given for the three heaviest elements. The values given for the two doubly occupied 3d orbitals and two SOMOs are averages.

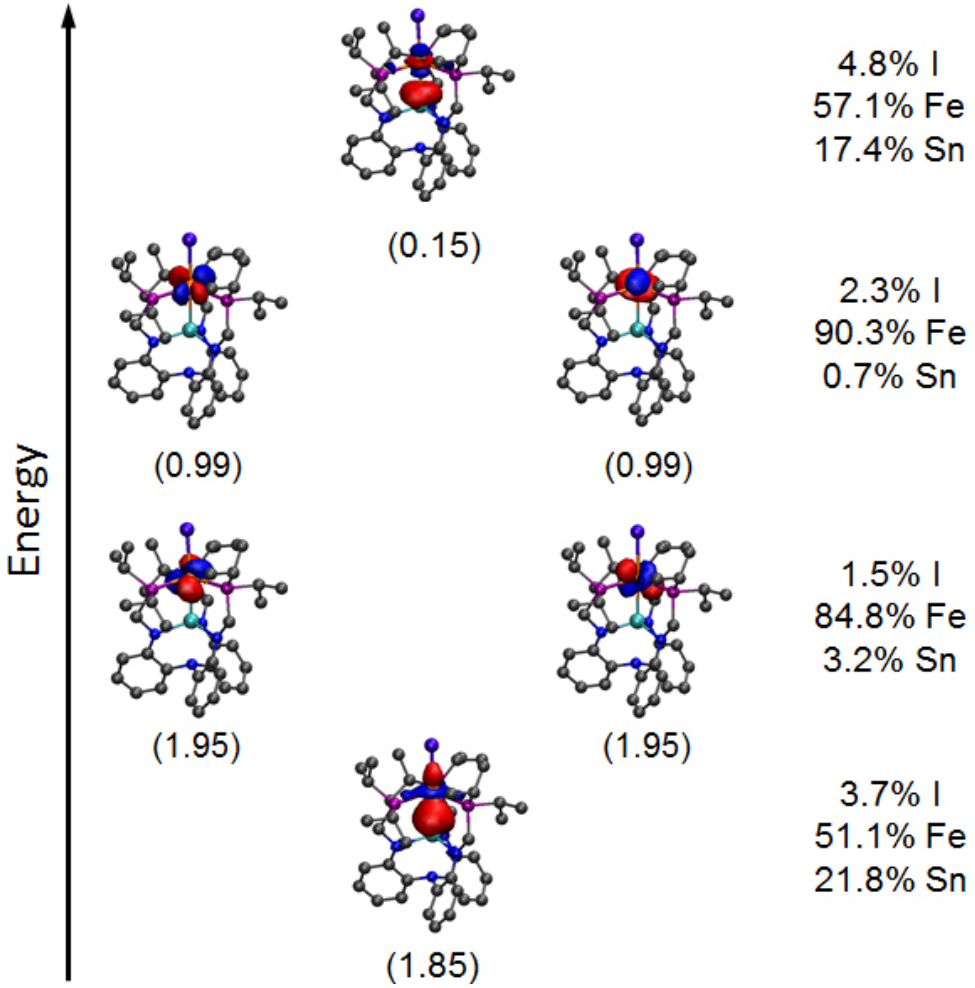

Figure S3.20 | Select active orbitals from the (8e,11o) active space (and occupation numbers) for 4. Atomic contributions to the molecular orbitals were computed via Hirshfeld decomposition and are given for the three heaviest elements. The values given for the two doubly occupied 3d orbitals and two SOMOs are averages.

Chapter 4: Magnetic Anisotropy in High-Spin Heterobimetallic Complexes

Coste, S. C.; Pearson, T. J.; Freedman, D. E. *Inorganic Chemistry* **2019**,

This section was written in collaboration with the co-authors listed above.

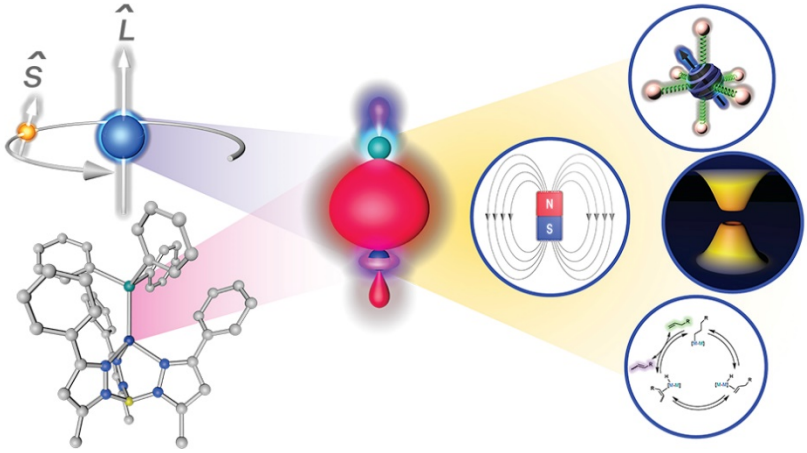

4.1 Introduction

Our results thus far outline two important goals towards understanding how covalency facilitates the heavy-atom effect on magnetic anisotropy. It is essential that heavy element character be present in the electronic ground and low-lying excited states. This goal requires the overall ligand field strength to be lowered to increase coupling to the states with more ligand character, i.e. the anti-bonding orbitals. Lowering the ligand field energy simultaneously puts it on par with the SOC energy, which then requires complete understanding of the ligand field to elucidate SOC transfer from heavier elements. Therefore, it is of equal importance to quantify the ligand field strength of the heavier p-block metals, which is also of importance for homogenous catalysis.[1] Next, we will outline the synthesis of novel heterobimetallic complexes that will allow us to achieve these goals. Through analysis of the magnetic properties and electronic structure of these complexes, we hope to pedagogically approach the experimental quantification of the ligand field strength of group 14 donors, and its interplay with SOC, on influencing *D*.

4.2 Towards Interactions between Spin and Heavy Ligand Orbitals

To study how covalency influences SOC transfer, we need to manipulate the ligand field such that there is more heavy-ligand contribution towards magnetic anisotropy. With an axially based heavy ligand, the best approach is to stabilize the d_{z^2}* orbital. Starting from the previous trigonal bipyramidal geometry, this is achieved by removal of an axial ligand and pyramidalization of the equatorial donors to obtain pseudo-tetrahedral geometry. Lowering the molecular orbital with heavy element character would then allow it to contribute more to the lowest lying excited states. Additionally, an electronically isotropic ground state (i.e. an orbital singlet ground state term of A or B symmetry) is ideal because orbital degeneracy introduces low-lying excited states, and this

convolutes analysis of the magnetic anisotropy. The foregoing analysis prompted us to engineer a new system with a weaker, symmetric ligand field to stabilize high-spin ground states. However, high-spin complexes with metal-metal bonds are uncommon due to the covalent metal-metal interaction. To significantly weaken the ligand field, it is necessary to employ lower-coordinate complexes with the help of unsupported metal-metal bonds. Relying on unsupported bonds would diminish secondary influences on magnetic anisotropy from ancillary ligands while weakening the ligand field. Using these design criteria, we seek to illustrate our synthetic approach to stabilize high-spin complexes to study how covalency affects SOC transfer.

We can access high-spin complexes featuring unsupported metal-metal bonds through precise synthetic design. Without the support of a scaffold ligand, an unsupported covalent bond requires a favorable electrostatic interaction for stabilization. Additionally, it is essential that the first-row transition metal is Lewis acidic to stabilize high-spin ground states, as opposed to the Lewis basic transition metals in most carbonyl-based main group metal-bonded complexes. In this scheme, we can stabilize a covalent bond by fusing a negatively charged heavy main group metal fragment with a positively charged transition metal moiety. An example of suitable capping ligands to promote a low-coordinate environment would be neutral or anionic tripodal ligands, which would leave an open axial site for heavy element coordination. A high-spin complex with an isotropic ground state is then acquired through

Scheme 4.1 Syntheses of paramagnetic complexes **1** – **3** with unsupported metal-metal bonds. (M = Li, K; E = Ge, Sn)

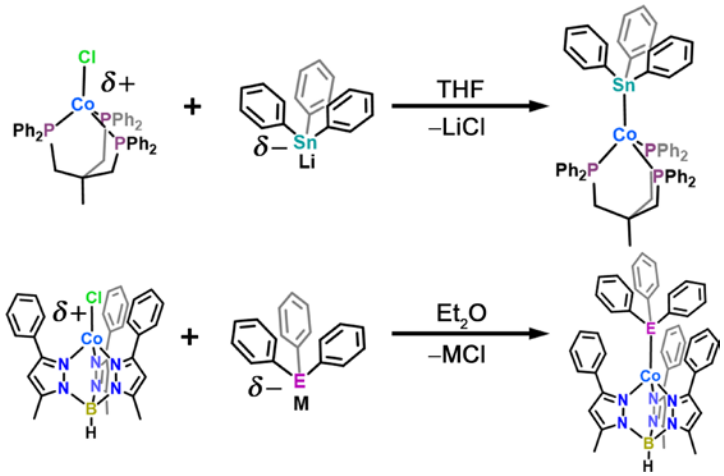

judicious choice of the transition metal ion. Thus, we will initially target divalent or monovalent first-row transition metals in pseudo-tetrahedral geometry; e.g. V^{2+}, Mn^{2+}, Co^{2+}, Co^{+}, and Ni^{2+} fit the outlined electronic structure criteria.

Huttner and coworkers demonstrated an initial success with this strategy in isolating [(triphos)$CoSnPh_3$] (**1**), a paramagnetic (S = 1) Co^{+} complex with an unsupported bond to tin.[2] We note this was one of the few crystallographically-characterized paramagnetic complexes featuring first-row metal-tin bonds until recently. The complex was electrostatically-stabilized by the metathesis reaction of a monocationic [(triphos)Co]$^{+}$ fragment with an anionic triphenyl stannide (Ph_3Sn^{-}) reagent (Scheme 4.1). The scarcity of paramagnetic complexes with first-row metal-heavy main group metal bonds prompted us to investigate the magnetic properties of **1**. Simulation of the magnetization data (Figure S4.3) with the Hamiltonian, $\hat{H} = D[\hat{S}_Z^2 - \frac{1}{3}S(S+1)] + g_{iso}\mu_B \boldsymbol{SH}$, yields values of 2.0(3) cm^{-1} and 2.06(4) for $|D|$ and g_{iso}, respectively. The low $|D|$ value is evident by the overlaying of isofield lines and is a consequence of the strong ligand field raising the energies of the lowest-lying excited states. This provides further impetus to stabilize the anti-bonding orbitals lowering the excited state energies.

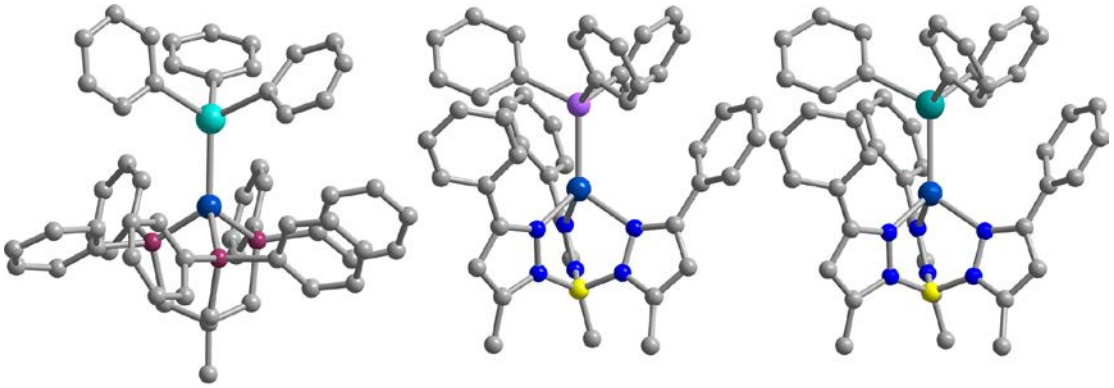

Figure 4.1 Molecular structures of **1**, **2**, and **3** determined from single-crystal X-ray diffraction. Turquoise, pink, cobalt blue, plum, gray, blue, and yellow spheres represent Sn, Ge, Co, P, C, N, and B, respectively; H atoms omitted for clarity.

To further weaken the ligand field, we targeted complexes with weaker donors such as nitrogen-based ligands. We chose to use the tetrahedrally-directing tris(pyrazolyl)borate ligand (Tp^-) to cap divalent transition metals serving as a cationic foundation for our system. The anionic ligand also provides extra stability to the transition metal fragment over neutral ligands that may dissociate in solution. For our initial studies, we will use Co^{2+} because its rich absorption spectrum in pseudo-tetrahedral complexes is well-studied providing a strong basis to quantify heavy donor ligand field influence. Drawing inspiration from Huttner and coworkers, we utilized the triphenyl group 14 anions as simple heavy donors to the Co^{2+} center. We synthesized the desired complexes via metathesis reactions of $LiGePh_3$ or $KSnPh_3$ with $[^{Ph,Me}TpCoCl]^3$ in Et_2O. The molecular structures of $[^{Ph,Me}TpCoGePh_3]$ (**2**) and $[^{Ph,Me}TpCoSnPh_3]$ (**3**), determined by single crystal X-ray diffraction, are shown in Figure 4.1. Both complexes exhibit approximate C_{3v} symmetry and feature unsupported metal-metal bond lengths (2.503(1) Å in **2** and 2.654(1) Å in **3**)

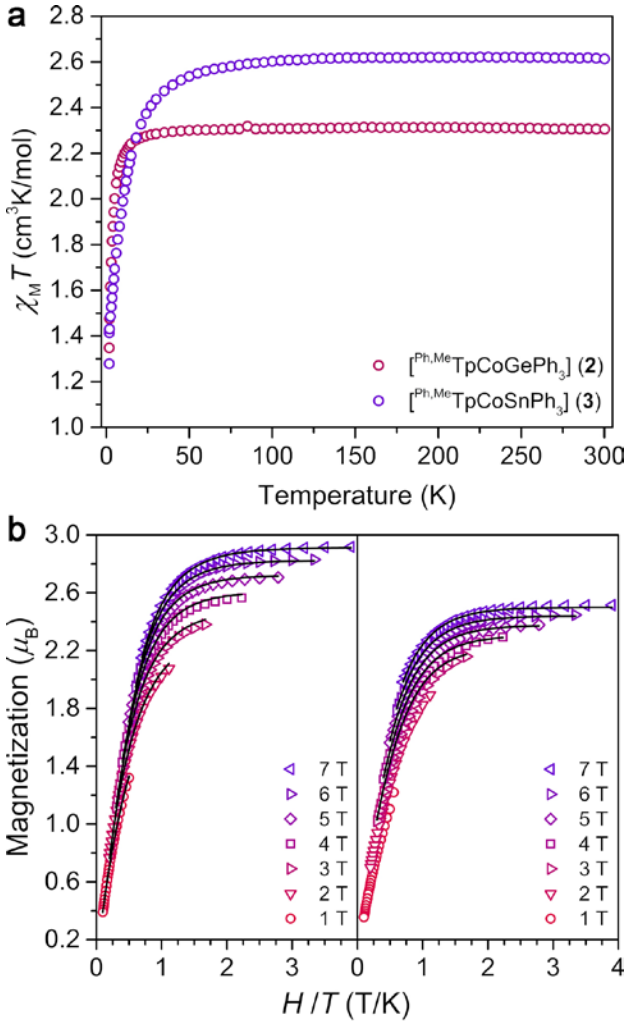

Figure 4.2 (a) Variable-temperature dc susceptibility data for **2** and **3** with H_{dc} = 0.1 T. (b) Variable-temperature, variable-field magnetization for 2 (left) and 3 (right), with black lines representing the best fit. The parameters for the fit are given in Table S3.4 in the Supporting Information.

shorter than the sum of their covalent radii (Co-Ge: 2.70 Å; Co-Sn: 2.89 Å). Importantly, the Co-N distances in **2** and **3** suggest that the complexes are high-spin.

To confirm the spin-state and probe the magnetic properties of **2** and **3**, we turned to EPR spectroscopy and SQUID-based magnetometry (Figure 4.2). Variable-temperature dc magnetic susceptibility data shows room temperature $\chi_M T$ values of 2.32 and 2.62 cm^3Kmol^{-1} corroborating an $S = 3/2$ ground state in **2** and **3**, respectively. Therefore, these are the first high-spin Co^{2+} complexes featuring Co-Ge and Co-Sn bonds, providing an ideal system to study the interplay of the ligand field and SOC towards *D*. The downturn in the susceptibility data is attributable to the presence of *D* which we can more accurately quantify through simulation of magnetization data. Starting with parameters obtained from X-band EPR spectra (Figure S3.4), we simulated magnetization data using the Hamiltonian, $\hat{H} = D[\hat{S}_Z^2 - 1/3 S(S+1)] + E(\hat{S}_x^2 - \hat{S}_y^2) + g\mu_B \boldsymbol{SH}$ to yield *D* values of 3.9(3) and 11.9(1) cm^{-1} for complexes **2** and **3**, respectively. The high-spin nature of the complexes enables observation of a clear increase in *D* with heavier donors owing to more axial ligand contribution.

4.3 Experimentally Deconvoluting the Influences of Ligand Field and SOC

The impact of SOC is more apparent with a weaker ligand field, however, we now need to thoroughly analyze the ligand field to better quantify SOC influence on *D*. Each excited state contribution to *D* is indirectly proportional to the energy separation and proportional to ξ_{eff}^2, where ξ_{eff} represents a combination of each donor atom's inherent SOC weighted by their contribution to the relevant molecular orbital.[39,42] In other words, the ligand SOC is anisotropic and states with more d_{z^2} character will contribute more to *D* in our series. The sign of a contribution is then determined by the symmetry relation between the two states: a negative contribution if related by

the L_z operator, and conversely positive if the states are related via $L_{x,y}$.[4] We note that orbital mixing in 3-fold symmetric systems induces a negative contribution to *D* when coupling between two E orbital sets (d_{x2-y2}, d_{xy} and $d_{xz,}$ d_{yz}).[5] Therefore, there are competing contributions between states with d_{z2} character (positive) and states with more E orbital character (negative). Maintaining an isostructural series is therefore vital where the identical pyrazole donors maintain control of the E orbital set energies. This allows any changes to the axial ligand to be our independent variable towards *D*. Understanding this axial influence is then the last piece of the puzzle.

Previous studies into the donor ability of group 14 elements toward transition metals relied on vibrational spectroscopy and trans- effects of ligand substitution. They demonstrated that the σ-donating ability of the group 14 elements ranked as Ge < Si < Sn towards Ir^+ and Rh^+ centers, differing from the halides and chalcogenides whose ligand fields weaken moving down the group.[6,7] A similar trend was observed in first-row transition metal complexes where the relative σ-donating and pi-accepting ability of numerous group 14 donors were compared using carbonyl and metal-metal stretching frequencies and quadrupolar splitting values.[8–11] This implies that the lowest-lying excited state is higher in energy in **3** rendering it a less positive *D* value, the opposite of what we observe.

We probed the ligand field strength of Ph_3Ge^- and Ph_3Sn^- using an angular overlap model (AOM) analysis of the electronic absorption spectra shown in Figure 4.3.[12] While we do not observe the two lowest transitions (the transition to the ^4E is in the mid-IR and $^4A_1$ band is symmetry forbidden in C_{3v} symmetry), we can fit the four higher lying transitions to estimate the energy of the low energy states. We fit the diffuse reflectance spectra using the program ddnfit starting with parameters derived by Telser and coworkers;[13,14] a detailed discussion of the fits is

in the supplementary information. The parameters from the best fit (Table S3.5) suggest a σ-donating ability of both tin (ϵ_σ = 2363 cm^{-1}) and germanium (ϵ_σ = 2145 cm^{-1}) similar to that of a chloride in a similar environment (ϵ_σ(Cl) = 2270 – 2290 cm^{-1}).[15] We note that the differences in ϵ_σ between tin and germanium corroborate the trend in Ir^+ and Rh^+ complexes, however, the parameter values are much smaller than we hypothesized. This may be due to mismatch between tin valence orbitals and metal 3d orbitals. As a consequence of the overall ligand field, the energy of the ^{4}E state in **2** is simulated to be higher than **3**. While this undoubtedly contributes to a more positive value of *D* observed in **3**, we can account for other low-lying states by simulating *D* with the inclusion of ξ_{eff} using the AOM. By systematic variation, we found that ξ_{eff} was much lower in **2** than **3**, 357 cm^{-1} versus 531 cm^{-1}, to replicate the measured *D* values. This suggests that SOC from the heavier tin donor is in fact contributing to the magnetic anisotropy of the Co center where the free-ion ξ value in Co^{2+} is 515 cm^{-1}.[12] The lower ξ_{eff} in **2** is likely a result of the orbital reduction from the covalent bond that is uncompensated by the SOC constant of the germanium donor.

The preceding ligand field analysis provides a framework to experimentally probe how covalency affects SOC conferral through metal-metal bonds. While covalency is a complex concept to quantify experimentally, the AOM provides parameters that together can paint an accurate picture of molecular orbitals. The ϵ_σ parameter represents orbital overlap and energy matching between two atomic orbitals by quantifying the destabilization of metal-ligand antibonding orbitals. Based on this description, we infer that the metal-metal bonding in **2** and **3** is similar in covalency to that of a chloride. Further, the Racah *B* parameters in **2** (677) and **3** (678) suggest a similar nephelauxetic effect compared to Tp-based Co^{2+} complexes. We presumed that tin, like iodide, would reduce the interelectronic repulsion further owing to its large polarizable 5s

and 5p orbitals. We will not speculate further about the implication because many factors contribute to the Racah *B* parameter. These ligand field parameters, however, do provide a starting point to analyze the covalency, and its influence on SOC transfer in high-spin complexes.

The outlined synthetic criteria and subsequent analysis establish a foundation to begin studying the influences of covalency on SOC transfer to first-row transition metal centers. Beyond the measurements discussed here, direct measurements of SOC and covalency is accessible using synchrotron-based techniques such as X-ray absorption spectroscopy (XAS) and X-ray magnetic circular dichroism (XMCD). Future experiments will rely on these direct experimental probes, in addition to those used in this work, to better understand the metal-metal bond's influence on magnetic anisotropy. Concurrent theoretical calculations are also vital to support the experimental data due to shortcomings of the AOM. While the AOM provides chemically-intuitive parameters to inform synthetic direction, it does not accurately depict the complexity of molecular orbitals and electronic structure such as anisotropic SOC ligand contributions. Future studies will

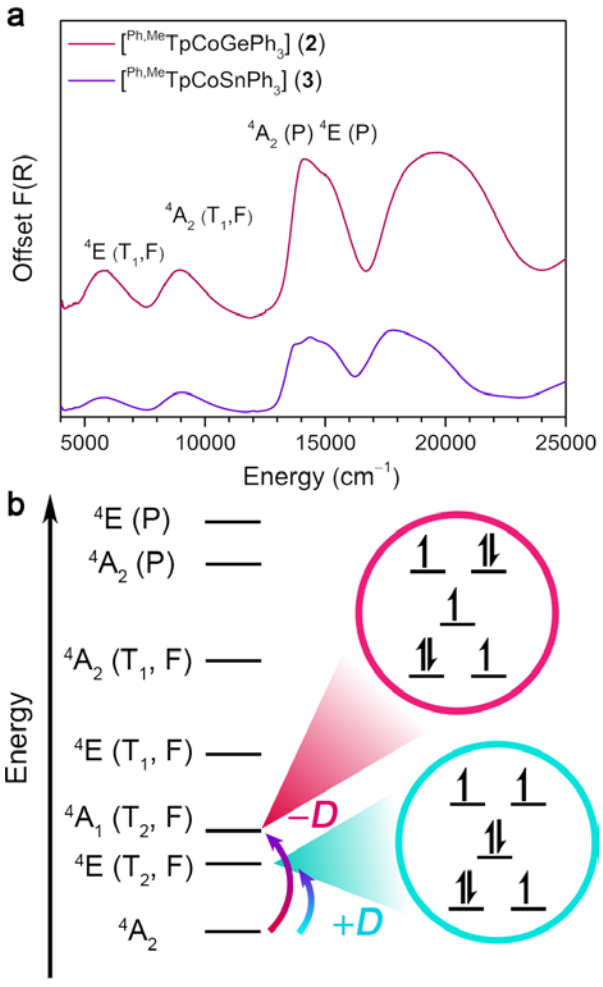

Figure 4.3 (a) Diffuse reflectance spectra of **2** and **3** measured at room temperature. (b) Energy level diagram of Co^{2+} in pseudo-tetrahedral C_{3v} symmetry ($^4A_2$ ground state) depicting most influential states towards *D* with the largest contributing electronic configuration to those states.

explore covalent bonds between first-row metals and heavier group 13 and 15 elements with the goal of exploiting the large SOC of the 6p elements to engender large magnetic anisotropy. The synthesis of the latter may, however, require more research towards a better fundamental understanding of the reactivity of 6p elements.

4.4 Conclusions and Outlook

The foregoing results and analysis demonstrate that spin-orbit coupling can powerfully modulate the magnetic properties of transition metals even in the absence of direct bonding in electronically-isotropic systems. We note, however, that use of high-spin complexes with electron density in the molecular orbitals with ligand character is crucial to quantifying this effect. Further, we have demonstrated that the covalency of the metal-metal interaction is vital in considering the spectral and magnetic properties of transition metal-main group heterobimetallics and has strong implications for the transfer of spin-orbit coupling from the ligand sphere to the transition metal.

These results provide a framework for synthetically controlling SOC in transition metal complexes and materials. This and subsequent research will enable the manipulation of SOC in transition metal complexes and will support advancements in fields as diverse as molecular magnetism, topological materials, and two-state reactivity in catalysis. Specific molecular targets to further this research are paramagnetic species featuring direct bonds 6p elements such as lead and bismuth. Further, we plan to pursue X-ray spectroscopy measurements to directly probe SOC and covalency to help deconvolute the influences of ligand field geometry and the heavy atom effect on the magnetic properties of these compounds.

4.5 Supplementary Information

Experimental Details.

General Considerations. All compounds were manipulated and handled under a dinitrogen atmosphere in an MBraun Unilab Pro glovebox. All glassware was either oven-dried at 150 °C for at least four hours or flame-dried prior to use. Diethyl ether (Et_2O), benzene, and n-hexane were dried using a commercial solvent purification system from Pure Process Technology and stored over 3 or 4 Å sieves for a minimum of one day prior to use. $CDCl_3$ and C_6D_6 were purchased from Cambridge Isotope Labs, deoxygenated by three successive freeze-pump-thaw cycles, filtered through a pad of activated alumina, and stored over 3 or 4 Å sieves prior to use. [(triphos)$CoSnPh_3$](**1**) and [^{Ph,Me}TpCoCl] were prepared according to literature procedures.[2,3] $HSnPh_3$ and $HGePh_3$ were purchased from MilliporeSigma and vacuum distilled prior to use. All other chemicals were used as received. Silylated Celite (Si-Celite) was prepared by stirring 25 g activated, dried Celite 545 in 100 mL toluene with 14 mL trimethylsilylchloride and 14 mL of triethylamine under N_2 overnight at 40 °C, followed by filtration, washing with 80 mL MeOH and 200 mL toluene, and drying for 24 hours at 100 °C.

[^{Ph,Me}TpCoGePh_3]·benzene(2). $LiGePh_3$ was generated by the deprotonation of $HGePh_3$ (264.1 mg, 0.866 mmol) with ^{n}BuLi (0.54 mL, 0.866 mmol) in 5 mL of Et_2O at room temperature to generate a clear, slightly yellow solution. This was added dropwise at room temperature to a fine suspension of [^{Ph,Me}TpCoCl] (401.1 mg, 0.694 mmol) in 10 mL of Et_2O to precipitate a purple micro-crystalline solid. After allowing the reaction mixture to stir overnight, the solid was filtered out and washed with 5 mL Et_2O then dried *in vacuo*. The solid was dissolved in 40 mL benzene, filtered over Si-Celite on a fritted funnel, then layered under 100 mL n-hexane. Purple, hexagonal

plates of **2** were obtained (Yield: 375.5 mg, 58.5 %). IR (ATR, cm^{-1}): 3055 (w), 3045 (w), 3034 (w), 2982 (w), 2933 (w), 2863 (w), 2529 (w), 1545 (m), 1507 (w), 1478 (m), 1452 (m), 1436 (s), 1425 (s), 1378 (w), 1362 (m), 1341 (m), 1332 (w), 1302 (w), 1288 (w), 1259 (w), 1221 (w), 1212 (w), 1183 (s), 1166 (m), 1113 (m), 1094 (m), 1074 (m), 1094 (m), 1074 (m), 1056 (s), 1030 (m), 1024 (m), 998 (w), 986 (w), 979 (m), 912 (m), 852 (w), 843 (w), 831 (w), 802 (m), 789 (w), 777 (s), 769 (s), 764 (s), 739 (s), 708 (s), 700 (s), 696 (s), 684 (m), 668 (vs), 661 (m), 656 (m), 636 (m), 617 (m), 603 (w) UV-Vis-NIR ($CDCl_3$) λ_{max}, nm (ε): 514 (1767), 655 (1058), 682 (1199), 703 (sh, 991), 1096 (94), 1679 (67). ^{1}H NMR (600 MHz, C_6D_6, 298 K): δ 58.22 (3H), 18.95 (9H), 18.43 (br, 6H), 14.54 (6H), 8.16 (3H), 6.63 (6H), 5.12 (br, 6H), 2.94 (3H), −10.15 (br, 1H) ppm. Anal. Calcd. for $GeCoN_6C_{48}BH_{43}\cdot(C_6H_6)$: 70.16 %C; 5.34 %H; 9.09 %N. Found: 67.51 %C; 5.32 %H; 9.12 %N; carbon analysis consistently gave lower values that would could not be accounted for by loss of solvent, we attribute this is to incomplete combustion of the organogermanium species.

[^{Ph,Me}TpCoSnPh$_3$]·benzene(3). Yellow $KSnPh_3$ was generated by stirring $HSnPh_3$ (222.2 mg, 0.633 mmol) and KH (25.3 mg, 0.633 mmol) in 5 mL of Et_2O for 4 hours at room temperature. To this, a suspension of [^{Ph,Me}TpCoCl] (241.6 mg, 0.418 mmol) in 15 mL Et_2O was added at room temperature, a white precipitate formed and the reaction was allowed to stir overnight at room temperature. The precipitate was filtered out and washed with 4 x 5 mL Et_2O and dried. Then, it was taken up in 80 mL benzene, filtered through Si-Celite on a fritted funnel, then layered under 100 mL n-hexane. Purple, hexagonal platelets of **3** were obtained (Yield: 142.7 mg, 35.2 %). IR (ATR, cm^{-1}): 3049 (w), 3025 (w), 2995 (w), 2975 (w), 2965 (w), 2932 (w), 2530 (w), 1543 (m), 1507 (w), 1475 (m), 1452 (m), 1435 (s), 1423 (s), 1376 (w), 1361 (m), 1341 (m), 1302 (w), 1286

(w), 1254 (w), 1215 (w), 1180 (s), 1094 (m), 1056 (s), 1031 (m), 996 (w), 977 (m), 912 (w), 842 (w), 802 (w), 777 (m), 764 (s), 731 (s), 697 (s), 677 (vs), 650 (s), 637 (s), 533 (m), 526 (m), 490 (m), 451 (s), 443 (s), 407 (w). UV-Vis-NIR ($CDCl_3$) λ_{max}, nm (ε): 516 (sh, 716) ,554 (1202), 650 (1221), 683 (1015), 715 (644), 1069 (101), 1678 (60). ^{1}H NMR (600 MHz, C_6D_6, 298 K): δ 63.93 (3H), 28.49 (6H), 18.63 (9H), 13.34 (6H), 8.82 (3H), 7.99 (6H), 7.06, 4.88 (3H), −22.41 (1H) ppm. Anal. Calcd. for $SnCoN_6C_{48}BH_{43}\cdot(C_6H_6)$: 66.83 %C; 5.09 %H; 8.66 %N. Found: 66.68 %C; 4.96 %H; 8.30 %N.

Magnetic Measurements. Magnetic data were collected using a Quantum Design MPMS-XL SQUID magnetometer. Measurements for all compounds were obtained on finely ground microcrystalline powders. The compounds were restrained in a frozen eicosane matrix and flame sealed in a quartz tube under vacuum. Dc magnetic susceptibility measurements were performed in the temperature range 1.8–300 K under dc fields of 0.1, 0.5 and 1 T. Dc magnetization measurements were performed under applied magnetic fields of 1, 2, 3, 4, 5, 6 and 7 T in the temperature range of 1.8–10 K. Dc magnetic susceptibility data were corrected for diamagnetic contributions from the sample holder and eicosane as well as for the core diamagnetism of each sample, estimated using Pascal's constants.[16] A temperature-independent paramagnetism (TIP) correction was applied for both **2** and **3** with values of 1.3×10^{-3} cm^3mol^{-1} and 1.1×10^{-3} cm^3mol^{-1}, respectively. Prior to full characterization, variable dc field magnetization data was collected from 0 to 4 T at 100 K to ensure the absence of curvature associated with ferromagnetic impurities.

Electron Paramagnetic Resonance (EPR) Spectroscopy. Polycrystalline samples of **2** and **3** were loaded into a 4 mm OD quartz EPR tube under a dinitrogen atmosphere and restrained with eicosane. Continuous-wave EPR spectra were measured at the University of Chicago EPR facility

using a Bruker Elexsys 500 X-band EPR spectrometer. Samples were cooled using an Oxford Systems continuous-flow He cryostat coupled with a 10 K He stinger from Bruker. Spectra were acquired with the Bruker Win-EPR software suite. Spectral simulations were carried out using Easyspin.[17]

X-ray Diffraction. Single crystal diffraction data collections were performed on single crystals coated with Paratone-N oil and mounted on a MicroMounts™ rod. The crystals were frozen while coated in Paratone-N oil under a stream of N_2 during the measurement. Structures for **2** and **3** were collected with CuKα (λ = 1.54178 Å) and MoKα (λ = 0.71073 Å) sealed tube diffraction sources respectively. Both sources were equipped with a graphite monochromator and a Bruker APEX2 CCD detector. Raw data were integrated and corrected for Lorentz and polarization effects using Bruker Apex3 v. 2013.[18] Absorption corrections were applied using SADABS.[19] Space group assignments were determined by examination of systematic absences, *E*-statistics, and successive refinement of the structures. The crystal structure was solved by direct methods with the aid of successive difference Fourier maps in SHELXS[20] operated with the OLEX2 interface.[21] The crystals showed no significant decay during data collection. Thermal parameters were refined anisotropically for all non-hydrogen atoms. Hydrogen atoms were placed in ideal positions and refined using a riding model for all structures. Compounds **2** and **3** crystallized with a benzene molecule that was disordered over a special position, so a solvent mask was used.

Powder X-ray Diffraction Measurements. Polycrystalline samples of **2** and **3** where loaded in a hollow metallic sample holder and both sides sealed with Kapton tape inside the glovebox. The powder X-ray diffraction (PXRD) patterns were measured in transmission geometry (with sample

spinning) using a STOE STADI P instrument equipped with a CuKα1 sealed tube source and a 1D strip detector covering 2θ range of 6°. All patterns were collected at room temperature.

All Other Physical Measurements. Combustion analysis of all complexes was performed by Midwest Microlabs (Indianapolis, IN). Infrared spectra were recorded on a Bruker Alpha FTIR spectrometer equipped with an attenuated total reflectance accessory. Solution-phase NMR spectra were collected with a Bruker Avance III 600 MHz spectrometer. Proton NMR spectra are referenced to d_6-benzene at 7.16 ppm. UV-vis-NIR and diffuse reflectance spectra were collected on a Varian Cary 5000 spectrometer at room temperature in $CDCl_3$ for the solutions or over KBr for solid measurements.

Ligand Field Theory (LFT) Analysis. LFT analysis of the electronic structures of **2** and **3** were performed with use of the angular overlap model (AOM).[22] The computer program DDN, which is available from J. Telser, was employed to perform the analysis. The program used the complete d^7 (equivalent to d^3) weak-field basis including interelectronic repulsion (Racah parameters: *B*, *C*), spin-orbit coupling (ζ_{eff}), and AOM ligand-field bonding parameters ($\epsilon_{\sigma,}$ ϵ_{π}). DDN allows use of a non-linear least-squares fitting subroutine (DSTEPIT, from QCPE, Bloomington, IN) to match observed electronic transition energies to those calculated by user-defined variable parameters. The general AOM procedure involved an initial fit of spin-allowed optical transitions with variation of *B* and AOM bonding parameters without ζ_{eff}; C was set to 4.7*B*. The geometric parameters used for the analysis were taken from the single-crystal X-ray diffraction data, and the bonding parameters for the three pyrazole N donors were set to be identical as they are crystallographically symmetric. In order to reduce overparameterization, the ϵ_{σ}(N) parameter was calculated using the $1/r^6$ dependence on bond distance from known ϵ_{σ}(N) parameters in similar Tp-

based Co^{2+} complexes and held constant throughout the analysis.[15] The analysis was performed assuming C_{3v} symmetry of the complexes; therefore we set $\epsilon_{\pi c}(Sn) = \epsilon_{\pi s}(Sn)$. From this initial fit, ξ_{eff} was varied until a reasonable match for $|D|$ was obtained. The resulting electronic structures were then checked to ensure that they were still in agreement with experiment.

Discussion of discrepancy between EPR and magnetometry g-values. We simulated the magnetization data from SQUID magnetometry with slightly lower g-values than what were used to simulate X-band EPR spectroscopy. We attribute this discrepancy to slight structural distortions that occur at lower temperatures. Structural distortions upon cooling is corroborated by the PXRD in Figure S6 which show deviations in the room temperature patterns from simulations of the single crystal data measured at 100 K.

Table S4.1 | Crystallographic information for the structural refinement of **2**.

Empirical Formula	$GeCoN_6C_{54}BH_{49}$
Formula weight	924.32 g/mol
Temperature	100.0 K
Wavelength	1.54178 Å
Crystal System	Trigonal
Space Group	$R\bar{3}$
Unit Cell Dimensions	a = 12.4224(6) Å, α = 90.0˚
	b = 12.4224(6) Å, β = 120.0˚
	c = 48.074(4) Å, γ = 90.0˚
Volume	6424.7(8) $Å^3$
Z	6
Density (calculated)	1.433 g/cm^3
Absorption coefficient	4.254 mm^{-1}
F_{000}	2874.0
Crystal color	Purple
Crystal size	0.398 × 0.384 × 0.110 mm^3
2θ range	2.757 to 68.026˚
Index ranges	$-14 \le h \le 9$
	$-14 \le k \le 14$
	$-57 \le l \le 56$
Reflections collected	27268
Independent reflections	2606 [R_{int} = 0.0228]
Completeness to θ = 60.128˚	99.92 %
Absorption correction	Multi-scan
Maximum and minimum transmission	0.3824 and 0.2160
Refinement method	Full-matrix least-squares on F^2
Data / restraints / parameters	2606 / 0 / 173
Goodness-of-fit on F^{2a}	1.075
Final R indices [I > 2σ(I) = 10408 data]^b	R_1 = 3.37 %, wR_2 = 8.62 %
R indices (all data, 0.80 Å)	R_1 = 3.40 %, wR_2 = 8.64 %
Largest diff. peak and hole	0.54 and –0.34 e.$Å^{-3}$

^{a} GooF = $[\Sigma[w(F_o^2-F_c^2)^2] / (n-p)]^{1/2}$ where n is the number of reflections and p is the total number of parameters refined. $^b R_1 = \Sigma||F_o|-|F_c|| / \Sigma|F_o|$; $wR_2 = [\Sigma[w(F_o^2-F_c^2)^2] / \Sigma[w(F_o^2)^2]]^{1/2}$

Table S4.2│ Crystallographic information for the structural refinement of **3**.

Empirical Formula	$SnCoN_6C_{54}BH_{49}$
Formula weight	970.42 g/mol
Temperature	100.0 K
Wavelength	0.71073 Å
Crystal System	Monoclinic
Space Group	$R\bar{3}$
Unit Cell Dimensions	a = 12.373(2) Å, α = 90.0˚
	b = 12.373(2) Å, β = 120.0˚
	c = 48.707(8) Å, γ = 90.0˚
Volume	6458(2) Å^3
Z	6
Density (calculated)	1.497 g/cm^3
Absorption coefficient	1.012 mm^{-1}
F_{000}	2982.0
Crystal color	Purple
Crystal size	0.516 × 0.344 × 0.050 mm^3
2θ range	3.892 to 64.18˚
Index ranges	$-17 \le h \le 17$
	$-17 \le k \le 17$
	$-70 \le l \le 70$
Reflections collected	51077
Independent reflections	4682 [R_{int} = 0.0371]
Completeness to θ = 64.18˚	100.0 %
Absorption correction	Multi-scan
Maximum and minimum transmission	0.2679 and 0.2211
Refinement method	Full-matrix least-squares on F^2
Data / restraints / parameters	4682 / 0 / 173
Goodness-of-fit on F^{2a}	1.055
Final R indices [I > 2σ(I) = 10408 data]^b	R_1 = 5.35 %, wR_2 = 14.83 %
R indices (all data, 0.80 Å)	R_1 = 6.87 %, wR_2 = 16.01 %
Largest diff. peak and hole	4.87 and –0.98 e.Å^{-3}

^{a} GooF = $[\Sigma[w(F_o^2-F_c^2)^2] / (n-p)]^{1/2}$ where n is the number of reflections and p is the total number of parameters refined. $^b R_1 = \Sigma||F_o|-|F_c|| / \Sigma|F_o|$; $wR_2 = [\Sigma[w(F_o^2-F_c^2)^2] / \Sigma[w(F_o^2)^2]]^{1/2}$

Table S4.3 | Simulation parameters for X-band EPR spectra of **2** and **3**.

Compound	D (cm^{-1})	E (cm^{-1})	$g_{\parallel}$	$g_{\perp}$
2	3.9	0.52	2.28	2.26
3	12.0	0.70	2.25	2.31

Table S4.4 | Fit parameters to the variable-temperature, variable-field magnetization curves for **1 – 3.**

Compound	D (cm^{-1})	E (cm^{-1})	$g_{\parallel}$	$g_{\perp}$
1	2.0(3)	--	2.06(4)	2.06(4)
2	3.9(3)	0.52(3)	2.20(2)	2.20(2)
3	11.9(1)	0.7(1)	2.28(2)	2.28(2)

Table S4.5 | Fitted AOM parameters for **2** and **3**. (E = Ge, Sn)

Compound	ζ_{eff} (cm^{-1})	*B*	ϵ_σ(N) (cm^{-1})	$\epsilon_{\pi s}$(N) (cm^{-1})	ϵ_σ(E) (cm^{-1})	ϵ_π(E) (cm^{-1})
2	357	677	3235	1	2145	-934
3	531	678	3401	129	2363	-633

Table S4.6 | Tabulated experimental and calculated band energies from the AOM analysis from a $^4A_2$ ground state, assignments in C_{3v} symmetry with T_d origins in parentheses. All values are given in units of cm^{-1}.

Compound	^4E (T_2, F)	$^4A_1$ (T_2, F)	^4E (T_1, F)	$^4A_2$ (T_1, F)	$^4A_2$ (T_1, P)*	^4E (T_1, P)
2						
observed	not obsd	forbidden	5956	9124	14225 14663	15267
calculated	2988	4500	5915	8966	14628	15303
3						
observed	not obsd	forbidden	5959	9355	14641	15384
calculated	2906	4628	5992	9308	14572	15452

*Multiple transitions observed to this spin-allowed state due to coupling to states arising from ^2G free-ion term.

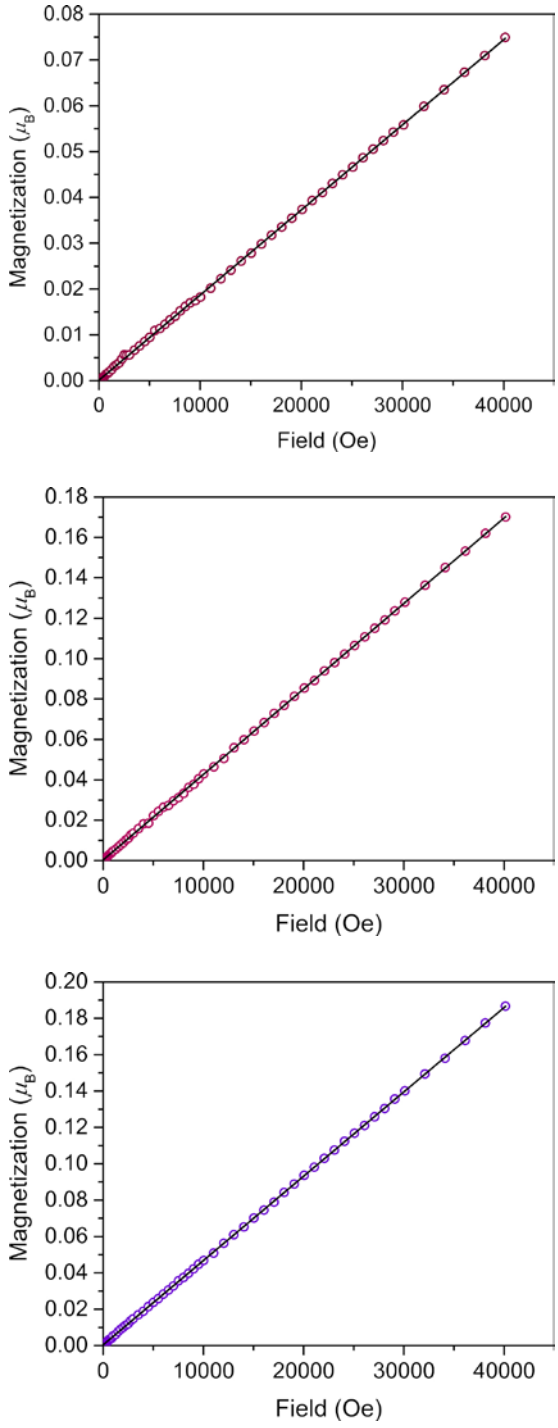

Figure S4.1 | Variable-field magnetization data for **1** (top), **2** (middle), and **3** (bottom) collected restrained under eicosane acquired at 100 K. The black line is a linear fit to the data illustrating the absence of ferromagnetic impurities.

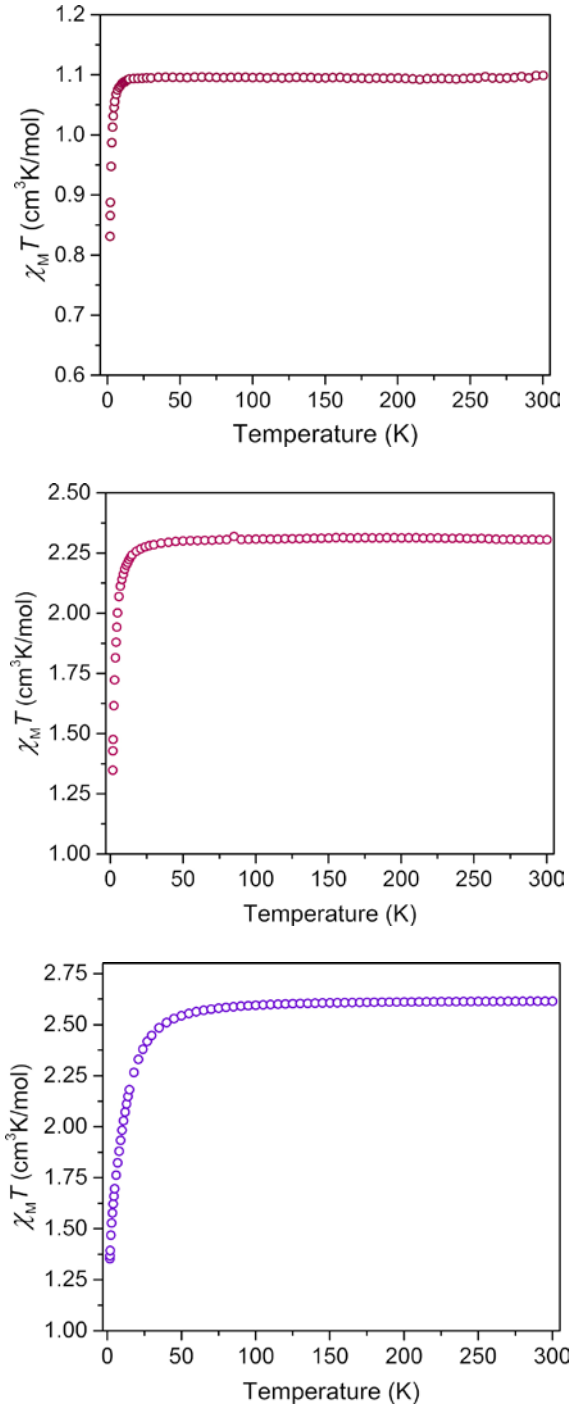

Figure S4.2 | Variable-temperature dc magnetic susceptibility data for **1** (top), **2** (middle), and **3** (bottom) collected from 1.8 K to 300 K under a dc field of 0.1 T.

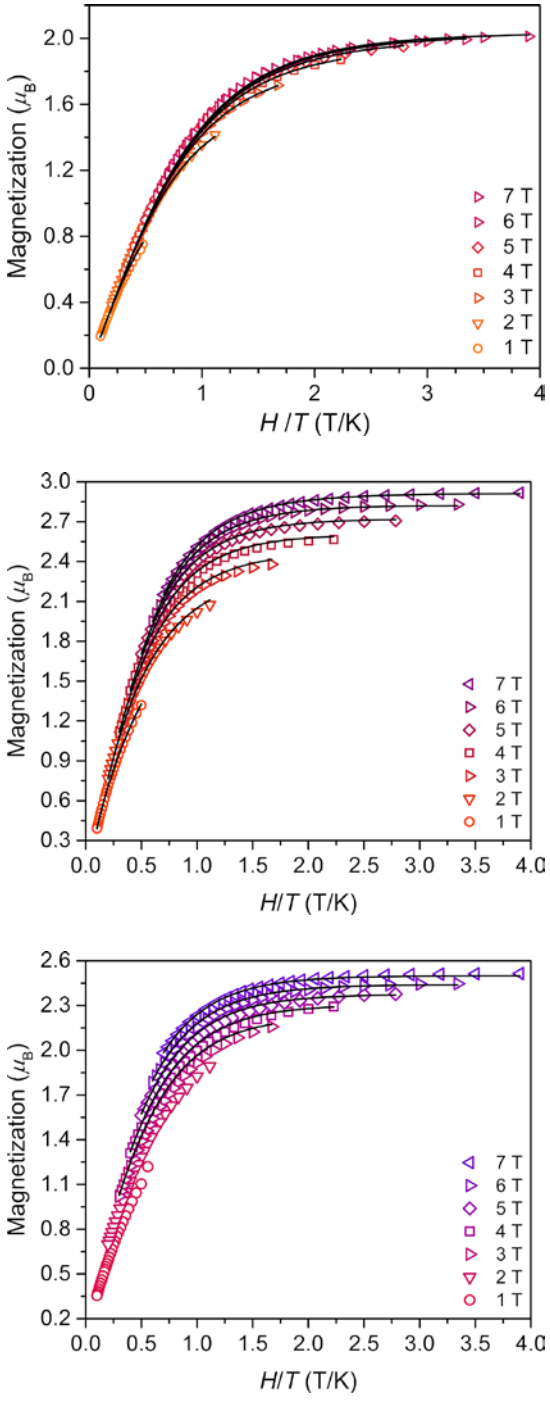

Figure S4.3 | Variable-temperature, variable-field magnetization data for **1** (top), **2** (middle), and 3 (bottom) collected between 1.8 and 10 K from 1 to 7 T in 1 T increments. Black lines are simulations of the data obtained from fits using DAVE 2.0 and the spin Hamiltonian, $\hat{H} = D[\hat{S}_z^2 - {}^1/_3S(S + 1)] + E(\hat{S}_x^2 - \hat{S}_y^2) + g\mu_B\mathbf{SH}$.

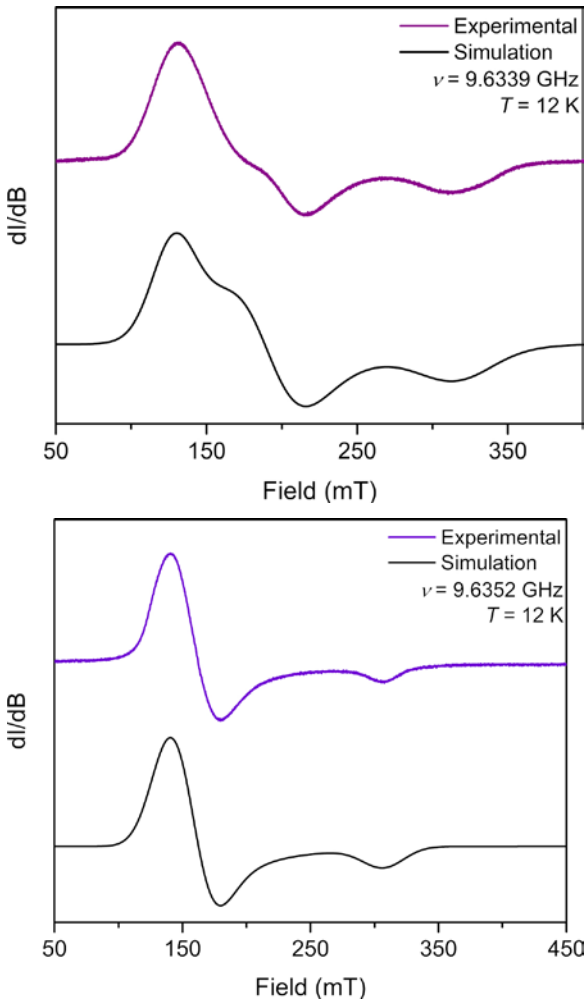

Figure S4.4 | X-band EPR spectra of **2** (top) and **3** (bottom) measured at 12 K encased in eicosane. Parameters for the simulation are given in Table S4.3.

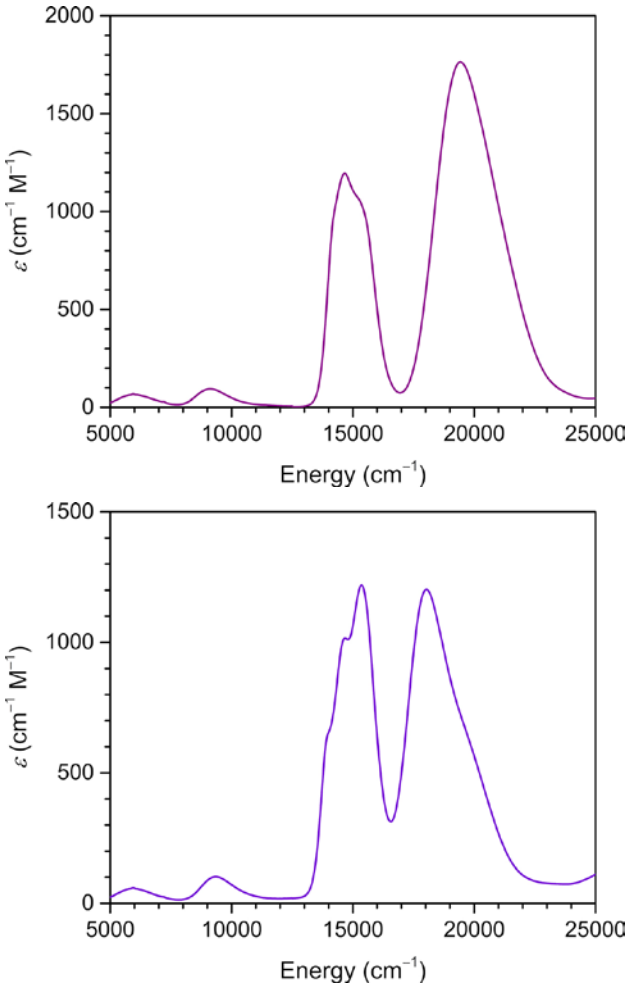

Figure S4.5 | Electronic absorption spectra of **2** (top) and **3** (bottom) measured at room temperature in $CDCl_3$.

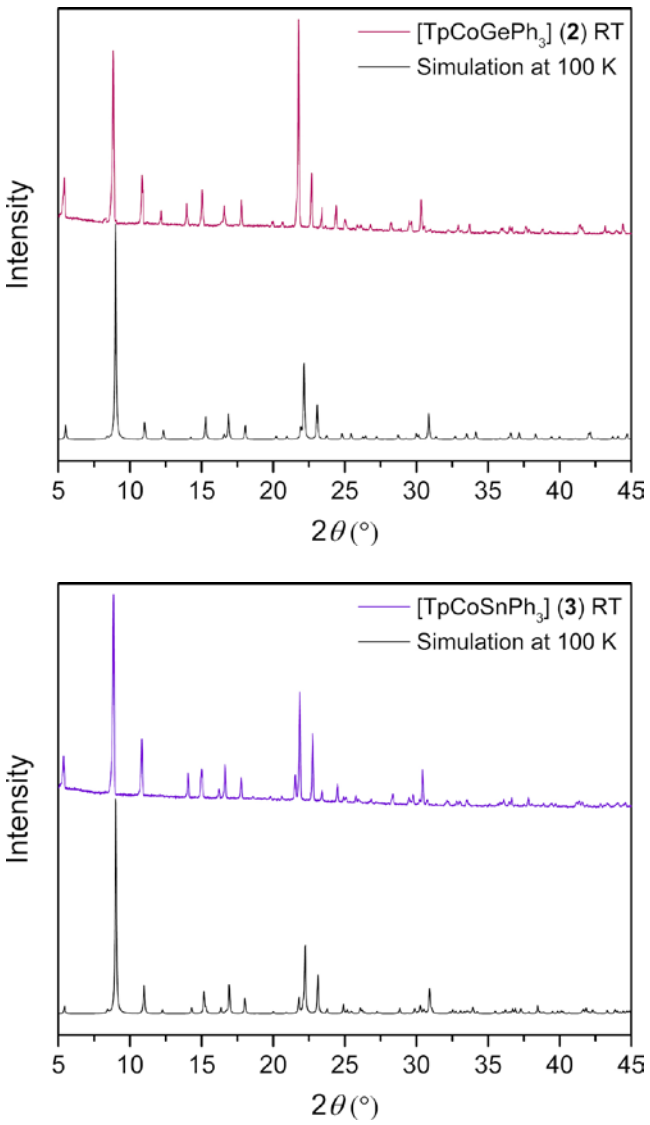

Figure S4.6 | Powder X-ray diffraction patterns for **2** (top) and **3** (bottom) measured at room temperature with CuKα radiation. The bottom patterns are simulations from the single crystal X-ray diffraction data measured at 100K.

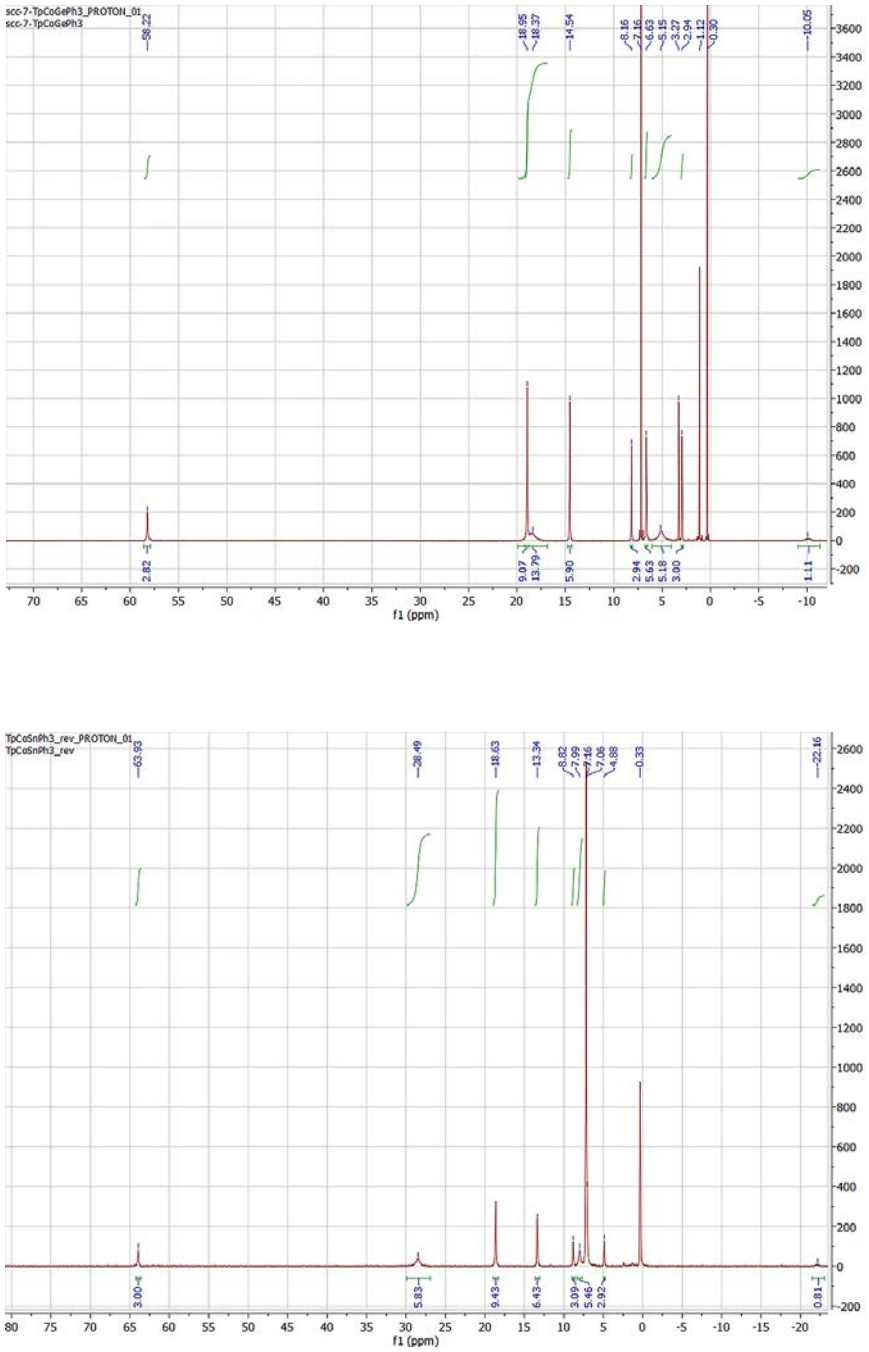

Figure S4.7 | ^{1}H nuclear magnetic resonance spectrum of **2** (top) and **3** (bottom) measured in C_6D_6 at room temperature.

Chapter 5: The Influence of Transition Metal-Tin Covalency on Spin-Orbit Coupling

Coste, S. C.; Klein, R. A.; Altman, A. B.; Hu, M. Y.; Alp E. E.; Brewe, D. L.; Freedman, D. E.

Unpublished work

This work was performed in collaboration with the co-authors listed above.

5.1 Introduction

Spin-orbit coupling (SOC) controls crucial properties in transition metal complexes such as magnetism,[1,2] quantum coherence,[3] luminescence,[4–6] and reactivity.[7–11] A fundamentally atomic phenomenon, SOC arises from the interaction between an electron's intrinsic spin (*S*) coupling to its respective orbital angular momentum (*L*). Since the strength of this coupling scales with the effective nuclear charge, Z_{eff}^2, first-row transition metals feature low SOC relative to their heavier counterparts.[12,13] As SOC dictates key aspects of electronic structure, such as spin-phonon coupling in qubit candidates or magnetic anisotropy in magnets, exerting synthetic control over SOC in first-row transition metal complexes would be advantageous for designing materials towards such specific applications.

A synthetically feasible approach to augment spin-orbit coupling of first-row transition metals is to introduce a heavy diamagnetic element into its primary coordination sphere. In this scheme, a heavy main-group element is ligated to a paramagnetic transition metal with weak SOC thus delegating the key components of SOC, spin and angular momentum, into two different atoms. This heavy atom effect was initially utilized to bolster intersystem crossing rates of organic molecules framing it's use in luminescent materials.[14,15] The approach was later adopted to enhance the magnetic anisotropy of first-row transition metal complexes where heavier donors induced an increase in magnetic anisotropy.[16–21] As key functions of metal complexes, such as reactivity and magnetism, are governed by metal-ligand orbital overlap, chemical intuition would suggest that the covalency of this two-atom interaction limits SOC transfer. In order to maximize the ligand SOC contribution, a relatively more covalent interaction is therefore required so that electron density is more shared between the metal-ligand bond.

An intuitive method to engender metal-ligand covalency is to employ relatively electropositive donors therefore decreasing the electronegativity difference between the two atoms. In this regard, we propose utilizing heavy main group metals, such as Sn, as ligands to confer SOC to a first-row transition metal. To optimize coupling between transition metal spin and ligand SOC, we hypothesize that matching the symmetry of the heavy donor orbitals and spin-bearing orbitals is essential based on previous studies with $S = 1$ Fe(II) and Co(III) complexes.[22,23] Thus, high-spin ground states in heterobimetallic complexes would be more amenable to this criterion because of the increased unpaired spin density in metal-ligand antibonding orbitals. This would embed more heavy-metal contribution to the ground and lowest-lying excited states that relate to magnetic anisotropy.

Towards this end, we recently synthesized the first high-spin transition metal-Sn complex and demonstrated the Sn donor indeed enhanced the SOC of the Co^{2+} metal center.[24] Modelling of the metal-metal interaction using the angular overlap model determined that the Sn was a weak sigma donor, which is surprising based on previous assessments using CO stretching frequencies and the trans effect.[25–27] Since metal-metal interactions dictate the electronic, magnetic, and reactive properties of heterobimetallic complexes, we are interested in better understanding the electronic structure through a molecular orbital perspective. Furthermore, we are interested in how the metal-metal bond covalency influences SOC transferral, which we will test through variation of the d-orbital configuration. We hypothesize that weakening the bond with larger d electron counts will weaken the contribution of ligand SOC towards magnetic anisotropy.

Herein, we report the synthesis and characterization of an isostructural series of transition metal-Sn complexes to test the influence of electronic configuration on the metal-metal interaction

and the ensuing magnetic properties. Following previously outlined design criteria, we synthesized and isolated the series [^{Ph,Me}TpMSnPh$_3$] (^{Ph,Me}Tp$^-$ = hydrotris(3-phenyl-5-methylpyrazolyl)borate; M = Mn^{2+}, Fe^{2+}, Co^{2+}, Ni^{2+}, Zn^{2+}). By relying on unsupported metal-metal bonds to help foster a weak ligand field environment, we isolated high-spin ground states in several of the new heterobimetallic complexes which are ideal for testing our hypotheses. We assessed metal-metal covalency using electron paramagnetic resonance, X-ray absorption, and Mössbauer spectroscopy. Then, we correlate the electronic structure changes to magnetic anisotropy, our proxy for SOC transfer, via SQUID magnetometry.

5.2 Results and Discussion

In order to synthesize high-spin complexes featuring metal-metal bonds between Sn and first-row transition metals, we targeted lower-coordinate transition metal complexes to decrease the ligand field strength at the metal center. Additionally, we sought unsupported metal-metal bonding to diminish the ancillary ligands' impact on the electronic structure. We designed a system where the unsupported metal-metal bond is stabilized electrostatically by fusing a positively charged transition metal fragment with an anionic Sn fragment. Towards this goal, we capped a divalent metal (Mn^{2+}, Fe^{2+}, Co^{2+}, Ni^{2+}, Zn^{2+}) with the tetrahedrally-directing, monoanionic ligand hydrotris(3-phenyl-5-methylpyrazolyl) borate (^{Ph,Me}Tp$^-$) . This generates a positively charged transition metal moiety as a Lewis acid and provides an open coordination site in the axial position for the Sn donor. Reacting this fragment with the Lewis basic organometallic anion, triphenyl stannide (Ph_3Sn^-), yields the desired four-coordinate complexes featuring unsupported metal-metal bonds between first row transition metals and Sn.

We accessed complexes **3** – **7** via two routes, either by salt metathesis of ^{Ph,Me}TpMCl (M = Mn^{2+}(**1**), Fe^{2+}, Co^{2+}, Zn^{2+}(**2**))[28,29] with $KSnPh_3$ in diethyl ether at room temperature or by elimination of tetramethylsilane from the reaction of [^{Ph,Me}TpNiCH_2SiMe_3][30] with $HSnPh_3$ in n-hexane at room temperature (Scheme 1); compound **5** was reported previously. The potassium salt was necessary for the metathesis reactions as Li^+ or Na^+ forms of Ph_3Sn^- yielded Sn^0 as a major side product. We attribute this to the ability for Li^+ and Na^+ to displace the transition metal in the $^{Ph,Me}Tp^-$ ligand, which we often observed by NMR in these reactions. To synthesize **6**, we relied on the weak Sn-H bond to react with the alkyl ligand on the parent nickel complex. The alkane elimination procedure was necessary to access **6** as the metathesis yielded the product, as observed by NMR, however it decomposed under the reaction conditions quickly. Thus, the less harsh environments of the elimination reaction allowed isolation of 6. We attempted to synthesize the Cu congener, but metathesis and elimination reactions (with [^{Ph,Me}TpCuO^{t}Bu]) yielded reduction to Cu^+ as evidenced by diamagnetic NMR signals and the colorless solution. Purification of the compounds followed by recrystallization from a benzene/n-hexane layering yielded hexagonal platelets suitable for X-ray diffraction experiments. Further synthetic details are available in the supporting information.

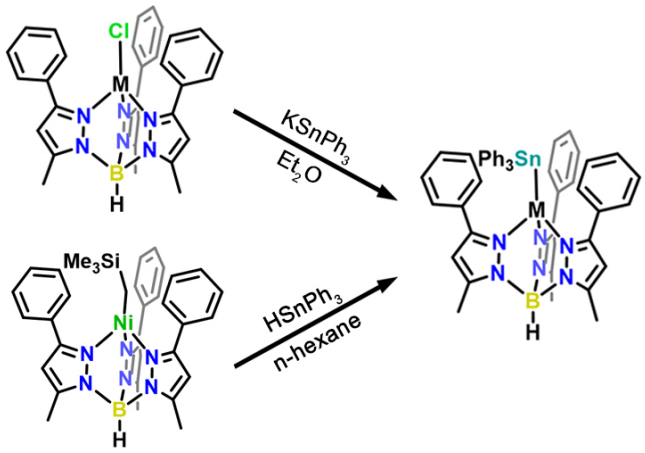

Scheme 5.1 Synthetic pathways to **3** – **7**. M = Mn, Fe, Co, Ni, Zn.

Single crystal X-ray diffraction revealed the structures of complexes **3** – **7**, as depicted in Figure 5.1, displaying unsupported metal-metal bonding. The transition metal-Sn complexes

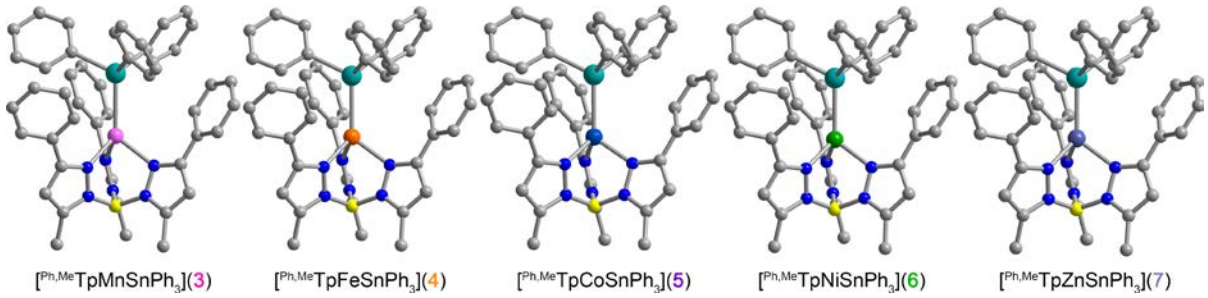

Figure 5.1 Molecular structures of the [^{Ph,Me}TpMSnPh$_3$] series determined by X-ray crystallography where M = Mn^{2+} (**3**), Fe^{2+} (**4**), Co^{2+} (**5**), Ni^{2+} (**6**), and Zn^{2+} (**7**). The blue, grey, yellow, turquoise, pink, orange, cobalt blue, green, and purple spheres represent nitrogen, carbon, boron, tin, manganese, iron, cobalt, nickel, and zinc atoms respectively. The hydrogens are omitted for clarity.

crystallize isostructurally in *R*−3, as corroborated by PXRD (Fig. S5.1), with the metal-metal bond coinciding with the 3-fold rotation axis. The M-Sn bond distances in complexes **3**, **4**, **5**, and **7** (2.757(1), 2.698(1), 2.654(1), 2.603(1) Å respectively) are all shorter than the sum of their covalent radii suggesting covalent bonding.[31] However, the Ni-Sn bond in compound **6** (2.668(1) Å) deviates by being slightly longer than the sum of the covalent radii (2.63 Å) hinting at a weakened bond relative to the rest of the series. Analysis of the metal-metal bonds using Cotton's formal shortness ratios (FSR's) better illustrates this where values for the complexes are 0.92 (3), 0.93 (4), 0.92 (5), 1.01 (6), and 1.00 (7); we used covalent radii from Alvarez and coworkers to calculate these values.[32] Though, the vibrational Raman spectra (presented in Figure S5.2) reveal the metal-metal stretching frequencies of **3** – **6** to be similar (170 – 173 cm^{-1}) despite the slightly elongated Ni-Sn bond. Interestingly, the stretching mode in **7** is 180 cm^{-1} suggesting Sn bonds more strongly to Zn, which could reflect differences between the way the Zn bonds to the Sn relative to the transition metals in **3** – **7**.

To examine the metal-metal covalency throughout complexes **3** – **7**, we employed X-ray absorption spectroscopy at the Sn K-edge. Specifically, characteristics of the X-ray absorption near edge structure (XANES) region are sensitive to aspects of electronic structure such as electron

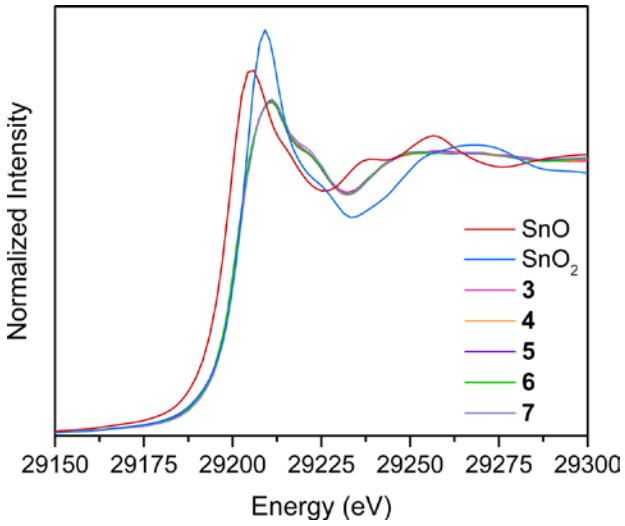

Figure 5.2 The XANES spectra at the Sn K-edge for polycrystalline samples of **3** – **7** (29200.4 eV for Sn metal reference), including SnO and SnO_2 standards, measured at 25 K.

distribution, geometry, and coordination number.[33] The spectra of **3** – **7**, shown in Figure 5.2 along with SnO and SnO_2 references, are similar in the XANES region. The onset energy, defined by the energy at the inflection point, for each compound is 29201.7 eV and the intensities overlay well. This indicates that the Sn electronic structure does not change significantly between **3** – **7** within the resolution limit of the Sn K-edge.[34–37] Importantly, the onset of the SnO and SnO_2 references are 29200.1 and 29203.4 eV, respectively, eluding to a Sn valency between +2 and +4. We note that the Sn coordination number between SnO and SnO_2 increases from **4** to **6**, however, comparison to the 4-coordinate Sn in SnO yields the same conclusion. This observation matches the valence trends in ^{119}Sn Mossbauer spectra of transition metal-Sn^{2+} complexes where the isomer shift values are closer to those of Sn^{4+} than Sn^{2+}. This observation was attributed to the presence of a covalent metal-metal bond.[38] As an additional control, we measured the X-ray absorption spectra of Ph_6Sn_2, Ph_4Sn, Ph_3SnCl, and Ph_3SnF, where high-valent Sn exists in similar C_{3v} symmetric environments. Shown in Figure S5.3, the onset energy for the organometallic controls, ~29201.1 eV, are similar to that of complexes **3** – **7** further corroborating the apparent valence state of Sn. With respect to previous ^{119}Sn Mossbauer parameters, this would suggest covalent bonding between the Sn and transition metals due to the lack of electron density at the tin.

With the presence of covalent bonding confirmed, we then probed complexes 3 – 6 using SQUID magnetometry to confirm their high-spin ground states and determine their magnetic properties as a function of the d-electron count. Variable-temperature dc magnetic susceptibility data (shown Figure 5.3) on polycrystalline samples of 3, 4, 5, and 6 display room-temperature $\chi_M T$ values of 4.32, 3.58, 2.11, and 1.36 cm^3 K mol^{-1} in accordance with S = ½, S = 2, S = ³⁄₂, and S = 1 ground states, respectively. Complexes **3** – **6** represent, to the best of our knowledge, the first high-spin paramagnetic complexes featuring M-Sn (where M = Mn, Fe, Co and Ni) bonds to date. Simultaneously, the spin states unambiguously confirm the divalent oxidation states of the transition metal and Sn. The room-temperature $\chi_M T$ value of complexes **3** and **6** persist down to ~15 K where it drops to 3.37 and 0.97 cm^3 K mol^{-1} at 1.8 K, respectively. On the other hand, complexes **4** and **5** begin to drop slowly starting at about 100 K down to 1.09 cm^3 K mol^{-1} for both complexes at 1.8 K. We attribute this difference in temperature dependence of the susceptibility data to higher zero-field splitting, $|D|$, values for complexes **4** and **5** relative to **3** and **6**.

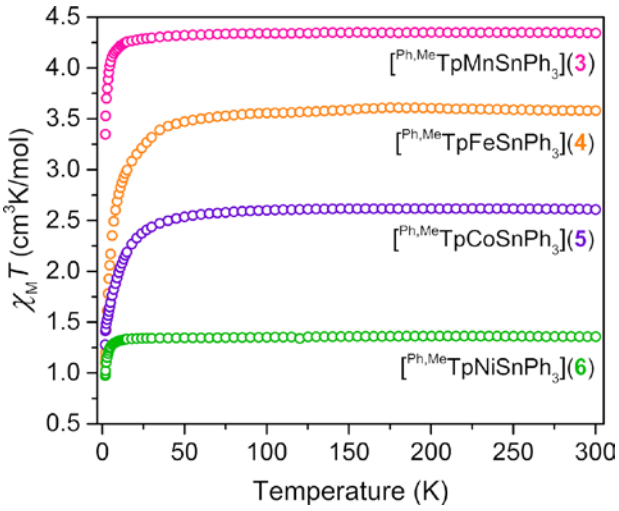

Figure 5.3 Temperature dependent magnetic susceptibility of polycrystalline powders of **3** – **6** collected under an applied field of 0.1 T.

As another probe of covalency, and to determine D in **3**, we used X-band EPR spectroscopy (Figure 5.4) as Mn^{2+} is easily addressable owing to its symmetric electronic structure. A solid state dilution of **3** in **7** (1:20 Mn:Zn) allowed the resolution of Sn hyperfine at room temperature which is most prevalent from the intra-Kramers (M_S = ±½) transition shown in the inset of

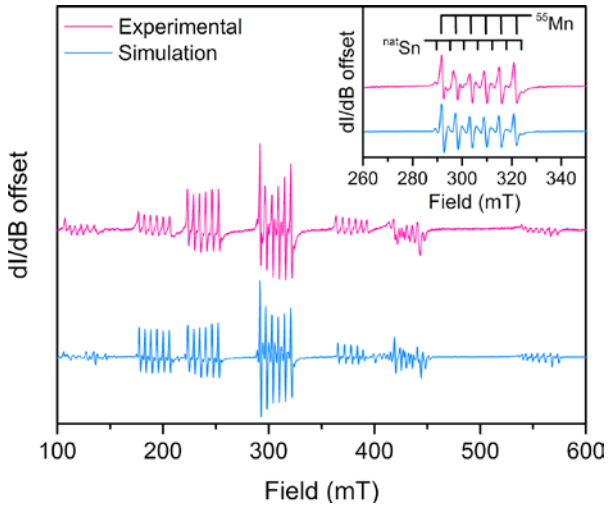

Figure 5.4 Overlay of the experimental (pink) cw-EPR spectrum of **3** diluted in a polycrystalline sample of **7** (Mn:Zn 1:20) and the simulation (light blue) at room temperature collected at X-band (ν = 9.6328 GHz). Inset: A zoomed image of the intra-Kramers (M_S = ±½) transition. The light blue spectrum was simulated using the following parameters: g_{iso} = 1.9933(2), S = 5/2, A_{iso}(^{55}Mn, I = 5/2) = 164(2) MHz, A_{iso}(^{nat}Sn, I = ½) = 141(3) MHz, D = 0.0939(4) cm^{-1}.

Figure 5.4. We modelled the spectrum using EASYSPIN[39] with the following spin Hamiltonian, $\hat{H} = g_{iso}\mu_B SH + AIS + D[\hat{S}_z^2 - S(S+1)/3]$ where g_{iso} is the isotropic g-value, μ_B is the Bohr magneton, S is the spin quantum number, H is the applied magnetic field, A is the hyperfine coupling tensor, I is the nuclear spin, and D is the axial zero-field splitting. The best simulation yields a ^{nat}Sn hyperfine coupling (I = ½) of 141(3) MHz that is comparable in magnitude to the ^{55}Mn hyperfine coupling (I = 5/2) suggesting considerable covalency of the metal-metal bond through the Mn d_{z^2} orbital. However, the ^{nat}Sn hyperfine in **3** is not as large as Sn-centered radicals, such as $Ph_3Sn\cdot$ (5230 MHz) suggesting much less localization near the Sn nucleus.[40] Furthermore, the ^{55}Mn hyperfine coupling parameter is low relative to other Mn^{2+} species analogous to the trend observed in Mn^{2+}-doped binary chalcogenides.[41] The hyperfine values here suggest a bond where the spin density is pulled away from both nuclei further corroborating covalent Mn-Sn bonding in **3**. This suggests that the Sn could have a large contribution to the magnetic anisotropy of the complexes.

Despite the measurable spin-density located at the heavy Sn donor, the zero-field splitting of **3** at room temperature, 0.0939(4) cm^{-1}, is surprisingly smaller than that of other Mn^{2+} complexes, and significantly less than that of iodide-based complexes.[42] For better comparison in

a similar ligand environment, the *D* value of the chloride congener [^{Ph,Me}TpMnCl](**1**) is more than double that of **3**. This observation is highly unusual as the *D* value of most Mn^{2+}-heavy ligand complexes are governed by the ligand SOC in both extended solid structures and discrete molecules. Interestingly, there is a temperature dependence to *D* where it exhibits an increase of 8% to 0.1015(6) cm^{-1} upon cooling to 12 K, which is uncommon in transition metal complexes. We attribute this temperature dependence to the thermal expansion/contraction of the lattice which would distort the local geometry about the Mn^{2+} center, a phenomenon similarly observed in Mn^{2+} doped $Cs_2NaLaCl_6$.[43]

We more precisely quantified *D* in complexes **4** and **6** via acquisition of variable-temperature, variable-field magnetization data (shown in Figure 5.5 and Figure S5.6); the magnetic properties of **5** were reported previously. Using the program DAVE 2.0,[44] we simulated the data with the spin Hamiltonian $\hat{H} = g_{iso}\mu_B \boldsymbol{SH} + D[\hat{S}_z^2 - S(S+1)/3] + E(\hat{S}_{X^2} - \hat{S}_{y^2})$ where all parameters hold their previous definitions and *E* is the transverse zero-field splitting parameter; the simulated Hamiltonian parameters are shown in Table S5.9. The *D* values extracted for **4** and **6** from the simulations are 12.9(3) cm^{-1} (E/D = 0.26) and −3.0(2) cm^{-1} (E/D = 0), agreeing with the trend in the variable-temperature susceptibility data. However, the magnitude and sign of *D* in **4** and **6** are unexpected based on reported complexes with similar electronic structures. The best fit to the magnetization data for **4** is surprising as other $S = 2$ C_{3v} symmetric Fe^{2+} centers generally exhibit large, negative *D* values with little rhombicity owing to the orbital doublet ground state, ^5E.[45,46,47,48] The positive *D* in **4** more closely resembles that of D_{2d} symmetric ferrous centers such as those observed in certain rubredoxin proteins.[49–54]

Complex **6** also exhibits an unusually small |*D*| relative to other known C_{3v} symmetric d^8 complexes with heavy donors such as iodide-based complexes.[55–57] Considering only SOC, replacement of the I^- with a Sn donor, a 5p element with comparable spin-orbit coupling, should yield a larger |*D*| owing to the larger covalency afforded by Sn's relative electropositivity. The *D* values reported here indicate that the axial Sn donor is unexpectedly affecting the magnetic properties. As *D* arises from the coupling of the ground electronic state to low-lying excited states, the foregoing results prompted us to interrogate the electronic structure to understand the covalent donor's ligand field influence.

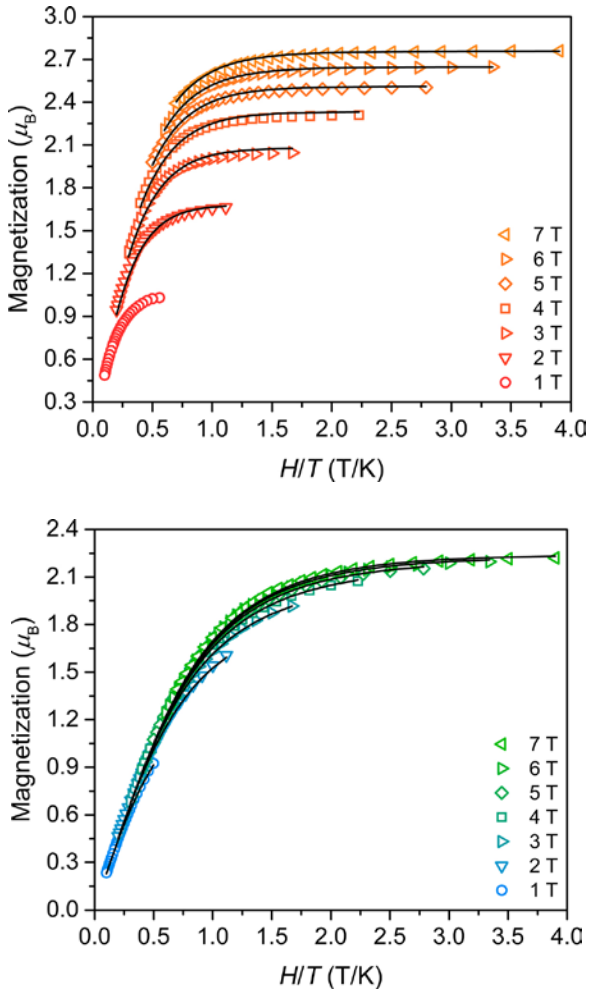

Figure 5.5 Variable-temperature, variable-field magnetization for **4** (top) and **6** (bottom) with black lines representing the best fit. The parameters for the fits are given in Table S5.9 in the electronic supplementary information.

To determine the energetic ordering of the frontier orbitals, we measured the electronic absorption spectra of **3** – **6** displayed in Figures S5.7 and S5.8. Direct comparison of the spectra between the solution and the solid-state show very similar band positions, which suggests the solid-state structures for **3** – **6** are close to the most energetically-stable conformation. We note that the shoulder around 16,600 cm^{-1} in **6** shifts slightly between the solid-state and solution due to

the slightly weakened Ni-Sn bond. Each spectrum exhibits d-d transitions at lower energies and charge transfers in the UV-Visible region. The intensity of the charge transfer bands are similar in magnitude (~103 L $mol^{-1}cm^{-1}$) to that of the higher energy d-d transitions in **4**, **5**, and **6** suggesting that these may be metal to metal charge transfers (MMCT).[58,59] The lack of charge transfer bands in the parent chloride compounds exclude the possibility of a transition involving the supporting $^{Ph,Me}Tp^{-}$ ligand. We assign these as $Ph_3Sn\rightarrow TM$ MMCTs reflecting the stability of Sn's higher oxidation states, and this is corroborated by the lack of a charge transfer in compound **7** which has a filled d-orbital manifold. Based on previously reported pseudotetrahedral C_{3v} symmetric complexes, the energies and intensities of the d-d transitions in **5** and **6** suggest $^4A_2$ and $^3A_2$ ground states, respectively, with the following frontier orbital energy ordering: $E(d_{xz}, d_{yz}) > A_1(d_{z^2}) > E(d_{xy}, d_{x^2-y^2})$.[60] However, it is difficult to resolve whether the NIR d-d band of **4** (~4700 cm^{-1}) is two overlapping peaks or one. The magnitude of this $^5T_2$ band splitting upon descent in symmetry from T_d to C_{3v} informs the relative energy of the d_{z^2} orbital to the lower E orbital set in **4**. The relative position of the d_{z^2} orbital will largely influence the magnetic anisotropy because of its significant contribution to the lowest-lying excited states. It is therefore essential that we determine the relative orbital ordering in **4**, and its consistency with the remainder of the series, to comprehensively assess Sn's covalent influence on magnetic anisotropy.

We turned to Mössbauer spectroscopy to confirm the electronic structure of **4** and its consistency with the remainder of the series. Specifically, the quadrupole splitting parameter (ΔE_Q) in ^{57}Fe Mössbauer spectroscopy provides additional insight into the electronic configuration as it is sensitive to the distribution of valence electrons about the metal center. Since the positive *D* of **4** is more comparable to that of D_{2d} symmetric high-spin ferrous complexes, instead of C_{3v}, this could suggest that the d_{z^2} orbital is lower in energy than the d_{xy} and $d_{x^2-y^2}$ orbitals. Simulation of the ^{57}Fe Mössbauer spectrum of **4** at 80 K (Figure 5.6) yields an isomer shift (δ) of 0.742(1) mm s^{-1} and a ΔE_Q value of 1.061(3) mm s^{-1}, comparable to pseudotetrahedral tris-carbene and -phosphine ferrous complexes.[61,62] We note that the isomer shift is higher in **4** than previously reported complexes suggesting more electron density at the ^{57}Fe nucleus. Importantly, the ΔE_Q value is much smaller than that of D_{2d} symmetric complexes, implying that the d_{z^2} orbital is indeed more destabilized than the lower E orbital set providing a ^{5}E ground state.[63–66]

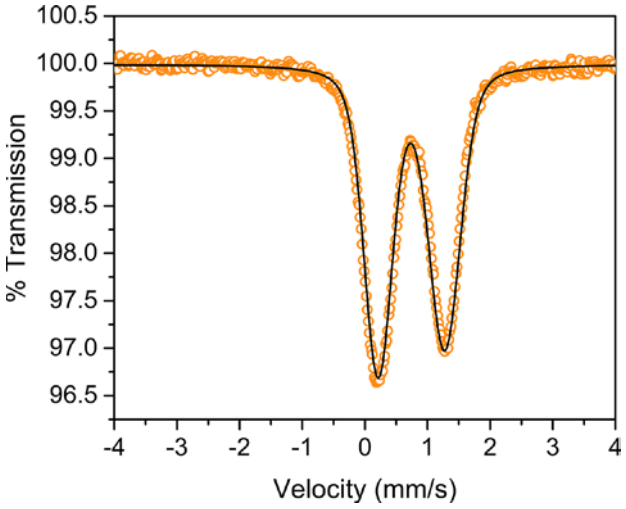

Figure 5.6 ^{57}Fe Mossbauer spectra for a powder sample of **4** collected at 80 K. Open circles represent the experimental data, and the black line represents the fit to the spectrum.

To more precisely examine the bonding throughout the series, we relied on synchrotron Mössbauer spectroscopy (SMS) of the ^{119}Sn nucleus. Also known as nuclear resonant forward scattering, SMS is a time-domain technique that probes the nuclear spin transition of nuclei using pulsed synchrotron radiation. This technique allows for the rapid collection of information

similarly obtained in conventional transmission-mode Mössbauer spectroscopy. The SMS data at 60 K are shown in Figure 5.7 (10, 20, and 80 K data are in Figures S5.9 – S5.12) with fits to the data yielding ΔE_Q values of 1.198(2), 1.198(4), 1.134(2), and 0.896(2) mm s^{-1} for complexes **4**, **5**, **6**, and **7**, respectively. Data for **3** could not be obtained due to experimental complications that will be discussed in the electronic supplementary information. Since the complexes are isostructural, we can exclude lattice contributions to the differences in ΔE_Q values in **4** – **7** rendering only changes in the bonding between complexes responsible. The ΔE_Q value for **7** deviates the most from the remainder of the series, which is apparent from the larger frequency of the quantum beats, suggesting that the orbitals comprising the Zn-Sn bond differs. We hypothesize that the empty p-orbitals of Zn contribute to the metal-metal bond, since the d-orbital manifold is completely filled, and this is reflected in the subtle differences in the bond's Raman stretching frequency where it is 180 cm^{-1} in **7** versus 170-173 cm^{-1} in **3** – **6**. We also note that the ΔE_Q value in **6** slightly differs from **4** and **5**. Importantly, the similar ΔE_Q values throughout the paramagnetic species imply that the bonding interactions do not vary significantly. Therefore, the molecular

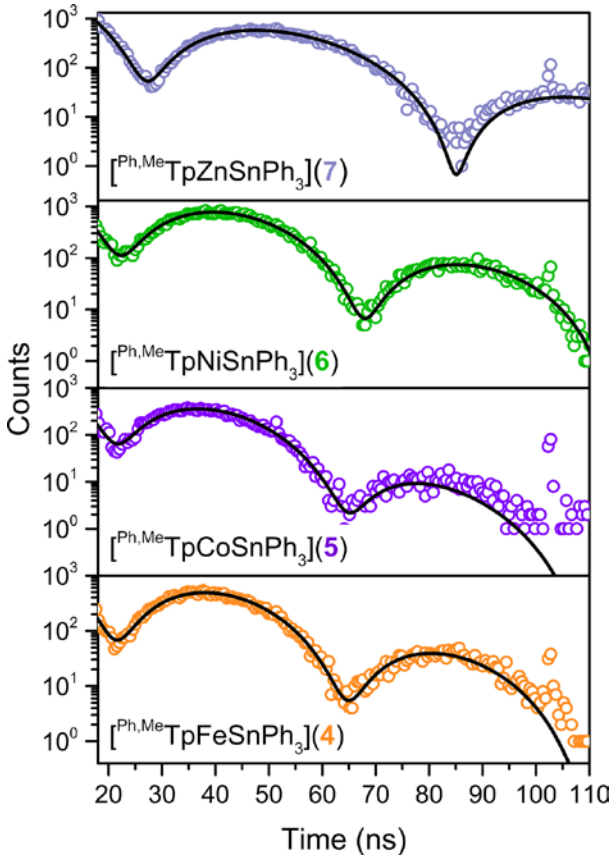

Figure 5.7 ^{119}Sn synchrotron Mössbauer spectra of **4** – **7** collected at 60 K. Open circles represent the experimental data, and the black lines represent fits to the spectra.

orbital picture, and d-orbital splitting, must be consistent throughout the transition metal series allowing better comparison of the electronic structures.

The aggregate experimental data here allow us to form a cohesive molecular orbital picture to explain how metal-metal bond covalency influences magnetic anisotropy. We will frame our discussion by defining covalency as the relative atomic contribution of each metal towards the bonding molecular orbital. The hyperfine parameters from EPR spectroscopy of **3** indicate that both nuclei contribute in a non-negligible manner towards the metal-metal bonding orbital. However, the onset energy in the XAS data of **3** – **7** elude to a Sn valency greater than 2+. We interpret this as significant donation of Sn electron density towards the metal-metal molecular orbital. This is not a complete charge transfer though, as SQUID magnetometry provides a definitive valency of the transition metal by the number of unpaired electrons. The lack of electron density at the Sn suggests that the metal-metal bond may be polarized towards the transition metal. This is corroborated by both the low Sn hyperfine in EPR and the larger isomer shift of **4** in the ^{57}Fe Mössbauer spectrum when compared to similar ferrous complexes. Importantly, the isomer shift in **4** is not as high as tetrahedral $S = 2$ ferrous halide complexes such as $[FeCl_4]^{2-}$ (δ = 1.01 mm s^{-1} at 80 K) which would suggest a more ionic Fe-Sn interaction.[67] From a molecular orbital perspective, a bond which is polarized towards the transition metal indicates that the energy bonding orbital is closer in energy to the transition metal d-orbitals than the Sn donor orbitals. Thus, I hypothesize the Sn donor orbitals are higher in energy than the metal d orbitals. Ionization potentials from optical spectra support this as the Sn ionization potential (7.344 eV) is closer to vacuum than the later first-row transitions metals where Mn is 7.432 eV.[68]

In comparing the covalency of the metal-metal bond throughout the series, there are two changes that occur upon increasing d electron count. Intuitively, adding more electrons into the d manifold as we move from compound **3** to **7** weakens the bonding interaction slightly through population of the antibonding orbitals. This is evident from the FSR values calculated based on crystallographic parameters. Additionally, the increasing electronegativity of the transition metals lowers the atomic d-orbitals. Moving to the right in the d-block then increases the ionization energy of the transition metal d-orbitals, and this is corroborated by the trend in charge transfer energies where the energy decreases between complexes **3**, **4**, and **5**. The foregoing electronic structure analysis leads us to conclude that a covalent interaction is present between the transition metals and Sn in the series, but that it is slightly polarized towards the transition metal. Importantly, the polarization increases as we increase the d electron count due to the increasing energy mismatch between Sn donor and metal d orbitals.

An increasing polarization as we increase d electron count implies that SOC transfer will concurrently decrease. As the molecular orbital gains more transition metal character, the Sn atomic contribution (i.e. SOC) will decrease. In relation to the *D* values, the coupling of states involving Sn will have less contribution as the transition metal electronegativity increases. We will illustrate how this influences magnetic anisotropy with the d-orbital diagrams in Figure 5.8. As *D* arises from coupling of the ground state to excited states through SOC, we can break down *D* into various contributions arising from the coupling to each excited state. The measured *D* value in each complex is then a combination of each contribution to *D*, which is weighted by the SOC of the orbitals involved and inversely proportional to the energy separation between the coupled states. In each complex, there are two major spin-orbital contributions towards *D*; coupling

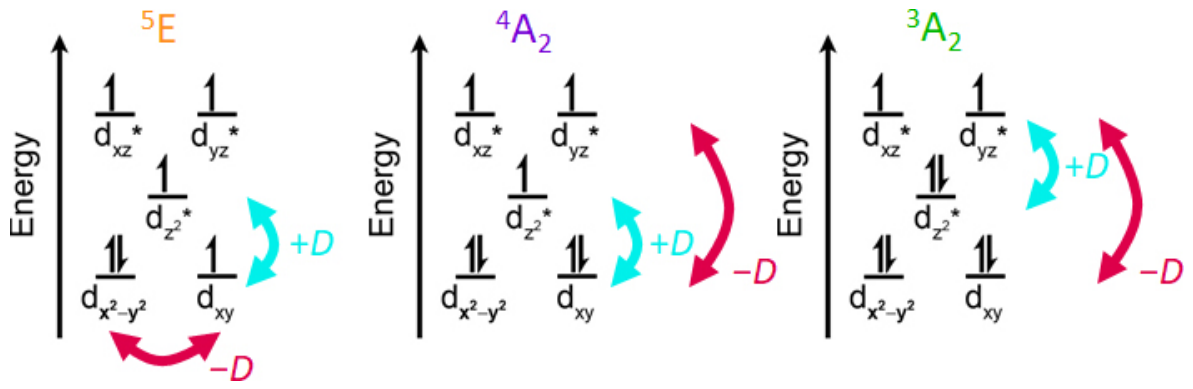

Figure 5.8 Qualitative d-orbital splitting diagrams for **4** – **6** highlighting the major contributions to *D*.

between orbitals with E symmetry (d_{xy}, $d_{x^2-y^2}$) (d_{xz}, d_{yz}) will provide a negative contribution towards *D* while coupling between E and A_1 (e.g. d_{z^2}) type orbitals contribute positively.[69] As the Sn donor interacts most strongly with the d_{z^2} orbital, the large SOC from Sn should induce strong positive contributions to the series of complexes. The effect of increasing polarity thus decreases the strength of this positive influence between **4** – **6**. This interpretation explains the unexpected *D* values reported here where the strong positive contribution provides an unexpected positive *D* value for **4** and the weakened contribution from Sn yields relatively negative value in complex **6**.

5.3 Conclusions

Harnessing control over SOC in transition metal complexes promises to enable manipulation of excited state and spin dynamics, catalytic pathways, and magnetism. Our two-atom approach provides a method to study how metal-ligand covalency mediates SOC, two components that are delicately intertwined in the orbital description of transition metal complexes. In order to study the influence of covalency on SOC transferred between two atoms, we synthesized the first high-spin complexes featuring covalent bonding between transition metals and a tin donor. We then probed changes in covalency through a series of spectroscopic techniques to determine how metal-metal covalency changes as a function of d electron count. To describe changes in covalency, we

established a molecular orbital model for the paramagnetic transition metal-tin interaction, and we determined that more electronegative transition metals induce a slight polarization in the metal-metal bond away from the tin donor. Zero-field splitting throughout our series, our probe for SOC, decreased as the electronegativity of the transition metal increased suggesting the increased polarization diminishes SOC transfer. The foregoing results provide a comprehensive picture for a heavy main-group metal- transition metal interaction, which is central to the design of functional magnets, catalysts, and spintronic materials. Future work will focus on two ideas to test. One aim will focus on main group metal interactions with less electronegative paramagnetic transition metals to test how polarization towards the main group element affect SOC transfer. Another effort will aim to use more electronegative transition metals in order to allow the metal-metal charge transfer, with significant tin character, to contribute more greatly to magnetic anisotropy.

5.4 Supplementary Information

Experimental Details.

General Considerations. All compounds were manipulated and handled under a dinitrogen atmosphere in an MBraun Unilab Pro glovebox. All glassware was either oven-dried at 150 °C for at least four hours or flame-dried prior to use. Dichloromethane (DCM), methanol (MeOH), Diethylether (Et_2O), benzene, toluene, and n-hexane were dried using a commercial solvent purification system from Pure Process Technology and stored over 3 or 4 Å sieves for a minimum of one day prior to use. $CDCl_3$ and C_6D_6 were purchased from Cambridge Isotope Labs, deoxygenated by three successive freeze-pump-thaw cycles, filtered through a pad of activated alumina, and stored over 3 or 4 Å sieves prior to use. $KTp^{Ph,Me}$, ^{Ph,Me}TpFeCl, ^{Ph,Me}TpCoCl, and [^{Ph,Me}TpNiCH_2SiMe_3]·½ hexane were prepared according to literature procedures.[70717273] $HSnPh_3$ was purchased from MilliporeSigma and vacuum distilled prior to use. All other chemicals were used as received. Silylated Celite was prepared by stirring 25 g activated, dried Celite 545 in 100 mL toluene with 14 mL trimethylsilylchloride and 14 mL of triethylamine under N_2 overnight at 40 °C, followed by filtration, washing with 80 mL MeOH and 200 mL toluene, and drying for 24 hours at 100 °C.

[^{Ph,Me}TpMnCl](1). A solution of KTp (1.0463 g, 2.00 mmol) in 15 mL DCM was added to a stirring solution of $MnCl_2$ (0.2573 g, 2.04 mmol) in 3 mL MeOH at room temperature. The white, cloudy solution then this was allowed to stir overnight at room temperature. The reaction mixture was subsequently pumped down to dryness. The product was extracted into 20 mL DCM, filtered through a Celite pad on a fritted filter, and then concentrated to about 4 mL. Crystalline product suitable for X-ray diffraction was obtained by adding 15 mL of n-hexane and allowing to sit at

room temperature overnight. The white needles were then isolated by decanting the mother liquor, washing with 3 x 5 mL n-hexane, and drying *in vacuo*. Yield: 0.4563 g (39.7%). IR (ATR, cm^{-1}): 3131 (w), 3057 (w), 2968 (w), 2927 (w), 2909 (w), 2570 (w), 1577 (w), 1570 (w), 1558 (w), 1541 (m), 1521 (w), 1507 (m), 1497 (w), 1486 (m), 1478 (m), 1464 (w), 1456 (w), 1450 (m), 1431 (m), 1410 (m), 1400 (w), 1387 (w), 1379 (w), 1357 (m), 1341 (m) , 1323 (m), 1304 (m), 1282 (w), 1188 (m), 1172 (m), 1156 (m), 1106 (m), 1096 (m), 1067 (s), 1041 (m), 1030 (w), 999 (w), 993 (w), 977 (m), 913 (m), 842 (w), 827 (w), 799 (m), 778 (s), 761 (vs), 690 (vs), 679 (vs), 668 (s), 658 (m), 640 (s), 619 (m), 603 (m). Anal. Calcd. for $MnClN_6C_{30}BH_{28}$: 62.80 %C; 4.92 %H; 14.65 %N. Found: 62.70 %C; 4.83 %H; 14.53 %N.

[^{Ph,Me}TpZnCl](2). A solution of KTp (1.3216 g, 2.53 mmol) in 15 mL DCM was added to a stirring solution of $ZnCl_2$ (0.3483 g, 2.56 mmol) in 3 mL MeOH at room temperature. The white, cloudy solution then this was allowed to stir overnight at room temperature. The reaction mixture was subsequently pumped down to dryness. The product was extracted into 20 mL DCM, filtered through a Celite pad on a fritted filter, and then concentrated to about 4 mL. Crystalline product suitable for X-ray diffraction was obtained by adding 15 mL of n-hexane and allowing to sit at room temperature overnight. The white needles were then isolated by decanting the mother liquor, washing with 3 x 5 mL n-hexane, and drying *in vacuo*. Yield: 0.6667g (45.1%) IR (ATR, cm^{-1}): 3139 (w), 3122 (w), 3089 (w), 3061 (w), 3046 (w), 3027 (w), 2988 (w), 2961 (w), 2930 (w), 2916 (w), 2546 (m), 1574 (w), 1568 (w), 1545 (m), 1508 (w), 1474 (m), 1438 (m), 1414 (m), 1385 (m), 1370 (m), 1342 (m), 1310 (w), 1282 (w), 1216 (w), 1186 (m), 1171 (s), 1129 (w), 1094 (m), 1064 (s), 1028 (w), 998 (w), 984 (m), 917 (w), 909 (w), 858 (w), 836 (w), 810 (m), 804 (m), 781 (m), 772 (m), 759 (vs), 721 (w), 704 (m), 691 (vs), 668 (m), 655 (m), 636 (s), 623 (w), 616 (w), 612

(w), 604 (w). ^{1}H NMR (500 MHz, $CDCl_3$, 298 K): δ 7.72 (d, 6H), 7.41 (t, 6H), 7.36 (t, 3H), 6.26 (s, 3H), 5.00 (br d, 1H), 2.57 (s, 9H) ppm. Anal. Calcd. for $ZnClN_6C_{30}BH_{28}$: 61.68 %C; 4.83 %H; 14.38 %N. Found: 61.46 %C; 4.91 %H; 14.17 %N.

[^{Ph,Me}TpMnSnPh$_3$]·benzene(3). Yellow $KSnPh_3$ was generated by stirring $HSnPh_3$ (482.0 mg, 1.373 mmol) and KH (55.1 mg, 1.374 mmol) in 5 mL of Et_2O for 4 hours at room temperature. To this, a suspension of **1** (504.0 mg, 0.8784 mmol) in 15 mL Et_2O was added at room temperature, a white precipitate formed and the reaction was allowed to stir overnight at room temperature. The precipitate was filtered out and washed with 4 x 5 mL Et_2O and dried. Then, it was taken up in 80 mL benzene, filtered through silylated Celite on a fritted funnel, then layered under 100 mL n-hexane. Colorless hexagonal platelets of **3** were obtained (Yield: 410.5 mg, 48.4%). The IR (ATR, cm^{-1}): 3048 (w), 3023 (w), 3001 (w), 2975 (w), 2964 (w), 2928 (w), 2527 (w), 1542 (m), 1506 (w), 1474 (m), 1450 (m), 1432 (s), 1423 (s), 1376 (w), 1358 (m), 1341 (m), 1303 (w), 1283 (w), 1254 (w), 1215 (w), 1178 (s), 1092 (m), 1060 (s), 1030 (m), 995 (w), 975 (m), 912 (w), 841 (w), 802 (w), 777 (m), 763 (s), 730 (s), 695 (s), 677 (vs), 656 (s), 638 (s), 531 (m), 522 (m), 489 (m), 451 (s), 442 (s), 409 (w). UV-Vis-NIR (C_6D_6) λ_{max}, nm (ε): 360 (2595). Anal. Calcd. for $SnMnN_6C_{48}BH_{43}\cdot{}^{1}\!/_{2}(C_6H_6)$: 66.04 %C; 5.00 %H; 9.06 %N. Found: 66.34 %C; 5.01 %H; 8.83 %N.

[^{Ph,Me}TpFeSnPh$_3$]·benzene(4). **4** was synthesized in a similar fashion to **3**, except that [^{Ph,Me}TpFeCl] (510.3 mg, 0.8879 mmol) was reacted with KSnPh3 (1.373 mmol). Orange, hexagonal platelets of **4** were obtained with a benzene/n-hexane layering (Yield: 295.9 mg, 34.4 %). IR (ATR, cm^{-1}): 3048 (w), 3024 (w), 2995 (w), 2975 (w), 2965 (w), 2919 (w), 2527 (w), 1541 (m), 1506 (w), 1474 (m), 1451 (m), 1433 (s), 1423 (s), 1376 (w), 1359 (m), 1342 (m), 1300 (w), 1285 (w), 1254 (w), 1214 (w), 1180 (s), 1093 (m), 1058 (s), 1030 (m), 995 (w), 976 (m), 912 (w),

841 (w), 802 (w), 776 (m), 763 (s), 730 (s), 696 (s), 677 (vs), 656 (s), 637 (s), 532 (m), 524 (m), 488 (m), 451 (s), 442 (s), 417 (w). UV-Vis-NIR (C_6D_6) λ_{max}, nm (ε): 356 (1331), 462 (1510), 513 (sh, 727). ^{1}H NMR (500 MHz, C_6D_6, 298 K): δ 59.90 (3H), 32.59 (6H), 29.33 (9H), 10.20 (6H), 8.86 (3H), 7.67 (6H), 6.29 (3H), 5.85 (6H), -15.79 (1H) ppm. Anal. Calcd. for $SnFeN_6C_{48}BH_{43}\cdot(C_6H_6)$: 67.05 %C; 5.11 %H; 8.69 %N. Found: 66.76 %C; 5.07 %H; 8.41 %N.

[^{Ph,Me}TpNiSnPh$_3$]·benzene(6). A solution of $HSnPh_3$ (107.0 mg, 0.3048 mmol) in 2 mL of n-hexane was added to a stirring solution of [^{Ph,Me}TpNiCH$_2$SiMe$_3$]·½ hexane (151.6 mg, 0.2261 mmol) in 15 mL of n-hexane at room temperature. After allowing the reaction mixture to stir for 5 hours at room temperature, the turquoise precipitate was filtered out and washed with 3 x 5 mL hexanes then dried *in vacuo*. Turquoise, hexagonal platelets of **6** were obtained by dissolving the product in 8 mL benzene, filtering through silylated Celite, and layering under 30 mL of n-hexane. (Yield: 107.9 mg, 49.2%) IR (ATR, cm^{-1}): 3048 (w), 3024 (w), 2995 (w), 2975 (w), 2965 (w), 2931 (w), 2521(w), 1543 (m), 1506 (w), 1475(m), 1451 (m), 1435 (s), 1423 (s), 1377 (w), 1361 (m), 1344 (m), 1300 (w), 1285 (w), 1253 (w), 1218 (w), 1186 (s), 1094 (m), 1057 (s), 1031 (m), 996 (w), 979 (m), 912(w), 838 (w), 803 (w), 779 (m), 763 (s), 730 (s), 697 (s), 676 (vs), 656 (s), 637 (s), 535 (m), 528 (m), 488 (m), 452 (s), 443 (s), 404 (w). UV-Vis-NIR (C_6D_6) λ_{max}, nm (ε): 367 (1975), 576 (1511), 709 (1191), 975 (348). ^{1}H NMR (500 MHz, C_6D_6, 298 K): δ 73.93, 14.39, 9.99, 9.55, 8.90, 8.01, 7.47, 7.08, −9.24 ppm. Anal. Calcd. for $SnNiN_6C_{48}BH_{43}\cdot(C_6H_6)$: 66.85 %C; 5.09 %H; 8.66 %N. Found: 66.54 %C; 5.09 %H; 8.82 %N.

[^{Ph,Me}TpZnSnPh$_3$]·benzene (7). **7** was synthesized in a similar fashion to **3**, except that **2** (559.0 mg, 0.9578 mmol) was reacted with $KSnPh_3$ (1.437 mmol). Colorless, hexagonal platelets of **7** were obtained with a benzene/n-hexane layering (Yield: 451.0 mg, 48.3 %). IR (ATR, cm^{-1}): 3050

(w), 3026 (w), 2996 (w), 2977 (w), 2966 (w), 2931 (w), 2513 (w), 1544 (m), 1507 (w), 1476 (m), 1451 (m), 1435 (s), 1424 (s), 1376 (w), 1362 (m), 1343 (m), 1301 (w), 1286 (w) 1255 (w), 1219 (w), 1186 (s), 1093 (m), 1059 (s), 1031 (m), 996 (w), 976 (m), 913 (w), 834 (w), 803 (w), 780 (m), 764 (s), 731 (s), 697 (s), 676 (vs), 656 (s), 637 (s), 532 (m), 527 (m), 489 (m), 451 (s), 443 (s), 410 (w). ^{1}H NMR (600 MHz, C_6D_6, 298 K): δ 7.50 (d, 6H), 7.14 (t, 3H), 7.09 (t, 6H), 7.04 (d, 6H), 6.75 (t, 3H), 6.50 (t, 6H), 5.93 (s, 3H), 5.00 (br s, 1H), 2.24 (s, 9H) ppm. ^{119}Sn NMR (223.8 MHz, C_6D_6, 298 K) −118.45 ppm Anal. Calcd. for $SnZnN_6C_{48}BH_{43}\cdot\frac{1}{2}(C_6H_6)$: 65.31 %C; 4.94 %H; 8.96 %N. Found: 65.39 %C; 4.82 %H; 9.15 %N.

Magnetic Measurements. Magnetic data were collected using a Quantum Design MPMS-XL SQUID magnetometer. Measurements for all compounds were obtained on finely ground microcrystalline powders. The compounds were restrained in a frozen eicosane matrix and flame sealed in a quartz tube under vacuum. Dc susceptibility measurements were collected in the temperature range 1.8–300 K under dc fields of 0.1, 0.5 and 1 T. Dc magnetization measurements were performed under applied magnetic fields of 1, 2, 3, 4, 5, 6 and 7 T in the temperature range of 1.8–10 K. Dc magnetic susceptibility data were corrected for diamagnetic contributions from the sample holder and eicosane as well as for the core diamagnetism of each sample, estimated using Pascal's constants.[74] Prior to full characterization, variable dc field magnetization data was collected from 0 to 4 T at 100 K to ensure the absence of curvature associated with ferromagnetic impurities.

X-ray Diffraction. Single crystal diffraction data collections were performed on single crystals coated with Paratone-N oil and mounted on a MicroMounts^{TM} rod. The crystals were frozen while coated in Paratone-N oil under a stream of N_2 during the measurement. Structures for **1 - 7** were

collected with a Mo Kα (λ = 0.71073 Å) sealed tube diffraction source with a graphite monochromator, and a Bruker APEX2 CCD detector. Raw data were integrated and corrected for Lorentz and polarization effects using Bruker Apex3 v. 2013.[75] Absorption corrections were applied using SADABS.[76] Space group assignments were determined by examination of systematic absences, *E*-statistics, and successive refinement of the structures. The crystal structure was solved by direct methods with the aid of successive difference Fourier maps in SHELXS[77] operated with the OLEX2 interface.[78] The crystals showed no significant decay during data collection. Thermal parameters were refined anisotropically for all non-hydrogen atoms. Hydrogen atoms were placed in ideal positions and refined using a riding model for all structures. Compounds **3** – **7** crystallized with a benzene molecule that was disordered over a special position, so a solvent mask was used.

Zero-field ^{57}Fe Mössbauer Spectroscopic Measurements. Measurement of **4** was performed under zero applied magnetic field and at 80 K on ca. 70 mg of ground, microcrystalline product. The sample was loaded into a circular plastic cap of 1 cm^2 area under an inert atmosphere covered in Paratone-N oil and transferred quickly to the cryostat to avoid sample decomposition. The spectrum was collected with a constant acceleration spectrometer and a ^{57}Co/Rh source. Prior to measurements, the spectrometer was calibrated at 295 K with α-Fe foil. Spectra were analyzed using the WMOSS Mössbauer Spectral Analysis Software (www.wmoss.org).

Raman Spectroscopy Measurements. Crystals of **3** – **7** were sealed in 0.7 mm capillaries with Illumabond UV Curable Epoxy in the glovebox. Raman spectra were collected using a Horiba LabRam HR Evolution confocal microscope. Individual crystals were excited with 633 nm (compounds **3** and **4**) and 532 nm (compounds **5** – **7**) continuous-wave diode lasers equipped with

a long working distance 50× microscope objective (NA = 0.50; Nikon) and 1800 grooves/mm grating at 0.95 mW (633 nm) and 2.5 mW (532 nm) power at room temperature. The spectra were collected for 10 minutes.

Powder X-ray Diffaction Measurements. Polycrystalline samples of **3** – **7** where loaded in a hollow metallic sample holder and both sides sealed with Kapton tape inside the glovebox. The powder X-ray diffraction (PXRD) patterns were measured in transmission geometry (with sample spinning) using a STOE STADI P instrument equipped with a CuKα1 sealed tube source and a 1D strip detector covering 2θ range of 6°. All patterns were collected at room temperature.

Electron Paramagnetic Resonance (EPR) Spectroscopy. Polycrystalline samples were loaded into a 4 mm OD quartz EPR tube under a dinitrogen atmosphere and restrained with eicosane. Continuous-wave EPR spectra were measured at the University of Chicago EPR facility using a Bruker Elexsys 500 X-band EPR spectrometer. Samples were cooled using an Oxford Systems continuous-flow He cryostat coupled with a 10 K He stinger from Bruker. Spectra were acquired with the Bruker Win-EPR software suite. Spectral simulations were carried out using Easyspin.[79]

All Other Physical Measurements. Combustion analysis of all complexes was performed by Midwest Microlabs (Indianapolis, IN). Infrared spectra were recorded on a Bruker Alpha FTIR spectrometer equipped with an attenuated total reflectance accessory. Solution-phase NMR spectra were collected with a Bruker Avance III 600 MHz spectrometer. Proton NMR spectra are referenced to $CDCl_3$ or d_6-benzene at 7.26 and 7.16 ppm, respectively. UV-vis-NIR and diffuse reflectance spectra were collected on a Varian Cary 5000 spectrometer at room temperature in $CDCl_3$ (compounds **3**, **4**, **5**, and **7**) or C6D6 (compound **6**) for the solutions or over KBr for solid measurements.

Table S5.1 | Crystallographic information for the structural refinement of **1**.

Empirical Formula	$MnClN_6C_{30}BH_{28}$
Formula weight	573.78 g/mol
Temperature	100.07 K
Wavelength	0.71073 Å
Crystal System	Trigonal
Space Group	*R*3c
Unit Cell Dimensions	a = 12.0230(1) Å, α = 90.0˚ b = 12.0230(1) Å, β = 90.0˚ c = 32.558(3) Å, γ = 120.0˚
Volume	4075.8(1) $Å^3$
Z	6
Density (calculated)	1.403 g/cm^3
Absorption coefficient	0.616 mm^{-1}
F_{000}	1782.0
Crystal color	Colorless
Crystal size	0.342 × 0.150 × 0.084 mm^3
2θ range	4.644 to 68.426˚
Index ranges	$-19 \le h \le 18$ $-19 \le k \le 18$ $-21 \le l \le 51$
Reflections collected	41720
Independent reflections	7916 [R_{int} = 0.0371]
Completeness to 2θ = 68.426˚	81.1 %
Absorption correction	Multi-scan
Maximum and minimum transmission	0.4853 and 0.4292
Refinement method	Full-matrix least-squares on F^2
Data / restraints / parameters	2860 / 1 / 119
Goodness-of-fit on F^{2a}	1.061
Final R indices [$I > 2\sigma(I)$]^b	R_1 = 3.10 %, wR_2 = 6.80 %
R indices (all data)	R_1 = 4.15 %, wR_2 = 7.18 %
Largest diff. peak and hole	0.31 and –0.36 e.$Å^{-3}$

[a] GooF = $[\Sigma[w(F_o^2-F_c^2)^2] / (n-p)]^{1/2}$ where n is the number of reflections and p is the total number of parameters refined. [b] $R_1 = \Sigma||F_o|-|F_c|| / \Sigma|F_o|$; $wR_2 = [\Sigma[w(F_o^2-F_c^2)^2] / \Sigma[w(F_o^2)^2]]^{1/2}$

Table S5.2 | Crystallographic information for the structural refinement of **2**.

Empirical Formula	$ZnClN_6C_{30}BH_{28}$
Formula weight	584.21 g/mol
Temperature	100.11 K
Wavelength	0.71073 Å
Crystal System	Monoclinic
Space Group	$P2_1/n$
Unit Cell Dimensions	a = 11.0364(8) Å, α = 90.0˚
	b = 15.2242(1) Å, β = 94.548(2)˚
	c = 16.1001(1) Å, γ = 90.0˚
Volume	2696.6(4) Å^3
Z	4
Density (calculated)	1.439 g/cm^3
Absorption coefficient	1.04 mm^{-1}
F_{000}	1208.0
Crystal color	Colorless
Crystal size	0.348 × 0.122 × 0.040 mm^3
2θ range	3.688 to 60.42˚
Index ranges	$-15 \leq h \leq 15$
	$-21 \leq k \leq 21$
	$-22 \leq l \leq 22$
Reflections collected	44426
Independent reflections	7978 [R_{int} = 0.0855]
Completeness to 2θ = 60.42˚	100.0 %
Absorption correction	Multi-scan
Maximum and minimum transmission	0.4932 and 0.4028
Refinement method	Full-matrix least-squares on F^2
Data / restraints / parameters	7978 / 0 / 355
Goodness-of-fit on F^{2a}	1.010
Final R indices [$I > 2\sigma(I)$]^b	R_1 = 4.69 %, wR_2 = 9.00 %
R indices (all data)	R_1 = 9.26 %, wR_2 = 10.48 %
Largest diff. peak and hole	0.72 and –0.69 e.Å^{-3}

[a] GooF = $[\Sigma[w(F_o^2-F_c^2)^2] / (n-p)]^{1/2}$ where n is the number of reflections and p is the total number of parameters refined. [b] $R_1 = \Sigma||F_o|-|F_c|| / \Sigma|F_o|$; $wR_2 = [\Sigma[w(F_o^2-F_c^2)^2] / \Sigma[w(F_o^2)^2]]^{1/2}$

Table S5.3 | Crystallographic information for the structural refinement of **3**.

Empirical Formula	$SnMnN_6C_{54}BH_{49}$
Formula weight	966.43 g/mol
Temperature	100.0 K
Wavelength	0.71073 Å
Crystal System	Trigonal
Space Group	$R\bar{3}$
Unit Cell Dimensions	a = 12.3824(6) Å, α = 90.0˚ b = 12.3824(6) Å, β = 120.0˚ c = 49.104(2) Å, γ = 90.0˚
Volume	6520.2(7) Å^3
Z	6
Density (calculated)	1.477 g/cm^3
Absorption coefficient	0.912 mm^{-1}
F_{000}	2970.0
Crystal color	Colorless
Crystal size	0.456 × 0.419 × 0.110 mm^3
2θ range	3.888 to 60.114˚
Index ranges	$-17 \le h \le 17$ $-17 \le k \le 16$ $-69 \le l \le 69$
Reflections collected	55305
Independent reflections	4263 [R_{int} = 0.0425]
Completeness to 2θ = 60.114˚	100.0 %
Absorption correction	Multi-scan
Maximum and minimum transmission	0.9927 and 0.7230
Refinement method	Full-matrix least-squares on F^2
Data / restraints / parameters	4263 / 0 / 173
Goodness-of-fit on F^{2a}	1.048
Final R indices [$I > 2\sigma(I)$]^b	R_1 = 5.33 %, wR_2 = 14.90 %
R indices (all data)	R_1 = 6.53 %, wR_2 = 16.47 %
Largest diff. peak and hole	5.01 and –1.62 e.Å^{-3}

^{a} GooF = $[\Sigma[w(F_o^2-F_c^2)^2] / (n-p)]^{1/2}$ where n is the number of reflections and p is the total number of parameters refined. $^b R_1 = \Sigma||F_o|-|F_c|| / \Sigma|F_o|$; $wR_2 = [\Sigma[w(F_o^2-F_c^2)^2] / \Sigma[w(F_o^2)^2]]^{1/2}$

Table S5.4 | Crystallographic information for the structural refinement of **4**.

Empirical Formula	$SnFeN_6C_{54}BH_{49}$
Formula weight	967.34 g/mol
Temperature	100.0 K
Wavelength	0.71073 Å
Crystal System	Trigonal
Space Group	$R\bar{3}$
Unit Cell Dimensions	a = 12.3722(2) Å, α = 90.0˚ b = 12.3722(2) Å, β = 120.0˚ c = 48.796(1) Å, γ = 90.0˚
Volume	6468.6(2) Å^3
Z	6
Density (calculated)	1.490 g/cm^3
Absorption coefficient	0.962 mm^{-1}
F_{000}	2976.0
Crystal color	Orange
Crystal size	0.127 × 0.056 × 0.025 mm^3
2θ range	2.504 to 60.128˚
Index ranges	$-16 \le h \le 15$ $-17 \le k \le 17$ $-68 \le l \le 68$
Reflections collected	37148
Independent reflections	4228 [R_{int} = 0.0295]
Completeness to θ = 60.128˚	100.0 %
Absorption correction	Multi-scan
Maximum and minimum transmission	0.9879 and 0.8782
Refinement method	Full-matrix least-squares on F^2
Data / restraints / parameters	4228 / 0 / 173
Goodness-of-fit on F^{2a}	1.049
Final R indices [I > 2σ(I) = 10408 data]^b	R_1 = 3.03 %, wR_2 = 7.06 %
R indices (all data, 0.80 Å)	R_1 = 4.15 %, wR_2 = 7.71 %
Largest diff. peak and hole	0.39 and –0.91 e.Å^{-3}

^{a} GooF = $[\Sigma[w(F_o^2-F_c^2)^2] / (n-p)]^{1/2}$ where n is the number of reflections and p is the total number of parameters refined. $^b R_1 = \Sigma||F_o|-|F_c|| / \Sigma|F_o|$; $wR_2 = [\Sigma[w(F_o^2-F_c^2)^2] / \Sigma[w(F_o^2)^2]]^{1/2}$

Table S5.5 | Crystallographic information for the structural refinement of **6**.

Empirical Formula	$SnNiN_6C_{54}BH_{49}$
Formula weight	970.20 g/mol
Temperature	100.0 K
Wavelength	0.71073 Å
Crystal System	Trigonal
Space Group	$R\bar{3}$
Unit Cell Dimensions	a = 12.3186(4) Å, α = 90.0˚
	b = 12.3186(4) Å, β = 120.0˚
	c = 49.082(2) Å, γ = 90.0˚
Volume	6450.4(5) $Å^3$
Z	6
Density (calculated)	1.499 g/cm^3
Absorption coefficient	1.066 mm^{-1}
F_{000}	2988.0
Crystal color	Turquoise
Crystal size	0.443 × 0.380 × 0.044 mm^3
2θ range	2.49 to 61.21˚
Index ranges	$-17 \le h \le 17$
	$-17 \le k \le 17$
	$-70 \le l \le 69$
Reflections collected	65036
Independent reflections	4430 [R_{int} = 0.0329]
Completeness to θ = 52.48˚	100.0 %
Absorption correction	Multi-scan
Maximum and minimum transmission	0.8872 and 0.6505
Refinement method	Full-matrix least-squares on F^2
Data / restraints / parameters	4430 / 0 / 173
Goodness-of-fit on F^{2a}	1.050
Final R indices [I > 2σ(I) = 10408 data]^b	R_1 = 3.27 %, wR_2 = 8.23 %
R indices (all data, 0.80 Å)	R_1 = 4.15 %, wR_2 = 8.71 %
Largest diff. peak and hole	0.60 and –0.90 e.$Å^{-3}$

^{a} GooF = $[\Sigma[w(F_o^2-F_c^2)^2] / (n-p)]^{1/2}$ where n is the number of reflections and p is the total number of parameters refined. $^b R_1 = \Sigma||F_o|-|F_c|| / \Sigma|F_o|$; $wR_2 = [\Sigma[w(F_o^2-F_c^2)^2] / \Sigma[w(F_o^2)^2]]^{1/2}$

Table S5.6│ Crystallographic information for the structural refinement of **7**.

Empirical Formula	$SnZnN_6C_{54}BH_{49}$
Formula weight	976.86 g/mol
Temperature	100.0 K
Wavelength	0.71073 Å
Crystal System	Monoclinic
Space Group	$R\bar{3}$
Unit Cell Dimensions	a = 12.3859(4) Å, α = 90.0˚
	b = 12.3859(4) Å, β = 120.0˚
	c = 48.738(2) Å, γ = 90.0˚
Volume	6475.2(5) Å^3
Z	6
Density (calculated)	1.503 g/cm^3
Absorption coefficient	1.181 mm^{-1}
F_{000}	3000.0
Crystal color	Colorless
Crystal size	0.470 × 0.260 × 0.044 mm^3
2θ range	3.888 to 58.378˚
Index ranges	$-16 \le h \le 16$
	$-16 \le k \le 16$
	$-66 \le l \le 66$
Reflections collected	54021
Independent reflections	3891 [R_{int} = 0.0448]
Completeness to θ = 58.378˚	99.96 %
Absorption correction	Multi-scan
Maximum and minimum transmission	0.9514 and 0.7101
Refinement method	Full-matrix least-squares on F^2
Data / restraints / parameters	3891 / 0 / 173
Goodness-of-fit on F^{2a}	1.088
Final R indices [I > 2σ(I) = 10408 data]^b	R_1 = 4.22 %, wR_2 = 10.96 %
R indices (all data, 0.80 Å)	R_1 = 5.01 %, wR_2 = 11.72 %
Largest diff. peak and hole	2.48 and –1.62 e.Å^{-3}

^{a} GooF = $[\Sigma[w(F_o^2-F_c^2)^2] / (n-p)]^{1/2}$ where n is the number of reflections and p is the total number of parameters refined. $^b R_1 = \Sigma||F_o|-|F_c|| / \Sigma|F_o|$; $wR_2 = [\Sigma[w(F_o^2-F_c^2)^2] / \Sigma[w(F_o^2)^2]]^{1/2}$

Table S5.7 | Results from peak-fitting XANES data at Sn K-edge for **3** – **7**, and SnO, SnO_2, Ph_6Sn_2, Ph_4Sn, Ph_3SnCl, and Ph_3SnF references. The step was fit with an arctangent function and the peaks were fit with pseudo-Voigt functions with γ = 0.5 for all compounds. Peak and step positions are reported in eV.

Compound	Step			Peak 1			Peak 2			Reduced
	Height	Center	Width	Height	Center	σ	Height	Center	σ	χ^2
3	0.847	29201.7	3.5	9.72	29209.1	18.09	0.701	29223.7	7.97	0.0047
4	0.829	29201.7	3.53	10.117	29209.1	18.24	0.828	29223.7	8.29	0.0049
5	0.830	29201.7	3.52	10.404	29208.7	18.84	0.779	29223.5	7.81	0.0055
6	0.829	29201.8	3.51	10.473	29208.7	18.85	0.85	29223.7	8.49	0.0056
7	0.771	29201.7	3.64	10.469	29209.1	17.20	2.62	29223.8	13.92	0.0051
Ph_6Sn_2	0.718	29201.0	1.59	9.272	29204.1	12.22	7.26	29224.5	22.58	0.0052
Ph_4Sn	0.719	29201.1	1.68	9.303	29204.1	12.10	7.29	29224.8	22.72	0.0057
Ph_3SnCl	0.749	29201.2	1.74	9.319	29204.1	12.02	7.27	29224.2	22.86	0.0099
Ph_3SnF	0.759	29202.1	2.21	9.704	29203.3	10.83	6.80	29225.0	24.30	0.0081
SnO	0.895	29200.1	4.73	10.796	29203.8	13.69	0.71	29215.4	7.66	0.0026
SnO_2	0.682	29203.4	5.18	14.65	29208.7	13.15	3.39	29224.6	13.16	0.0099

Table S5.8│ Fit parameters to the cw-EPR spectra of samples of **1** and **3** diluted in a polycrystalline sample of **7** in a 1:20 (Mn:Zn) ratio.

Compound	Temperature (K)	g_{iso}	D (cm^{-1})	A_{iso} (^{55}Mn, MHz)	A_{iso} (^{nat}Sn, MHz)
1	298	1.999(2)	0.230(1)	-	-
	10	1.999(2)	0.236(1)	-	-
3	298	1.9933(2)	0.0939(4)	164(2)	141(3)
	12	1.9933(3)	0.1015(6)	164(3)	-

Table S5.9│ Fit parameters to the variable-temperature, variable field magnetization data of **3**, **4**, **5**, **6**. Parameters for **4** were reported previously, but are displayed here for easier comparison.

Compound	D (cm^{-1})	E (cm^{-1})	g_{iso}
3	−0.2(1)	0	1.99(2)
4	12.9(3)	3.3(2)	2.14(1)
5	11.9(1)	0.7(1)	2.28(2)
6	−3.0(2)	0	2.28(2)

Table S5.10 | Fit parameters to the ^{119}Sn synchrotron Mössbauer spectra of polycrystalline samples of **4** – **7** at various temperatures.

Compound		Temperature			
		10 K	40 K	60 K	80 K
4	ΔE_Q (mm s^{-1})	1.215(2)	1.197(2)	1.198(2)	1.182(3)
	(χ^2)	2.79	1.95	2.08	2.72
5	ΔE_Q (mm s^{-1})	1.17(1)	1.221(4)	1.198(4)	-
	(χ^2)	3.83	2.56	2.11	-
6	ΔE_Q (mm s^{-1})	1.134(2)	1.130(3)	1.134(2)	1.123(5)
	(χ^2)	2.47	2.71	1.99	1.97
7	ΔE_Q (mm s^{-1})	0.904(3)	0.899(2)	0.896(2)	0.882(3)
	(χ^2)	5.72	2.46	2.58	1.31

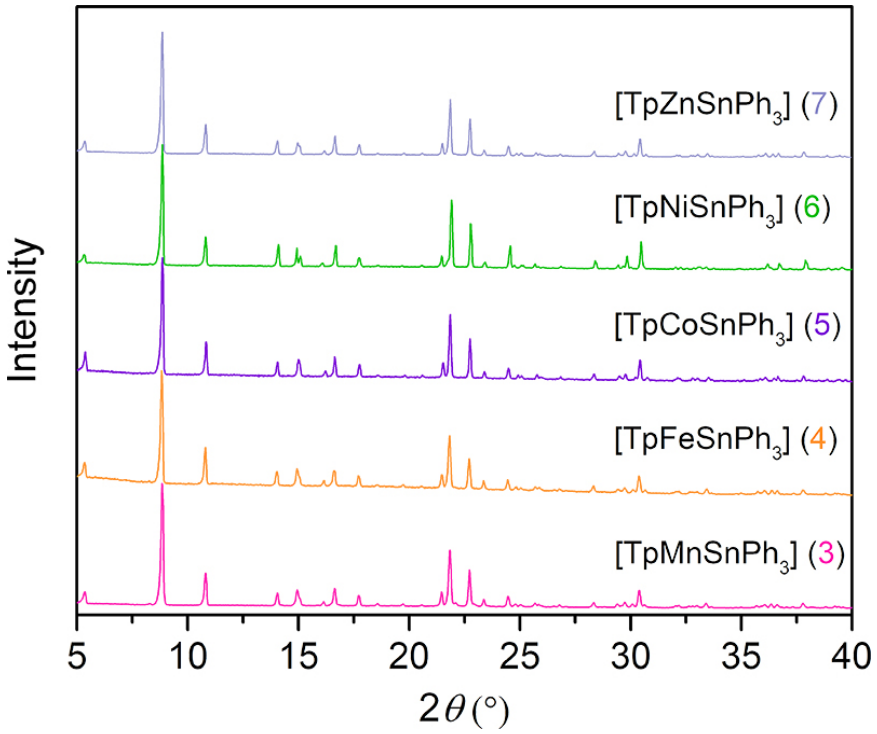

Figure S5.3 | Overlay of PXRD patterns for **3** – **7** collected at room temperature under N_2.

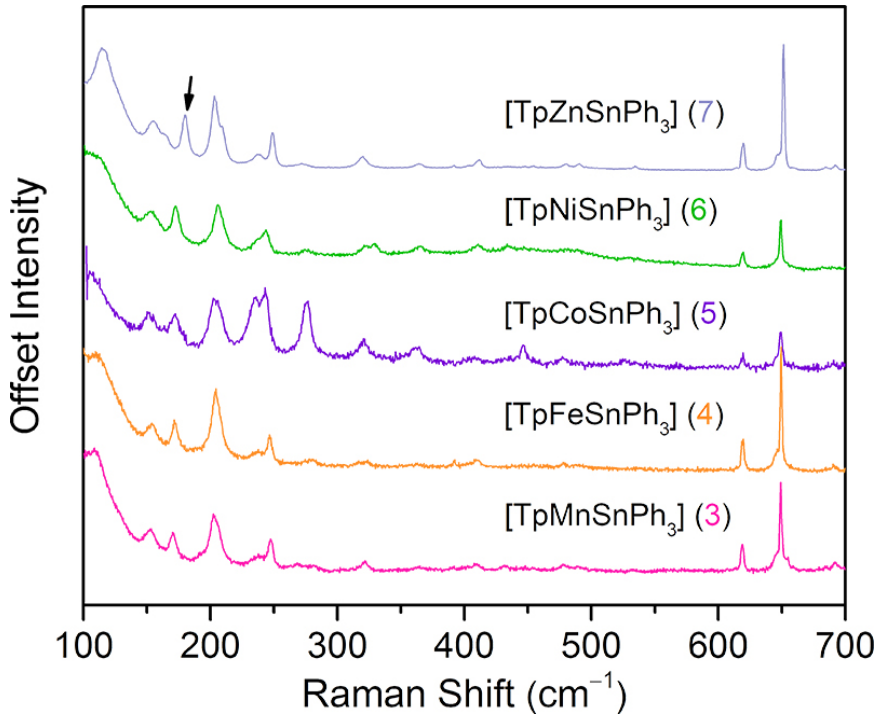

Figure S5.2 | Overlay of Raman spectra for **3** – **7** collected at room temperature under N_2. The black arrow highlights the TM-Sn bond stretching frequency.

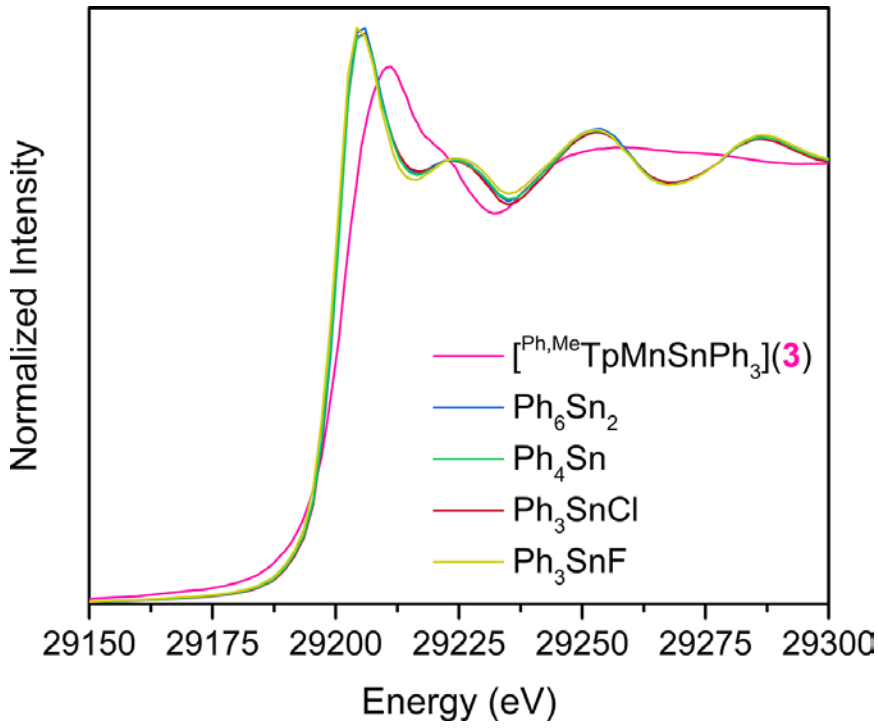

Figure S5.3 | Overlay of XANES spectra at the Sn K-edge for powder samples of Ph_6Sn_2, Ph_4Sn, Ph_3SnCl, and Ph_3SnF, shown with the spectrum of **3** for reference, measured at 25 K.

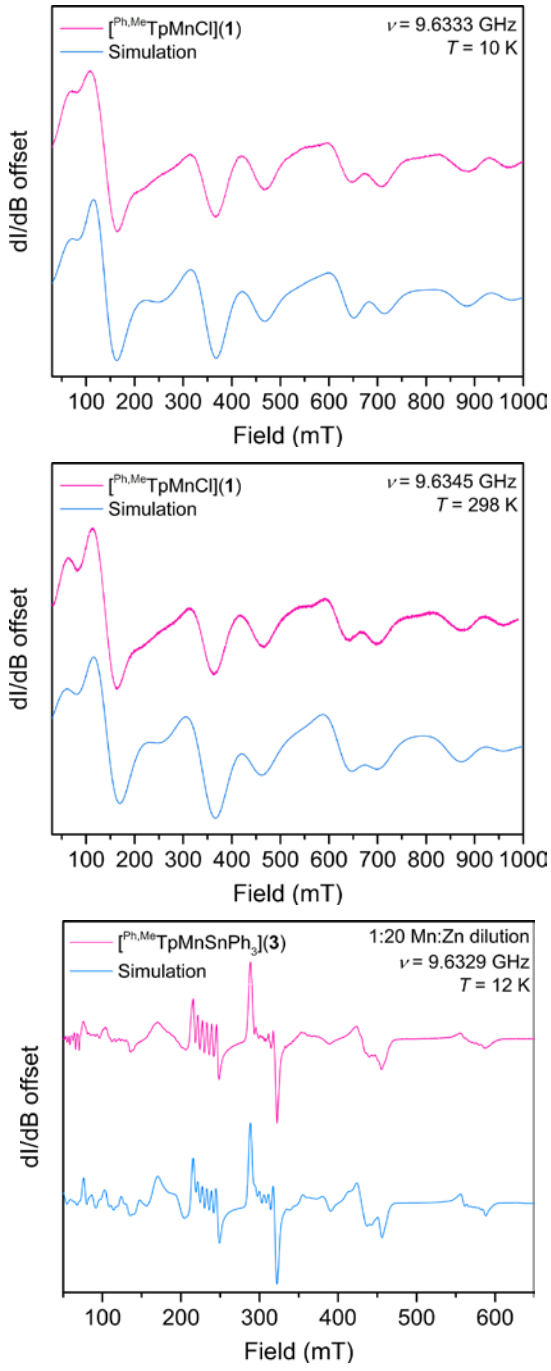

Figure S5.4 | X-band cw-EPR spectrum of [^{Ph,Me}TpMnCl](**1**) (top and middle) and **3** (bottom) diluted in a polycrystalline sample of **7** in a 1:20 (Mn:Zn) ratio encased in eicosane. Simulations of the data were obtained from fits using Easyspin with the spin Hamiltonian, $\hat{H} = g_{iso}\mu_B SH + AIS + D[\hat{S}_z^2 - {}^1/_3 S(S+1)]$. Parameters for the simulation are given in Table S5.8.

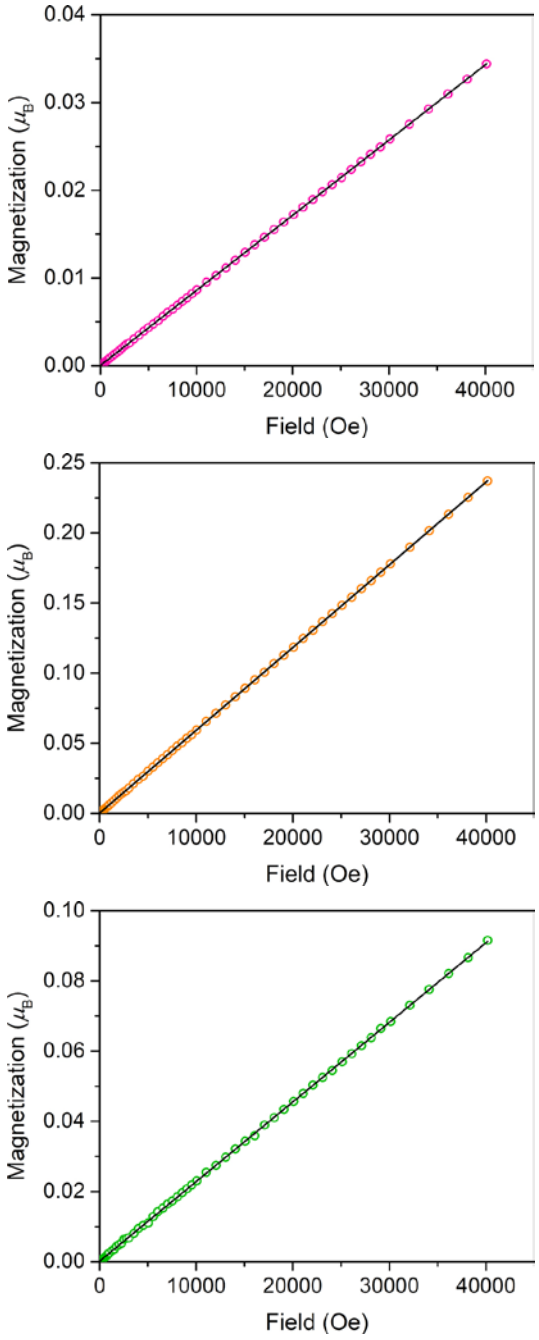

Figure S5.5 | Variable-field magnetization of polycrystalline samples of **3** (top), **4** (middle), **6** (bottom) restrained under eicosane acquired at 100 K. The black line is a linear fit to the data illustrating the absence of ferromagnetic impurities.

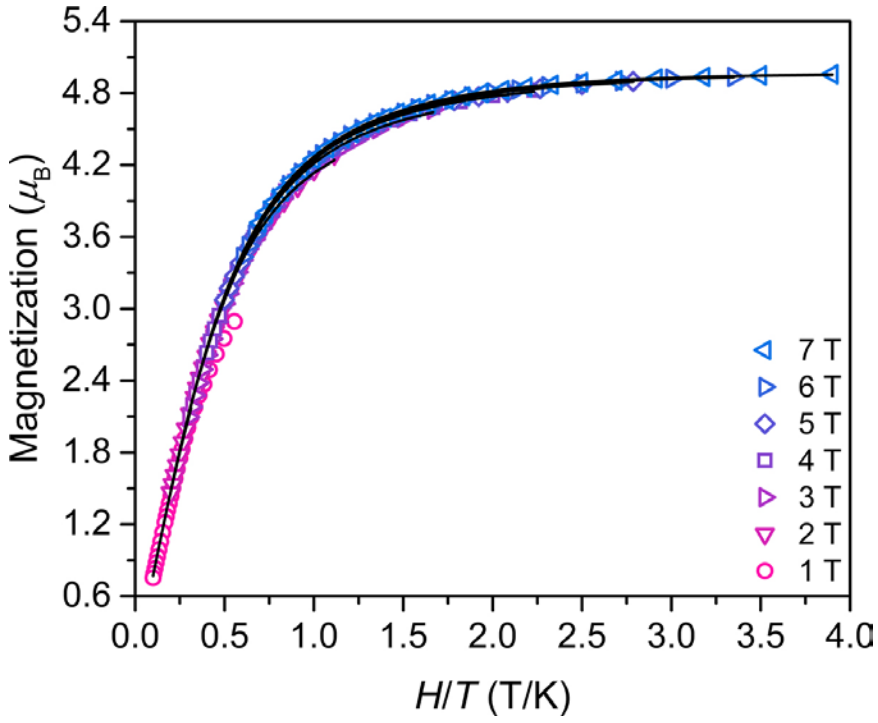

Figure S5.6 | Variable-temperature, variable-field magnetization data for **3** collected between 1.8 and 10 K from 1 to 7 T in 1 T increments. Black lines are simulations of the data obtained from fits using DAVE 2.0 and the spin Hamiltonian, $\hat{H} = g_{iso}\mu_B SH + D[\hat{S}_z^2 - {}^1/_3 S(S + 1)]$. The parameters for the simulation are given in Table S9.

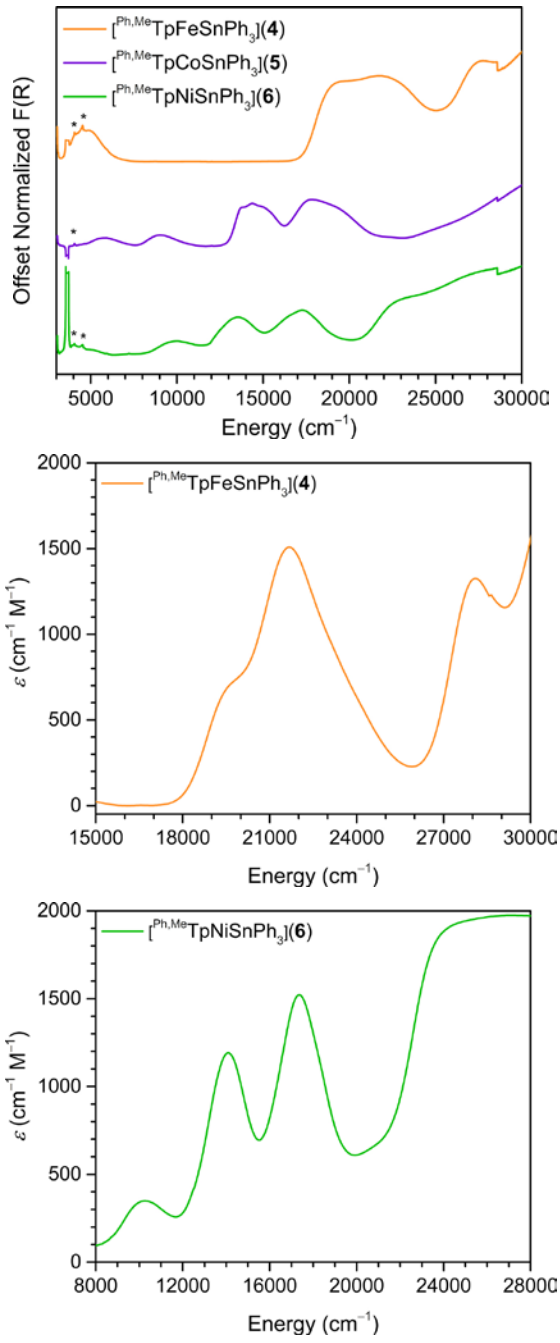

Figure S5.7 | Electronic absorption spectra of **4** – **6** measured at room temperature; the spectrum of **5** was reported previously but is shown here for easy comparison. The top is the solid-state diffuse reflectance measured over KBr, the middle and bottom are the solution phase spectra of **4** and **6**, respectively, measured in C_6D_6. (*) denotes vibrational bands from ligand backbone.

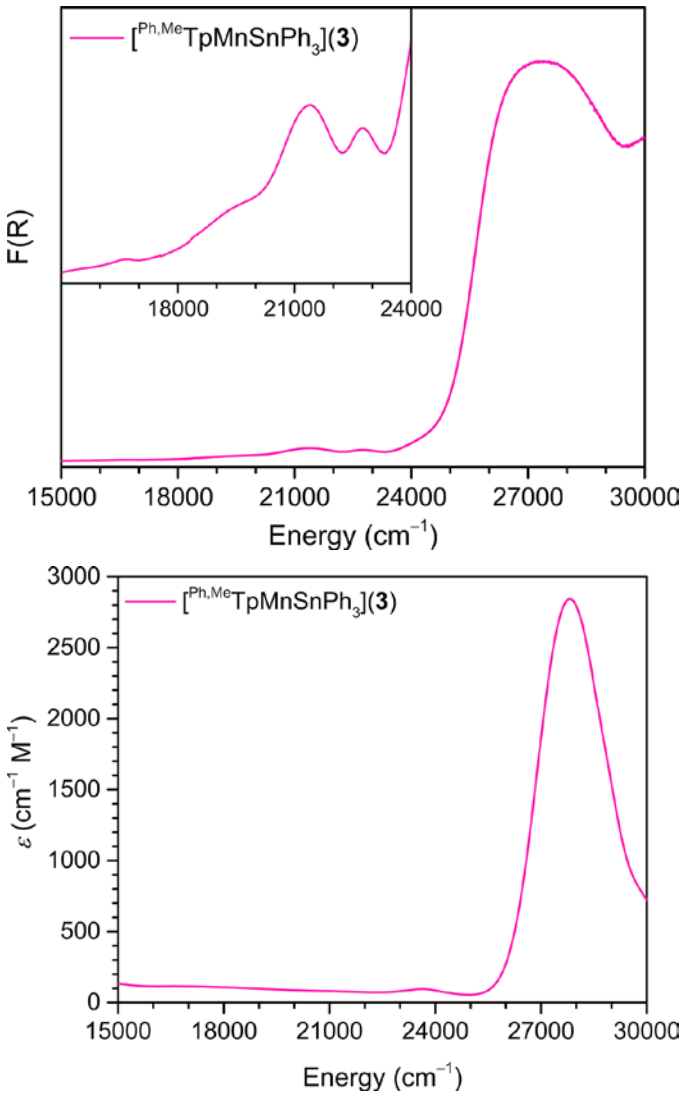

Figure S5.8 | Electronic absorption spectra of **3** measured at room temperature. The top is the solid-state diffuse reflectance measured over KBr with an inset of the spectra zoomed in for easier visualization of the spin-forbidden transitions. The bottom is the solution phase spectrum measured in C_6D_6; the peak at ~23,600 cm^{-1} is an artifact from background subtraction.

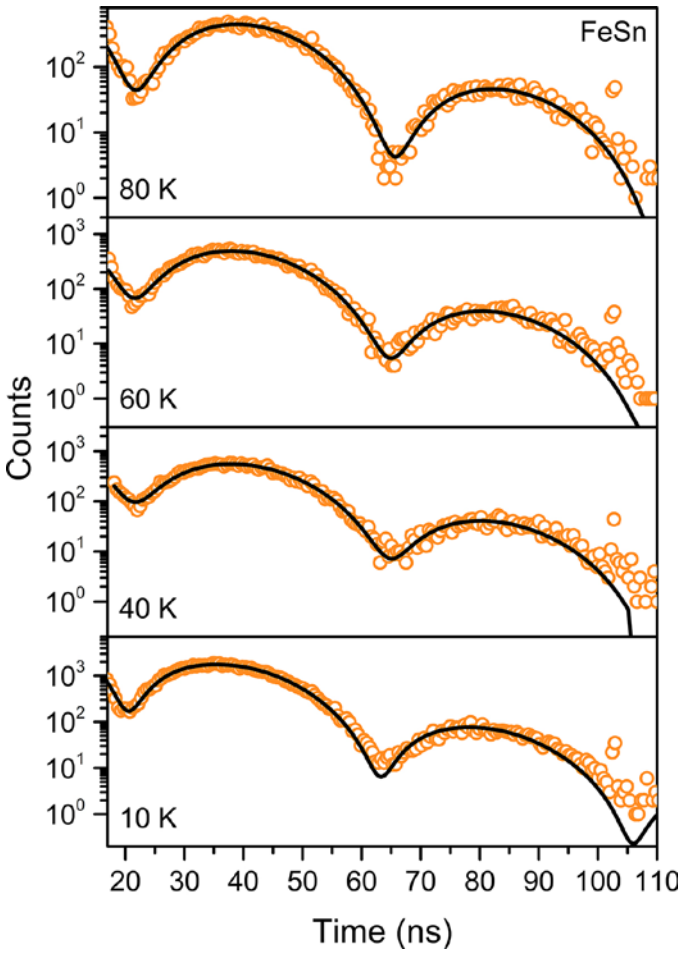

Figure S5.9 | Variable-temperature ^{119}Sn synchrotron Mossbauer spectra for **4** from 10 to 80 K. Parameters for the fits are given in table S5.10.

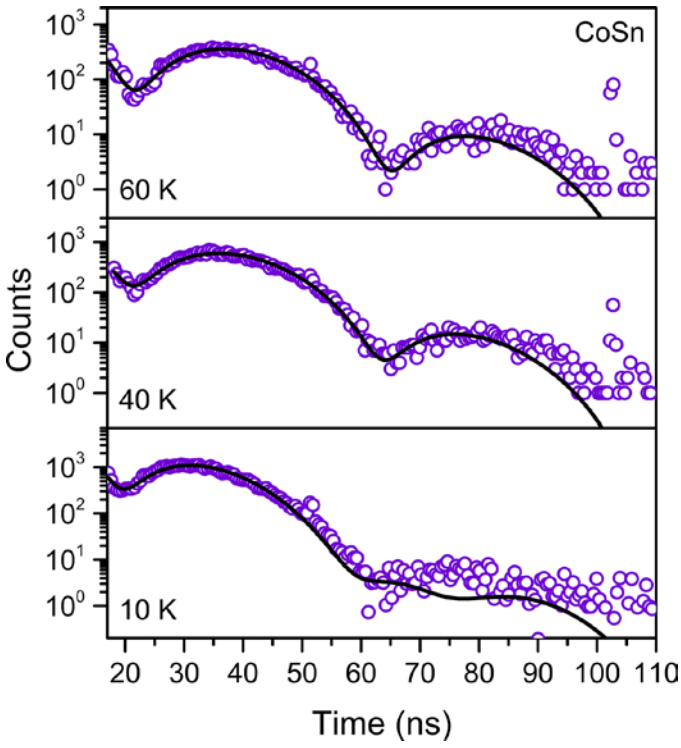

Figure S5.10 | Variable-temperature ^{119}Sn synchrotron Mossbauer spectra for **5** from 10 to 60 K. Parameters for the fits are given in table S5.10.

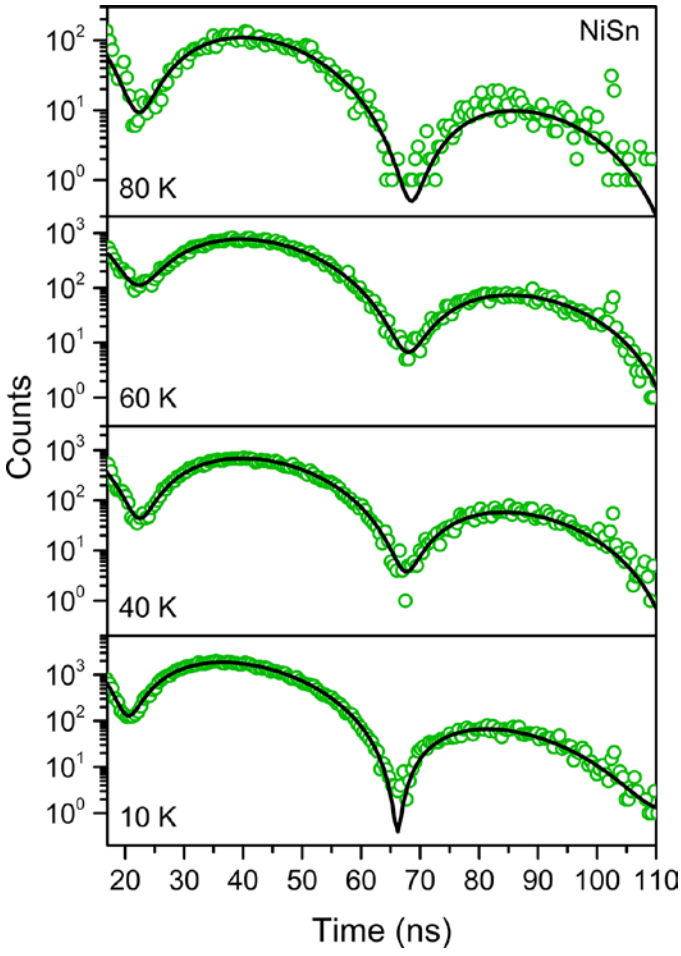

Figure S5.11 | Variable-temperature ^{119}Sn synchrotron Mossbauer spectra for **6** from 10 to 80 K. Parameters for the fits are given in table S5.10.

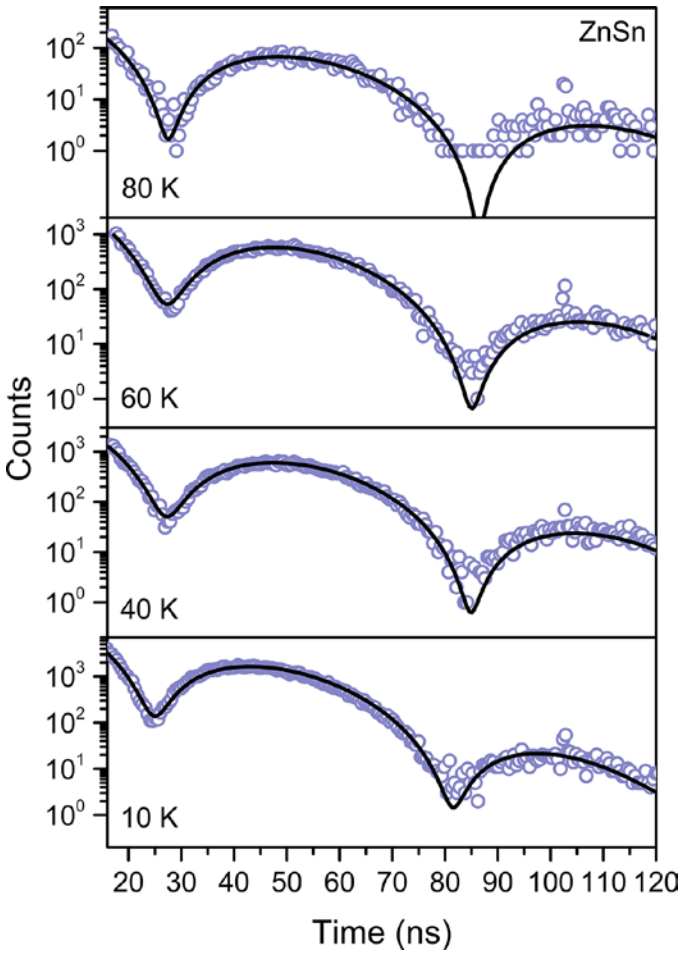

Figure S5.12 | Variable-temperature ^{119}Sn synchrotron Mossbauer spectra for **7** from 10 to 80 K. Parameters for the fits are given in table S5.10.

References

References for Chapter One

(1) Moulder, J. F.; Stickle, W. F.; Sobol, P. E.; Bomben, K. D. *Handbook of Photoelectron Spectroscopy*; Perkin-Elmer Corporation: Eden Prairie, Mn, 1992.

(2) Toro Iniesta, J. C. On the Discovery of the Zeeman Effect on the Sun and in the Laboratory. *Vistas Astron.* **1996**, 40, 241−256.

(3) Zeeman, P. The Effect of Magnetization on the Nature of Light Emitted by a Substance. *Nature* **1897**, 55, 347.

(4) Kong, D.; Cui, Y. Opportunities in Chemistry and Materials Science for Topological Insulators and their Nanostructures. *Nat. Chem.* **2011**, 3, 845−849.

(5) Müchler, L.; Zhang, H.; Chadov, S.; Yan, B.; Casper, F.; Kübler, J.; Zhang, S.-C.; Felser, C. Topological Insulators from a Chemist's Perspective. *Angew. Chem. Int. Ed.* **2012**, 51, 7221−7225.

(6) Cava, R. J.; Ji, H.; Fuccillo, M. K.; Gibson, Q. D.; Hor, Y. S. Crystal Structure and Chemistry of Topological Insulators. *J. Mater. Chem. C* **2013**, 1, 3176−3189.

(7) Gatteschi, D.; Kahn, O.; Miller, J. S.; Palacio, F. *Magnetic Molecular Materials*; Springer Science & Business Media, 2012; Vol. 198.

(8) Kahn, O. *Molecular Magnetism*; VCH: Weinheim, Germany, 1993.

(9) Marian, C. M. Spin-Orbit Coupling and Intersystem Crossing in Molecules. *WIREs Comput. Mol. Sci.* **2012**, 2, 187−203.

(10) Tao, Y.; Yuan, K.; Chen, T.; Xu, P.; Li, H.; Chen, R.; Zheng, C.; Zhang, L.; Huang, W. Thermally Activated Delayed Fluorescence Materials towards the Breakthrough of Organoelectronics. *Adv. Mater.* **2014**, 26, 7931–7958.

(11) Yersin, H.; Rausch, A. F.; Czerwieniec, R.; Hofbeck, T.; Fischer, T. The Triplet State of Organo-Transition Metal Compounds. Triplet Harvesting and Singlet Harvesting for Efficient OLEDs. *Coord. Chem. Rev.* **2011**, 255, 2622–2652.

(12) Eaton, S. S.; Eaton, G. R. In *Biological Magnetic Resonance*; Berliner, L. J., Eaton, S. S., Eaton, G. R., Eds.; Klewer Academic/Plenum Publishers: New York, 2000; Vol. 19, Distance Measurments in Biological Systems by EPR, pp 29−154.

(13) Danovich, D.; Shaik, S. Spin- Orbit Coupling in the Oxidative Activation of H- H by FeO^+. Selection Rules and Reactivity Effects. *J. Am. Chem. Soc.* **1997**, 119, 1773–1786.

(14) Schröder, D.; Shaik, S.; Schwarz, H. Two-State Reactivity as a New Concept in Organometallic Chemistry. *Acc. Chem. Res.* **2000**, 33, 139–145.

(15) Poli, R.; Harvey, J. N. Spin Forbidden Chemical Reactions of Transition Metal Compounds. New Ideas and New Computational Challenges. *Chem. Soc. Rev.* **2003**, 32, 1–8.

(16) Sun, Y.; Tang, H.; Chen, K.; Hu, L.; Yao, J.; Shaik, S.; Chen, H. Two-state Reactivity in Low-Valent Iron-Mediated C-H Activation and the Implications for Other First-Row Transition metals. *J. Am. Chem. Soc.* **2016**, 138, 3715−3730.

(17) Bellows, S. M.; Cundari, T. R.; Holland, P. L. Spin-Crossover During □-Hydride Elimination in High-Spin Fe(II)- and Co(II)-Alkyl Complexes. *Organometallics*, **2013**, 32, 4741−4751.

(18) Bunting, P. C.; Atanasov, M.; Damgaard-Møller, E.; Perfetti, M.; Crassee, I.; Orlita, M.; Overgaard, J.; van Slageren, J.; Neese, F.; Long, J. R. A Linear Cobalt(II) Complex with Maximal Orbital Angular Momentum from a Non-Aufbau Ground State. *Science* **2018**, 362, eaat7319.

(19) Guo, F.-S.; Day, B. M; Chen, Y.-C.; Tong, M.-L.; Mansikkamäki, A.; Layfield, R. A. Magnetic Hysteresis Up to 80 Kelvin in a Dysprosium Metallocene Single-Molecule Magnet. *Science* **2018**, 362, 1400−1403.

(20) Thiele, S.; Balestro, F.; Ballou, R.; Klyatskaya, S.; Ruben, M.; Wernsdorfer, W. Electrically Driven Nuclear Spin Resonance in Single-Molecule Magnets. *Science* **2014**, 344, 1135−1138.

(21) Pyykkö, P. Relativistic Effects in Chemistry: More Common Than You Thought. *Annu. Rev. Phys. Chem.* **2012**, 63, 45−64.

(22) Pyykkö, P. The Physics Behind Chemistry and the Periodic Table. *Chem. Rev.* **2012**, 112, 371−384.

(23) Kasha, M. Collisional Perturbation of Spin-Orbital Coupling and the Mechanism of Fluorescence Quenching. A Visual Demonstration of the Perturbation. *J. Chem. Phys.* **1952**, 20, 71−74.

(24) Koziar, J. C.; Cowan, D. O. Photochemical Heavy-Atom Effects. *Acc. Chem. Res.* **1978**, 11, 334−341.

(25) Klemmer, T.; Hoydick, D.; Okumura, H.; Zhang, B.; Soffa, W. Magnetic Hardening and Coercivity Mechanisms in L10 Ordered FePd Ferromagnets. *Scr. Metall. Mater.* **1995**, 33, 1793–1805.

(26) Gutfleisch, O.; Lyubina, J.; Müller, K.-H.; Schultz, L. FePt Hard Magnets. *Adv. Eng. Mater.* **2005**, 7, 208– 212.

(27) Adams, E.; Hubbard, W. M.; Syeles, A. M. A New Permanent Magnet from Powdered Manganese Bismuthide. *J. Appl. Phys.* **1952**, 23, 1207– 1211.

(28) Yang, Y.; Chen, X.; Guo, S.; Yan, A.; Huang, Q.; Wu, M.; Chen, D.; Yang, Y.; Yang, J. Temperature Dependences of Structure and Coercivity for Melt-Spun MnBi Compound. *J. Magn. Magn. Mater.* **2013**, 330, 106–110.

(29) Abragam, A.; Bleaney, B. *Electron Paramagnetic Resonance of Transition Ions*; Clarendon Press: Oxford, 1970.

(30) Duboc, C. Determination and Prediction of the Magnetic Anisotropy of Mn Ions. *Chem. Soc. Rev.* **2016**, 45, 5834–5847.

(31) Zein, S.; Duboc, C.; Lubitz, W.; Neese, F. A Systematic Density Functional Study of the Zero-Field Splitting in Mn(II) Coordination Compounds. *Inorg. Chem.* **2008**, 47, 134–142.

(32) Duboc, C.; Phoeung, T.; Zein, S.; Pécaut, J.; Collomb, M.-N.; Neese, F. Origin of the Zero-Field Splitting in Mononuclear Octahedral Dihalide Mn(II) Complexes: An Investigation by Multifrequency High-Field Electron Paramagnetic Resonance and Density Functional Theory. *Inorg. Chem.* **2007**, 46, 4905–4916.

(33) Brackett, G. C.; Richards, P. L.; Caughey, W. S. Far-infrared Magnetic Fe(III) and Mn(III) Porphyrins, Myoglobin, Hemoglobin, Ferrichrome A, and Fe(III) Dithiocarbamates. *J. Chem. Phys*. **1971**, 54, 4383–4401.

(34) Stavretis, S. E.; Atanasov, M.; Podlesnyak, A. A.; Hunter, S. C.; Neese, F.; Xue, Z.-L. Magnetic Transitions in Iron Porphyrin Halides by Inelastic Neutron Scattering and Ab Initio Studies of Zero-Field Splittings. *Inorg. Chem.* **2015**, 54, 9790–9801.

(35) Craig, G. A.; Murrie, M. 3d Single-Ion Magnets. *Chem. Soc. Rev.* **2015**, 44, 2135–2147.

(36) Zadrozny, J. M.; Telser, J.; Long, J. R. Slow Magnetic Relaxation in the Tetrahedral Cobalt (II) Complexes $[Co(EPh)_4]^{2-}$ (E = O, S, Se). *Polyhedron* **2013**, 64, 209–217.

(37) Suturina, E. A.; Maganas, D.; Bill, E.; Atanasov, M.; Neese, F. Magneto-Structural Correlations in a Series of Pseudotetrahedral $[Co^{II}(XR)_4]^{2-}$ Single Molecule Magnets: An ab Initio Ligand Field Study. *Inorg. Chem.* **2015**, 54, 9948–9961.

(38) Collingwood, J. C.; Day, P.; Denning, R. G. Magnetic Circular Dichroism Spectrum of the Tetraiodonickelate(II) Ion. *J. Chem. Soc., Faraday Trans. 2* **1973**, 591–607.

(39) Atanasov, M.; Rauzy, C.; Baettig, P.; Daul, C. Calculation of Spin-Orbit Coupling within the LFDFT: Applications to $[NiX_4]^{2-}$ ($X = F^-, Cl^-, Br^-, I^-$). *Int. J. Quantum Chem.* **2005**, 102, 119–131.

(40) Krzystek, J.; Ozarowski, A.; Telser, J. Multi-Frequency, High-Field EPR as a Powerful Tool to Accurately Determine Zero-Field Splitting in High-Spin Transition Metal Coordination Complexes. *Coord. Chem. Rev.* **2006**, 250, 2308–2324.

(41) Desrochers, P. J.; Telser, J.; Zvyagin, S. A.; Ozarowski, A.; Krzystek, J.; Vicic, D. A. Electronic Structure of Four-Coordinate C_{3v} Nickel(II) Scorpionate Complexes: Investigation by High-Frequency and -Field Electron Paramagnetic Resonance and Electronic Absorption Spectroscopies. *Inorg. Chem.* **2006**, 45, 8930–8941.

(42) Ye, S.; Neese, F. How Do Heavier Halide Ligands Affect the Signs and Magnitudes of the Zero-Field Splittings in Halogenonickel(II) Scorpionate Complexes? A Theoretical Investigation Coupled to Ligand-Field Analysis. *J. Chem. Theory Comput.* **2012**, 8, 2344–2351.

(43) Karunadasa, H. I.; Arquero, K. D.; Berben, L. A.; Long, J. R. Enhancing Magnetic Anisotropy of Cyano-Ligated Chromium(II) and Chromium(III) Complexes via Heavy Halide Ligand Effects. *Inorg. Chem.* **2010**, 49, 4738–4740.

(44) Smolko, L.; Černák, J.; Dušek, M.; Miklovič, J.; Titiš, J; Boča, R. Three Tetracoordinate Co(II) Complexes $[Co(biq)X_2]$ (X = Cl, Br, I) with easy-plane magnetic anisotropy as field-induced single-molecule magnets. *Dalton Trans*. **2015**, 44, 17565–17571.

(45) Brazzolotto, D.; Gennari, M.; Yu, S.; Pécaut, J.; Rouziéres, M.; Clérac, R.; Orio, M.; Duboc, C. An Experimental and Theoretical Investigation on Pentacoordinated Cobalt(III) Complexes with an Intermediate S = 1 Spin State: How Halide Ligands Affect their Magnetic Anisotropy. *Chem. Eur. J.* **2016**, 22, 925–933.

(46) Smolko, L.; Černák, J.; Kuchár, J.; Rajnák, C.; Titiš, J; Boča, R. Field-Induced Slow Magnetic Relaxation in Mononuclear Tetracoordinate Cobalt(II) Complexes Containing a Neocuproine Ligand. Eur. J. *Inorg. Chem.* **2017**, 2080–3086.

(47) Wang, L.; Zlatar, M.; Vlahović, F.; Demeschko, S.; Philouze, C.; Molton, F.; Gennari, M.; Meyer, F.; Duboc, C.; Gruden, M. Experimental and Theoretical Identification of the Origin of Magnetic Anisotropy in Intermediate Spin Fe(III) Complexes. *Chem. Eur. J.* **2018**, 24, 5091–5094.

(48) Saber, M. R.; Dunbar, K. M. Ligands Effects on the Magnetic Anisotropy of Tetrahedral Cobalt Complexes. *Chem. Commun.* **2014**, 50, 12266–12269.

(49) Christian, J. H.; Brogden, D. W.; Bindra, J. K.; Kinyon, J. S.; van Tol, J.; Wang, J.; Berry, J. F.; Dalal, N. S. Enhancing the Magnetic Anisotropy of Linear Cr(II) Chain Compounds Using Heavy Metal Substitutions. *Inorg. Chem.* **2016**, 55, 6376–6383.

(50) Power, P. P. Main-Group Elements as Transition Metals. *Nature* **2010**, 463, 171–177.

(51) Pearson, T. J.; Fataftah, M. S.; Freedman, D. E. Enhancement of Magnetic Anisotropy in a Mn–Bi Heterobimetallic Complex. *Chem. Commun.* **2016**, 52, 11394–11397.

(52) Azarkh, M.; Penkova, L. V.; Kats, S. V.; Varzatskii, O. A.; Voloshin, Y. Z.; Groenen, E. J. A Mononuclear Mn (II) Pseudoclathrochelate Complex Studied by Multi-Frequency Electron-Paramagnetic-Resonance Spectroscopy. *J. Phys. Chem. Lett.* **2014**, 5, 886–889.

(53) Sunatsuki, Y.; Kishima, Y.; Kobayashi, T.; Yamaguchi, T.; Suzuki, T.; Kojima, M.; Krzystek, J.; Sundberg, M. R. A Single Tripodal Ligand Stabilizing Three Different Oxidation States (II, III, and IV) of Manganese. *Chem. Commun.* **2011**, 47, 9149–9151.

(54) Pichon, C.; Mialane, P.; Rivière, E.; Blain, G.; Dolbecq, A.; Marrot, J.; Sécheresse, F.; Duboc, C. The Highest D Value for a MnII Ion: Investigation of a Manganese(II) Polyoxometalate Complex by High-Field Electron Paramagnetic Resonance. *Inorg. Chem.* **2007**, 46, 7710–7712.

(55) Lomont, J. P.; Nguyen, S. C.; Harris, C. B. Ultrafast Studies of Stannane Activation by Triplet Organometallic Photoproducts. *Organometallics* **2012**, 31, 3947–3957.

(56) Lomont, J. P.; Nguyen, S. C.; Harris, C. B. Should External Heavy-Atom Effects be Expected in Transition Metal Complexes? *ChemRxiv* **2018**, DOI: 10.26434/chemrxiv.6987605.

(57) Churchill, M. R.; Fettinger, J. C.; Whitmire, K. H.; Lagrone, C. B. X-ray Structural Characterization of [Et4N]3[BiFe4(CO)16]. *J. Organomet. Chem.* **1986**, 303, 99–109.

(58) Whitmire, K. H.; Lagrone, C. B.; Churchill, M. R.; Fettinger, J. C.; Biondi, L. V. Synthesis and Characterization of an Iron Carbonyl Cluster Containing Bismuth: Crystal and Molecular Structure of Tetraethylammonium (μ_3-Bismuthido)nonacarbonyl(μ_3-carbonyl)-*triangulo*-triferrate(1−), [Et_4N][(μ_3-Bi)$Fe_3(CO)_9$(μ_3-CO)], a Closo Cluster of the First Transition Series with a Large Heteroatom. *Inorg. Chem.* **1984**, 23, 4227–4232.

(59) Petz, W. Transition-Metal Complexes with Derivatives of Divalent Silicon, Germanium, Tin, and Lead as Ligands. *Chem. Rev*. **1986**, 86, 1019–1047.

(60) Lappert, M. F.; Rowe, R. S.; The Role of Group 14 Element Carbene Analogues in Transition Metal Chemistry. *Coord. Chem. Rev.* **1990**, 100, 267–292.

(61) Fischer, R. A. Weiß, J. Coordination Chemistry of Aluminum, Gallium, and Indium at Transition Metals. *Angew. Chem., Int. Ed.* **1999**, 38, 2830–2850.

(62) Braunschweig, H.; Cogswell, P.; Schwab, K. Synthesis, Structure, and Reactivity of Complexes Containing a Transition Metal-Bismuth Bond. *Coord. Chem. Rev.* **2011**, 255, 101–117.

(63) Whitmire, K. H. The Interface of Main Group and Transition Metal Cluster Chemistry. *J. Coord. Chem.* **1988**, 17, 95–204.

(64) Whitmire, K. H. Main Group-Transition Metal Cluster Compounds of the Group 15 Elements. Adv. Inorg. Chem. 1998, 42, 1–145.

(65) Martinengo, S.; Ciani, G. Bismuth-Cobalt Heteronuclear Carbonyl Cluster Compounds. Synthesis and X-ray Characterization of the Neutral $[BiCo_3(CO)_9]$ and of the Paramagnetic Anion $[Bi_2Co_4(CO)_{11}]^-$. *J. Chem. Soc., Chem. Commun.* **1987**, 1589–1591.

(66) Zouchoune, B.; Ogliaro, F.; Halet, J.-F.; Saillard, J.-Y.; Eveland, J. R.; Whitmire, K. H. Bonding Analysis in Inorganic Transition-Metal Cubic Clusters. 3. Metal-Centered Tetracapped $M_9(\mu_5\text{-}E)_4Ln_n$ Species with a Tetragonal Distortion. *Inorg. Chem.* **1998**, 37, 865–875.

References for Chapter Two

(1). L. Bogani, W. Wernsdorfer. *Nature Mater.* 2008, **7**, 179-1730.

(2). M. Mannini, F. Pineider, P. Sainctavit, C. Danieli, E. Otero, C. Sciancalepore, A. M. Talarico, M.-A. Arrio, A. Cornia, D. Gatteschi, R. Sessoli. *Nature Mater.* 2009, **8**, 194–197.

(3). D. Gatteschi, R. Sessoli. *Angew. Chem. Int. Ed.* 2003, **42**, 268-297.

(4). M. S. Fataftah, J. M. Zadrozny, D. M. Rogers, D. E. Freedman, *Inorg. Chem.* 2014, **53**, 10716.

(5). M. S. Fataftah, J. M. Zadrozny, S. C. Coste, M. J. Graham, D. M. Rogers, D. E. Freedman, *J. Am. Chem. Soc.* 2016, **138**, 1344.

(6). (a) K. R. Meihaus, J. R. Long, *Dalton Trans.*, 2015, **44**, 2517. (b) S. Ghosh, S. Datta, L. Friend, S. Cardona-Serra, A. Gaita-ariño, E. Coronado, S. Hill. *Dalton Trans.* 2012, **41**, 13697.

(7). (a) D. E. Freedman, W. H. Harman, T. D. Harris, G. J. Long, C. J. Chang, J. R. Long. *J. Am. Chem. Soc.* 2010, **132**, 1224. (b) W. H. Harman, T. D. Harris, D. E. Freedman, H. Fong, A. Chang, J. D. Rinehart, A. Ozarowski, M. T. Sougrati, F. Grandjean, G. J. Long, J. R. Long, C. J. Chang. *J. Am. Chem. Soc.* 2010, **132**, 18115. (c) D. Weismann, Y. Sun, Y. Lan, G. Wolmershauser, A. K. Powell, H. Sitzmann. *Chem.-Eur. J.* 2011, **17**, 4700. (d) J. M. Zadrozny, J. R. Long. *J. Am. Chem. Soc.* 2011, **133**, 20732. (e) S. Mossin, B. L. Tran, D. Adhikari, M. Pink, F. W. Heinemann, J. Sutter, R. K. Szilagyi, K. Meyer, D. J. Mindiola. *J. Am. Chem. Soc.* 2012, **134**, 13651. (f) J. M. Zadrozny, M. Atanasov, A. M. Bryan, C.-Y. Lin, B. D. Rekken, P. P. Power, F. Neese, J. R. Long. *Chem. Sci.* 2013, **4**, 125. (g) J. M. Zadrozny, J. Telser, J. R. Long. *Polyhedron*, 2013, **64**, 209. (h) Y.-Y. Zhu, C. Cui, Y.-Q. Zhang, J.-H. Jia, X. Guo, C. Gao, K. Qian, S.-D. Jiang, B.-W. Wang, Z.-M. Wang, S. Gao, *Chem. Sci.* 2013, **4**, 1802. (i) J. Martínez-Lillo, T. F. Mastropietro, E. Lhotel, C. Paulsen, J. Cano, G. De Munno, J. Faus, F. Lloret, M. Julve, S. Nellutla, J. Kryzystek. *J. Am. Chem. Soc.* 2013, **135**, 13737. (j) K. E. R. Marriott, L. Bhaskaran, C. Wilson, M. Medarde, S. T. Ochsenbein, S. Hill, M. Murrie. *Chem. Sci.* 2015, **6**, 6823-6828. (k) A. K. Bar, C. Pichon, J.-P. Sutter, *Coord. Chem. Rev.*, 2016, **308**, 346-380. (l) S. Gómez-Coca, D. Aravena, R. Morales, E. Ruiz, *Coord. Chem. Rev.*, 2015, **289**, 379-392.

(8). D. Gatteschi, R. Sessoli, J. Villain. Molecular Nanomagnets; Oxford University Press: Oxford, 2006.

(9). J. M. Zadrozny, S. M. Greer, S. Hill, D. E. Freedman. *Chem. Sci*, 2016, **7**, 416.

(10). (a) J. M. Zadrozny, J. Telser, J. R. Long, *Polyhedron* 2013, **64**, 209-217. (b) K. Fukui, H. Ohya-Nishiguchi, N. Hirota, *Bull. Chem. Soc. Jpn.* 1991, **64**, 1205. (c) E. A. Suturina, D. Maganas,

E. Bill, M. Atanasov, F. Neese, *Inorg. Chem.* 2015, **54**, 9948-9961. (d) M. Idešicova, J. Titiš, J. Krzystek, R. Boča, *Inorg. Chem.* 2013, **52**, 9409-9417.

(11). (a) J. A. Mydosh, Spin Glasses; Taylor and Francis: London/Washington DC, 1993. (b) J. Hertz, K. A. Fischer, Spin Glasses; Cambridge University Press: New York, 1989.

(12). (a) J. R. Dorfman, C. P. Rao, R. H. Holm, *Inorg. Chem.* 1985, **24**, 453-453. (b) W. P. Chung, J. C. Dewan, M. Tuckerman, M. A. Walters, *Inorg. Chim. Acta*, 1999, **291**, 388-394. (c) P. C. Tellinghuisen, W. T. Robinson, C. J. Wilkins, *J. Chem. Soc. Dalton Trans.* 1985, **7**,1289-1293. (d) T.-A. Okamura, S. Takamizawa, N. Ueyama, A. Akamura, *Inorg. Chem.* 1998, **37**, 18-28.

(13). (a) D. Dai, H. Xiang, M.-H. Whangbo, *J. Comp. Chem.* 2008, **29**, 2187. (b) M.-H. Whangbo, E. E. Gordon, H. Xiang, H.-J. Koo, C. Lee, *Acc. Chem. Res.* 2015, **48**, 3080.

(14). R. T. Azuah, L. R. Kneller, Y. Qiu, P. L. W. Tregenna-Piggot, C. M. Brown, J. R. D. Copley, R. M. Dimeo, *J. Res. Natl. Inst. Stand. Technol.* 2009, **114**, 341-358.

(15). (a) S, Gómez-Coca, A. Urtizberea, E. Cremades, P. J. Alonso, A. Camón, E. Ruiz, F. Luis, *Nature Commun.* 2014, DOI:10.1038/ncomms5300. (b) J. Vallejo, A. Pasual-Álvarez, J. Cano, I. Castro, M. Julve, F. Lloret, J. Krzystek, G. De Munno, D. Armentano, W. Wernsdorfer, R. Ruiz-García, E. Pardo, *Angew. Chemie. Int. Ed.* 2013, **52**, 14075-14079. (c) I. Banerjee, A. Jana, S. Singh, J. Marek, E. del Barco, M. Ali, *Polyhedron* 2013, **66**, 162-166.

(16). (a) R. Boča, J. Miklovic, J. Titiš, *Inorg. Chem.* 2014, **53**, 2367. (b) J. Miklovic, D. Valigura, R. Boča, J. Titiš, *Dalton Trans.* 2015, **44** 12484. (c) M. Dolai, M. Ali, J. Titiš, R. Boča, *Dalton Trans.* 2015, **44**, 13242.

(17). (a) K. S. Cole, R. H. Cole. *J. Chem. Phys*. 1941, **9**, 341. (b) C. J. F. Bottcher. Theory of Electric Polarization. Elsiever: New York, 1952. (c) S. M. J. Aubin, Z. M. Sun, L. Pardi, J. Kryzystek, K. Folting, L. C. Brunel, A. L. Rheingold, G. Christou, D. N. Hendrickson. *Inorg. Chem.* 1999, **38**, 5329.

(18). J. Miklovic, D. Valigura, R. Boča, J. Titiš, *Dalton Trans.* 2015, **44** 12484.

(19). (a) K. R. Meihaus, J. R. Long. *J. Am. Chem. Soc.* 2013, **135**, 17952. (b) S. McHugh, M. P. Sarachik. *Mod. Phys. Lett. B* 2011, **25**, 1795. (c) M. Sarachik. Magnetic Avalanches in Molecular Magnets. In *Molecular Magnets: Physics and Applications*; J. Batolome, F. Luis, J. F. Fernandez, Eds.; Springer: New York, 2014.

(20). A. Abragam and B. Bleaney, *Electron Paramagnetic Resonance of Transition Metals*, Dover Publications, Inc., New York, 1986.

(21). (a) J. M. Zadrozny, D. J. Xiao, M. Atanasov, G. J. Long, F. Grandjean, F. Neese, J. R. Long. *Nature Chem.* 2013, **5**, 577. (b) V. V. Novikov, A. A. Pavlov, Y. V. Nelyubina, M.-E. Boulon, O. A.

Varzatskii,Y. Z. Voloshin, R. E. P. Winpenny, *J. Am. Chem. Soc.* 2015, **137**, 9792-9795. (c) Y. Rechkemmer, F. D. Breitgoff, M. van der Meer, M. Atanasov, M. Hakl, M. Orlita, P. Neugebauer, F. Neese, B. Sarkar, J. van Slageren, *Nature Commun.* 2016, DOI: 10.1038/ncomms10467. (d) Y.-Y. Zhu, C. Cui, Y.-Q. Zhang, J.-H. Jia, X. Gao, C. Gao, K. Qian, S.-D. Jiang, B.-W. Wang, Z.-M. Wang, S. Gao, *Chem. Sci*. 2013, **4**, 1802.

(22). (a) J. M. Zadrozny, D. J. Xiao, M. Atanasov, J. R. Long, M. Atanasov, F. Neese, F. Grandjean, G. J. Long, *Inorg. Chem.* 2013, **52**, 13123-13131. (b) M. Atanasov, J. M. Zadrozny, J. R. Long, F. Neese, *Chem. Sci.*, 2013, **4**, 139-156.

(23). (a) T. Fukuda, K. Matsumura, N. Ishikawa, *J. Phys. Chem. A.*, 2013, **117**, 10447-10454. (b) N. Ishikawa, M. Sugita, W. Wernsdorfer, *J. Am. Chem. Soc.*, 2005, **127**, 3650- 3651.

(24). (a) B. O. Roos, P. R. Taylor, P. E. M.Siegbahn, *Chem. Phys.* 1980, **48**, 157. (b) K. Andersson, P.-A. Malmqvist, B. Roos, A. J. Sadlej, K. Wolinski, *J. Phys. Chem.* 1990, **94**, 5483. (c) K. Andersson, P.-A. Malmqvist, B. O. Roos, *J. Chem. Phys.* 1992, **96**, 1218.

(25). F. Aquilante, L. De Vico, N. Ferre, G. Ghigo, P.-A. Malmqvist, P. Neograd*y*, T. B. Pedersen, M. Pitonak, M. Reiher, B. O. Roos, L. Serrano-Andres, M. Urban, V. Veryazov, R. Lindh, *J. Comput. Chem.* 2010, **31**, 224.

(26). S. Stoll, A. Schweiger, *J. Magn. Reson.* 2006, **178**, 42–55.

(27). B. Horvath, R. Möseler, and E. G. Horvath, *Z. Anorg. Allg. Chem.* 1979, **450**, 165.

(28). T. K. Hansen, J. Becher, T. Jorgensen, K. S. Varma, R. Khedekar, and M. P. Cava, *Org. Synth.* 1996, **73**, 270.

(29). M. S. Fataftah, J. M. Zadrozny, D. M. Rogers, D. E. Freedman, *Inorg. Chem.* 2014, **53**, 10716.

(30). A. E. Carpenter, G. W. Margulieux, M. D. Millard, C. E. Moore, N. weidemann, A. L. Rheingold, and J. S. Figueroa, *Angew. Chem. Int. Ed.* 2012, **51**, 9412–9416.

(31). D. Marcoux, and A. B. Charette, *J. Org. Chem.* 2008, **73**, 593.

(32). G. A. Bain, and J. F. Berry, *J. Chem. Educ.* 2008**, 85**, 532-536.

(33). *APEX2*, v. 2009 ; Bruker Analytical X-Ray Systems, Inc: Madison, WI, 2009.

(34). G. M. Sheldrick, *SADABS,* Version 2.03; Bruker Analytical X-ray Systems, Inc: Madison, WI, 2000.

(35). G. M. Sheldrick, *SHELXTL*, Version 6.12; Bruker Analytical X-ray Systems, Inc: Madison, WI, 2000.

(36). L. J. Farrugia, *J. Appl. Cryst.* 1999, **32**, 837-838.

(37). J. S. Hyde, B. Bennett, E. D. Walter, G. L. Millhauser, G. W. Sidabras and W. E. Antholine, *Biophys. J.* 2009, **96**, 3354-3362.

(38). B. O. Roos, P. R. Taylor, P. E. M. Siegbahn, *Chem. Phys.* 1980, **48**, 157.

(39). K. Andersson, P. Malmqvist, B. Roos, A. J. Sadlej, K. Wolinskit, *J. Phys. Chem.* 1990, **94**, 5483.

(40). K. Andersson, P.-A. Malmqvist, B. O. Roos, *J. Chem. Phys.* 1992, **96**, 1218.

(41). M. Douglas, N. M. Kroll, *Ann. Phys.* (N. Y). 1974, **82**, 89.

(42). B. A. Hess, *Phys. Rev. A* 1986, **33**, 3742.

(43). B. O. Roos, R. Lindh, P. Å. Malmqvist, V. Veryazov, P. O. Widmark, *J. Phys. Chem. A* 2004, **108**, 2851.

(44). B. O. Roos, R. Lindh, P. Å. Malmqvist, V. Veryazov, P. O. Widmark, *J. Phys. Chem. A* 2005, **109**, 6575.

(45). F. Aquilante,; L. De Vico, N. Ferre, G. Ghigo, P.-A. Malmqvist, P. Neogrady, T. B. Pedersen, M. Pitonak, M. Reiher, B. O. Roos, L. Serrano-Andrés, M. Urban, V. Veryazov, R. Lindh, *J. Comput. Chem.* 2010, **31**, 224.

(46). (a) Aquilante, F.; Pedersen, T. B.; Lindh, R. *J. Chem. Phys.* 2007, **126**, 194106. (b) Aquilante, F.; Lindh, R.; Pedersen, T. B. *J. Chem. Phys.* 2008, **129**, 034106. (c) Aquilante, F.; Malmqvist, P. Å.; Pedersen, T. B.; Ghosh, A.; Roos, B. O. *J. Chem. Theory Comput.* 2008, **4**, 694. (d) Aquilante, F.; Gagliardi, L.; Pedersen, T. B.; Lindh, R. *J. Chem. Phys.* 2009, **130**, 154107.

(47). Malmqvist, P.-A.; Roos, B. O.; Schimmelpfennig, B. *Chem. Phys. Lett.* 2002, **357**, 230−240.

(48). Aquilante, F.; De Vico, L.; Ferre, N.; Ghigo, G.; Malmqvist, P.-́ A.; Neogrady, P.; Pedersen, T. B.; Pitonak, M.; Reiher, M.; Roos, B.́ O.; Serrano-Andres, L.; Urban, M.; Veryazov, V.; Lindh, R.́ J. Comput. Chem. 2010 , 31, 224 −247.

(49). S. Stoll, J. Schweiger, *J. Magn. Reson.* 2006, **178**, 42-55.

(50). (a) E. Bertolomé, P. J. Alanso, A. B. Arauzo, J. Luzón, J. Bertolomé, C. Racles, C. Turta, *Dalton Trans.* 2012, **41**, 10382-10389. (b) S. Gómez-Coca, A. Urtizberea, E. Cremades, P. J. Alonso, A. Camón, E. Ruiz, F. Luis, *Nature Commun.* 2014, **5**, 4300: doi:10.1038/ncomms4300.

(51). J. H. van der Waals, Optical Properties of Excited States in Solids, The Study of Paramagnetic Excited States by Electron Paramagnetic Resonance; Springer US: NATO ASI series, 1992, 301.

References for Chapter Three

(1) *Magnetic Molecular Materials*; Gatteschi, D., Kahn, O., Miller, J. S., Palacio, F., Eds.; NATO ASI series E: Volume 198; Kluwer Academic Publishers: Dordrecht, The Netherlands, 1991.

(2) Kahn, O. *Molecular Magnetism*; VCH Publishers, Inc.: Weinheim, Germany, 1993.

(3) Danovich, D.; Shaik, S. Spin-Orbit Coupling in the Oxidative Activation of H–H by FeO^+. Selection Rules and Reactivity Effects. *J. Am. Chem. Soc.* **1997**, 119, 1773–1786.

(4) Schröder, D.; Shaik, S.; Schwarz, H. Two-State Reactivity as a New Concept in Organometallic Chemistry. *Acc. Chem. Res.* **2000**, 33, 139–145.

(5) Poli, R.; Harvey, J. N. Spin Forbidden Chemical Reactions of Transition Metal Compounds. New Ideas and Computation Challenges. *Chem. Soc. Rev.* **2003**, 32, 1–8.

(6) Harvey, J. N.; Poli, R.; Smith, K. M. Understanding the Reactivity of Transition Metal Complexes Involving Multiple Spin States. *Coord. Chem. Rev.* **2003**, 238, 347–361.

(7) Harvey, J. N. Spin-Forbidden Reactions: Computational Insight into Mechanisms and Kinetics. *WIREs Comput. Mol. Sci*. **2014**, 4, 1–14.

(8) Holland, P. L. Distinctive Reaction Pathways at Base Metals in High-Spin Organometallic Catalysis. *Acc. Chem. Res.* **2015**, 48, 1696–1702.

(9) Yersin, H.; Rausch, A. F.; Czerwieniec, R.; Hofbeck, T.; Fischer, T. The Triplet State of Organo-Transition Metal Compounds. Triplet Harvesting and Singlet Harvesting for Efficient OLEDs. *Coord. Chem. Rev.* **2011**, 255, 2622–2652.

(10) Marian, C. M. Spin-Orbit Coupling and Intersystem Crossing in Molecules. *WIREs Comput. Mol. Sci.* **2012**, 2, 187–203.

(11) Tao, Y.; Yuan, K.; Chen, T.; Xu, P.; Li, H.; Chen, R.; Zheng, C.; Zhang, L.; Huang, W. Thermally Activated Delayed Fluorescence Towards the Breakthrough of Organoelectronics. *Adv. Mater.* **2014**, 26, 7931–7958.

(12) Griffiths, D. J. *Introduction to Quantum Mechanics*, 2nd ed,.; Prentice-Hall: Upper Saddle River, NJ, 1995; Chapter 6.

(13) Craig, G. A.; Murrie, M. 3d Single-Ion Magnets. *Chem. Soc. Rev.* **2015**, 44, 2135–2147.

(14) Atanasov, M.; Aravena, D.; Suturina, E.; Bill, E.; Maganas, D.; Neese, F. First Principles Approach to the Electronic Structure, Magnetic Anisotropy and Spin Relaxation in Mononuclear 3d-Transition Metal Single Molecule Magnets. *Coord. Chem. Rev.* **2015**, 289, 177–214.

(15) Gómez-Coca, S.; Aravena, D.; Morales, R.; Ruiz, E. Large Magnetic Anisotropy in Mononuclear Metal Complexes. *Coord. Chem. Rev.* **2015**, 289, 379–392.

(16) Bar, A. K.; Pichon, C.; Sutter, J.-P. Magnetic Anisotropy in Two- and Eight-Coordinated Transition-Metal Complexes: Recent Developments in Molecular Magnetism. *Coord. Chem. Rev.* **2016**, 308, 346–380.

(17) Freedman, D. E.; Harman, W. H.; Harris, T. D.; Long, G. J.; Chang, C. J.; Long, J. R. Slow Magnetic Relaxation in a High-Spin Iron(II) Complex. *J. Am. Chem. Soc.* **2010**, 132, 1224–1225.

(18) Harman, W. H.; Harris, T. D.; Freedman, D. E.; Fong, H.; Chang, A.; Rinehart, J. D.; Ozarowski, A.; Sougrati, M. T.; Grandjean, F.; Long, G. J.; Long, J. R.; Chang, C. J. Slow Magnetic Relaxation in a Family of Trigonal Pyramidal Iron (II) Pyrrolide Complexes. *J. Am. Chem. Soc.* **2010**, 132, 18115–18126.

(19) Weismann, D.; Sun, Y.; Lan, Y.; Wolmershäuser, G.; Powell, A. K.; Sitzmann, H. High-Spin Cyclopentadienyl Complexes: A Single-Molecule Magnet Based on the Aryl-Iron(II) Cyclopentadienyl Type. *Chem. Eur. J.* **2011**, 17, 4700–4704.

(20) Zadrozny, J. M; Long, J. R. Slow Magnetic Relaxation at Zero Field in the Tetrahedral Complex $[Co(SPh)_4]^{2-}$. *J. Am. Chem. Soc.* **2011**, 133, 20732–20734.

(21) Zadrozny, J. M.; Xiao, D. J.; Atanasov, M.; Long, G. J.; Grandjean, F.; Neese, F.; Long, J. R. Magnetic Blocking in a Linear Iron(I) Complex. *Nature Chem.* **2013**, 5, 577–581.

(22) Zadrozny, J. M.; Atanasov, M.; Bryan, A. M.; Lin, C.-Y.; Rekken, B. D.; Power, P. P.; Neese, F.; Long, J. R. Slow Magnetization Dynamics in a Series of Two-Coordinate Iron(II) Complexes. *Chem. Sci.* **2013**, 4, 125–138.

(23) Zhu, Y.-Y.; Cui, C.; Zhang, Y.-Q.; Jia, J.-H.; Guo, X.; Gao, C.; Qian, K.; Jiang, S.-D.; Wang, B.-W.; Wang, Z.-M.; Gao, S. Zero-Field Slow Magnetic Relaxation from Single Co(II) Ion: A Transition Metal Single-Molecule Magnet with High Anisotropy Barrier. *Chem. Sci.* **2013**, 4, 1802–1806.

(24) Marriott, K. E. R.; Bhaskaran, L.; Wilson, C.; Medarde, M.; Ochsenbein, S. T.; Hill, S.; Murrie, M. Pushing the Limits of Magnetic Anisotropy in Trigonal Bipyramidal Ni(II). *Chem. Sci.* **2015**, 6, 6823–6828.

(25) Fataftah, M. S.; Zadrozny, J. M.; Rogers, D. M.; Freedman, D. E. A Mononuclear Transition Metal Single-Molecule Magnet in a Nuclear Spin-Free Ligand Environment. *Inorg. Chem.* **2014**, 53, 10716–10721.

(26) Mantel, C.; Baffert, C.; Romero, I.; Deronzier, A.; Pécaut, J.; Collomb, M.-N.; Duboc, C. Structural Characterization and Electronic Properties Determination by High-Field and High-Frequency EPR of a Series of Five-Coordinated Mn(II) Complexes. *Inorg. Chem.* **2004**, 43, 6455–6463.

(27) Desrochers, P. J.; Telser, J.; Zvyagin, S. A.; Ozarowski, A.; Krystek, J.; Vicic, D. A. Electronic Structure of Four-Coordinate C_{3v} Nickel(II) Scorpionate Complexes: Investigation by High-Frequency and –Field Electron Paramagnetic Resonance and Electronic Absorption Spectroscopies. *Inorg. Chem.* **2006**, 45, 8930–8941.

(28) Duboc, C.; Phoeung, T.; Zein, S.; Pécaut, J.; Collomb, M.-N.; Neese, F. Origin of the Zero-Field Splitting in Mononuclear Octahedral Dihalide Mn^{II} Complexes: An Investigation by Multifrequency High-Field Electron Paramagnetic Resonance and Density Functional Theory. *Inorg. Chem.* **2007**, 46, 4905–4916.

(29) Krzystek, J; Ozarowski, A.; Zvyagin, S. A.; Telser, J. High Spin Co(I): High-Frequency and –Field EPR Spectroscopy of $CoX(PPh_3)_3$ (X = Cl, Br). *Inorg. Chem.* **2012**, 51, 4954–4964.

(30) Kasha, M. Collisional Perturbation of Spin-Orbital Coupling and the Mechanism of Fluorescence Quenching. A Visual Demonstration of the Perturbation. *J. Chem. Phys.* **1952**, 20, 71–74.

(31) Koziar, J. C.; Cowan, D. O. Photochemical Heavy-Atom Effects. *Acc. Chem. Res.* **1978**, 11, 334–341.

(32) Saber, M. R.; Dunbar, K. R. Ligands Effects on the Magnetic Anisotropy of Tetrahedral Cobalt Complexes. *Chem. Commun.* **2014**, 50, 12266–12269.

(33) Zadrozny, J. M.; Telser, J.; Long, J. R. Slow Magnetic Relaxation in the Tetrahedral Cobalt(II) Complexes $[Co(EPh_4)]^{2-}$ (E = O, S, Se). *Polyhedron* **2013**, 64, 209–217.

(34) Suturina, E. A.; Maganas, D.; Bill, E.; Atanasov, M.; Neese, F. Magneto-Structural Correlations in a Series of Pseudotetrahedral $[Co^{II}(XR)_4]^{2-}$ Single Molecule Magnets: An ab Initio Ligand Field Study. *Inorg. Chem.* **2015**, 54, 9948–9961.

(35) Zein, S.; Duboc, C.; Lubitz, W.; Neese, F. A Systematic Density Functional Study of the Zero-Field Splitting in Mn(II) Coordination Compounds. *Inorg. Chem.* **2008**, 47, 134–142.

(36) Karunadasa, H. I.; Arquero, K. D.; Berben, L. A.; Long, J. R. Enhancing the Magnetic Anisotropy of Cyano-Ligated Chromium(II) and Chromium(III) Complexes via Heavy Halide Ligand Effects. *Inorg. Chem.* **2010**, 49, 4738–4740.

(37) Brazzolotto, D.; Gennari, M.; Yu, S.; Pécaut, J.; Rouziéres, M.; Clérac, R.; Orio, M.; Duboc, C. An Experimental and Theoretical Investigation on Pentacoordinated Cobalt(III) Complexes with an Intermediate S = 1 Spin State: How Halide Ligands Affect their Magnetic Anisotropy. *Chem. Eur. J.* **2016**, 22, 925–933.

(38) Ye, S.; Neese, F. How Do Heavier Halide Ligands Affect the Signs and Magnitudes of the Zero-Field Splittings in Halogenonickel(II) Scorpionate Complexes? A Theoretical Investigation Coupled to Ligand-Field Analysis. *J. Chem. Theory Comput.* **2012**, 8, 2344–2351.

(39) Power, P. P. Main-Group Elements as Transition Metals. *Nature* **2010**, 463, 171–177.

(40) Petz, W. Transition-Metal Complexes with Derivatives of Divalent Silicon, Germanium, Tin, and Lead as Ligands. *Chem. Rev.* **1986**, 86, 1019–1047.

(41) Lappert, M. F.; Rowe, R. S. The Role of Group 14 Element Carbene Analogues in Transition Metal Chemistry. *Coord. Chem. Rev.* **1990**, 100, 267–292.

(42) Weiß, J.; Fischer, R. A. Coordination Chemistry of Aluminum, Gallium, and Indium at Transition Metals. *Angew. Chem. Int. Ed.* **1999**, 38, 2830–2850.

(43) Braunschweig, H.; Cogswell, P.; Schwab, K. Synthesis, Structure, and Reactivity of Complexes Containing a Transition Metal–Bismuth Bond. *Coord. Chem. Rev.* **2011**, 255, 101–117.

(44) Rudd. P. A.; Liu, S.; Gagliardi, L.; Young, V. G.; Lu, C. C. Metal-Alane Adducts with Zero-Valent Nickel, Cobalt, and Iron. *J. Am. Chem. Soc.* **2011**, 133, 20724–20727.

(45) Cammarota, R. C.; Lu, C. C. Tuning Nickel with Lewis Acidic Group 13 Metalloligands for Catalytic Olefin Hydrogenation. *J. Am. Chem. Soc.* **2015**, 137, 12486–12489.

(46) Holt, M. S.; Wilson, W. L.; Nelson, J. H. Transition Metal–Tin Chemistry. *Chem. Rev.* **1989**, 89, 11–49.

(47) Hellmann, K. W.; Friedrich, S.; Lu, W.-S.; McPartlin, M.; Gade, L. H. Tripodal Triamidostannates as Building Blocks in the Generation of Sn–M Bonded Heterobimetallics (M = Fe, Ru). *Chem. Ber.* **1995**, 128, 29–34.

(48) Fjeldberg, T.; Hope, H.; Lappert, M. F.; Power, P. P.; Thorne, A. J. Molecular Structures of the Main Group 4 Metal(II) bis(trimethylsilyl)-amides $M[N(SiMe_3)_2]_2$ in the Crystal (X-ray) and Vapour (Gas-Phase Electron Diffraction). *J. Chem. Soc. Chem. Commun.* **1983**, 639–641.

(49) Chorley, R. W.; Hitchcock, P. B.; Power, P. P.; Olmstead, M. M.; Lappert, M. F.; Leung, W.-P. Subvalent Group 14 Metal Compounds XIV*. The X-ray Crystal Structures and Two Monomeric Group 14 Metal Bisamides, $Ge[N(SiMe_3)_2]_2$ and $Sn[NC(Me_2)(CH_2)_3CMe_2]_2$. *Inorg. Chim. Acta.* **1992**, 198, 203–209.

(50) Cordero, B.; Gómez, V.; Platero-Prats, A. E.; Revés, M.; Echeverría, J.; Cremades, E.; Barragán, F.; Alvarez, S. Covalent Radii Revisited. *Dalton Trans.* **2008**, 2832–2838.

(51) Inoue, S.; Driess, M. Isolable Metallo-Germylene and Metallo-Stannylene σ-Complexes with Iron. *Organometallics* **2009**, 28, 5032–5035.

(52) Lei, H; Guo, J.-D.; Fettinger, J. C; Nagase, S.; Power, P. P. Synthesis, Characterization, and CO Elimination of Ferrio-Substituted Two-Coordinate Germylenes and Stannylenes. *Organometallics* **2011**, 30, 6316–6322.

(53) Mankad, N. P.; Whited, M. T.; Peters, J. C. Terminal Fe^{I}–N_2 and Fe^{II}---H–C Interactions Supported by Tris(phosphino)silyl Ligands. *Angew. Chem. Int. Ed.* **2007**, 46, 5768–5771.

(54) Lee, Y.; Mankad, N. P.; Peters, J. C. Triggering N_2 Uptake via Redox-Induced Expulsion of Coordinated NH_3 and N_2 Silylation at Trigonal Bipyramidal Iron. *Nature Chem*. **2010**, 2, 558–565.

(55) Rittle, J.; Peters, J. C. Fe–N_2/CO Complexes that Model a Possible Role for the Interstitial C Atom of FeMo-cofactor (FeMoco). *Proc. Natl. Acad. Sci. U.S.A.* **2013**, 110, 15898–15903.

(56) DAVE: A comprehensive software suite for the reduction, visualization, and analysis of low energy neutron spectroscopic data, Azuah, R. T.; Kneller, L. R.; Qiu, Y.; Tregenna-Piggott, P. L. W.; Brown, C. M.; Copley, J. R. D.; Dimeo, R. M. *J. Res. Natl. Inst. Stan. Technol.* **2009**, 114, 341.

(57) Chilton, N. F.; Anderson, R. P.; Turner, L. D.; Soncini, A.; Murray, K. S. PHI: A Powerful New Program for the Analysis of Anisotropic Monomeric and Exchange-Coupled Polynuclear *d*- and *f*-block Complexes. *J. Comput. Chem.* **2013**, 34, 1164–1175.

(58) Axtmann, R. C.; Hazony, Y.; Hurley, J. W. 3d Electron Delocalization from Mössbauer Measurements on Ferrous Halides. *Chem. Phys. Lett.* **1968**, 2, 673–676.

(59) Sawatzky, G. A.; van der Woude, F. Covalency Effects in Divalent Iron Compounds. *Chem. Phys. Lett.* **1969**, 4, 335–337.

(60) Levason, W.; Ogden, J. S.; Spicer, M. D. Coordination Chemistry of Higher Oxidation States. 30. Five-Coordinate Cobalt(III) Phosphine Complexes. Spectroscopic and Cobalt K-Edge EXAFS Studies. *Inorg. Chem.* **1989**, 28, 2128–2131.

(61) Whangbo, M.-H.; Gordon, E. E.; Xiang, H.; Koo, H.-J.; Lee, C. Prediction of Spin Orientations in Terms of HOMO-LUMO Interactions Using Spin-Orbit Coupling as Perturbation. *Acc. Chem. Res.* **2015**, 48, 3080–3087.

(62) Ruamps, R.; Batchelor, L. J.; Guillot, R.; Zakhia, G.; Barra, A.-L.; Wernsdorfer, W.; Guihéry, N.; Mallah, T. Ising-Type Magnetic Anisotropy and Single Molecule Magnet Behavior in Mononuclear Trigonal Bipyramidal Co(II) Complexes. *Chem. Sci.* **2014**, 5, 3418–3424.

(63) Shao, F.; Cahier, B.; Guihéry, N.; Riviére, E.; Guillot, R.; Barra, A.-L.; Lan, Y.; Wernsdorfer, W.; Campbell, V. E.; Mallah, T. Tuning the Ising-Type Anisotropy in Trigonal Bipyramidal Co(II) Complexes. *Chem. Commun.* **2015**, 51, 16475–16478.

(64) Cahier, B.; Maurice, R.; Bolvin, H.; Mallah, T.; Guihéry, N. Tools for Predicting the Nature and Magnitude of Magnetic Anisotropy in Transition Metal Complexes: Application to Co(II) Complexes. *Magnetochemistry* **2016**, 2, 31.

(65) Woods, T. J.; Ballesteros-Rivas, M. F.; Gómez-Coca, S.; Ruiz, E.; Dunbar, K. R. Relaxation Dynamics of Identical Trigonal Bipyramidal Cobalt Molecules with Different Local Symmetries and Packing Arrangements: Magnetostructural Correlations and *ab initio* Calculations. *J. Am. Chem. Soc.* **2016**, 138, 16407–16416.

(66) Schweinfurth, D.; Sommer, M. G.; Atanasov, M.; Demeshko, S.; Hohloch, S.; Meyer, F.; Neese, F.; Sarkar, B. The Ligand Field of the Azido Ligand: Insights into Bonding Parameters and Magnetic Anisotropy in a Co(II)-Azido Complex. *J. Am. Chem. Soc.* **2015**, 137, 1993–2005.

(67) Rudd. P. A.; Liu, S.; Gagliardi, L.; Young, V. G.; Lu, C. C. Metal-Alane Adducts with Zero-Valent Nickel, Cobalt, and Iron. *J. Am. Chem. Soc.* **2011**, 133, 20724–20727.

(68) Ward, A. L.; Lukens, W. W.; Lu, C. C.; Arnold, J. Photochemical Route to Actinide-Transition Metal Bonds: Synthesis, Characterization and Reactivity of a Series of Thorium and Uranium Heterobimetallic Complexes. *J. Am. Chem. Soc.* **2014**, 136, 3647–3654.

(69) Bain, G. A.; Berry, J. F. Diamagnetic Corrections and Pascal's Constants. *J. Chem. Educ.* **2008**, 85, 532–536.

(70) APEX2, v. 2009; Bruker Analytical X-ray Systems, Inc.: Madison, WI, 2009.

(71) Sheldrick, G. M. SADABS, Version2.03; Bruker Analytical X-ray Systems, Inc.: Madison, WI, 2000.

(72) Sheldrick, G. M. SHELXTL, Version 6.12; Bruker Analytical X-ray Systems, Inc.: Madison, WI, 2000.

(73) Farrugia, L. J. *WinGX* Suite for Small-Molecule Single-Crystal Crystallography. *J. Appl. Cryst.* **1999**, 32, 837–838.

(74) Perdew, J. P; Burke, K. Ernzerhof, M. Generalized Gradient Approximation Made Simple. *Phys. Rev. Lett.* **1996**, 77, 3865 – 3868.

(75) Weigend, F.; Ahlrichs, F. Balanced Basis Sets of Split Valence, Triple Zeta Valence and Quadruple Zeta Valence Quality for H to Rn: Design and Assessment of Accuracy. *Phys. Chem. Chem. Phys.* **2005**, **7**, 3297–3305.

(76) TURBOMOLE V6.5 2013, a development of University of Karlsruhe and Forschungszentrum Karlsruhe GmbH, 1989-2007, TURBOMOLE GmbH, since 2007; available from http://www.turbomole.com.

(77) Eichkorn, K.; Weigend, F.; Treutler, O.; Ahlrichs, R. Auxiliary Basis Sets for Main Row Atoms and Transition Metals and Their Use to Approximate Coulomb Potentials. *Theor. Chem. Acc.* **1997**, 97, 119 – 124.

(78) Eichkorn, K.; Treutler, O.; Ohm, H.; Haser, M.; Ahlrichs, R. Auxiliary Basis Sets to Approximate Coulomb Potentials. *Chem. Phys. Lett.* **1995**, 240, 283 – 289.

(79) Von Arnim, M.; Ahlrichs, R. Performance of Parallel TURBOMOLE for Density Functional Calculations. *J. Comput. Chem.* **1998**, 19, 1746 – 1757.

(80) Roos, B. O.; Taylor, P. R.; Siegbahn, P. E. M. A Complete Active Space SCF Method (CASSCF) Using a Density Matrix Formulated Super-CI Approach. *Chemical Physics* **1980,** *48*, 157-173.

(81) Andersson, K.; Malmqvist, P. Å.; Roos, B. O. Second-Order Perturbation Theory with a Complete Active Self-Consistent Field Reference Function. *The Journal of Chemical Physics* **1992,** *96*, 1218-1226.

(82) Andersson, K.; Malmqvist, P. A.; Roos, B. O.; Sadlej, A. J.; Wolinski, K. Second-Order Perturbation Theory with a CASSCF Reference Function. *The Journal of Physical Chemistry* **1990,** *94*, 5483-5488.

(83) Aquilante, F.; Autschbach, J.; Carlson, R. K.; Chibotaru, L. F.; Delcey, M. G.; De Vico, L.; Fdez. Galván, I.; Ferré, N.; Frutos, L. M.; Gagliardi, L.; Garavelli, M.; Giussani, A.; Hoyer, C. E.; Li Manni, G.; Lischka, H.; Ma, D.; Malmqvist, P. Å.; Müller, T.; Nenov, A.; Olivucci, M.; Pedersen, T. B.; Peng, D.; Plasser, F.; Pritchard, B.; Reiher, M.; Rivalta, I.; Schapiro, I.; Segarra-Martí, J.; Stenrup, M.; Truhlar, D. G.; Ungur, L.; Valentini, A.; Vancoillie, S.; Veryazov, V.; Vysotskiy, V. P.; Weingart, O.; Zapata, F.; Lindh, R. MOLCAS 8: New Capabilities for

Multiconfigurational Quantum Chemical Calculations Across the Periodic Table. *Journal of Computational Chemistry* **2016,** *37*, 506-541.

(84) Douglas, M.; Kroll, N. M. Quantum Electrodynamical Corrections to the Fine Structure of Helium. *Annals of Physics* **1974,** *82*, 89-155.

(85) Hess, B. Relativistic Electronic-Structure Calculations Employing a Two-Component No-Pair Formalism with External-Field Projection Operators. *Physical Review A* **1986,** *33*, 3742-3748.

(86) Roos, B. O.; Lindh, R.; Malmqvist, P.-Å.; Veryazov, V.; Widmark, P.-O., Main Group Atoms and Dimers Studied with a New Relativistic ANO Basis Set. *The Journal of Physical Chemistry A* **2004,** *108*, 2851-2858.

(87) Roos, B. O.; Lindh, R.; Malmqvist, P.-Å.; Veryazov, V.; Widmark, P.-O. New Relativistic ANO Basis Set for Transition Metal Atoms. *The Journal of Physical Chemistry A* **2005,** *109*, 6575-6579.

(88) Aquilante, F.; Gagliardi, L.; Pedersen, T. B.; Lindh, R. Atomic Cholesky Decompositions: A Route to Unbiased Auxiliary Basis Sets for Density Fitting Approximation with Tunable Accuracy and Efficiency. *J. Chem. Phys.* **2009**, 130, 154107.

(89) Aquilante, F.; Lindh, R.; Pedersen, T. B. Analytic Derivatives for the Cholesky Representation of the Two-Electron Integrals. *J. Chem. Phys.* **2008**, 129, 034106.

(90) Aquilante, F.; Malmqvist, P. A.; Pedersen, T. B.; Ghosh, A.; Roos, B. O. Cholesky Decomposition-Based Multiconfiguration Second-Order Perturbation Theory (CD-CASPT2): Application to the Spin-State Energetics of Co^{II}(diiminato)(NPh). *J. Chem. Theory Comput.* **2008**, 4, 694 – 702.

(91) Aquilante, F.; Pedersen, T. B.; Lindh, R. Low-Cost Evaluation of the Exchange Fock Matrix from Cholesky and Density Fitting Representations of the Electron Repulsion Integrals. *J. Chem. Phys.* **2007**, 126, 194106.

(92) Gagliardi, L.; Lindh, R.; Karlström, G. J. Local Properties of Quantum Chemical Systems: The LoProp Approach. *Chem. Phys.* **2004**, 121, 4494−4500.

(93) Mulliken, R. Electronic Population Analysis on LCAO-MO Molecular Wave Functions. 1. *J. Chem. Phys*. **1955**, 23, 1833−1840.

(94) Hirshfeld, F. L. Bonded-Atom Fragments for Describing Molecular Charge Densities. *Theor. Chim. Acta* **1977**, 44, 129−138.

(95) Mayer, I. Charge, Bond Order and Valence in the AB initio SCF Theory. *Chem. Phys. Lett.* **1983**, 97, 270−274.

(96) Lu, T.; Chen, F. Multiwfn: A Multifunctional Wavefunction Analyzer. *J. Comp. Chem.* **2012**, 33, 580-592.

References for Chapter Four

(1) Maser, L.; Schneider, C.; Vondung, L.; Alig, L.; Langer R. Quantifying the Donor Strength of Ligand-Stabilized Main Group Fragments. *J. Am. Chem. Soc.* **2019**, Article ASAP, DOI: 10.1021/jacs.9b02598.

(2) Winterhalter, U.; Zsolnai, L.; Kircher, P.; Heinze, K.; Huttner, G. Reductive Activation of Tripod Cobalt Compounds: Oxidative Additions of H-H, P-H, and Sn-H Functions. Eur. J. *Inorg. Chem.* **2001**, 89–103.

(3) Uehara, K.; Hikichi, S.; Akita, M. Highly Labile Cationic tris-acetonitrile Complexes, $[Tp^{R}M(NCMe)_3]OTf$ (M = Ni, Co; Tp^{R}: hydrotrispyrazolylborato, R = Ph, Me, and iPr_2): Versatile Precursors for TpR-Containing Nickel and Cobalt Complexes. *J. Chem. Soc., Dalton Trans.* **2002**, 3529–3538.

(4) Whangbo, M.-H.; Gordon, E. E.; Xiang, H.; Koo, H.-J.; Lee, C. Prediction of Spin Orientations in Terms of HOMO-LUMO Interactions Using Spin-Orbit Coupling as a Perturbation. *Acc. Chem. Res.* **2015**, 48, 3080–3087.

(5) Cahier, B.; Maurice, R.; Bolvin, H.; Mallah, T.; Guihéry, N. Tools for Predicting the Nature and Magnitude of Magnetic Anisotropy in Transition Metal Complexes: Application to Co(II) Complexes. *Magnetochemistry* **2016**, 2, 31.

(6) Kameo, H.; Ishii, S.; Nakazawa, H. Synthesis and Reactivity of Rhodium Complexes Bearing $[E(o\text{-}C_6H_4PPh_2)_3]$-Type Tetradentate Ligands (E = Si, Ge, and Sn) *Organometallics* **2012**, 31, 2212–2218.

(7) Kameo, H.; Ishii, S.; Nakazawa, H. Synthesis of Iridium Complexes Bearing $\{o\text{-}Ph_2P)C_6H_4\}_3E$ type (E = Si, Ge, and Sn) Ligand and Evaluation of Electron Donating Ability of Group 14 Elements E. *Dalton Trans.* **2012**, 41, 8290–8296.

(8) Graham, W. A. G. An Approach to the Separation of Inductive and Mesomeric Effects in Complexes of the Types $LMn(CO)_5$ and $LMo(CO)_5$. *Inorg. Chem.* **1968**, 7, 315–321.

(9) Watters, K. L.; Butler, W. M.; Risen Jr., W. M. Spectroscopic Studies of Metal-Metal Bonding. II. The Variation of Metal-Metal Bond Strengths with Substituents from the Vibrational Analyses of $X_3MCo(CO)_4$ (M = Sn, Ge; X = I, Br, Cl). *Inorg. Chem.* **1971**, 10, 1970–1978.

(10) Bancroft, G. M.; Clark, H. C.; Kidd, R. G.; Rake, A. T.; Spinney, H. G. Manganese-55 Nuclear Magnetic Resonance Studies of Compounds Containing Mn-M (M = Si, Ge, Sn, Pb) Bonds and the Signs of e^2qQ in Manganese(I) Compounds. *Inorg. Chem.* **1973**, 12, 728– 731.

(11) Terzis, A.; Strekas, T. C.; Spiro, T. G. Raman Spectra and Metal-Metal Bonding in the Molecules X_3M'-$M(CO)_5$ (X = CH_3, Cl; M' = Ge, Sn; M = Mn, Re). *Inorg. Chem.* **1974**, 13, 1346–1349.

(12) Figgis, B. N; Hitchman, M. A. *Ligand Field Theory and its Applications*; Wiley-VCH: New Yor, 2000.

(13) Telser, J. A Perspective on Applications of Ligand-Field Analysis: Inspiration from Electron Paramagnetic Resonance Spectroscopy of Coordination Complexes of Transition Metal Ions. *J. Braz. Chem. Soc.* **2006**, 17, 1501–1505.

(14) Bucinsky, L.; Breza, M.; Malček, M.; Power, D. C.; Hwang, S. J.; Krzystek, J.; Nocera, D. G.; Telser, J. High-Frequency and -Field EPR (HFEPR) Investigation of a Pseudotetrahedral Cr^{IV} Siloxide Complex and Computational Studies of Related $Cr^{IV}L_4$ Systems. *Inorg. Chem.* **2019**, 58, 4907–4920.

(15) Krzystek, J.; Swenson, D. C.; Zvyagin, S. A.; Smirnov, D.; Ozarowski, A.; Telser, J. Cobalt(II) "Scorpionate" Complexes as Models for Cobalt-Substituted Zinc Enzymes: Electronic Structure Investigation by High-Frequency and -Field Electron Paramagnetic Resonance Spectroscopy. *J. Am. Chem. Soc.* **2010**, 132, 5241–5253.

(16) Bain, G. A.; Berry, J. F. Diamagnetic Corrections and Pascal's Constants. *J. Chem. Educ.* **2008**, 85, 532–536.

(17) Stoll, S.; Schweiger, A. EasySpin, a Comprehensive Software Package for Spectral Simulation and Analysis in EPR. *J. Magn. Reson.* **2006**, 178, 42–55.

(18) APEX3, v. 2017.3; Bruker Analytical X-ray Systems, Inc.: Madison, WI, 2017.

(19) Sheldrick, G. M. SADABS, Version 2.03; Bruker Analytical X-ray Systems, Inc.: Madison, WI, 2000.

(20) Sheldrick, G. M. SHELXTL, Version 6.12; Bruker Analytical X-ray Systems, Inc.: Madison, WI, 2000.

(21) Farrugia, L. J. *WinGX* Suite for Small-Molecule Single-Crystal Crystallography. *J. Appl. Cryst.* **1999**, 32, 837–838.

(22) Figgis, B. N.; Hitchman, M. A. *Ligand Field Theory and its Applications*; Wiley-VCH: New York, 2000.

References for Chapter Five

(1) Gatteschi, D.; Kahn, O.; Miller, J. S.; Palacio, F. *Magnetic Molecular Materials*; Springer Science & Business Media, 2012; Vol. 198.

(2) Kahn, O. *Molecular Magnetism*; VCH: Weinheim, Germany, 1993.

(3) Eaton, S. S.; Eaton, G. R. In *Biological Magnetic Resonance*; Berliner, L. J., Eaton, S. S., Eaton, G. R., Eds.; Klewer Academic/Plenum Publishers: New York, 2000; Vol. 19, Distance Measurments in Biological Systems by EPR, pp 29−154.

(4) Marian, C. M. Spin-Orbit Coupling and Intersystem Crossing in Molecules. *WIREs Comput. Mol. Sci.* **2012**, 2, 187−203.

(5) Tao, Y.; Yuan, K.; Chen, T.; Xu, P.; Li, H.; Chen, R.; Zheng, C.; Zhang, L.; Huang, W. Thermally Activated Delayed Fluorescence Materials towards the Breakthrough of Organoelectronics. *Adv. Mater.* **2014**, 26, 7931–7958.

(6) Yersin, H.; Rausch, A. F.; Czerwieniec, R.; Hofbeck, T.; Fischer, T. The Triplet State of Organo-Transition Metal Compounds. Triplet Harvesting and Singlet Harvesting for Efficient OLEDs. *Coord. Chem. Rev.* **2011**, 255, 2622–2652.

(7) Danovich, D.; Shaik, S. Spin- Orbit Coupling in the Oxidative Activation of H- H by FeO^+. Selection Rules and Reactivity Effects. *J. Am. Chem. Soc.* **1997**, 119, 1773–1786.

(8) Schröder, D.; Shaik, S.; Schwarz, H. Two-State Reactivity as a New Concept in Organometallic Chemistry. *Acc. Chem. Res.* **2000**, 33, 139–145.

(9) Poli, R.; Harvey, J. N. Spin Forbidden Chemical Reactions of Transition Metal Compounds. New Ideas and New Computational Challenges. *Chem. Soc. Rev.* **2003**, 32, 1–8.

(10) Bellows, S. M.; Cundari, T. R.; Holland, P. L. Spin-Crossover During β-Hydride Elimination in High-Spin Fe(II)- and Co(II)-Alkyl Complexes. *Organometallics*, **2013**, 32, 4741−4751.

(11) Sun, Y.; Tang, H.; Chen, K.; Hu, L.; Yao, J.; Shaik, S.; Chen, H. Two-state Reactivity in Low-Valent Iron-Mediated C-H Activation and the Implications for Other First-Row Transition metals. *J. Am. Chem. Soc.* **2016**, 138, 3715−3730.

(12) Pyykkö, P. The Physics Behind Chemistry and the Periodic Table. *Chem. Rev.* **2012**, 112, 371−384

(13) Pyykkö, P. Relativistic Effects in Chemistry: More Common Than You Thought. *Annu. Rev. Phys. Chem.* **2012**, 63, 45−64.

(14) Kasha, M. Collisional Perturbation of Spin-Orbital Coupling and the Mechanism of Fluorescence Quenching. A Visual Demonstration of the Perturbation. *J. Chem. Phys.* **1952**, 20, 71–74.

(15) Koziar, J. C.; Cowan, D. O. Photochemical Heavy-Atom Effects. *Acc. Chem. Res.* **1978**, 11, 334–341.

(16) Zein, S.; Duboc, C.; Lubitz, W.; Neese, F. A Systematic Density Functional Study of the Zero-Field Splitting in Mn(II) Coordination Compounds. *Inorg. Chem.* **2008**, 47, 134−142.

(17) Karunadasa, H. I.; Arquero, K. D.; Berben, L. A.; Long, J. R. Enhancing the Magnetic Anisotropy of Cyano-Ligated Chromium(II) and Chromium(III) Complexes via Heavy Halide Ligand Effects. *Inorg. Chem.* **2010**, 49, 4738−4740.

(18) Ye, S.; Neese, F. How Do Heavier Halide Ligands Affect the Signs and Magnitudes of the Zero-Field Splittings in Halogenonickel(II) Scorpionate Complexes? A Theoretical Investigation Coupled to Ligand-Field Analysis. *J. Chem. Theory Comput.* **2012**, 8, 2344−2351.

(19) Zadrozny, J. M.; Telser, J.; Long, J. R. Slow Magnetic Relaxation in the Tetrahedral Cobalt(II) Complexes [Co(EPh4)]2− (E = O, S, Se). *Polyhedron* **2013**, 64, 209−217.

(20) Saber, M. R.; Dunbar, K. R. Ligands Effects on the Magnetic Anisotropy of Tetrahedral Cobalt Complexes. *Chem. Commun.* **2014**, 50, 12266−12269.

(21) Wang, L.; Zlatar, M.; Vlahović, F.; Demeschko, S.; Philouze, C.; Molton, F.; Gennari, M.; Meyer, F.; Duboc, C.; Gruden, M. Experimental and Theoretical Identification of the Origin of Magnetic Anisotropy in Intermediate Spin Iron(III) Complexes. *Chem. Eur. J.* **2018**, 24, 5091–5094.

(22) Coste, S. C.; Vlaisavljevich, B.; Freedman, D. E. Magnetic Anisotropy from Main-Group Elements: Halides versus Group 14 Elements. *Inorg. Chem.* **2017**, 56, 8195–8202.

(23) Brazzolotto, D.; Gennari, M.; Yu, S.; Pécaut, J.; Rouziéres, M.; Clérac, R.; Orio, M.; Duboc, C. An Experimental and Theoretical Investigation on Pentacoordinated Cobalt(III) Complexes with an Intermediate S = 1 Spin State: How Halide Ligands Affect their Magnetic Anisotropy. *Chem. Eur. J.* **2016**, 22, 925–933.

(24) Coste, S. C.; Pearson, T. J.; Freedman, D. E. Magnetic Anisotropy in Heterobimetallic Complexes. *Inorg. Chem.* **2019**, *accepted.*

(25) Kameo, H.; Ishii, S.; Nakazawa, H. Synthesis and Reactivity of Rhodium Complexes Bearing [E(o-$C_6H_4PPh_2)_3$]-Type Tetradentate Ligands (E = Si, Ge, and Sn) *Organometallics* **2012**, 31, 2212–2218.

(26) Kameo, H.; Ishii, S.; Nakazawa, H. Synthesis of Iridium Complexes Bearing {o-$Ph_2P)C_6H_4\}_3$E type (E = Si, Ge, and Sn) Ligand and Evaluation of Electron Donating Ability of Group 14 Elements E. *Dalton Trans.* **2012**, 41, 8290–8296.

(27) Graham, W. A. G. An Approach to the Separation of Inductive and Mesomeric Effects in Complexes of the Types $LMn(CO)_5$ and $LMo(CO)_5$. *Inorg. Chem.* **1968**, 7, 315–321.

(28) McSkimming, A.; Harman, W. H. A Terminal N_2 Complex of High-Spin Iron(I) in a Weak, Trigonal Ligand Field. *J. Am. Chem. Soc.* **2015**, 137, 8940–8943.

(29) Uehara, K.; Hikichi, S.; Akita, M. Highly Labile Cationic Tris-Acetonitrile Complexes, $[Tp^RM(NCMe)_3]OTf$ (M = Ni, Co; Tp^R: hydrotrispyrazolylborato, R = Ph, Me and iPr_2): Versatile Precursors for Tp^R-Containing Nickel and Cobalt Complexes. *J. Chem. Soc., Dalton Trans.* **2002**, 3529–3538.

(30) Abubekerov, M.; Gianetti, T. L.; Kunishita, A.; Arnold, J. Synthesis and Characterization of Coordinatively Unsaturated Nickel(II) and Manganese(II) Alkyl Complexes Supported by the hydrotris(3-phenyl-5-methylpyrazolyl)borate ($Tp^{Ph,Me}$) Ligand. *Dalton Trans.* **2013**, 42, 10525–10532.

(31) Cordero, B.; Gómez, V.; Platero-Prats, A. E.; Revés, M.; Echeverría, J.; Cremades, E.; Barragán, F.; Alvarez, S. Covalent Radii Revisited. *Dalton Trans.*, **2008**, 2832–2838.

(32) Cotton, F. A.; Murillo, C. A.; Walton, R. A. *Multiple Bonds Between Metal Atoms*, 3rd Ed.; Springer: New York, 2005.

(33) Solomon, E. I.; Hedman, B.; Hodgson, K. O.; Dey, A.; Szilagyi, R. K. Ligand K-edge X-ray Absorption Spectroscopy: Covalency of Ligand-Metal Bonds. Coord. Chem. Rev. 2005, 249, 97–129.

(34) Farges, F.; Linnen, R. L.; Brown Jr., G. E. Redox and Speciation of Tin in Hydrous Silicate Glasses: A Comparison with Nb, Ta, Mo, and W. *Can. Mineral.* **2006**, 44, 795–810.

(35) Aluri, E. R.; Grosvenor, A. P. An X-ray Absorption Spectroscopic Study of the Effect of Bond Covalency on the Electronic Structure of $Gd_2Ti_{2-x}Sn_xO_7$. *Phys. Chem. Chem. Phys.* **2013**, 15, 10477–10486.

(36) Wang, H.-T.; Srivastava, M. K.; Wu, C.-C.; Hsieh, S.-H.; Wang, Y.-F.; Shao, Y.-C.; Liang, Y.-H.; Du, C.-H.; Chiou, J.-W.; Cheng, C.-M.; Chen, J.-L.; Pao, C.-W.; Lee, J.-F.; Kuo, C. N.; Lue, C. S.; Wu, M.-K.; Pong, W.-F. Electronic and Atomic Structures of the $Sr_3Ir_4Sn_{13}$ Single Crystal: A Possible Charge Density Wave Material. *Sci. Rep.* **2017**, 7, 40886.

(37) Masai, H.; Ina, T.; Okumura, S.; Mibu, K. Validity of Valence Estimation of Dopants in Glasses Using XANES Analysis. *Sci. Rep.* **2018**, 8, 415.

(38) Holt, M. S.; Wilson, W. L.; Nelson, J. H. Transition Metal-Tin Chemistry. *Chem. Rev.* **1989**, 89, 11–49.

(39) Stoll, S.; Schweiger, A. EasySpin, A Comprehensive Software Package for Spectra Simulation and Analysis in EPR. *J. Magn. Reson.* **2006**, 178, 42–55.

(40) Lee, V. Y.; Sekiguchi, A. Organometallic Compounds of Low-Coordinate Si, Ge, Sn, and Pb; John Wiley and Sons: West Sussex, UK, 2010.

(41) Jain, V. K.; Lehmann, G. Electron Paramagnetic Resonance of Mn^{2+} in Orthorhombic and Higher Symmetry Crystals. *Phys. Stat. Sol. B* **1990**, 159, 495–544.

(42) Duboc, C. Determination and Prediction of the Magnetic Anisotropy of Mn Ions. *Chem. Soc. Rev.* **2016**, 45, 5834–5847.

(43) Açikgöz, M. An Investigation on the Temperature Dependent Zero-Field Splitting (ZFS) of Mn^{2+} doped $Cs_2NaLaCl_6$. *Opt. Mater.* **2015**, 47, 285–291.

(44) Azuah, R. T.; Kneller, L. R.; Qiu, Y.; Tregenna-Piggott, P. L. W.; Brown, C. M.; Copley, J. R. D.; Dimeo, R. M. DAVE: A Comprehensive Software Suite for the Reduction, Visualization, and Analysis of Low Energy Neutron Spectroscopic Data. *J. Res. Natl. Inst. Stand. Technol.* 2009, **114**, 341–358.

(45) Freedman, D. E.; Harman, W. H.; Harris, T. D.; Long, G. J.; Chang, C. J.; Long, J. R. Slow Magnetic Relaxation in a High-Spin Iron(II) Complex. *J. Am. Chem. Soc.* **2010**, 132, 1224–1225.

(46) Harman, W. H.; Harris, T. D.; Freedman, D. E.; Fong, H.; Chang, A.; Rinehart, J. D.; Ozarowski, A.; Sougrati, M. T.; Grandjean, F.; Long, G. J.; Long, J. R.; Chang, C. J. Slow Magnetic Relaxation in a Family of Trigonal Pyramidal Iron(II) Pyrrolide Complexes. *J. Am. Chem. Soc.* **2010**, 132, 18115–18126.

(47) Pinkowicz, D.; Birk, F. J.; Magott, M.; Schulte, K.; Dunbar, K. R. Systematic Study of Open-Shell Trigonal Pyramidal Transition-Metal Complexes with a Rigid-Ligand Scaffold. *Chem. Eur. J.* **2017**, 23, 3548–3552.

(48) Popescu, C. V.; Mock, M. T.; Stoian, S. A.; Dougherty, W. G.; Yap, G. P. A.; Riordan, C. G. A High-Spin Organometallic Fe-S Compound: Structural and Mössbauer Spectroscopic Studies of [Phenyltris(tert-butylthio)methyl)borate]Fe(Me). *Inorg. Chem.* **2009**, 48, 8317–8324.

(49) Champion, P. M.; Sievers, A. J. Far Infrared Magnetic Resonance in $FeSiF_6 \cdot 6H_2O$ and $Fe(SPh)_4^{2-}$. *J. Chem. Phys.* **1977**, 66, 1819–1825.

(50) Coucouvanis, D.; Swenson, D.; Baenziger, N. C.; Murphy, C.; Holah, D. G.; Sfarnas, N.; Simopoulos, A.; Kostikas, A. Tetrahedral Complexes Containing the $Fe(II)S_4$ Core. The Syntheses, Ground-State Electronic Structures and Crystal and Molecular Structures of the bis(tetraphenylphosphonium) tetrakis(thiophenolato)ferrate(II) and bis(tetraphenylphosphonium) bis(dithiosquarato)ferrate(II) Complexes. An Analog for the Active Site in Reduced Rubredoxins (Rdred). *J. Am. Chem. Soc.* **1981**, 103, 3350–3362.

(51) Knapp, M. J.; Krzystek, J.; Brunel, L.-C.; Hendrickson, D. N. High-Frequency EPR Study of the Ferrous Ion in the Reduced Rubredoxin Model $[Fe(SPh)_4]^{2-}$. *Inorg. Chem.* **2000**, 39, 281–288.

(52) Barra, A. L.; Hassan, A. K.; Janoschka, A.; Schmidt, C. L.; Schünemann, V. Broad-Band Quasi-Optical HF-EPR Spectroscopy: Application to the Study of the Ferrous Iron Center from a Rubredoxin Mutant. *Appl. Magn. Reson.* **2006**, 30, 385–397.

(53) Mathies, G.; Chatziefthimiou, S. D.; Maganas, D.; Sanakis, Y.; Sottini, S.; Kyritsis, P.; Groenen, E. J. J. High-Frequency EPR Study of the High-Spin FeII Complex $Fe[(SPPh_2)_2N]_2$. *J. Magn. Reson.* **2012**, 224, 94–100.

(54) Zadrozny, J. M.; Greer, S. M.; Hill, S.; Freedman, D. E. A Flexible Iron(II) Complex in which Zero-Field Splitting is Resistant to Structural Variation. *Chem. Sci.* **2016**, 7, 416–423.

(55) Desrochers, P. J.; Telser, J.; Zvyagin, S. A.; Ozarowski, A.; Krzystek, J.; Vivic, D. A. Electronic Structure of Four-Coordinate C_{3v} Nickel(II) Scorpionate Complexes: Investigation by High-Frequency and -Field Electron Paramagnetic Resonance and Electronic Absorption Spectroscopies. *Inorg. Chem.* **2006**, 45, 8930–8941.

(56) Rose, M. J.; Bellone, D. E.; Di Bilio, A. J.; Gray, H. B. Spectroscopic and Magnetic Properties of an Iodo Co^{I} Tripodal Phosphine Complex. *Dalton Trans.* **2012**, 41, 11788–11797.

(57) Krzystek, J.; Ozarowski, A.; Zvyagin, S. A.; Telser, J. High Spin Co(I): High-Frequency and -Field EPR Spectroscopy of $CoX(PPh_3)_3$ (X = Cl, Br). *Inorg. Chem.* **2012**, 51, 4954–4964.

(58) Tereniak, S. J.; Carlson, R. K.; Clouston, L. J.; Young Jr., V. G.; Bill, E.; Maurice, R.; Chen, Y.-S.; Kim, H. J.; Gagliardi, L.; Lu, C. C. Role of the Metal in the Bonding and Properties of

Bimetallic Complexes Involving Manganese, Iron, and Cobalt. *J. Am. Chem. Soc.* **2014**, 136, 1842−1855.

(59) Eisenhart, R. J.; Carlson, R. K.; Clouston, L. J.; Young Jr., V. G.; Chen, Y.-S.; Bill, E.; Gagliardi, L.; Lu, C. C. Influence of Copper Oxidation State on the Bonding and Electronic Structure of Cobalt-Copper Complexes. *Inorg. Chem.* **2015**, 54, 11330−11338.

(60) Lever, A. B. P. *Inorganic Electronic Spectroscopy*; Elsevier Science Publishers B. V.: Amsterdam, 1984.

(61) Scepaniak, J. J.; Harris, T. D.; Vogel, C. S.; Sutter, J.; Meyer, K.; Smith, J. M. Spin Crossover in a Four-Coordinate Iron(II) Complex. *J. Am. Chem. Soc.* **2011**, 133, 3824–3827.

(62) Creutz, S. E.; Peters, J. C. Spin-State Tuning at Pseudo-tetrahedral d^6 Ions: Spin Crossover in $[BP_3]Fe^{II}$-X Complexes. *Inorg. Chem.* **2016**, 55, 3894–3906.

(63) Kostikas, A.; Petrouleas, V.; Simopolous, A.; Coucouvanis, D.; Holah, D. G. Mössbauer Effect in Synthetic Analogs of Rubredoxin. *Chem. Phys. Lett.* **1976**, 38, 582–584.

(64) Werth, M. T.; Kurtz, D. M.; Howes, B. D.; Boi, H. H. Observation of $S = 2$ EPR Signals from Ferrous Iron-Thiolate Complexes. Relevance to Rubredoxin-type Sites in Proteins. *Inorg. Chem.* **1989**, 28, 1357−1361.

(65) Vrajmasu, V. V.; Bominaar, E. L; Meyer, J.; Münck, E. Mössbauer Study of Reduced Rubredoxin As Purified and in Whole Cells. Structural Correlation Analysis of Spin Hamiltonian Parameters. *Inorg. Chem.* **2002**, 41, 6358−6371.

(66) Jacques, A.; Clémancey, M.; Blondin, G.; Fourmond, V.; Latour, J.-M.; Sénèque, O. A Cyclic Peptide-based Redox-active Model of Rubredoxin. *Chem. Commun.* **2013**, 49, 2915−2917.

(67) Edwards, P. R.; Johnson, C. E.; Williams, R. J. P. Mössbauer Spectra of Some Tetrahedral Iron (II) Compounds. *J. Chem. Phys.* **1967**, 47, 2074−2082.

(68) Moore, C. E.; Ionization Potentials and Limits Derived from the Analyses of Optical Spectra; NSRDS-NBS 34, National Bureau of Standards: Washington DC, 1970.

(69) Whangbo, M.-H.; Gordon, E. E.; Xiang, H.; Koo, H.-J.; Lee, C. Prediction of Spin Orientations in Terms of HOMO-LUMO Interactions Using Spin-Orbit Coupling as a Perturbation. *Acc. Chem. Res.* **2015**, 48, 3080–3087.

(70) Puerta, D. T.; Cohen, S. M. $[(Tp^{Me,Ph})_2Zn_2(H_3O_2)]ClO_4$: A New H_3O_2 Species Relevant to Zinc Proteinases. *Inorg. Chim. Acta* **2002**, 337, 459−462.

(71) McSkimming, A.; Harman, W. H. A Terminal N_2 Complex of High-Spin Iron(I) in a Weak, Trigonal Ligand Field. *J. Am. Chem. Soc.* **2015**, 137, 8940–8943.

(72) Uehara, K.; Hikichi, S.; Akita, M. Highly Labile Cationic Tris-Acetonitrile Complexes, $[Tp^RM(NCMe)_3]OTf$ (M = Ni, Co; Tp^R: hydrotrispyrazolylborato, R = Ph, Me and iPr_2): Versatile Precursors for Tp^R-Containing Nickel and Cobalt Complexes. *J. Chem. Soc., Dalton Trans.* **2002**, 3529–3538.

(73) Abubekerov, M.; Gianetti, T. L.; Kunishita, A.; Arnold, J. Synthesis and Characterization of Coordinatively Unsaturated Nickel(II) and Manganese(II) Alkyl Complexes Supported by the hydrotris(3-phenyl-5-methylpyrazolyl)borate ($Tp^{Ph,Me}$) Ligand. *Dalton. Trans.* **2013**, 42, 10525–10532.

(74) Bain, G. A.; Berry, J. F. Diamagnetic Corrections and Pascal's Constants. *J. Chem. Educ.* **2008**, 85, 532–536.

(75) APEX3, v. 2017.3; Bruker Analytical X-ray Systems, Inc.: Madison, WI, 2017.

(76) Sheldrick, G. M. SADABS, Version2.03; Bruker Analytical X-ray Systems, Inc.: Madison, WI, 2000.

(77) Sheldrick, G. M. SHELXTL, Version 6.12; Bruker Analytical X-ray Systems, Inc.: Madison, WI, 2000.

(78) Farrugia, L. J. *WinGX* Suite for Small-Molecule Single-Crystal Crystallography. *J. Appl. Cryst.* **1999**, 32, 837–838.

(79) Stoll, S.; Schweiger, A. EasySpin, a Comprehensive Software Package for Spectral Simulation and Analysis in EPR. *J. Magn. Reson.* **2006**, 178, 42–55.